日本原子力研究開発機構

JAEA-Tokai Tandem Annual Report 2009

April 1, 2009 – March 31, 2010

Department of Research Reactor and Tandem Accelerator

Nuclear Science Research Institute
Tokai Research and Development Center

JAEA-Review

JAEA-Tokai Tandem Annual Report 2009
April 1, 2009 – March 31, 2010

Department of Research Reactor and Tandem Accelerator

Nuclear Science Research Institute
Tokai Research and Development Center
Japan Atomic Energy Agency
Tokai-mura, Naka-gun, Ibaraki-ken

The JAEA-Tokai tandem accelerator complex has been used in various research fields such as nuclear science and material science by researchers not only of JAEA but also from universities, research institutes and industrial companies. This annual report covers developments of accelerators and research activities carried out using the tandem accelerator, superconducting booster, and radioactive nuclear beam accelerator, from April 1, 2009 to March 31, 2010. Fifty-seven summary reports were categorized into seven research/development fields:
  (1) accelerator operation and development
  (2) nuclear structure
  (3) nuclear reaction
  (4) nuclear chemistry
  (5) nuclear theory
  (6) atomic physics and solid state physics
  (7) radiation effects in materials.
This report also lists publications, meetings, personnel, committee members, cooperative researches and common use programs.

Editors: Makoto MATSUDA, Satoshi CHIBA, Norito ISHIKAWA, Shin-ichi MITSUOKA, Yosuke TOH, Kazuaki TSUKADA and Suehiro TAKEUCHI

原子力機構東海タンデム加速器 2009 年度年次報告

日本原子力研究開発機構
東海研究開発センター原子力科学研究所
研究炉加速器管理部

　原子力機構東海タンデム加速器施設は、原子核科学や物質科学などの様々な分野において、原子力機構を始めとして、大学や公立研究機関、民間企業に利用されている。本年次報告書は、タンデム加速器、ブースター加速器、放射性核種加速装置を利用し、2009 年 4 月 1 日から 2010 年 3 月 31 日までの期間に実施された研究活動の英文要約をまとめたものである。総数 57 件の要約を下記の 7 部門に分類した。

（1）加速器の運転状況と開発
（2）原子核構造
（3）原子核反応
（4）核化学
（5）原子核理論
（6）原子物理及び固体物理
（7）材料の照射効果

また、発表論文と会議での口頭発表、タンデム加速器に関与した職員、タンデム加速器専門部会委員、大学等との共同研究課題、及び施設共用課題のリストを掲載した。

原子力科学研究所：〒319-1195　茨城県那珂郡東海村白方白根 2-4
　編集者：松田　誠、千葉　敏、石川　法人、光岡　真一、藤　暢輔、塚田　和明、
　　　　　竹内　末広

Foreword

This report covers research and development activities with the tandem accelerator, its superconducting booster and TRIAC radioactive ion accelerator at JAEA Tokai, for the period of FY 2008 (April 1, 2009 to March 31, 2010). During this period, the tandem accelerator was operated over a total of 172 days and delivered 25 different ion beams to the experiments in the fields of nuclear physics, nuclear chemistry, atomic physics, solid state physics and radiation effects in materials. Thirty-six research programs were carried out in collaboration with a total of about 250 researchers from universities and research institutes. The TRIAC accelerator was operated for 26 days. The following are some of the highlights in FY 2009.

In the development of the tandem accelerator and the booster, an intense boron beam of 1 particle μA was supplied to experiments. A molecular beam of CO_2^+ was accelerated from the in-terminal ECR ion source. The average acceleration field gradient all over the 40 superconducting resonators was recovered to 4.4 MV/m as a result of applying high-pressure water-jet rinsing to 28 resonators. Ion-beam analysis of RBS method using a Ne beam was demonstrated to have high mass resolution.

In the development of TRIAC, a beam bunching system consisting of a pseudo saw-tooth wave pre-buncher and a multi-layer chopper has been developed to provide an intense stable pulsed beam with a width of less than 10 ns in a repetition rate of 2 MHz. The purity of radioactive ^{142}Ba beams of 1.1 MeV/u were investigated so that the experiment of the Coulomb excitation of ^{142}Ba was found to be feasible.

In research of nuclear structure, B(E2) and Q_β values of neutron-rich Eu isotopes were measured using the ISOL with a surface ionization source equipped with UC target. The energies of the first 2^+ states in neutron-deficient Pu and Cm nuclei, measured by α-ray spectroscopy, suggest that deformations of these nuclei decrease towards N=126. In-beam γ-ray spectroscopy experiment of ^{173}W using GEMINI-II shows low-spin signature inversion associated with strong configuration mixing. A new technique of laser spectroscopy for radioactive isotopes in the rhenium region has been developed. A candidate of a halo analog state of ^{11}Li was searched in ^{11}Be, using a ^{9}Li beam accelerated by TRIAC.

In research of nuclear reactions, excitation functions of fusion-fission cross sections in the reactions of ^{34,36}S + ^{204,206,208}Pb were measured around the Coulomb barrier. Fusion enhancement at sub-barrier energies in the ^{34}S projectile reactions was larger than in the ^{36}S cases. Fission following nuclear transfer in the ^{238}U (^{18}O, ^{16}O) reaction was studied as a surrogate for the ^{239}U(n, f) reaction. The obtained fission barrier height of the compound nucleus ^{240}U agreed with that determined in the (t, p) reaction.

In research of nuclear chemistry, the cation exchange behavior of rutherfordium, $_{104}$Rf, together with its homologues Zr and Hf in H_2SO_4/HNO_3 mixed solution has been investigated. The result clearly demonstrates that the sulfate complex formation of Rf is much weaker than that of Zr and Hf. The successful reduction of mendelevium from Md^{3+} to Md^{2+} using an electrochemistry apparatus is presented.

In the field of nuclear theory, researches to support a surrogate method were carried out. A general criterion

that validates the surrogate ratio method was found. A Dubna's "unified model" was applied to reactions between ^{18}O and $^{236, 238}U$, and validity of the above criterion was confirmed. Shell structure of oxygen isotopes, which will serve as projectiles in the surrogate method, were also investigated. A new formulation to evaluate incomplete and complete fusion was carried out with CDCC theory, and a global trend of competition between allowed and first-forbidden transitions relevant to the r-process nucleosynthesis was found.

In research of atomic physics and solid state physics, charge state distributions were measured for penetrations of 2 MeV/u S^{6+} to S^{16+} ions through C-foil targets of 0.9 - 200 $\mu g/cm^2$ in thickness, and a simulation of the distributions was performed. Li diffusion coefficients were measured for LiI and LiGa ionic conductors of NaTl-type inter-metallic compounds and $La_{2/3-x}Li_{3x}TiO_3$ perovskite-type lithium ion conductor.

In research of radiation effects in materials, an elongation of ion-irradiated Zn nano-particles embedded in SiO_2 was clearly observed even at relatively low fluence by using the linearly-polarized optical spectroscopy, indicating that such a method is sensitive enough to detect tiny elongations of metallic nano-particles. By experimentally simulating the electric device operation in a satellite orbit environment exposed to radiation, the error frequency in on-orbit environment for Virtex-5 FPGA (Field Programmable Gate Array), which is to be used for astrometric satellites, was evaluated as an acceptable level.
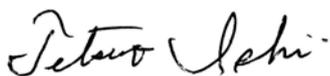
Tetsuro ISHII, Deputy Director, Department of Research Reactor and Tandem Accelerator

Contents

目　　　次

CHAPTER 1

Accelerator Operation and Development

This is a blank page.

1.1 Operation and usage of tandem accelerator and booster

T. Ishii[1], S. Abe[1], S. Hanashima[1], N. Ishizaki[1], A. Osa[1], H. Tayama[1], M. Matsuda[1], T. Nakanoya[1],

H. Kabumoto[1], M. Nakamura[1], K. Kutsukake[1], Y. Otokawa[1], T. Asozu[1] and Y. Tsukihashi[1]

The tandem accelerator and booster were operated for experiments from July 11, 2009 to October 20, 2009, and from December 10, 2009 to May 10, 2010. The total operation time of the tandem accelerator for FY2009 (from April 1, 2009 to March 31, 2010) was 172 days and 25 different beams were delivered for experiments. The experimental proposals and the usage of the beam times for FY2009 are summarized in Table 1 and Table 2, respectively.

In FY2009, an intense boron beam of 1 particle μA was supplied to experiments. A molecular beam of CO_2^+ was accelerated from the in-terminal 14.5-GHz ECR ion source.

Table 1. Experimental Proposals.

Research proposals accepted	
by the program advisory committee:	
In-house staff proposals	7
Collaboration proposals	14
Number of experiment proposed	92
Total number of scientists participating in research	
from outside	355
in-house	432
Number of institutions presented	40

Table 2. Usage of beam-times in different research fields.

Research field	Beam time (days)	(%)
Nuclear physics	86	48.3
Nuclear chemistry	23	12.9
Atomic and material sciences	50	28.1
Accelerator development	19	10.7
total	178	100

Distributions of the terminal voltage and ion species for experiments are shown in Fig. 1 and Fig. 2, respectively. Most of the beams were extracted from three negative ion sources, SNICS-2. The hydrogen beam and multiply charged ion beams of helium-3, nitrogen, oxygen and rare gases were accelerated from the in-terminal ECR ion source. The ECR ion source was used as much as 41 % of all the beam time.

The superconducting booster was operated for a total of 21 days to boost the energies of 5 different beams from the tandem accelerator, as is summarized in Table 3. These beams were used mainly for experiments of nuclear physics. Twelve resonators out of 40 resonators were treated by a high-pressure water jet spray rinse (HPWR).

The [7]Li and proton beams were supplied to the TRIAC (Tokai Radioactive Ion Accelerator Complex)

---

[1]Japan Atomic Energy Agency (JAEA)

experiments for 17 days. The radioactivities of ^{8}Li, ^{123}In and ^{142}Ba were ionized and separated by the ISOL and injected into the TRIAC.
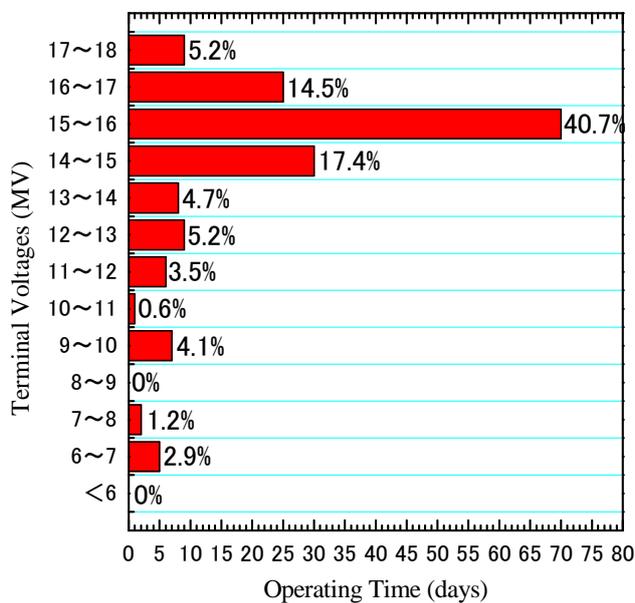
Fig. 1 Distribution of terminal voltages.
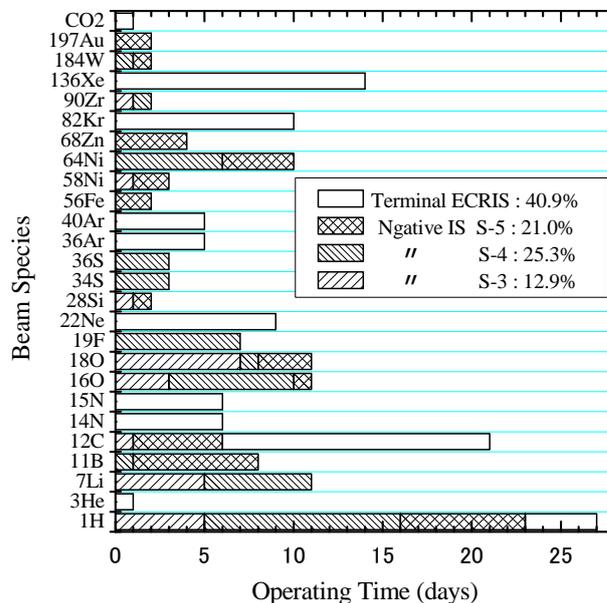
Fig. 2   Distribution of beam species accelerated for experiments.

Table 3. Boosted ion beams for experiments.

Beam species	Boosted energies (MeV)	Beam times (days)
^{16}O	183	1
^{58}Ni	589, 623, 653	1
^{64}Ni	317-362 (29 energy points)	3
	310-385 (15 energy points)	3
^{68}Zn	374	4
^{82}Kr	377, 380, 393	5, 1, 3

1.2 KEK-JAEA joint RNB project

S.C. Jeong[1] on behalf of TRIAC Collaboration

The Tokai Radioactive Ion Accelerator Complex (TRIAC) has been operated for nuclear physics and materials science experiments at JAEA-Tokai tandem accelerator facility under collaboration between KEK and JAEA (TRIAC collaboration). Produced by the proton-induced fission reactions of ^{nat}UC, the radioactive ion beams (RIBs) are extracted and mass-separated as singly charged ions by the isotope separator on-line (ISOL) of JAEA. They are charge-bred to higher charge states with a charge-to-mass ratios of about 1/7 using charge breeding electron cyclotron resonance ion source (CB-ECRIS) called as KEKCB. And then, the charge-bred RIBs are accelerated by using a series of heavy ion linacs, the split-coaxial radiofrequency quadrupole (SCRFQ) and the inter-digital H (IH) linacs. In FY 2009, radioactive isotope beam of ^{142}Ba at 1.1 MeV/A has been developed for a future experiment. The background ion which had the same q/A ratio of ^{142}Ba^{22+} and originated from KEKCB was identified as ^{71}Ga^{11+}. The following experiments were carried out in FY 2009: (1) Search for highly excited states in ^{11}Be states in ^{9}Li + d reactions (RNB08-K08), (2) Diffusion study of ionic conductors using the short-lived isotopes (RNB09-K01/K07). Some details of the experiments can be found in this report.

In addition to the experiments with RIBs, we are also going to directly measure the ^{12}C(α,γ)^{16}O reaction cross sections at stellar energies using a stable α beam. To carry out the experiment, an intense pulsed beam with the width less 10 ns and the interval between 250 ns and 500 ns is needed. We have developed a brand-new pseudo saw-tooth wave pre-buncher and a multi-layer chopper. The pre-buncher is a two-gaps buncher having a single drift tube. The RF voltage applied on the tube is synthesized with two and three times higher harmonics waves and the fundamental wave, giving a rise to a pseudo saw-tooth wave form. Particles passing through the two gaps are bunched effectively by the pseudo saw-tooth wave voltage. The pre-buncher was installed at the entrance of SCRFQ. In order to efficiently deflect the beam particles of out-of-bunch phase, which are generated by the transient time portion of the saw-tooth wave-form,
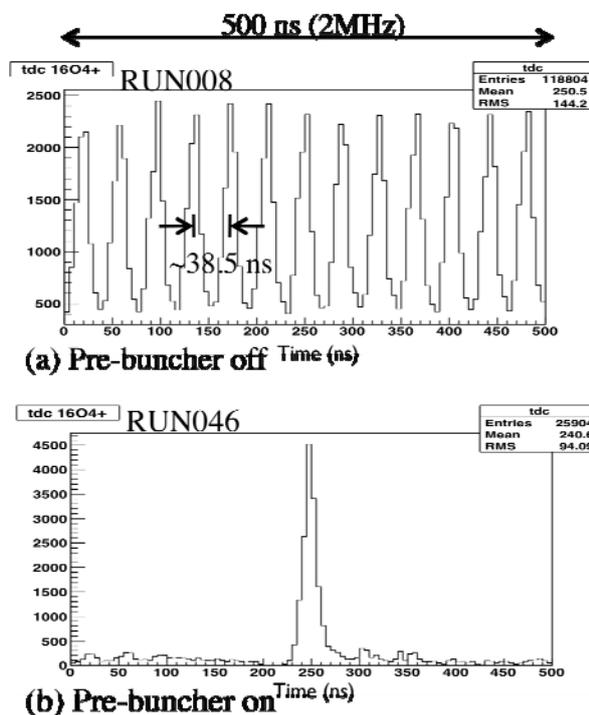
Fig. 1 Beam bunch structure with pre-buncher off (a) and pre-buncher on (b).

[1] High Energy Accelerator Research Organization(KEK), corresponding author: N. Imai,
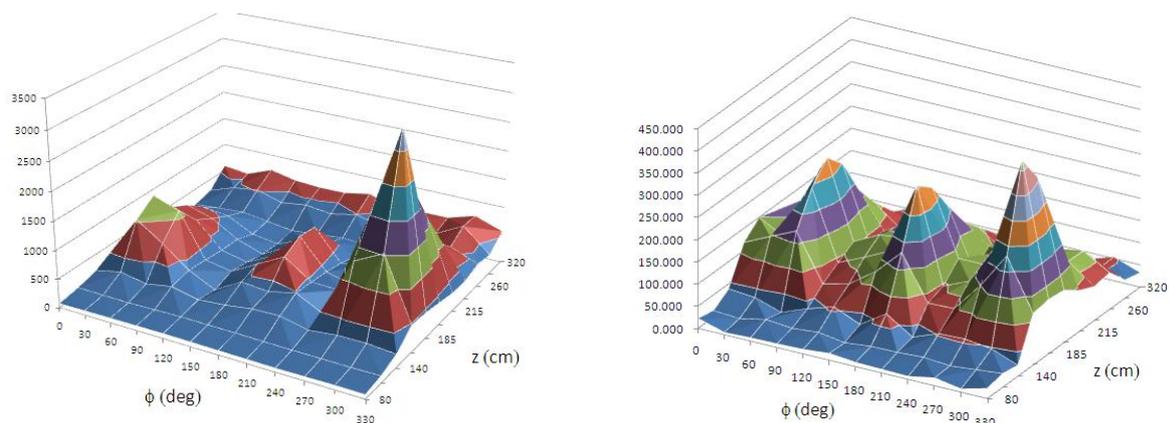
Fig. 2 (Left) Distribution of residual activities of ^{111}In in the plasma chamber as a function of azimuthal angle (φ) and longitudinal position (z). Residual activities of [140]Xe (Right). See the text for details.

the beam chopper was also placed upstream of the pre-buncher. The chopper has 19 electrodes of 40 mm wide, 10 mm long, and 0.1 mm thick piled up with gaps of 1.9 mm vertically to the beam direction and a square-shape electric potential (120 V in maximum, 2-4 MHz in repetition frequency) is applied to every two electrode (One grounded electrode is interposed between two electrodes on the electric potential).

The beam test of the pre-buncher with 2 MHz frequency was performed using $^{16}O^{4+}$ and $^{12}C^{3+}$ beams supplied by KEKCB. The clear bunch structure with an interval of 500 ns was observed as shown in Fig.1, although there exists a small fraction of the beam failed to be bunched. A typical pulse width of the beam after acceleration (1.1 MeV/nucleon) was achieved to have a 2 ns in standard deviation at the target position about 10 m away from the exit of IH-linac. The incomplete beam-bunching could be removed by the operation of the beam chopper to be installed upstream of the pre-bunchar.

The origin of smaller charge breeding efficiencies for the non-gaseous elements as compared to those of gaseous elements was investigated. The charge breeding efficiencies can be regarded as the product of two efficiencies; the capture efficiency for single charged ions by the ECR plasma and the ionization efficiency for step-by-step charge breeding. In general, for the ECRIS the latter efficiency is supposed to be independent of the element. And thus, the difference of charge breeding efficiencies may attribute to the inadequate capture by the ECR plasma in the charge breeding processes. In order to study the difference in the capture process, we injected a metallic element ^{111}In into the ECR plasma in FY2008. The ions were charge-bred as usual, then the activities from the indium failed to be extracted as multi-charged ions were measured. In the FY 2009, we injected a gaseous element [140]Xe into the ECR plasma. The distribution of residual activities of [140]Xe was compared with that of ^{111}In as shown in Fig.2. We observed well-localized in azimuthal distribution with 120-degrees periodicity for both elements, particularly prominent around the minimum (B_{min} at Z~200 mm) of the axial field configuration for electron confinement. However, for the ^{111}In, the asymmetric distribution with a strongly localized around φ~300 deg. and Z~200 mm was observed around B_{min}, while the [140]Xe distribution had almost same peak heights (symmetric). Further analysis is in progress.

1.3   Release of radioactive ion beams from a new ion source system in the JAEA-ISOL

Y. Otokawa[1], A. Osa[1], T. K. Sato[1] and M. Matsuda[1]

We have improved an ion source system in the isotope separator on-line at Japan Atomic Energy Agency (JAEA-ISOL), in order to separate of short-lived isotopes produced by proton-induced fission of ^{238}U. The ion source system is a forced electron beam induced arc discharge (FEBIAD) type ion source with a target container. The system attained operation temperature of nearly 2000 $^{\circ}$C at the target container, as a result of reduction in volume of the ion source and the target container, introduction of heating method by electron bombardment, and improvement to the heat shield. A schematic view of the ion source is shown in Fig. 1.

We measured time intervals between production and separation (release time) of radioactive ion beams from the ion source system, using ^{238}U of 640 mg/cm^2 with a proton primary beam of 30 MeV, 350 nA from JAEA-Tokai tandem accelerator. Mass-separated isotopes, after turning off the proton primary beam, were collected using Mylar tape from the tape transport system for the measurement of release time. The collected isotopes were periodically transported to a measuring position. The γ-ray spectra of each interval were stored in one of 16 blocks of 64 k channels memories. The storing block was switched on at the same time as the collected radioactive source was transported to the measuring position. The whole measurement cycle was repeated in order to increase the statistics. Release time distributions of ^{121g}In are shown in Fig. 2. The release properties were evaluated based on a phenomenological analysis. Time dependences of the decay corrected counts were fitted by the following equation:

$$N'(t) = \sum_{i=1,2} A_i \exp(-\lambda_i t).$$

The release time $\tau_i = 1 / \lambda_i$ and the fractional rate A_i / λ_i for Kr, In, and Xe atoms deduced from the fit to the present date are summarized in Table 1 together with those of the previous FEBIAD, the surface ionization ion source system at JAEA-ISOL [1,2], and reported values at different facilities [3-6]. We successfully shortened the release times for indium, krypton and xenon. As a result, we obtained short-lived isotopes of ^{93}Kr (T$_{1/2}$ = 1.286 s), ^{129}In (T$_{1/2}$ =0.61 s) and ^{141}Xe (T$_{1/2}$ =1.73 s) with the intensity of 10^3 ions/s using the JAEA-ISOL with the new ion source system.

---

[1] Japan Atomic Energy Agency (JAEA)
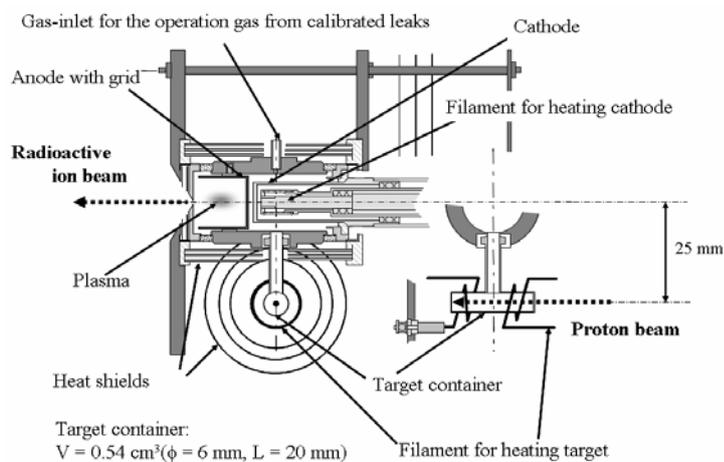
Fig. 1 Schematic view of the new ion source system.
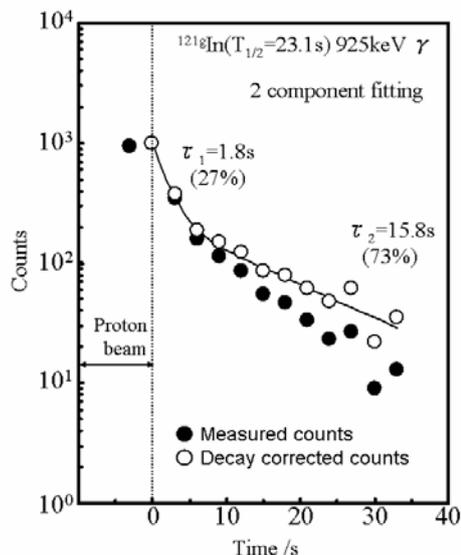
Fig. 2 Release time distributions of ^{121g}In at the target temperature of 1950 ^{o}C

Table 1. Release times and fractional rates obtained from a one and/or two component fit to the Kr, In, and Xe release data.

Isotope	Half-life /s	Ion source	Release time /s	Fraction rate	Reported value /s[d]
^{91}Kr	8.57	FEBIAD[a]	τ_1:**2.3**	20%	1.5[e], 3.5[f], 16[g]
			τ_2:54.1	80%	
		Previous FEBIAD[b]	τ_1:3.1	21%	
			τ_2:46.9	79%	
^{121g}In	23.1	FEBIAD[a]	τ_1:**1.8**	27%	
			τ_2:15.8	73%	
^{123g}In	5.98	Previous FEBIAD[b]	τ_1:7	100%	1.8[e], 1.6[f], 6[h]
		SIS[c]	τ_1:1.7 at 2250℃	100%	
^{139}Xe	39.68	FEBIAD[a]	τ_1:**4.6**	21%	22[e], 11.7[f], 30[g]
			τ_2:91.9	79%	
		Previous FEBIAD[b]	τ_1:12		
			τ_2:>300		

[a]FEBIAD operated at 1950 ^{o}C.   [e]OSIRIS at 2400 ^{o}C.
[b]Previous FEBIAD operated at 1550 ^{o}C.   [f]ISOLDE at 1900-2000 ^{o}C.
[c]SIS(Surface ionization type ion source) operated at 2250 ^{o}C.   [g]IRIS at 2050-2100 ^{o}C.
[d]Value was converted to mean life.   [h]PARRNe at 2000 ^{o}C.

References

[1] A. Osa et al., Nucl. Instrum. Methods Phys. Res., B266 (2008) 4394-4397.

[2] A. Osa et al., Nucl. Instrum. Methods Phys. Res., B266 (2008) 4373-4377.

[3] Fogelberg et al., Nucl. Instrum. Methods Phys. Res., B70 (1992) 137-141.

[4] H. M. Evensen et al., Nucl. Instrum. Methods Phys. Res., B126 (1997) 160-165.

[5] Andrighetto et al., Nucl. Instrum. Methods Phys. Res., B204 (2003) 267-271.

[6] Roussire et al., Nucl. Instrum. Methods Phys. Res., B246 (2006) 288-296.

1.4 Recovery of acceleration field gradients of the superconducting booster using high pressure water jet rinsing

H. Kabumoto[1], N. Ishizaki[1], S. Takeuchi[1], T. Yoshida[2], T. Ishiguro[2] and K. Yamaguchi[2]

We have carried out the high pressure water jet rinsing (HPWR) to re-condition the superconducting booster since 2006. The HPWR is a technology of removing small contaminations on resonator surfaces, and a very effective method to recover the acceleration field gradients of superconducting resonators. We applied the HPWR to 12 resonators of 3 cryostats (No.6, 7, 8) in 2009.

Figure 1 shows how the average acceleration field gradient E_{acc} across the superconducting booster changed in the years between 2003 and 2010. The average E_{acc} was decreasing little by little each year, and it was about 3.9MV/m in 2005 and 2006. We started the HPWR to on-line resonators in 2006. It required about 4 weeks to carry out the HPWR for every 4 resonators of 1 cryostat, in which period we disassembled and re-assembled all parts in the cryostat, including the resonators, mechanical tuners, RF couplers, thermometers, etc. Furthermore, the inside of cryostat needed to be cleaned up. There were many small contaminations on the inner and bottom walls of cryostat, mainly powders of molybdenum coming from the molybdenum coated gears of mechanical slow frequency tuners, with which low friction has been realized. It seemed that the field emission was caused by this molybdenum powder on the surface of superconducting resonators. We have finished the 28 resonators of 7 cryostats (No.3, 5, 6, 7, 8, 9, 10) by 2009. The average acceleration field gradient E_{acc} all over the 40 resonators was recovered to 4.4MV/m.
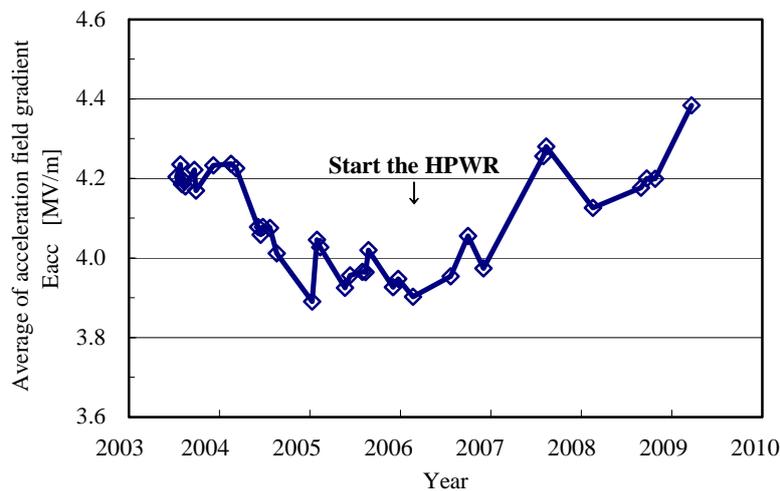
Fig. 1 The average acceleration field gradient E_{acc} across the superconducting booster changed in the years between 2003 and 2010.

[1] Japan Atomic Energy Agency(JAEA)
[2] ATOX Co., Ltd.

References

[1] H. Kabumoto et al., JAEA-Tokai TANDEM Ann. Rep. 2008, JAEA-Review 2009-036 (2009) 13-14.

[2] H. Kabumoto et al., JAEA-Tokai TANDEM Ann. Rep. 2007, JAEA-Review 2008-054 (2008) 16.

[3] H. Kabumoto et al., JAEA-Tokai TANDEM Ann. Rep. 2006, JAEA-Review 2007-046 (2008) 15-16.

1.5   Cluster beam acceleration project

M. Matsuda[1], T. Asozu[1] and K. Kutsukake[1]

On the high voltage terminal of the JAEA-tandem accelerator, an ECR ion source (ECRIS) has been installed to extract and accelerate positive ions such as rare gas ones. By taking advantage of the ECRIS, we have attempted to accelerate cluster ions such as C_{60}, expecting high energy and intense cluster beams, since the charge exchange is unnecessary.

The schematic diagram of the accelerator system is shown in Fig. 1. The cluster beam extracted from the ECRIS is bent upwards with a 90° injection magnet (BM EC-1) and is pre-accelerated by 80 kV acceleration tube. A 180° bending magnet (BM TL-1) is used to select a cluster ion having specific mass and charge state and to guide it to the 20 MV acceleration tube. Here, since the magnetic field strength of the BM EC-1 is $ME/q^2 \leqq 0.28$, extraction voltage is decreased to several kV. On the other hands, since the strength of the BM TL-1 is enough as $ME/q^2 \leqq 55$, in many cases, it is not necessary to decrease the pre-acceleration voltage. Table 1 shows the relation between extraction voltage and accelerable ion mass (carbon atoms). The accelerated cluster beam was guided to the new target room in the second basement level. To accelerate cluster ions with reasonable transmission efficiency and to know the maximum m/q value, the performance of existing beam handling system was checked. A test was carried out to guide the beam through the 20 mm diameter duct of BM 04-1 and focus
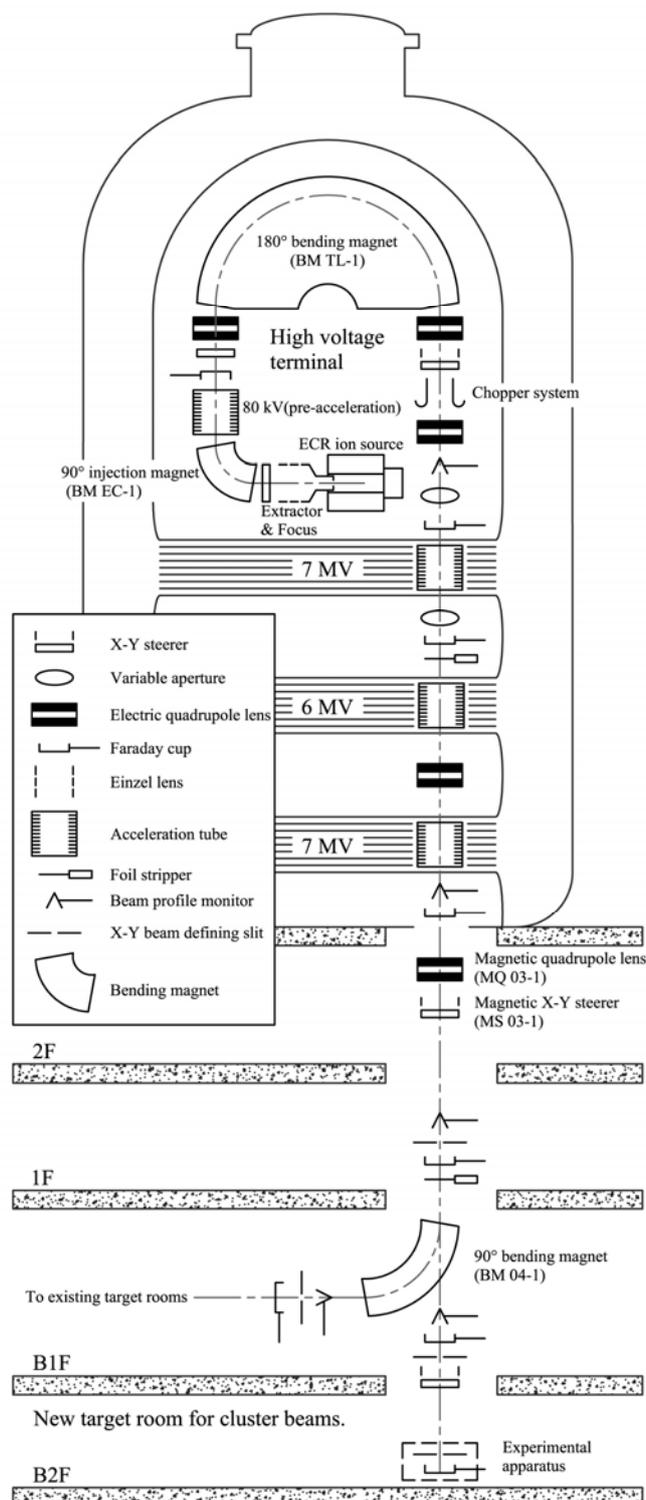
Fig. 1 Schematic diagram of the accelerator

---

[1] Japan Atomic Energy Agency (JAEA)

the beam at a target position using Xe beams with various charge states. A beam profile monitor (BPM) and a Faraday cup (FC) were newly installed directly under the BM 04-1 12 m downstream of the magnetic quadrupole lens (MQ 03-1). At the terminal voltage of 15 MV, the beam transport through the BM 04-1 was succeeded without a significant loss of the beam current. From this test we obtained the data shown in Fig.2, which represents the current to drive MQ 03-1 needed to guide and focus the beam. Considering the maximum current of 25 A for MQ 03-1 and the drift length to a target position (focus point) located 16 m downstream from MQ 03-1, it was found that cluster ions up to m/q = 200 can be available.

We are planning to install a beam chopper system at the high voltage terminal for beam current attenuation and time-of-flight (TOF) experiments. The repetition frequency will be 50 kHz and pulse width 0.1 to 10 μs. We expect single ion hit experiments such as coulomb explosion imaging using an attenuated beam about 10-1000 ions per second and a TOF experiment which measures the mass and energy of a secondary ion using a pulsed cluster beam. The intense cluster beams will also enable more progressive researches into solid-state physics and materials sciences as well as cluster physics.

Table. 1 Extraction voltage and accelerable ion mass number.

Extraction voltage [kV]	20	15	10	5	3	2	1	0.39
Mass [amu]	14	18	28	56	93	140	280	720
Carbon atoms	C_1	C_1	C_2	C_4	C_7	C_{11}	C_{23}	C_{60}
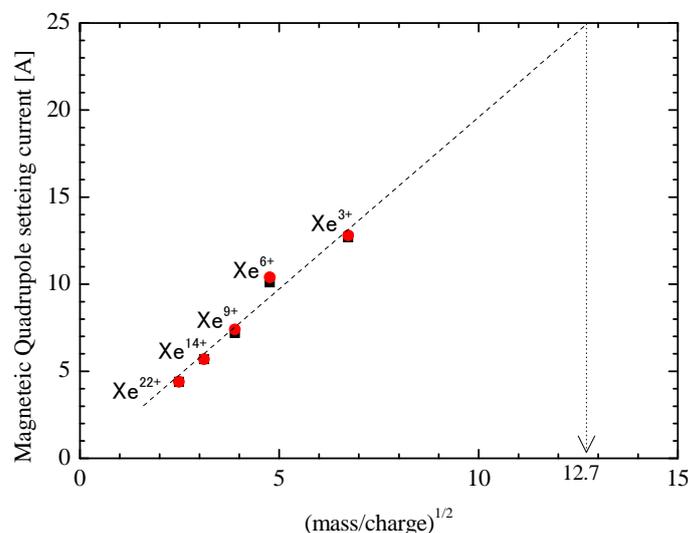
Fig. 2 The relation between a mass to charge ratio of Xe ions and magnetizing current of MQ 03-1.

References

[1] M. Matsuda et al., JAEA-Tokai Tandem Ann. Rep. 2008, JAEA-Review 2009-036 (2009)11-12.

1.6 High energy heavy ion Rutherford backscattering spectrometry at the JAEA-Tokai tandem accelerator

M. Nakamura[1], M. Matsuda[1], T. Asozu[1], M. Sataka[1], K. Takahiro[2] and N. Matsunami[3]

The heavy ion Rutherford backscattering spectrometry (HIRBS) is an ion beam analysis method that has an advantage for the analysis of heavy elements in materials. The dependence of mass resolution (δM) on target mass (M) and projectile mass (m) can be estimated as follows [1]:

$$\delta M = \frac{\delta E}{E_i} \cdot \left(\frac{dM}{dK} \right), \quad K = \left\{ \frac{\left(M^2 - m^2 \cdot \sin^2 \theta \right)^{\frac{1}{2}} + m \cdot \cos \theta}{m + M} \right\}^2,$$

where K is the kinematic factor, $\delta E/E_i$ is the energy resolution of the detection system, E_i is incident energy of the projectile and θ is the scattering angle of projectile with respect to the beam axis. Figure 1 shows the dependences of δM on M for projectiles of $m = 1, 2, 4, 12, 22$ and 40. Here $\delta E/E_i = 0.01$ and $\theta = 165°$ are assumed. Projectiles of $m = 12$ and 22 are expected to offer better mass resolution than H and ^{4}He ion for targets of $M > 40$.

We started the experiment to measure the HIRBS at JAEA-Tokai tandem accelerator facility. The mass resolution of the HIRBS depends on the mass of projectile and target, the energy resolution of scattering ion, the optimization of kinematics geometry and so on. Since the resolution was expected to be high for the target mass around 70, ^{22}Ne ion was selected as a projectile. In kinematics, the higher the energy of ion beams, the higher energy resolution is provided, but we need to stay in the region that nuclear reactions do not occur. ^{22}Ne ions were accelerated by the tandem accelerator up to 1.25 MeV/u. The targets were a thin Au foil (1 nm) and Cu foil (10 nm) deposited on Si substrate, GaAs single crystal and Ge single crystal. The ion detector was a Si detector (ORTEC: BU-012-050-100) with a 3.2 mm$^{\varphi}$ aperture. A schematic view of the experimental set-up is shown in Fig. 2.

Figure 3 shows HIRBS spectra from Au foil (A), Cu foil (B), GaAs crystal (C) and Ge crystal (D). The measurement time was several hours per spectrum. The energy resolution of the detection system was about 1.2 % (FWHM@18MeV) from the analysis of a Au foil spectrum. Enough mass resolution was achieved, although the energy resolution was less than that of a typical RBS using He beam and high resolution detection system. Mass resolution higher than 2 amu was performed as shown in Fig. 3 (B) and (C).

We confirmed that the high energy HIRBS has enough mass resolution to analyze heavy elements in materials with a Si detector. Presently, we are also pursuing the RBS for depth profiling and another ion beam analyses.

---

[1] Japan Atomic Energy Agency (JAEA)
[2] Kyoto Institute of Technology
[3] Nagoya University EcoTopia Science Institute
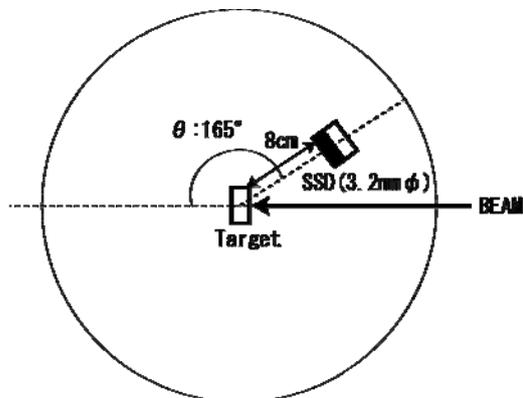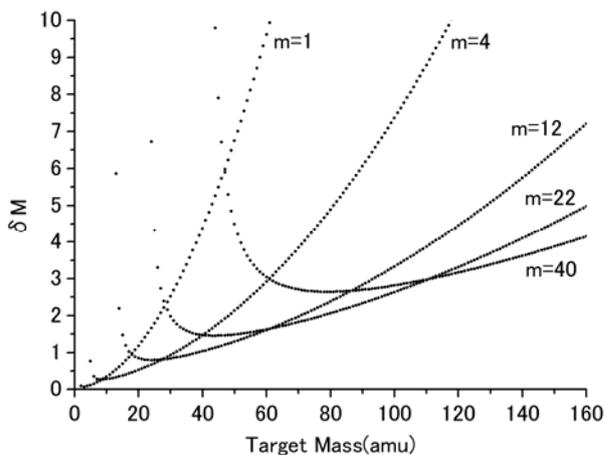
Fig. 1 Mass resolution (δM) on target mass (M) for projectile mass (m).

Fig. 2 Schematic view of the detection set-up.
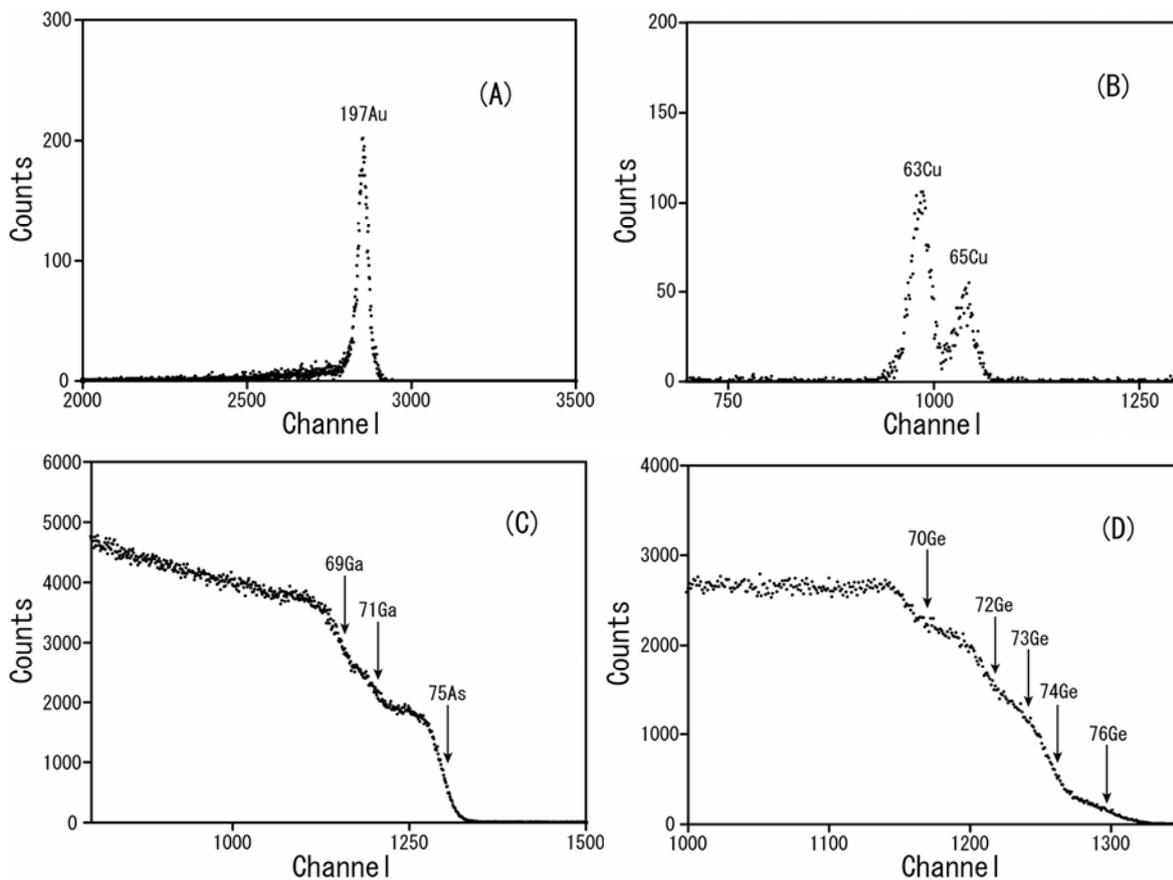
Fig. 3 HIRBS spectra from Au foil (A), Cu foil (B), GaAs crystal (C) and Ge crystal (D).

References

[1] J.R. Tesmer and M. Nastasi, "Handbook of modern ion beam materials analysis" (1995).

CHAPTER 2

Nuclear Structure

This is a blank page.

2.1 Lifetime measurement for the first 2^+ state in ^{162}Gd

D. Nagae[1], T. Ishii[1], R. Takahashi[2], M. Asai[1], H. Makii[1], A. Osa[1], T.K. Sato[1] and S. Ichikawa[1]

Gadolinium isotopes lie in a well deformed region between the proton closed shells of $Z = 50$ and 82. In previous experiments, we identified new neutron-rich europium isotopes $^{163, 164, 165, 166}$Eu [1, 2], and found that the energies of the first 2^+ states $E(2^+)$ in even-even $_{64}$Gd isotopes show the local minimum at $N = 98$, which is similar to those in $_{66}$Dy isotopes [3]. On the other hand, the $E(2^+)$ values of $_{68}$Er, $_{70}$Yb, and $_{72}$Hf isotopes monotonously decrease with the neutron number approaching the $N = 104$ midshell. In order to study the mechanism of the local minimum at $N = 98$, we have measured the lifetime of the first 2^+ state at 71.5 keV in ^{162}Gd to deduce the B(E2) value by means of the β–γ delayed coincidence technique for mass-separated ^{162}Eu isotope.

The experiment was performed using an isotope separator on-line (ISOL) [4]. The ^{162}Eu isotope was produced in 32-MeV proton-induced fission with an UCx target (630 mg/cm^2) set in the surface ionization type ion source [1]. Reaction products were ionized in the ion source, extracted, and mass-separated by the ISOL. The mass-separated ^{162}Eu ($T_{1/2} = 10.6(10)$ s) isotope was transported to a tape system. In the tape system, ^{162}Eu isotope was collected on aluminized Mylar tape, and transported to the detection port at prescribed time intervals. The tape was moved every 20 s. The detection position was equipped with a Pilot-U plastic scintillator (60 mm × 63 mm × 1-mm thickness) and a BaF$_2$ scintillator (38-mm diameter × 5-mm thickness) to detect β and γ rays, respectively. A Ge detector was placed at the detection position to monitor the implanted RI beam. Time signals of the plastic scintillator and the BaF$_2$ scintillator were generated by ORTEC-583B constant fraction differential discriminators. An ORTEC-567 time-to-amplitude converter (TAC) was used for measuring a time interval from the time signal of the plastic scintillator to that of the BaF$_2$ scintillator. The lifetime was deduced from the slope of the time interval spectrum.

A γ-ray spectrum measured with the Ge detector is shown in Fig. 1. In this spectrum, KX rays of Gd and some γ rays associated with the β decay of ^{162}Eu are observed. γ rays associated with the β decay of ^{143}Ba are also observed, which were mass-separated as a fluoride form. In Fig. 1, a γ-ray spectrum measured with the BaF$_2$ detector in coincidence with TAC signals is also shown. In this spectrum, KX-ray and the 71.5 keV γ-ray peaks are observed. The energy gate was set at the high-energy portion of the 71.5 keV peak to avoid the influence of the KX rays. A time interval spectrum for the first 2^+ state was obtained as shown in Fig. 2. This spectrum includes the prompt time components from Compton events caused by higher-energy γ rays. The lifetime was deduced by fitting an exponential decay curve, $a\exp(-t/\tau) + b$, by a least-χ^2 method. Contributions of the lifetimes of higher-lying states were neglected because their lifetimes are expected to be short. From the fitting analysis, we obtained the lifetime of the first 2^+ state as

---

[1] Japan Atomic Energy Agency (JAEA)
[2] Tokyo University of Science (TUS)
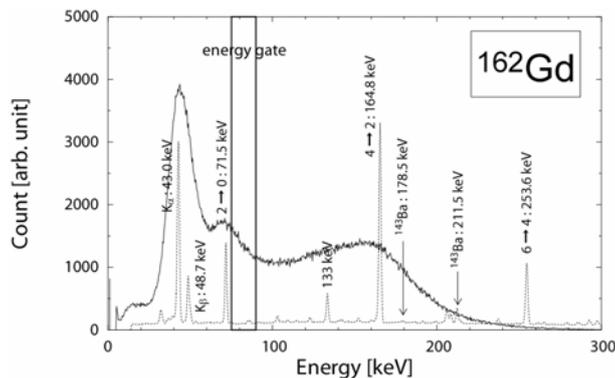
Fig. 1 Energy spectra for ^{162}Gd. γ-ray spectrum measured with the Ge detector (dashed line), and γ-ray spectrum measured with the BaF$_2$ detector (solid line) in coincidence with TAC signals.

$\tau = 3.98(8)$ ns; the error was estimated from the spread of various fitted values obtained by changing the fitting range.

The B(E2;$0^+ \rightarrow 2^+$) value was calculated from the measured lifetime, total internal conversion coefficient α_T, and the transition energy E_γ by using the formula

$$B\left(E2;0^+ \rightarrow 2^+\right) = \frac{40.81 \times 10^{13}}{\left(1 + \alpha_T\right)E_\gamma^5 \tau} .$$

The internal conversion coefficient was taken from the ICC code in the program ESCL8R [5] as $\alpha_T = 9.063$. The transition energy was measured in the previous experiment [1] as $E_\gamma = 71.52(5)$ keV. The B(E2;$0^+ \rightarrow 2^+$) value of ^{162}Gd was deduced as B(E2;$0^+ \rightarrow 2^+$) = 5.45(11) e^{2}b^2.
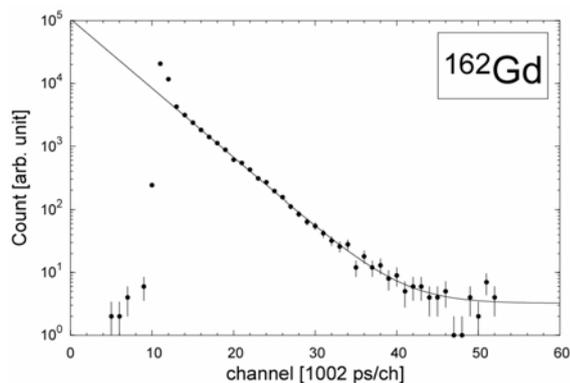
Fig. 2 Time spectrum of ^{162}Gd. The result of the fitting analysis is shown by a solid curve.

References

[1] A. Osa et al., Nucl. Instrum. Methods Phys. Res., B266 (2008) 4394-4397.

[2] T.K. Sato et al., JAEA Tandem Ann. Rep. 2006, JAEA-Review 2007-046 (2008) 32-33.

[3] M. Asai et al., Phys. Rev., C59 (1999) 3060-3065.

[4] S. Ichikawa et al., Nucl. Instrum. Methods Phys. Res., B70 (1992) 93-100.

[5] D. C. Radford, Nucl. Instrum. Methods Phys. Res., A361 (1995) 297-305.

2.2 Decay study on fission products with on-line isotope separator

M. Shibata[1], H. Hayashi[1], M. Asai[2], A. Osa[2], M. Oshima[2], A. Kimura[2], M. Koizumi[2] and T.K. Sato[2]

Beta-decay energies (Q_β) are important for evaluation of the decay heat of the nuclear power plants in nuclear engineering. They are also important to determine atomic masses precisely which are fundamental physical quantities and play an important role for study on structure of unstable nuclei or nucleosynthesis in astrophysics. We had studied Q_β measurements of fission products with a total absorption detector, composed of a clover detector and BGO Compton suppressors [1]. In this year, the Q_β of fission products Eu and Gd (A>160) were measured and the results were compared to systematics or some theoretical predictions.

Uranium carbide (UC$_2$) target containing 670 mg・cm^{-2} ^{238}U was bombarded with 32 MeV proton beams with the intensity of about 0.6-1 μA generated by the TANDEM accelerator at JAEA. The ^{160,161,163,165,166}Eu and daughter nuclei ^{163,165}Gd were separated from the fission products with an on-line mass separator(ISOL) and mass-separated nuclides were implanted into a computer-controlled movable thin Mylar tape. The half-lives of the nuclei of interest are between 1 s and 60 s. The Gd isotopes were measured after decaying out of their parent Eu isotopes. Singles spectrum and coincidence spectrum with the BGO detectors were measured simultaneously for each nucleus. Each nuclide was measured over 10 hours to accumulate adequate statistics. The detector was shielded with 10 cm thick lead blocks and 10cm thick 10% borated polyethylene ones. The counting rate was lower than 0.2 kcps for all nuclides, then, pulse pile-up does not matter. The total absorption events were extracted according to the method in the previous report.[1]

Typical spectra and analysis with folding method including one component approximation for ^{165}Eu are shown in Fig. 1. In this method, the spectra were analyzed by assuming an allowed β-transition, which is mixed with an unique first forbidden with ratio α, depopulating to a pseudo level. The method was described in the previous reports[1,2]. The ^{165}Eu was analyzed properly with applying the level at 1500 keV and only allowed β-transition. This method was applied to each nuclide and the folded spectrum reproduced the experimental one well in the region of ~1 MeV below endpoint of each spectrum. The Q_βs of the ^{160,161,163,165,166}Eu and daughter nuclei ^{163,165}Gd were preliminarily determined to be 4480(30), 3722(30), 4829(65), 5729(65), 7322(300), 3187(40) and 4113(65) keV, respectively. The value for the new isotopes ^{166}Eu[3] was proposed for the first time. The others are in agreement with the previous values determined with the BGO total absorption detector[4] and each uncertainty is smaller. Figure 2 shows differences between AME2003[5] and the present result or some theoretical mass formulae in this mass region. AME2003 and some theoretical model predict the experimental atomic mass well. On the other hand, some model cannot predict them in the region which have no experimental data. It says the experimental values can be useful to check the reliability of theoretical mass formulae and it is also respectful to improve the model. In conclusion, the Q_β of seven nuclides were determined with the total absorption detector. The experimental data are useful to check of the reliability of mass formulae and also useful to develop nuclear models.

[1]Nagoya University

[2]Japan Atomic Energy Agency (JAEA)

Present study is the result of "Study on nuclear data by using a high intensity pulsed neutron source for advanced nuclear system" entrusted to Hokkaido University by the Ministry of Education, Culture, Sports, Science and Technology of Japan (MEXT).
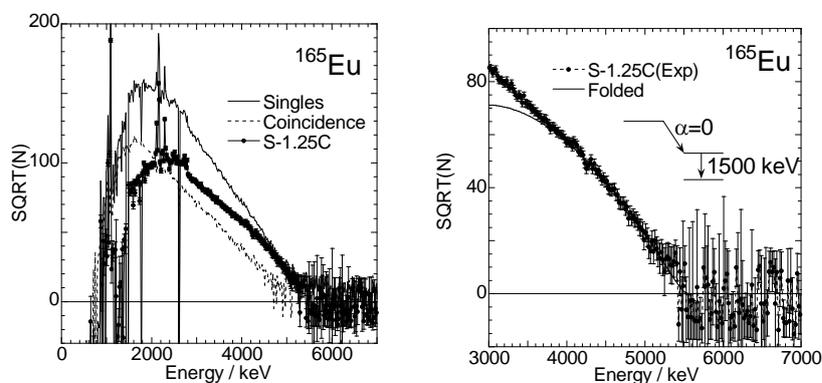
Fig. 1   Typical spectra (Singles, Coincidence with BGO and total absorption (S-1.25C))(left) and the analyzing results by folding methods (right) for ^{165}Eu.
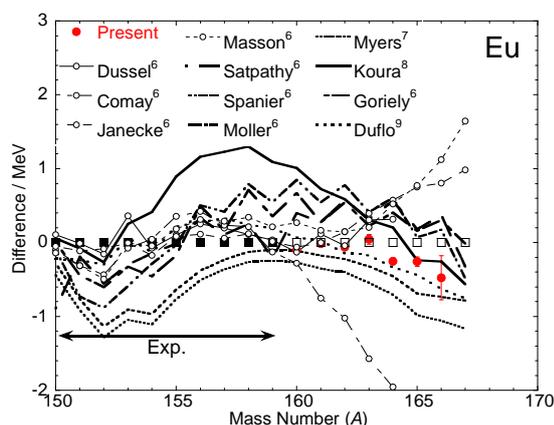
Fig. 2 The differences between AME2003[5] and the present results, some theoretical predictions[6-9]. AME2003 is agreement with the present results. On the other hand, some predictions show no predictability far off the stability.

References

[1] M. Shibata, et al., JAEA-Tokai Tandem Annual Report 2008, JAEA-Review 2009-036(2009) 33-34.

[2] H. Hayashi et al., Nucl. Instrum. Methods Phys. Res., A613 (2010) 79-89.

[3] H. Hayashi et al., Eur. Phys. J., A34 (2007) 363-370.

[4] T. K. Sato et al., JAEA-Tandem Annual Report 2006, JAEA-Review 2007-046 (2007) 32-33.

[5] G. Audi, A. H. Wapstra and C. Thibault, Nucl. Phys., A729 (2003) 337-676.

[6] These values are summarized in At. Data Nucl. Data Tables, 39 (1998).

[7] W. D. Myers et al., Ann. Phys. (N.Y.), 204 (1990) 401-431.

[8] H. Koura et al., Prog. Theor. Phys., 113 (2005) 305-325.

[9] J. Duflo and A.P Zuker, Phys. Rev., C52 (1995) R23-R27.

2.3 Alpha-decay properties of ^{240,241}Cf and the new isotope ^{236}Cm

M. Asai[1], K. Tsukada[1], N. Sato[1], T.K. Sato[1], A. Toyoshima[1], T. Ishii[1] and Y. Nagame[1]

Energy of the first 2^+ state $E(2^+)$ in even-even nuclei is a good probe to explore nuclear shell structure and deformation in frontier regions of nuclear chart. In general, $E(2^+)$ takes the maximum at the closed shell, decreases with increasing number of valence nucleons, and takes the minimum around the midshell where nuclei are well-deformed. Actinide nuclei are known to be well-deformed, indicating that they should be located around the midshell. However, because of lack of experimental data, systematic trend of $E(2^+)$ in actinide nuclei is still unclear. In this research program, we systematically measured $E(2^+)$ of even-even Pu, Cm, Cf, and Fm isotopes through high-resolution α-fine structure measurements. Although the data analysis is still in progress, we report here some experimental results obtained in the α-fine structure measurement for ^{240}Cf: α-decay properties of ^{240,241}Cf and the new isotope ^{236}Cm.

An ^{233}U target with a thickness of 480 μg/cm^2 was bombarded with a ^{12}C beam to produce ^{240}Cf. The beam energy was 80 MeV on target. Reaction products recoiling out of the target were transported through a 25-m long capillary with a He/KCl aerosol jet into a rotating-wheel α detection system [1], and deposited on a thin foil eighty of which were set on the wheel. The wheel periodically rotated at 60-s intervals to move the deposited sources to six consecutive detector stations each of which was equipped with a high-resolution Si detector (PIPS). To measure α fine structure (α energies and intensities) very precisely, the Si detectors were set at the distance with a solid angle of 12% of 4π from the source. This setup reduces a low-energy tail of α peaks and also reduces energy sum between α particles and subsequently emitted conversion electrons, Auger electrons, and low-energy X rays which considerably distorts the measured α-energy spectrum. The α-energy resolution of 12 keV FWHM was achieved.

Figure 1(a) shows an α-particle spectrum measured at the first detector station. The 7581(4) and 7535(4) keV α lines were clearly observed which correspond to the α transitions from ^{240}Cf to the ground- and the first 2^+ state in ^{236}Cm, respectively. The half-life of 40.3(9) s was derived from the decay curve of these α events as depicted in Fig. 2. These values are more accurate than the literature values of 7590(10) keV and 1.06(15) min [2]. The energy difference between the 7581 and 7535 keV α transitions was deduced to be 46.6(4) keV (preliminary), leading to $E(2^+)$ = 47.4(4) keV in ^{236}Cm. The 7328(4) keV α line was attributed to the α decay of ^{241}Cf, and the half-life of 141(11) s was derived from its decay curve. The literature values of α energy and half-life of ^{241}Cf are 7335(5) keV and 3.78(70) min, respectively [2]. The present results revised these data more accurately.

Figure 1(b) shows a sum of α-particle spectra measured at the 4th, 5th, and 6th detector stations. In this spectrum, we found unknown α transitions of 6947(5) and 6894(5) keV which probably originate from the α decay of ^{236}Cm, the daughter nucleus of ^{240}Cf. The ^{236}Cm is a new isotope whose decay properties have

---

[1] Japan Atomic Energy Agency

never been reported. The half-life of these α events was about 10 min though it has a large uncertainty. From the α-energy difference, $E(2^+)$ of ^{232}Pu was deduced to be 54(4) keV (preliminary). These results revealed that $E(2^+)$ in Cm and Pu isotopes increases with decreasing neutron number, reflecting the decreasing deformation towards the neutron closed shell at $N = 126$.
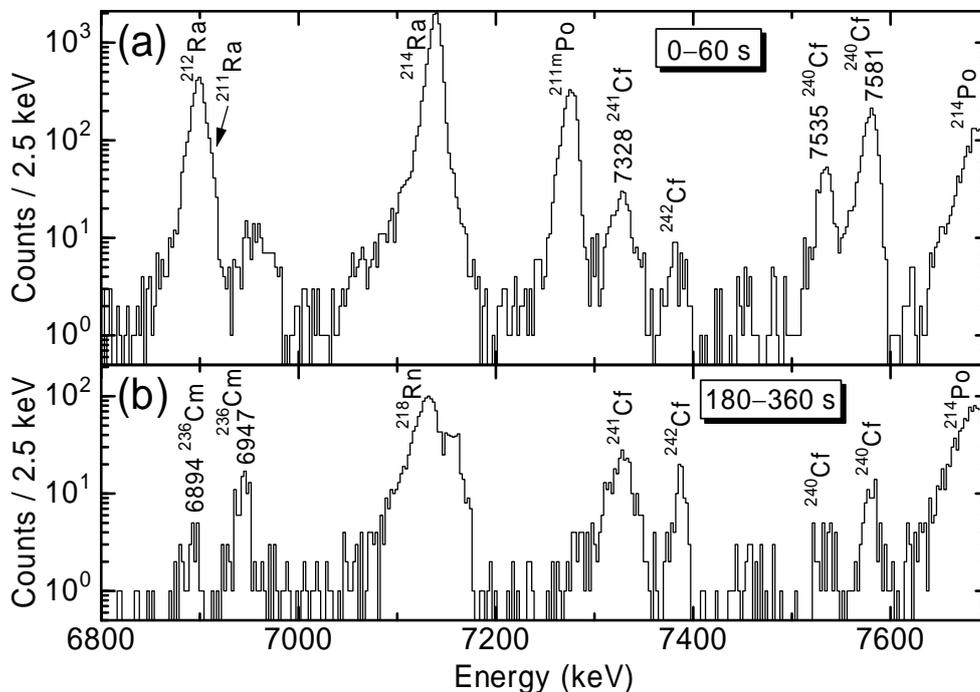
Fig. 1 (a) α-particle spectrum measured at the first detector station. (b) Sum of α-particle spectra measured at the 4th, 5th, and 6th detector stations. Ra isotopes and ^{211m}Po are produced in the reactions with Pb impurity included in the target.
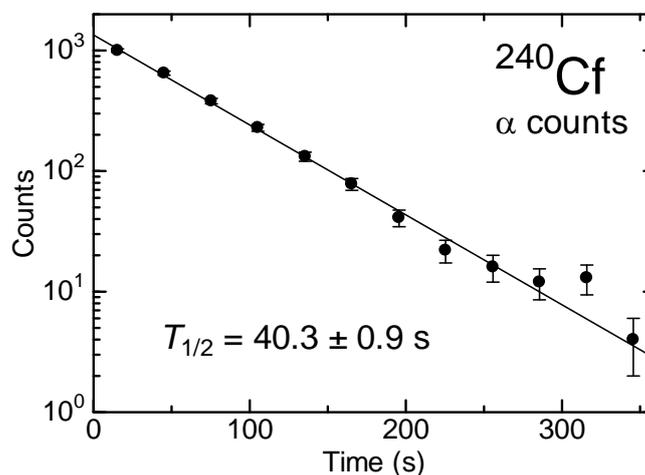
Fig. 2 Decay curve of α particles of ^{240}Cf.

Reference

[1] Y. Nagame *et al.*, J. Nucl. Radiochem. Sci. 3 (2002) 85-88.

[2] R. J. Silva *et al.*, Phys. Rev. C 2 (1970) 1948-1951.

2.4 Signature splitting property in the one-quasiparticle bands of ^{173}W

Y.H. Zhang[1], X.H. Zhou[2], M. Oshima[2], M. Koizumi[2], Y. Toh[2], A. Kimura[2],

H. Harada[2], K. Furutaka[2], F. Kitatani[2], S. Nakamura[2], Y. Hatsukawa[2], M. Ohta[2],

K. Hara[2], T. Kin[2] and J. Meng[3]

An in-beam γ-spectroscopy of ^{173}W has been studied in the Japan Atomic Energy Agency (JAEA) via the ^{150}Nd(^{28}Si,5nγ)^{173}W reaction. The purpose of this experiment is to search for low-spin signature inversion in the ν5/2⁻[512] band of ^{173}W, which could be the reason of signature inversion recently observed in the π1/2⁻[541]⊗ν5/2⁻[512] band of odd-odd ^{174}Re [1]. The high-spin states of ^{173}W was investigated by Walker et al., and a level scheme up to 31/2⁻ had been reported for the ν5/2⁻[512] band [2]. In this experiment, a ^{28}Si beam of 1 pnA was provided by the tandem accelerator in JAEA. The target was an enriched ^{150}Nd oxidized powder of 2.0 mg/cm^2 thick evaporated onto a gold metallic foil of 7.8 mg/cm^2 in thickness. The GEMINI-II [3] γ-ray detector array was employed to detect the in-beam γ rays. x-γ, γ-γ-t coincidences have been measured at 135-, and 140-MeV beam energies. A total of 1.7×10^8 γ-γ coincidence events was accumulated. These coincidence events were sorted into a symmetric and a non-symmetric (DCO sorting) matrices for off-line analysis.
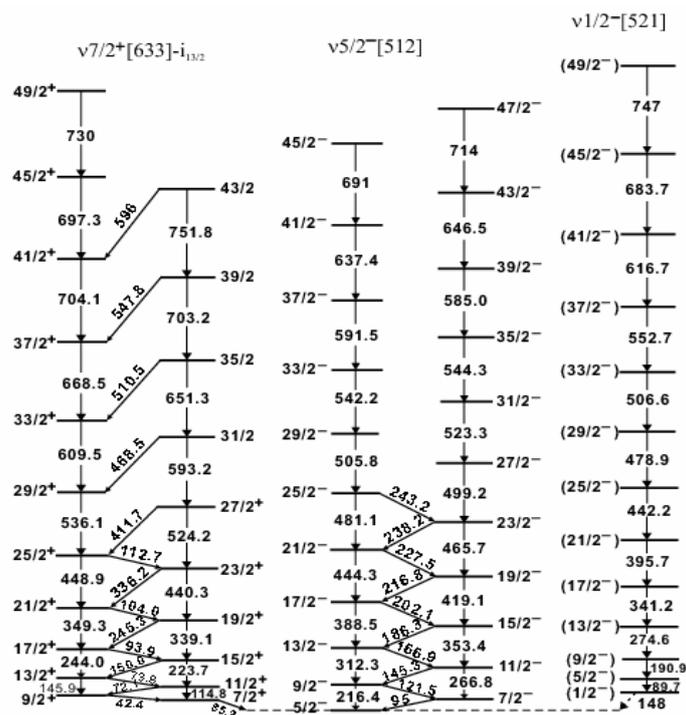
Fig. 1 Level scheme of ^{173}W deduced from the present work

Fig. 1 presents the level scheme of ^{173}W deduced from the present work. In comparison with the previous study [2], three bands have been extended up to high-spin states.

[1] Institute of Modern Physics, Chinese Academy of Sciences
[2] Japan Atomic Energy Agency (JAEA)
[3] Peking University

The signature splitting, defined as $S(I) = E(I+1) - E(I-1) - 1/2 [E(I+1) - E(I) + E(I-1) - E(I-2)]$, is plotted in Fig 2 for the $\nu5/2^-[512]$, $\nu i_{13/2}$ bands in ^{173}W, and the $\pi1/2^-[541] \otimes \nu5/2^-[512]$ band in ^{174}Re. One can see in this figure that the $\nu i_{13/2}$ band exhibits a normal signature splitting, i.e., the favored signature ($\alpha_f = 1/2$) levels keep lower-lying along the whole band. Usually the signature splitting for this band is small at lower spins, and it increases significantly at higher-spin states but keeping the $\alpha = -1/2$ (α is the signature quantum number and $I = \alpha$ Mod 2) $\Delta I = 2$ sequence lower in energy along the whole band. However, a close inspection of the $5/2^-[512]$ band shown in Fig. 2 reveals that it is the $\alpha = 1/2$ signature branch that lies lower rather than the $\alpha = -1/2$ sequence at lower-spin states. At higher-spin states beyond $I \sim 33/2$, the normal signature splitting is restored, say, with the $\alpha = -1/2$ signature branch lying lower in energy. This phenomenon has been observed in a number of 2-quasiparticle bands in odd-odd nuclei and has been referred to as signature inversion or anomalous signature splitting.
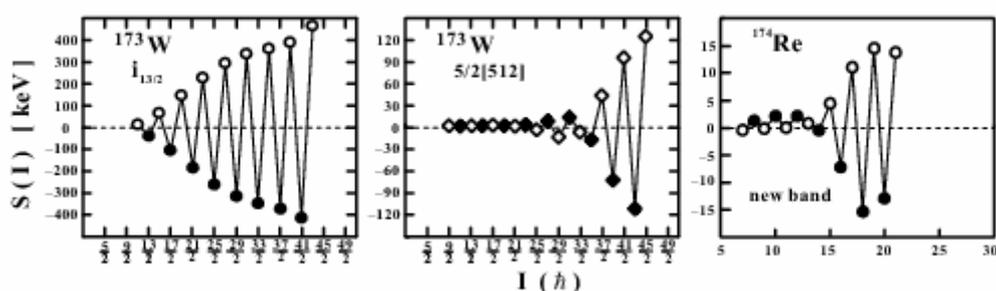
Fig. 2 Plot of signature splitting S(I) against spin I for the three bands in ^{173}W and ^{174}Re

An important issue from present investigations may be the observation of low-spin signature inversion in the $\nu5/2^-[512]$ band of ^{173}W. As is well known, the low-spin signature inversion has been observed in a number of two-quasiparticle bands of odd-odd nuclei in this mass region. The inversion phenomenon has also been observed in some odd-Z nuclei, but in these cases, signature inversion occurs at higher rotational frequencies beyond bandcrossing [4].

The present result provides an interesting testing ground for different theoretical approaches. For instance, one may certainly disregard the effects of proton-neutron residual interactions in such one-quasiparticle bands. Furthermore, the nuclear triaxiality should be of less importance for the inversion phenomenon since the $\nu i_{13/2}$ band in the same nucleus has normal signature splitting. Given the fact that the $\nu5/2^-[512]$ and $\nu5/2^-[523]$ Nilsson orbitals have strong interactions, the configuration mixing may play an important role for the low-spin signature inversion in the $\nu5/2^-[512]$ band of ^{173}W. Similarly, the inversion phenomenon in the $\pi1/2^-[541] \otimes \nu5/2^-[512]$ band of ^{174}Re could be associated also with the configuration mixing. This is in need of further theoretical investigations.

References

[1] Y. H. Zhang et al., CHIN. PHYS. LETT., 24 (2007) 1203-1206.
[2] P. M. Walker et al., J. Phys. (London), G4 (1978) 1655-1677.
[3] M. Oshima et al., J. Radioanal. Nucl. Chem., 278 (2008) 257-262.
[4] A. Ikeda et al., Phys. Rev., C42 (1990) 149-166.

2.5   Structure evolution of the yrast band in ^{101}Pd

X. H. Zhou[1], H. B. Zhou[1],Y. H. Zhang[1], Y. Zheng[1], M. L. Liu[1], N. T. Zhang[1], Y. D. Fang[1],

M. Oshima[2], Y. Toh[2], M. Koizumi[2], Y. Hatsukawa[2] and M. Sugawara[3]

Nuclear shape evolution is a major theme in nuclear structure research. This evolution is intimately related to the mechanisms by which atomic nuclei generate angular momentum. The transitional nuclei in A~100 mass region, which are located below the closed shell Z=50, have attracted a lot of experimental and theoretical interests. The experimental study led to the identification of the phase transition from vibrational structure to rotational structure along the yrast line in the even-even nuclei while increasing spin [1]. For an odd-*A* nuclide in this mass region, its high-spin states may be formed by coupling weakly the valence nucleon to the respective core excitations. Therefore, the odd-*A* nuclei would be expected to exhibit phase evolution as their neighboring even-even nuclei. It is our primary aim to extend the level scheme of ^{101}Pd to high-spin states, and to study the structure evolution phenomenon.

High spin states in ^{101}Pd have been investigated using the ^{76}Ge (^{28}Si, 3n) reaction at beam energies of 85 and 95 MeV. The ^{28}Si beam was provided by the tandem accelerator at the Japan Atomic Energy Agency (JAEA). The target was an isotopically enriched ^{76}Ge metallic foil of 2.0 mg/cm^2 thickness with an 8.0 mg/cm^2 Pb backing. The GEMINI-II [2] γ-ray detector array was employed to detect the in-beam γ rays. A total of 2.3×10^8 coincidence events were recorded. After accurate gain matching, the coincidence events were sorted into symmetric and ADO matrices for off-line analysis. Based on the analysis of γ-γ coincidence relationships, γ-ray relative intensities, and energy sum, a level scheme of ^{101}Pd has been established and presented in Fig. 1(a). As compared with the previous work [3, 4], we extended band 1 from 29/2$^+$ up to 33/2$^+$. Band 3 has been reported up to 35/2$^-$ in Ref.[3]. In the present work, it was confirmed and extended with two additional levels up to excitation energy of 9.04 MeV. We have identified a new cascade labeled as structure 2, consisting of 526-, 920-, 902-, and 1028-keV transitions.

To reveal the structure evolution in the yrast band of ^{101}Pd, we plotted the $R_{\text{E-GOS}} = E_\gamma (I \rightarrow I - 2)/I$ versus I trajectory, so-called E-GOS curve, which is sensitive to a transition between vibrational and rotational states [1]. For a vibrator, this ratio gradually diminishes to zero as the spin increases, while for an axially symmetric rotor it approaches a constant, $4[\hbar^2/(2J)]$. Here, J is the static moment of inertia. In Fig.1 (b), we compare the E-GOS curves for the yrast lines of $^{100\text{-}102}$Pd. The behavior of the E-GOS curve of ^{101}Pd is in good agreement with the assumption that the low-spin yrast states show a vibrational structure, whereas the higher-spin states have a rotational character.

---

[1] Institute of Modern Physics, Chinese Academy of Sciences, Lanzhou 730000, China

[2] Japan Atomic Energy Agency, Tokai, Ibaraki 319-1195, Japan

[3] Chiba Institute of Technology, Narashino, Chiba 275-0023, Japan
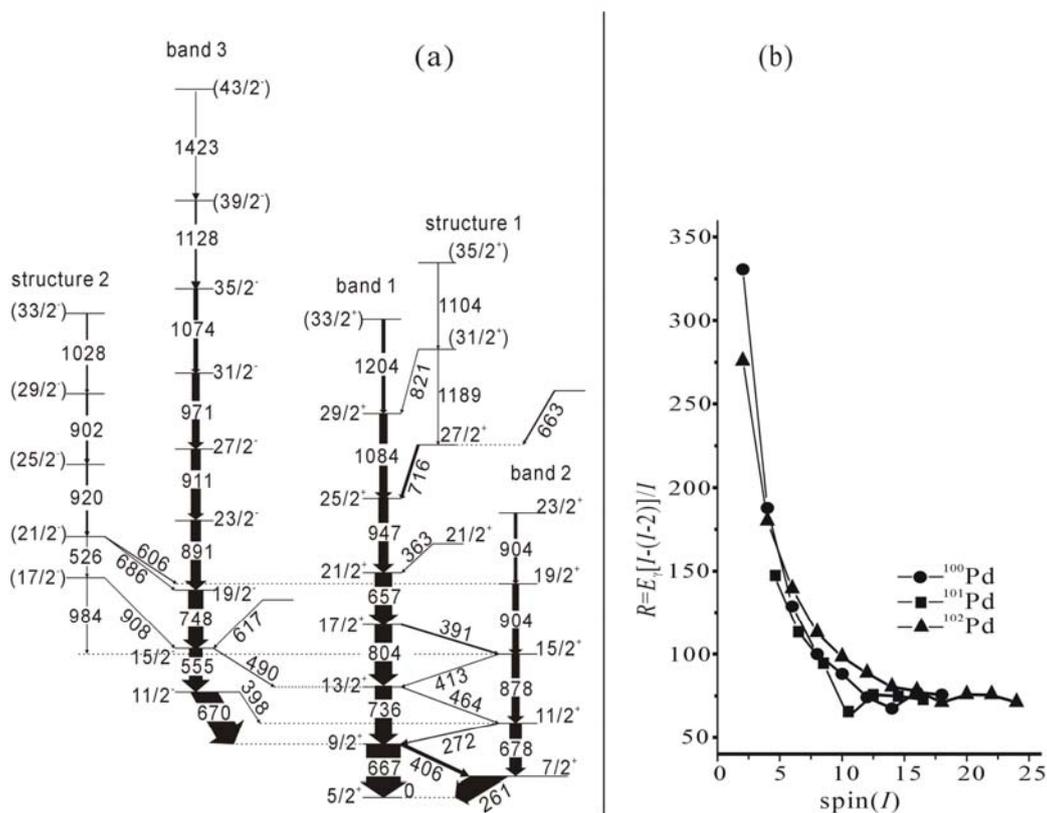
Fig. 1 (a) Level scheme of ^{101}Pd deduced from the present work. (b) E-GOS curve for the ground-state band of ^{101}Pd. The E-GOS curves for the ground-state bands of ^{100,102}Pd are also shown for comparison.

References

[1] P. H. Regan et al., Phys. Rev. Lett., 90 (2003) 152502.

[2] M. Oshima et al., J. Radioanal. Nucl. Chem., 278 (2008) 257-262.

[3] R. Popli et al., Phys. Rev., C22 (1980) 1121-1125.

[4] P. C. Simms et al., Phys. Rev., C9 (1974) 684-698.

2.6   Proton resonance elastic scattering of ^{68}Zn
with thick target inverse kinematics method

N. Imai[1], Y. Hirayama[1], H. Ishiyama[1], S.C. Jeong[1], H. Miyatake[1], Y.X. Watanabe[1], H. Makii[2],
S. Mitsuoka[2], D. Nagae[2], I. Nishinaka[2], K. Nishio[2] and K. Yamaguchi[3]

When much more neutrons are added onto a nucleus than usual, how does the nuclear structure change ? The basic question can be answered by investigating the single particle structures of neutron-rich nuclei. We proposed measurement of isobaric analog resonances (IARs) to study single particle states of such unstable nuclei. Owing to the isospin symmetry of nuclear force, the neutron wave functions of a nucleus $^{A+1}$Z are identical with proton wave functions appeared in the high excitation energies in the daughter nucleus $^{A+1}$(Z+1), called "isobaric analog states". The analog states can be accessed by the proton elastic scattering of ^{A}Z [1]. When we measure the excitation function of differential cross sections at a given angle, the cross section at the excitation energy corresponding to the analog state will be enhanced as a resonance. By analyzing the shape of the excitation function, we can determine the wave function.

In this study, we measured the excitation function of proton elastic scattering at 180 degrees in the center of mass frame by employing the thick target inverse kinematics method. The scattering angle corresponds to 0 degree in the laboratory frame. In the case of the elastic scattering at 0 degree in the lab frame, which is sensitive to the resonances, the energy of recoil proton reaches 4 times higher than the c.m energy ($E_{c.m}$). Thus, even if the single particle levels are crowded, it is much easier to separate them. By using the thick target, a wide range of the excitation function of the elastic scattering can be measured with a beam of a fixed incident energy corresponding to the highest end of the range. When a resonance state has a proton width as large as several keV, it can be observed in the excitation function as an interference of potential and resonance scattering. The resonance energy, width, and spin-parity (J^π) can be extracted from the excitation function by employing R-matrix analysis.

As the first test of measuring the isobaric analog states in medium nuclei using the inverse kinematics proton elastic scattering, we searched for the isobaric analog states of ^{69}Zn with ^{68}Zn beam with a proton target. The analog states were well studied with the normal kinematic condition [2].

The experiment was performed at JAEA tandem accelerator facility. A ^{68}Zn beam of 5.5 MeV/nucleon was accelerated by tandem accelerator and superconducting booster linac. The beam of around several epA was focused on a 3 mg/cm^2 thick polyethylene (CH$_2$) target. Downstream of the CH$_2$ target, 10 mg/cm^2 thick carbon was placed to stop the beam. In order to evaluate the contribution from carbon in CH$_2$ target, we removed the CH$_2$ and measured the resonance elastic scattering only with carbon foil. The energies of recoil protons were measured by the three layers of silicon semiconductors (SSDs) of 50 x 50 mm^2 which

---
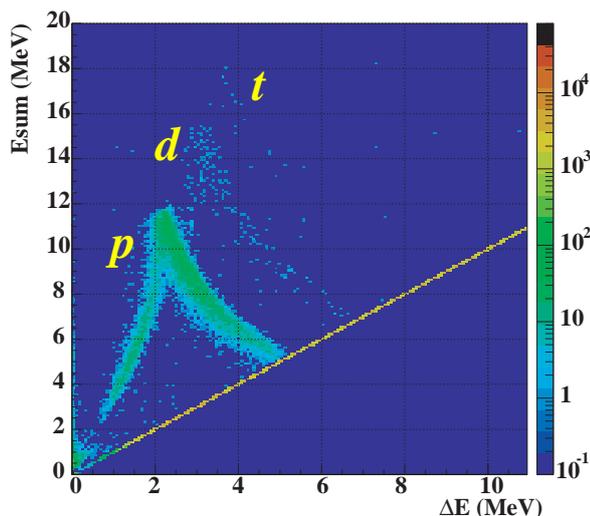
Fig. 1 Energy correlation between ΔE and E. Indexes *p, d, t* indicate loci for protons, deuterons, and tritons, respectively.
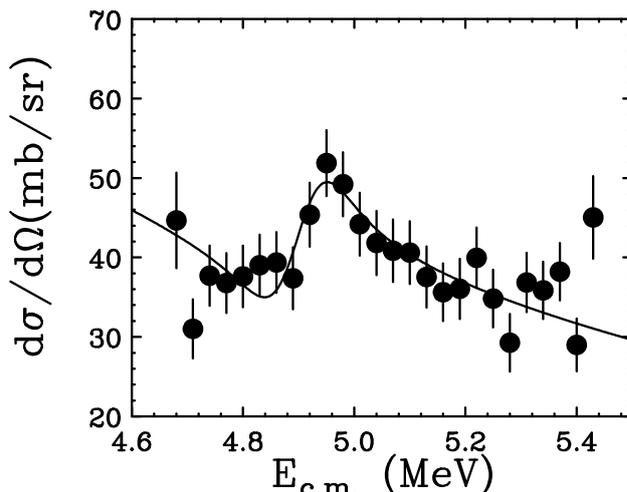
Fig. 2 Excitation function of proton elastic scattering around $E_{c.m.}$=5 MeV. Red line indicates the best fitted R-matrix curve for $l = 0$.

were located 50 cm downstream of the target. The thickness of each SSD was 300 μm. The highest energy of recoil proton was calculated to be around 20 MeV. To completely stop the proton, we needed a 3 mm thick SSDs. Instead of using such thick SSDs in the experiment, we put a 1.5 mm thick aluminum plate just downstream the SSDs and compensated the energy loss in the aluminum.

Figure 1 shows the correlation between the energy deposit in the first layer SSD (ΔE) and the sum of the energy deposits in all SSDs (Esum). In addition to protons, deuterons and tritons were clearly observed. The Esum of protons was converted to the excitation function by considering the detection efficiency and conversion function of experimental energy deposits to the reaction energy in the center of mass frame. Both parameters were obtained by performing Monte Carlo simulations.

The resultant excitation function is presented in Fig.2, representing a resonance around $E_{c.m.}$= 5 MeV. When we searched for χ^2 minimum by changing Γ_p with the assumed angular momentum $l = 0$. The best fitted curve was obtained with $\Gamma_p = 19$ +/- 5 keV, which reproduced the reference value of $\Gamma_p = 20$ keV [2]. Note that the parameters were not converged with l = 1 and 2, ruling out those angular momenta.

In summary, we applied the proton resonance elastic scattering with thick target inverse kinematics method to obtain the single particle structure of ^{69}Zn. The proton width obtained in the present experiment reprouced the reference value, demonstrating that the proton resonance elastic scattering in inverse kinematics for IAR is a powerful tool for studying neutron single particle states in neutron-rich nuclei.

References

[1] V.Z. Goldberg, in ENAM98, edited by B.M. Sherrill, D.J. Morrisey, and C.N. Davids, AIP Conf. Proc. No.455, p319.

[2] W.S. Steiner, et al., Phys. Rev., C4 (1971) 1684.

2.7 Development of laser spectroscopy for radioactive isotopes in the rhenium region

H. Iimura[1], M. Koizumi[1], M. Miyabe[1], M. Oba[1] and I. Wakaida[1]

Laser spectroscopy of the hyper-fine structures (HFS) and isotope shifts (IS) in atomic spectra has been providing much information on the studies of nuclear structure since nuclear moments and nuclear charge radii determined from the HFS and IS, respectively, strongly reflect nucleon motions in a nucleus and nuclear shapes. Neutron-deficient nuclei in the rhenium region (Z~75) have been attracting much interest because axially asymmetric shapes are predicted theoretically for them [1]. However, the laser spectroscopy for these isotopes is very scarce because elements in this region are refractory and are difficult to be evaporated from a sample. In order to perform the laser spectroscopy for these isotopes, we are developing two new techniques, namely off-line laser-ablation laser spectroscopy for relatively long-lived isotopes and on-line gas cell laser spectroscopy for short-lived ones. Following is our recent progress in developing these techniques.

Laser ablation is a promising technique for producing an atomic beam for laser spectroscopy of radioactive isotopes of refractory elements not accessible via the normal resistance heating method. A setup of the laser-ablation laser spectroscopy is schematically shown in Fig. 1. A beam from a pulsed Nd:YAG laser (1.06 μm in wave length) was focused on the target of metallic disk of natural rhenium in vacuum or in a few hPa of ambient Ar gas. The power density of the pulsed Nd:YAG laser was about 1 J/cm^2 on the target, which was high enough to ablate rhenium metal. The repetition rate of the Nd:YAG laser was 10 Hz and the pulse width was 6 ns. Another CW Nd:YAG laser (0.53 μm) was used to pump a tunable ring dye laser. This dye-laser beam was introduced perpendicularly to the pulsed Nd:YAG laser beam so that it irradiated the rhenium atoms evaporated from the target by laser ablation. The distance between the dye-laser beam and the surface of the target was 1 mm. Laser-induced fluorescence was collected by a lens system and transferred to a photomultiplier tube through an optical fiber. A monochromator was used to observe the fluorescence of a specific de-excitation transition. In order to reduce the background light emitted from the ablation plume, appropriate time gate was set in counting the photomultiplier tube signals. The resonance peaks were observed by scanning the
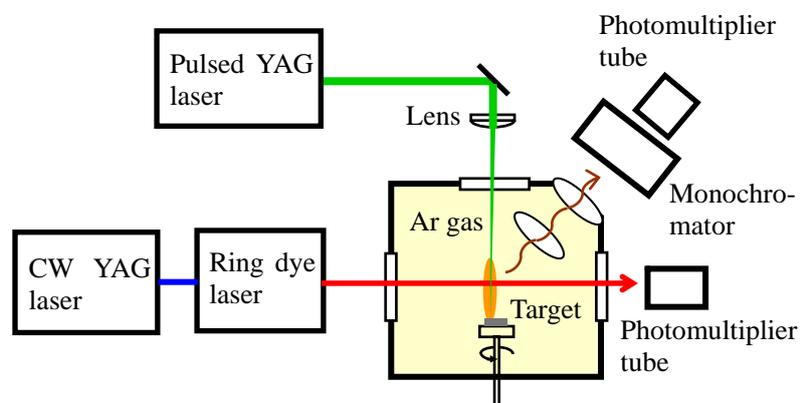
Fig. 1 Setup of the laser-ablation laser spectroscopy.

frequency of the tunable laser. The width of the resonance peaks was about 1 GHz which is approximately one order better than our previous value obtained by using a broad band dye laser pumped by a pulsed XeCl excimer laser. Although the line width we obtained is narrow enough to resolve the isotope shifts, the sensitivity of this apparatus is still insufficient for the measurement of minute amount of radioactive isotopes. Presently we are working on improving the sensitivity so as to measure long-lived isotopes such as ^{186m}Re ($T_{1/2}=2 \cdot 10^5$ y) which we have already produced by using the JAEA-Tokai tandem accelerator [2].

Another apparatus we are developing for the laser spectroscopy of refractory elements is an on-line gas cell in which the reaction products recoiling out of the target are stopped. These reaction products are then irradiated with a laser beam before diffusing through the gas to the wall of the gas cell. Laser-induced fluorescence is collected on a photomultiplier tube by using a mirror and lenses. The gas cell for this experiment has been set at a beam line of the JAEA-Tokai tandem accelerator. Prior to the studies of radioactive isotopes, we are working with stable isotopes to optimize the sensitivity of the apparatus. In order to simulate the tungsten isotopes (Z=74) produced by heavy-ion fusion reactions, a beam of stable ^{184}W was accelerated to 100 MeV by using the tandem accelerator and injected into the gas cell without setting the target. After passing through two 2.5 μm Ni foils which isolate the gas cell from the accelerator beam line, energy of the tungsten beam became the same as that of the reaction-produced isotopes. The pressure of Ar gas was set at 19 hPa to stop ^{184}W at the center of the cell. Since the production rate of radioactive isotopes by heavy-ion fusion reactions is expected to be less than 10^5 atoms/s, it is important to reduce background light to observe the laser-induced fluorescence signals. The largest part of the background is the light coming from the collisions between the gas and the accelerator beam. Since the reaction products are expected to remain in the gas for a few seconds, it may be possible to reduce this background by chopping the accelerator ion beam and counting the laser-induced fluorescence signals only when the ion beam is off. We examined this method by chopping the ^{184}W ion beam at the repetition rate of 10 Hz. As a result, the background was suppressed more than one order, demonstrating the effectiveness of this method. Additional methods, such as removing impurities in the gas by cooling the wall of the cell, are in progress to further improve the sensitivity of the apparatus. After these improvements, on-line laser spectroscopy of short-lived tungsten isotopes is planned.

References

[1] P. Möller et al., At. Data Nucl. Data Tables, 59 (1995) 185-381.
[2] H. Iimura et al., J. Phys. Soc. Jpn., 77 (2008) 025004.

2.8 Development of Si Δ*E-E* telescope using an annular-type *E* detector for in-beam γ-ray spectroscopy

R. Takahashi[1,2], T. Ishii[2], H. Makii[2], M. Asai[2], Y. Wakabayashi[2], D. Nagae[3], K. Tsukada[2], A. Toyoshima[2], M. Matsuda[2], A. Makishima[4], T. Shizuma[2], T. Kohno[5] and M. Ogawa[6]

We have developed a spectroscopic method of combining particle and γ-ray measurements using Si Δ*E-E* telescopes for heavy-ion transfer reactions [1]. This method was so far successfully applied to measuring in-beam γ-rays of actinide nuclei such as ^{245,246}Pu ($Z = 94$), ^{249,250}Cm ($Z = 96$), and ^{248,250,252}Cf ($Z = 98$) [2-5]. In these experiments, the excitation energies of the residual nuclei are obtained by the kinematics analyses of scattered particles. However, the excitation energy has an ambiguity of approximately 2 MeV owing to the covering angle (±10°) of the Si Δ*E-E* telescope. In order to improve the ambiguity, we have developed a new Si Δ*E-E* telescope consisting of an annular-type *E* detector and four Δ*E* detectors (Fig. 1) to measure the scattering angles with higher accuracy.

The Si detector (designed by Micron Semiconductor Ltd) has an annular active-area whose inside diameter is 47.9 mm and outside diameter is 96.1 mm. This active area is divided into 16 lanes annularly. By setting this telescope 4 cm apart from the target, we can measure scattering angles with the accuracy of approximately ±0.5°. Energy resolution using this telescope was tested using a 0.4 mg/cm^2 thick ^{197}Au target which was vacuum-evaporated onto a 0.54 mg/cm^2 aluminum foil and a 144 MeV ^{16}O beam adjusted to be 1.4 mm in diameter.

Fig. 1 Si Δ *E-E* telescope consisting of an annular-type *E* detector and four Δ*E* detectors.

Fig. 2 shows an energy spectrum of the ^{16}O + ^{197}Au elastic scattering, which is obtained by the sum of energies of a Δ*E* detector and the second annular lane (from the inside) of the *E* detector. The energy resolution of the peak is 0.7 MeV (0.5%) [FWHM]. It was found that the improved Δ*E-E* telescope has enough resolution to be used for in-beam γ-ray spectroscopy. We have applied this Δ*E-E* telescope to in-beam γ-ray spectroscopy of ^{249}Cm using the (^{16}O,^{15}O) transfer reaction.
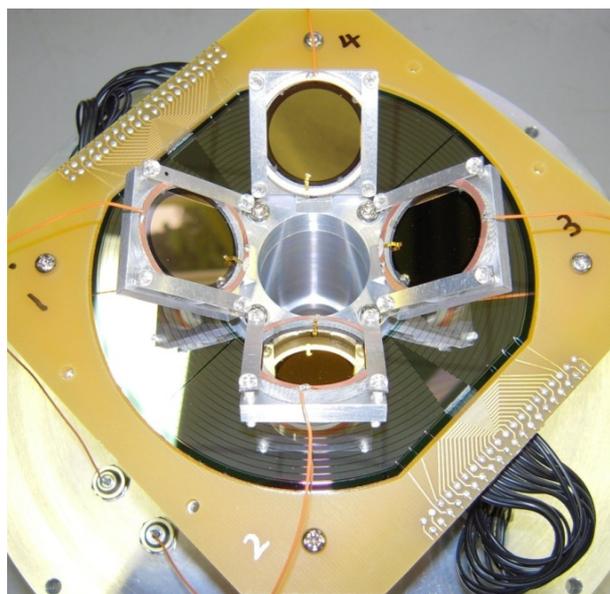
---

[1] Tokyo University of Science

[2] Japan Atomic Energy Agency (JAEA)

[3] University of Tsukuba

[4] National Defense Medical College

[5] Tokyo Institute of Technology

[6] Komazawa University
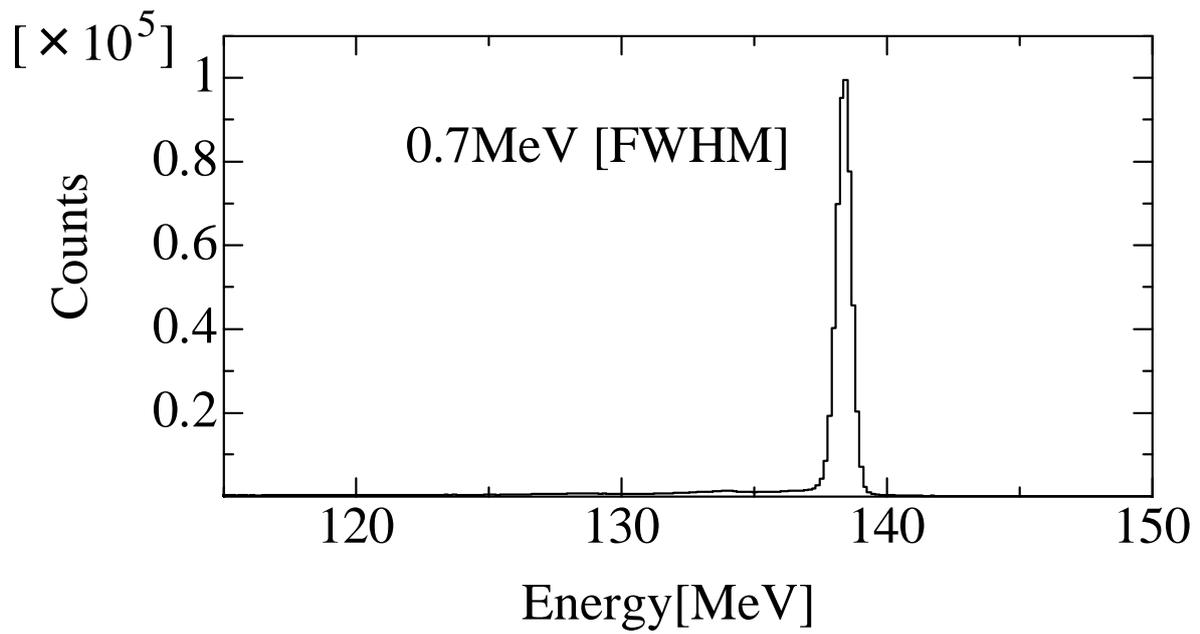
Fig. 2　Energy spectrum of the ^{16}O + ^{197}Au elastic scattering. This spectrum was obtained by the sum of energies of a ΔE detector and the second annular lane (from the inside) of the E detector.

References

[1]　T. Ishii et al., Phys. Rev., C72 (2005) 021301(R) (1-5).

[2]　T. Ishii et al., J. Phys. Soc. Jpn, 75 (2006) 043201 (1-4).

[3]　H. Makii et al., Phys. Rev., C76 (2007) 061301(R) (1-5).

[4]　T. Ishii et al., Phys. Rev., C78 (2008) 054309 (1-11).

[5]　R. Takahashi et al., Phys. Rev., C81 (2010) 057303 (1-4).

2.9 Coulomb excitation of ^{130}Ba at 1.1 MeV/nucleon

N. Imai[1], Y. Hirayama[1], H. Ishiyama[1], S.C. Jeong[1], H. Miyatake[1], Y.X. Watanabe[1], H. Makii[2],

S. Mitsuoka[2], I. Nishinaka[2], K. Nishio[2] and Y. Wakabayashi[2]

Barium isotopes are located in an island of octupole deformation. The B(E2) and B(E1) values in these nuclei give us crucial information on the octupole correlations to the dipole or quadrupole moments in nuclei. A recent lifetime measurement of the first 2^+ (2^+_1) state of ^{142}Ba gave a B(E2) value inconsistent with the past experimental data [1]. Up to date, the B(E2) values of ^{142}Ba have been deduced using the lifetime measurements of the 2^+_1 state produced in the spontaneous fission of ^{252}Cf. The inconsistency among the past data can be attributed to how to take into account the effects of cascade transitions and recoil velocities of fission products. Instead of lifetime measurement, we proposed to use the Coulomb excitation of ^{142}Ba by employing Tokai Radioactive Accelerator Complex (TRIAC) [2]. TRIAC can accelerate radioactive isotopes extracted by JAEA ISOL upto 1.1 MeV/nucleon, which is far below the Coulomb barrier. Thus, the cascade transition is negligible since the probability of multi-step excitation should be very small.

As a test of the whole experimental system including charge-breeding electron cyclotron resonance ion source called as KEKCB [3], we performed an experiment of Coulomb excitation with a stable ^{130}Ba beam of 1.1 MeV/nucleon. The energy of 2^+_1 state of ^{130}Ba is 359 keV, which is close to the 357 keV for ^{142}Ba. The present experiment simulates the measurement of ^{142}Ba.

A ^{130}Ba^{1+} beam was supplied by JAEA ISOL using the enriched BaCO$_3$. Typical beam intensity was about 30 enA. The beam was injected into the KEKCB for charge-breeding the singly charged ions ^{130}Ba^{1+} to multi-charged ones ^{130}Ba^{19+}. The charge breeding efficiency achieved was around 1%. The ^{130}Ba^{19+} beam was transported to two linear accelerators, split-coaxial radiofrequency quadrupole (SCRFQ) and inter-digital H (IH) linacs. Using the two linacs, the beams energy was increased to 1.1 MeV/nucleon.

At the final focal plane of TRIAC, a secondary target of 3 μm thick ^{nat}V was placed and irradiated by the beam. Three NaI(Tl) detectors of 9 x 9 x 18 cm^3 were placed to detect the de-excitation γ rays from the excited ^{130}Ba around the target. The NaI(Tl)s were mounted in the 2 cm thick lead box to suppress the background γ rays or X rays. To measure the recoiled particles, an annular type SSD of a large solid angle was placed 18 cm downstream of the target. The detector covered from 12 to 24 degrees in the laboratory frame, which corresponds to angles from 48 to 160 degrees in the center of mass frame. While 92% of inelastic scattering channel can be measured by the detector, the elastic channel can be reduced to be 0.016 % of total cross section.

---

[1] High Energy Accelerator Research Organization (KEK)

[2] Japan Atomic Energy Agency (JAEA)

Figure 1 (a) shows the two γ-ray energy spectra measured by a NaI(Tl) detector with different timing gates. The solid line indicates γ rays which were coincident with the SSD, while the dashed line represents the accidentally coincident γ rays. The γ ray spectrum obtained by subtracting the accidental ones from the coincident ones is shown in Fig.1 (b), presenting that only a 360 keV line were clearly observed.

The beam development of ^{142}Ba was also performed independently. The beam intensity is expected to be several 10^3 particles/s at the secondary target. The measurement of B(E2) value of the 2^+_1 state of ^{142}Ba is scheduled in this summer.
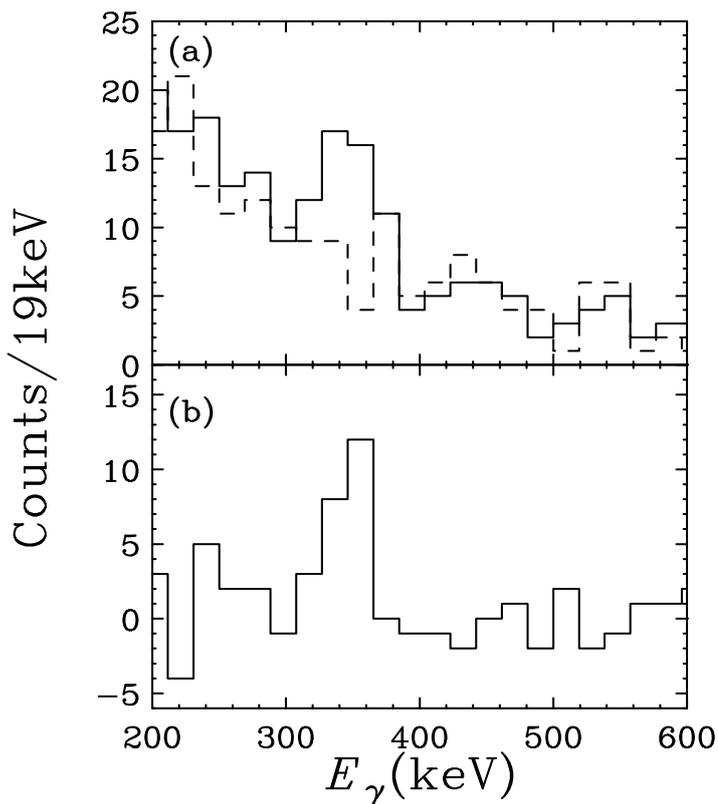
Fig. 1 (a) γ ray energy spectra coincident with SSD (solid line) and accidentally coincident with SSD (dashed line). (b) γ ray energy spectrum obtained by subtracting the accidental γ rays.

References

[1] D.C. Biswas, et al., Phys. Rev., C71 (2005) 011301.

[2] H. Miyatake et al., Nucl. Instrum. Methods Phys. Res., B204 (2003) 420-427.

[3] S.C. Jeong, et al., Nucl. Instrum. Methods Phys. Res., B266 (2008) 4411-4414.

2.10 Search for highly excited ^{11}Be states in ^{9}Li+d reactions

T. Teranishi[1], H. Ishiyama[2], H. Miyatake[2], S.C. Jeong[2], Y.X. Watanabe[2], N. Imai[2], Y. Hirayama[2],

A. Osa[3], T.K Sato[3], S. Mitsuoka[3], K. Nishio[3], M. Matsuda[3], H. Makii[3], Y. Wakabayashi[3],

T. Hashimoto[4], Y. Ito[5], Y. Kenmoku[5] and K. Yamaguchi[6]

An excited level at 18.2 MeV in ^{11}Be has been suggested from observations of beta-delayed deuteron, triton, and α emissions in ^{11}Li beta decay experiments [1]. This level is above and close to the ^{9}Li+d threshold at 17.9 MeV and possibly enhances the beta delayed deuteron emission probabilities [2] (Fig. 1). This level is also a candidate of a "halo analog state" of ^{11}Li, which is populated by a GT transition of the two halo neutrons in ^{11}Li, namely ^{11}Li (^{9}Li+2n) → ^{11}Be* (^{9}Li+d) [3]. Clear determination of the energy, width, and spin-parity may be therefore useful for studying the GT transitions of ^{11}Li and its halo structure. However the signature of the level was not so clear in the beta decay experiments: the energy and width of the level were deduced from fitting of a spectrum containing unresolved deuterons and tritons without any sharp peak, and also from fitting of an unresolved ^{4,6}He spectrum in the decay ^{11}Li(β)^{11}Be* → ^{6}He+α+n, which did not also show any peak of the level because of the three body decay. Moreover, a recent observation of beta delayed deuterons did not indicate any resonance signature [4]. Further experimental investigation with a different approach is necessary.
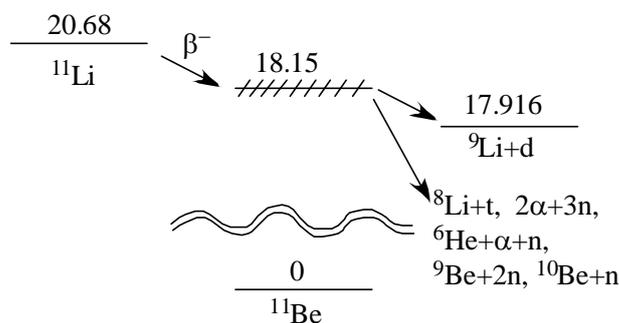
Fig. 1 β-delayed particle emission from ^{11}Li via the 18.2 MeV level in ^{11}Be.

In the present experiment we have studied ^{9}Li+d reactions to search for a resonance signature attributed to the 18.2 MeV level. We measured deuteron, triton, α spectra from ^{9}Li+d elastic scattering, ^{9}Li(d,t), and ^{9}Li(d,α) reactions, respectively. The ^{9}Li+d reaction experiment was performed at TRIAC (Tokai Radioactive Ion Accelerator Complex). A primary beam of ^{7}Li at 70 MeV from the JAEA tandem accelerator bombarded an ISOL target of BN. Secondary ^{9}Li ions extracted from the ISOL target were accelerated by TRIAC up to 0.85 MeV/u. Fig. 2 shows the experimental setup for the ^{9}Li+d reactions. The

---

[1] Kyushu University
[2] High Energy Accelerator Research Organization (KEK)
[3] Japan Atomic Energy Agency (JAEA)
[4] Center for Nuclear Study (CNS), the University of Tokyo
[5] Osaka University
[6] University of Tsukuba

secondary beam ions were counted on an event-by-event basis using an MCP detector with a 0.1 mg/cm^2 Mylar foil. After passing through the MCP detector, the ^{9}Li beam bombarded a $(CD_2)_n$ target of 2.3 mg/cm^2 with an average beam intensity of approximately 3×10^4 particles/s. To deduce the excitation functions of ^{9}Li+d scattering, ^{9}Li(d,t), and ^{9}Li(d,α) reactions, we utilized a thick target method in inverse kinematics (TTIK), where the target thickness was chosen to be thick enough to stop most of the incident ^{9}Li ions in the target. The recoil deuteron, triton, and α particles suffered relatively small energy losses in the target and detected by a Si detector array (SDA) located 26 cm downstream of the target with its center at 0°. SDA consisted of 3×3 Si detectors, each of which was 300 μm thick and had a 28×28 mm^2 sensitive area. Particle identification was made using time-of-flight (TOF) information from MCP to SDA and energy (E) information of SDA. Fig. 3 shows an example of the measured TOF-E spectrum. There was a background component below 2 MeV, which was due to accidental α particles from the beta decay of ^{9}Li. The timing distribution of the accidental α particles was essentially uniform and their energy distribution could be easily estimated. Then, the accidental background component was subtracted from the deuteron, triton, and α spectra.

Though analysis is in progress, a preliminary result of the ^{9}Li+d spectrum contains no sharp peak but shows monotonically increasing cross sections toward the low energy side. The low energy limit of the spectrum due to the detector threshold was $E \sim 0.6$ MeV ($E_{c.m.} \sim 0.3$ MeV), which was unfortunately almost the same as the expected resonance energy for the 18.2 MeV level. This means that only the upper half of the resonance shape might be observed. A possibility of resonance contribution to the spectral shape above $E_{c.m.} = 0.3$ MeV will be examined by utilizing R-matrix analysis. We will also analyze the triton and α spectra on the same R-matrix basis by assuming some resonance contributions.
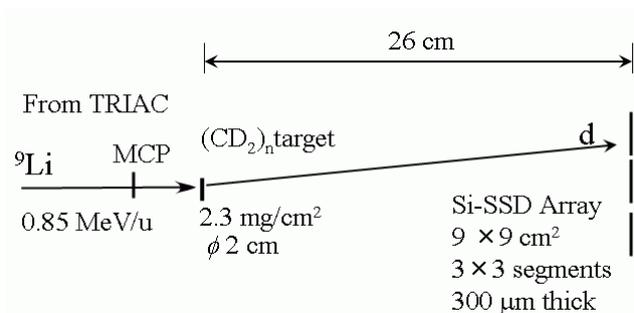
Fig. 2 Experimental setup for ^{9}Li+d reactions.
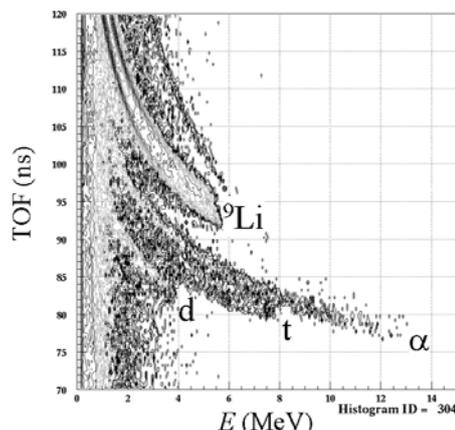
Fig. 3 E-TOF spectrum for recoil particles.

References

[1] M.J.G. Borge et al., Nucl. Phys., A613 (1997) 199 and references therein.

[2] D. Baye et al., Phys. Rev., C74 (2006) 064302 and references therein.

[3] M.V. Zhukov et al., Phys. Rev. C52 (1995) 2461.

[4] R. Raabe et al., Phys. Rev. Lett., 101 (2008) 212501.

CHAPTER 3

Nuclear Reaction

This is a blank page.

3.1   Measurement of fission cross-sections in the reactions of ^{34,36}S + ^{204,206,208}Pb

J. Khuyagbaatar[1], D. Ackerman[1], M. Block[1], S. Heinz[1], F.P. Heβberger[1], S. Hofmann[1], H. Ikezoe[2],

B. Kindler[1], B. Lommel[1], H. Makii[2], S. Mitsuoka[2], I. Nishinaka[2], K. Nishio[2], Y. Wakabayashi[2] and S. Yan[3]

Measurements of the decay properties and the structures of very heavy nuclei are important to understand the limit of stability of nucleus. The most successful reaction for the production of heavy nuclei is fusion of two colliding nuclei forming an excited compound nucleus which de-excites by evaporation of neutrons. However, the cross-sections for the production of heavier nuclei are strongly decreasing with increasing number of protons. Thus, the accuracy for investigating nuclear structures for heavy nuclei is limited by production rates. Selection of fusion-evaporation reactions having highest cross-sections is important.

 (i) The cross-sections of the fusion-evaporation reactions of ^{36}S+$^{206\text{-}208}$Pb and ^{34}S+^{208}Pb which produce the neutron-deficient isotopes of Cf were measured recently at SHIP [2]. The cross-sections for the 2n and 3n evaporation channels for the ^{36}S+$^{206\text{-}208}$Pb reactions were on the order of a few hundred nanobarn which are unexpectedly higher than the values in [3] and calculated values by HIVAP code [4]. Further the comparison of the cross-sections of 2n and 3n channels from fusion reactions ^{36}S+^{206}Pb and ^{34}S+^{208}Pb leading to the compound nucleus ^{242}Cf, reveals significant differences which can not be explained by differences of the reaction Q-values alone. Additional effects could also be the reason for the different cross-sections.

 (ii) The fusion reaction of colliding nuclei with proton and neutron numbers close to magic and semi-magic numbers are characterized by a steep falloff in the capture cross-sections at energies below the Coulomb barrier [1]. Combinations of ^{36}S and ^{34}S projectiles with various lead-isotope targets at absent deformation effect are very suitable for the study of the influence of the nuclear structure of ^{36}S and ^{34}S (semi-magic) nuclei on the fusion reaction.

 The purpose of this experiment was to investigate the entrance channel effects which include subjects of (i) and (ii) by measuring the fission fragments from the ^{36}S+Pb and ^{34}S+Pb reactions. Here, we present preliminary results on the capture cross-sections which are directly connected to (ii).

 The experiment was performed at the tandem accelerator of JAEA. Isotopically enriched material of 40% and 60% for ^{36}S and ^{34}S, respectively, was used for the negative ion source. The beams were accelerated up to energies of 200 MeV and the average beam current was 3 pnA. Pure metallic Pb targets with thicknesses of 100 µg/cm^2 were prepared at the target laboratory of GSI. The targets were prepared by evaporating isotopically enriched (≥99%) ^{204,206,208}Pb materials on carbon backing foils with average thicknesses of 40 µg/cm^2. The opposite side of the targets was covered by a 10 µg/cm^2 carbon layer. The targets were mounted at an angle of 45° to the beam axis with the thinner carbon layer in the beam direction. Two Multi-Wire-Proportional-Counters (MWPCs) were used to detect the fission fragments in coincidence. The beam dose was deduced using the number of elastically scattered particles at an angle of 26.5° relative to the beam axis and with a solid angle of 1.96 msr. The experimental setup and the analysis of the fission

---

data were the same as described in [5].

Preliminary results of the capture cross-sections are shown in fig. 1 as a function of the center-of-mass energy. The behavior of the excitation functions of ^{36}S+^{204,206,208}Pb reactions is similar and it is characterized by a steep falloff of cross-sections at low energies (same for ^{34}S). This indicates that the change of nuclear structures of the proton magic target nuclei ^{204,206,208}Pb has not much influence on the entrance channel. However, the slopes of the falloff are different in the case of ^{36}S and ^{34}S, whereas the behavior of the cross-sections at energies around and above the barrier is similar. The cross-sections calculated using the CCFULL code [6] are also plotted in fig. 1. The dotted curves represent the calculated results from a one-dimensional barrier penetration model without coupling to excited states. These calculations cannot describe the cross-sections at energies below the Coulomb barriers. The cross-sections down to the lowest energies are well described by the calculations where coupling of the first 2^+ and 3^- states in the projectile and the target nuclei, respectively, were included (solid curves). These results show that the enhancement of the fusion process at sub-barrier energies is higher for ^{34}S than for ^{36}S. This is due to the strong couplings to the 2^+ state in ^{34}S which is located at lower excitation energy of 2.127 MeV than the couplings to the ^{36}S state of 3.291 MeV.
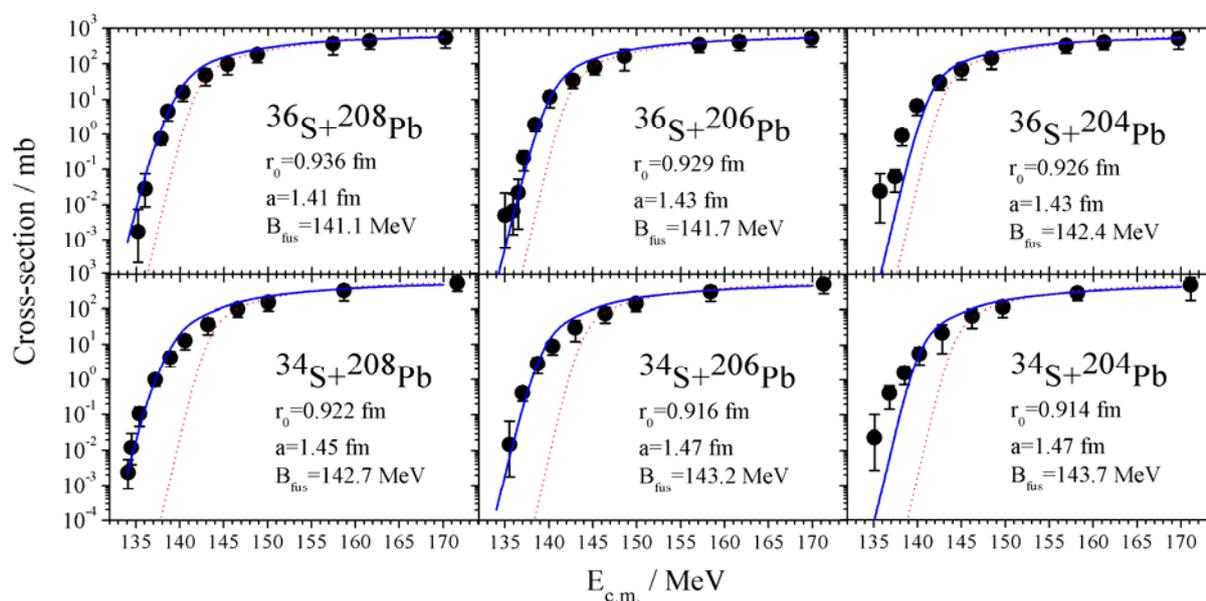
Fig. 1 Cross-sections deduced from the measured fission events from the ^{36}S+Pb and ^{34}S+Pb reactions as a function of the center-of-mass energy. Curves represent the calculated cross-sections (see text). Radius (r_0), diffuseness (a) and corresponding fusion barrier (B_{fus}) are given for each reaction.

References
[1] C.L. Jiang et al., Phys. Lett., B640 (2006) 18 and reference therein.
[2] J. Khuyagbaatar et al., to be published.
[3] Yu. Lazarev et al., Nucl. Phys., A588 (1995) 501.
[4] W. Reisdorf and M. Schaedel, Z.Phys., A343 (1992) 47.
[5] K. Nishio et al., Phys. Rev., C77 (2008) 064607.
[6] Modified version of the CCFULL code, K. Hagino et al., Computer Phys. Comm. 123 (1999) 143.

3.2 Coulomb barrier distribution of quasi-elastic backscattering in ^{64}Ni + ^{238}U

S. Mitsuoka[1], H. Ikezoe[1], K. Nishio[1], Y.X. Watanabe[2], S.C. Jeong[2],

Y. Hirayama[2], N. Imai[2], H. Ishiyama[2] and H. Miyatake[2]

Coulomb barrier distributions have been systematically measured [1,2] and theoretically studied [3,4,5] in ^{48}Ti, ^{54}Cr, ^{56}Fe, ^{64}Ni, ^{70}Zn, ^{76}Ge and ^{86}Kr + ^{208}Pb reactions relating to Pb-based cold fusion reactions for the production of super-heavy elements Z=104, 106, 108, 110, 112, 114 and 118, respectively. The barrier distributions were well reproduced by taking account of the coupling effects of quadrupole vibration for the projectiles and of the octupole vibration for the ^{208}Pb target [1,3]. Also super-heavy elements up to Z=118 have been produced in hot fusion reactions with actinide targets. Recently, the production of Z=120 element has been tried in ^{64}Ni + ^{238}U reaction. Since ^{238}U nucleus is prolately deformed, the Coulomb barrier depends on the orientation of the target nucleus. Such orientation effects of the deformed ^{238}U on fusion and fission processes have been systematically investigated in reactions of ^{30}Si, ^{36}S and ^{40}Al + ^{238}U [6]. In this experiment we measured the Coulomb barrier distributions and the fission mass distributions in the ^{64}Ni + ^{238}U reaction as a function of the bombarding energy.

The experiment was carried out by using a large-volume scattering chamber (1.2 m in diameter) newly set in the JAEA tandem-booster experimental hole. A ^{238}U target prepared by electrodeposition on a Ni foil was bombarded by ^{64}Ni beams of 310 - 385 MeV with changing the energies in steps of 1.5 MeV. The fission fragments were detected in coincidence by two position-sensitive multi-wire proportional counters (MWPCs) covering the emission angles of 35° - 85°. The backward scattered particles were detected by 16 solid state detectors (SSDs) arranged annularly with respect to the beam axis at 172° and 164°. Another two SSDs at 18° monitored the beam. The barrier distributions were obtained by taking the first derivative of the quasi-elastic (QE) cross section $\sigma_{QE}(E)$ relative to the Rutherford scattering cross section $\sigma_R(E)$ as a function of center-of-mass energy E, that is $-d\{\sigma_{QE}(E)/\sigma_R(E)\}/dE$. Detailed analysis is in progress for QE cross sections where deep-inelastic scattering should be carefully excluded by considering the reaction Q-values of inelastic and transfer channels.

References

[1] S. Mitsuoka el al., Phys. Rev. Lett., 99 (2007) 182701.

[2] S.S. Ntshangase et al., Phys. Lett., B651 (2007) 27-32.

[3] Z. Muhammad el al., Phys. Rev., C77 (2008) 034604.

[4] G. Pollarolo, Phys. Rev. Lett., 100 (2008) 252701.

[5] V. I. Zagrebaev, Phys. Rev., C78 (2008) 047602.

[6] K. Nishio el al., Phys. Rev., C77 (2008) 064607.

---

[1] Japan Atomic Energy Agency (JAEA)

[2] High Energy Accelerator Research Organization (KEK)

3.3 Measurement of fission fragment mass distribution in the reaction of ^{40}Ar + ^{238}U

K. Nishio[1], I. Nishinaka[1], S. Mitsuoka[1], H. Makii[1], Y. Wakabayashi[1], H. Ikezoe[1],

K. Hirose[2] and T. Ohtsuki[2]

In the fusion reactions between ^{48}Ca beams and actinide target nuclei, elements up to 118 have been produced [1]. The striking feature in the reaction is that the cross-sections do not drop with atomic number but maintain a few pico-barn values even for the production of the heaviest elements, which makes large difference from the cold fusion reactions using lead or bismuth targets [2,3]. A possible explanation for keeping the larger cross-section would be associated with the static deformation of the target nuclei. Because of the prolate deformation of ^{238}U, there is a configuration that projectile collides on the equatorial side of ^{238}U, which would result in larger fusion probability than the reactions using lead or bismuth target. To investigate the orientation effects on fusion and fission process, we are measuring the fission fragment properties at the tandem accelerator.

In the reaction of ^{36}S + ^{238}U, we observed strong variation of the fragment mass distribution on the bombarding energy [4]. The data revealed a transition from symmetry to asymmetry mass distribution when the beam energies were decreased from the above-barrier to sub-barrier values. The symmetric fission results from fusion-fission and the asymmetric fission is associated with quasifission. The relative yield for quasifission increases when the reaction energy decreases down to the sub-barrier energy, where projectile collides dominantly on the polar side of ^{238}U. On the other hand, it is suggested that the equatorial collision results in larger fusion-fission probability. In this report, we show the results of the mass distribution for reactions using heavier projectile ^{40}Ar.

The experiment was carried out by using ^{40}Ar beams extracted from the ECR ion source and accelerated by the tandem accelerator. The ^{238}U target was made by an electro-deposition method. The fission fragments were detected in coincidence by position-sensitive multi-wire proportional counters (MWPCs). Fragment masses are determined by using a conservation law for the mass and momentum. Results for the mass distributions are shown in Fig. 1. In all the energy range, the distribution has asymmetric shape, which means that quasifission dominates. The asymmetric fission has a peak at around $A_L / A_H = 78 / 200$ in $E_{c.m.} < 187$ MeV. In the region of $E_{c.m.} > 187$ MeV, an additional asymmetric channel appears at around $A_L / A_H = 110 / 168$. In spite of the dominant mass asymmetry, the symmetric yields are present. With decreasing bombarding energy, the yield for symmetric fission decreases. The relative change of the symmetric/asymmetric fission yields represents the orientation effects.

---

[1] Japan Atomic Energy Agency (JAEA)
[2] Tohoku University
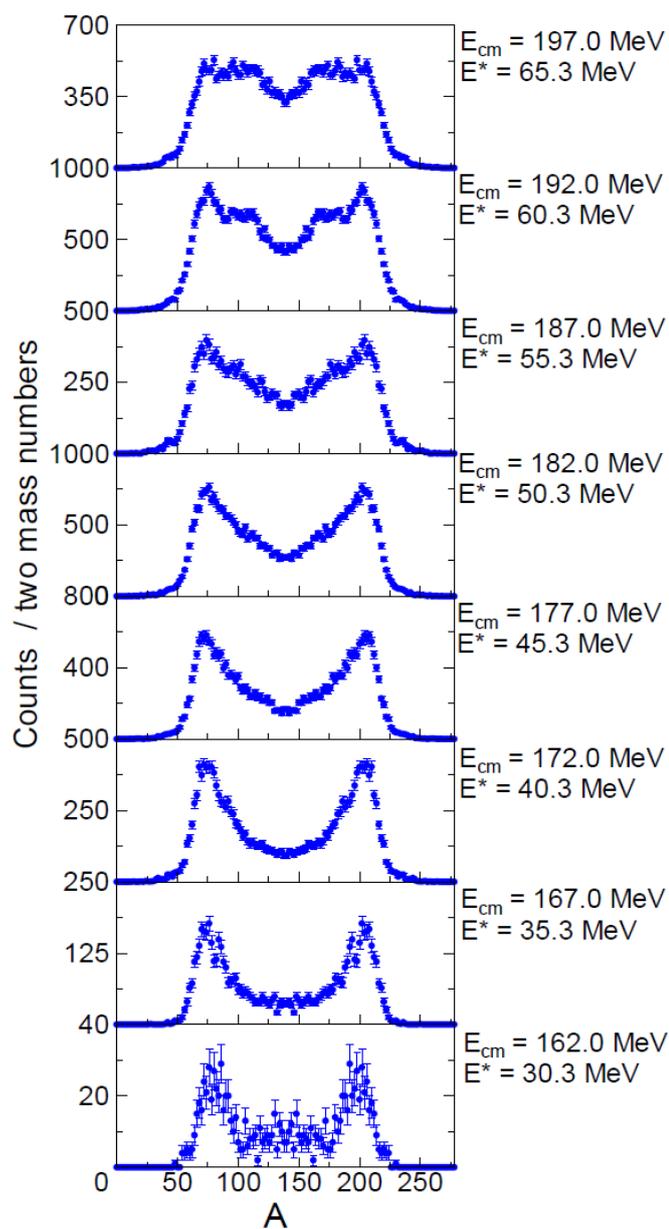
Fig. 1   Fission fragment mass distributions in the reacition of ^{40}Ar + ^{238}U.

References

[1] Yu.Ts. Oganessian, J. Phys., G34 (2007) R165.

[2] S. Hofmann and G. Münzenberg, Rev. Mod. Phys., 72 (2000) 733.

[3] K. Morita et al., J. Phys. Soc. Jpn, 73 (2004) 1738.

[4] K. Nishio et al., Phys. Rev., C77 (2008) 064607.

3.4   Fission properties of the neutron-deficient nucleus ^{180}Hg produced in heavy ion fusion reactions

A.N. Andreyev[1], R. Chapman[1], S. Pain[1], I. Tsekhanovich[2], M. Venhart[3], K. Nishio[4], S. Mitsuoka[4],

I. Nishinaka[4], H. Makii[4], Y. Wakabayashi[4], H. Ikezoe[4], J. Khuyagbaatar[5], S. Yan[6], K. Hirose[7]

and T. Ohtsuki[7]

This research project is motivated by the recent study of the low-energy beta-delayed fission (βDF) of ^{180}Tl at ISOLDE (CERN). In the ISOLDE experiment we measured the fission fragment mass distributions of the weakly-excited nucleus ^{180}Hg populated by the beta decay of ^{180}Tl. An asymmetric mass distribution with the most probable mass split into 80 u and 100 u was observed. This is in a strong contrast to the expected symmetrical mass split in two semi-magic spherical ^{90}Zr nuclei. Also from the calculations of the potential energy at scission [2], the symmetric fission with equal mass split was expected to have the deepest fission valley. However, our calculations based on the five dimensional deformation space [3], suggests that the observed asymmetric fission originates from the low-lying *asymmetrical* saddle point at about E*~10 MeV.

The calculations suggest several fission channels in this nucleus. In order to investigate the presence of the anticipated fission saddle points and the associated fission channels, we propose to measure the fission properties from the excited compound nucleus in a broad range in the excitation energies to cover all the possible saddle point configurations. The most straightforward tool to populate the highly excited compound nucleus is to utilize the heavy ion fusion reactions. Therefore, we propose to study fission of ^{180}Hg* produced in several fusion reactions. As a first step, we have carried out the experiment to measure the fission fragment mass distributions for ^{36}Ar + ^{144}Sm → ^{180}Hg* in the excitation energy range between 30 – 65 MeV.

The experiment was carried out at the JAEA tandem accelerator. The ^{36}Ar beams were supplied from the ECR ion source installed at the terminal section of the tandem accelerator. The beam energies were changed from 153 MeV to 195 MeV, corresponding to the excitation energy E^* =28 – 65 MeV of ^{180}Hg. The typical beam intensity was 3 paritcle-nA. The ^{144}Sm target of 100 μ g/cm^2 were prepared at the target laboratory of GSI. Two multi-wire proportional counters (MWPCs) were used to detect the fission fragments in coincidence. The beam dose was deduced using the number of elastically scattered particles at an angle of 26.5° relative to the beam axis and with a solid angle of 1.96 msr. The experimental setup was the same as described in [4]. The data analysis is in progress.

---

[1] University of the West Scotland
[2] The University of Manchester
[3] Instituut voor Kern- en Stralighsfysica, KU Leuven
[4] Japan Atomic Energy Agency (JAEA)
[5] GSI, Germany
[6] CIAE, China
[7] Tohoku University

References

[1] A. Andreyev et al, ISOLDE proposal IS466, the experiment performed in June 2008.

[2] T. Ichikawa, private communication.

[3] P. Möller et al.,"Nuclear fission modes and fragment mass asymmetries in five-dimention deformation space", Nature, 409 (2001) 709 and private communication.

[4] K. Nishio *et al.*, Phys. Rev. C77, 064607 (2008).

3.5   Fission fragment anisotropy in heavy-ion-induced fission of actinides

I. Nishinaka[1], K. Nishio[1], M. Tanikawa[2], H. Makii[1], S. Mitsuoka[1],
Y. Wakabayashi[1] and A. Yokoyama[3]

Fission fragment angular distribution in light-ion-induced fission has been explained well by the standard saddle point model [1]. However, in heavy-ion-induced fission of actinides at near-barrier energies, fission fragment anisotropy has been found to become anomalously high compared with that expected from the standard saddle point model [2, 3]. This anomaly of fission fragment anisotropy was thought to originate from non-equilibrium fission process. The pre-equilibrium K-states model suggests that entrance channel mass asymmetry $\alpha=(A_t-A_p)/(A_t+A_p)$ plays an important role for fission fragment anisotropy in heavy-ion-induced fission of actinides [4, 5]. A_t and A_p refer to mass numbers of target and projectile nuclei, respectively. A limited number of experiments have been carried out to study the effect of different entrance channels leading to the same compound nucleus, ^{248}Cf (^{16}O+^{232}Th and ^{12}C+^{236}U) [6] and ^{246}Bk (^{14}N+^{232}Th and ^{11}B+^{235}U) [7]. In order to study the effect of fission fragment anisotropy on entrance channels, we measured fission fragment angular distributions in the reactions of ^{22}Ne+^{232}Th (α =0.827) and ^{12}C+^{242}Pu (α =0.906), populating the same compound nucleus ^{254}Fm.

A ^{232}Th target was irradiated with ^{22}Ne ions of energy E_{lab} = 120, 116, 112, and 108 MeV at the JAEA tandem accelerator, excitation energies of the compound nucleus being 56.1, 52.5 48.8, and 45.2 MeV, respectively. The ^{232}Th target with thickness of 68 μg/cm^2 was prepared by molecular electrodeposition onto 89 μg/cm^2 nickel foil. Fission fragments were measured by four position-sensitive parallel-plate avalanche counters (PPACs) and a silicon surface barrier detector (SSD) as schematically shown in Fig.1. Each PPAC has the sensitive area of 20×8 cm^2 for horizontal (X) and vertical (Y) directions in the reaction plane. The PPACs have horizontal angles of $\theta = 25^\circ$-67°, 73°-105°, 205°-247°, and 253°-285° in laboratory system. The SSD located at $\theta = 176^\circ$ has a solid angle of 0.8 msr. The experiment for ^{12}C+^{242}Pu was carried out with the same experimental setup at beam energies of E_{lab} = 86.4, 82.6, 78.7, and 74.9 MeV, using a ^{242}Pu target with thickness of 37 μg/cm^2. These beam energies correspond to the same excitation energies of the compound nucleus ^{254}Fm produced by the reaction ^{22}Ne+^{232}Th.
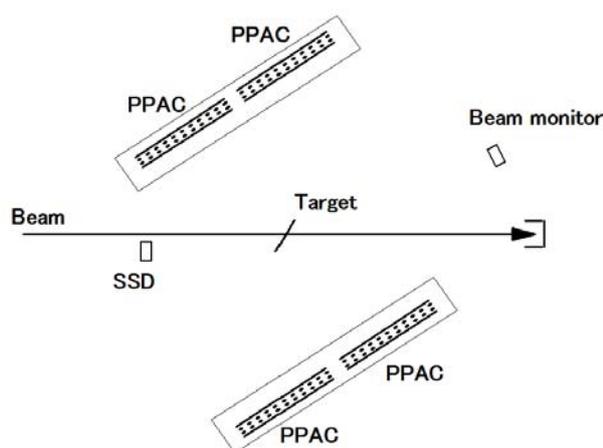
Fig. 1 Experimental setup.

[1] Japan Atomic Energy Agency (JAEA)
[2] University of Tokyo
[3] Kanazawa University

Figure 2 shows the center-of-mass angular distribution of fission fragments in the 86.4 MeV ^{12}C+^{242}Pu, using the fission fragment kinetic energy predicted by the systematics of Viola *et al.*[8]. The center-of-mass angular distribution provides the fission fragment anisotropy defined as $A = W(180^\circ)/ W(90^\circ)$.   Figure 3 represents preliminary results of the fission fragment anisotropy as a function of the excitation energy of the compound nucleus by solid circles for ^{12}C+^{242}Pu and open ones for ^{22}Ne+^{232}Th. The error bar indicates the uncertainty of experimental angular distribution as shown by dashed lines in Fig. 2. The anisotropy for ^{22}Ne+^{232}Th with smaller entrance channel mass asymmetry $\alpha = 0.827$ shows large values compare with those for ^{12}C+^{242}Pu with $\alpha = 0.906$. This implies that entrance channel mass asymmetry plays a role for fission fragment anisotropy in the present fissioning systems.
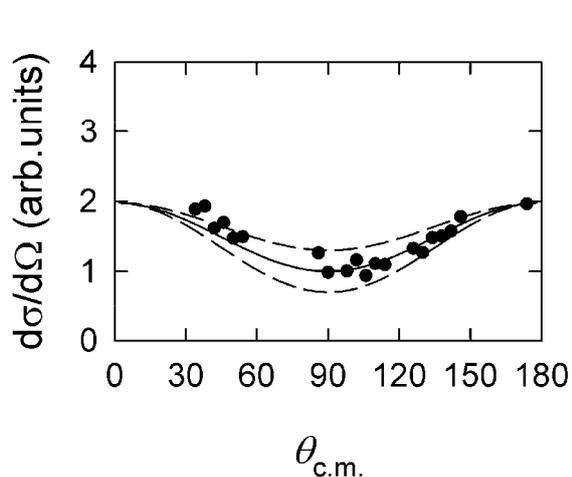
Fig. 2 The center-of-mass angular distributions of fission fragments in the 86.4 MeV ^{12}C+^{242}Pu reaction.
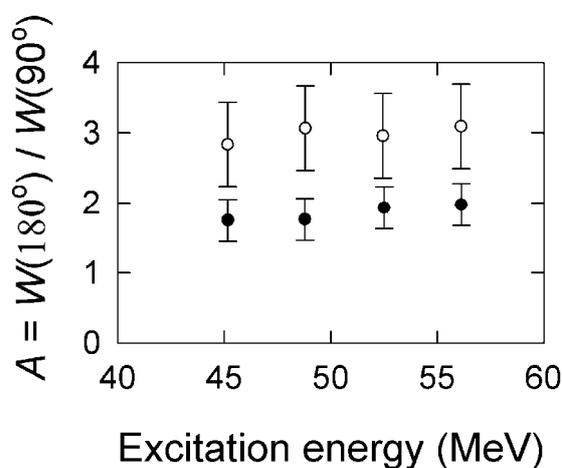
Fig. 3 Preliminary results of the fission fragment anisotropy for ^{12}C+^{242}Pu (solid circles) and ^{22}Ne+^{232}Th (open circles) as a function of the excitation energy of the compound nucleus ^{254}Fm.

References

[1] R. Vandenbosch and J. R. Huizenga, Nuclear Fission (Academic, New York, 1973).

[2] S. Kailas, J. Phys., G23 (1997) 1227-1233.

[3] J. P. Lestone et al., J. Phys., G23 (1997) 1349-1357.

[4] V. S. Ramamurthy et al., Phys. Rev. Lett., 65 (1990) 25-28.

[5] Z. Liu *et al.*, Phys. Lett., B353 (1995) 173-178.

[6] R. Vandenbosh et al., Phys. Rev., C54 (1996) R977-R980.

[7] B. R. Behera et al., Phys. Rev., C69 (2004) 064603-1-10.

[8] V. E. Viola. et al., Nucl. Data Tables, A1 (1966) 391.

3.6 Search for the new isotope ^{220}Pu produced in the fusion reaction ^{82}Kr + ^{140}Ce

K. Nishio[1], Y. Wakabayashi[1], S. Mitsuoka[1], I. Nishinaka[1], H. Makii[1], H. Ikezoe[1], M. Matsuda[1],

K. Hirose[2], T. Ohtsuki[2], S. Yan[3], J. Khuyagbaatar[4] and H. Miyatake[5]

Because of the increased binding energy due to the neutron shell at N=126, neutron deficient actinide isotopes up to element around 100 (Fm) [1] are expected to exist with a life-time detectable in a current experimental technique, and the nuclei in the vicinity of N = 126 form a 'peninsula' in the chart of nuclei. Search for such nuclei is important to know if the N=126 shell exists or survives in the extreme of neutron deficient region. As a first step to investigate this region, we are attempting to produce ^{220}Pu (N=126) in the fusion-evaporation reaction ^{82}Kr + ^{140}Ce → ^{220}Pu (2n). The beam energy was chosen so that the center-of-mass energy at the middle of the ^{nat}Ce-target layer is 228 MeV, at which the maximum cross-section for ^{220}Pu is expected. Based on the extrapolation of the fusion probability determined in the reactions of ^{82}Se + ^{140}Ce [2] and ^{86}Kr + ^{134,138}Ba [3] and the statistical model code HIVAP, we calculated the cross-section to be 5 – 60 pb. The ^{220}Pu is expected to decay by emitting alpha particle, and half-life is predicted to be 0.3 – 50 ms [1,2]. The decay chain is linked to the known isotopes ^{212}Th (E_α=7.80MeV, $T_{1/2}$=30ms) and ^{208}Ra(7.13MeV, 1.3s) via the new isotope ^{216}U, thus we can make unambiguous identification of the production of ^{220}Pu by observing a few decay chains.

The experiment was carried out by using the JAEA-tandem and booster accelerator. The ^{82}Kr beams (12^+) are extracted by the ECR ion source placed at the terminal section of the tandem accelerator. Typical beam current on the target position was about 160 pnA. The rotating target was made by sputtering the ^{nat}Ce metallic material on an aluminum foil with thickness 1.0 μm. The thickness of the ^{nat}Ce layer is about 450 μg/cm^2. After the sputtering, we have coated the surface of the Ce-metalic layer by carbon of about 10μ mg/cm^2 to prevent the oxidation of the material and the loss of material due to the irradiation by the intense heavy-ion beams. We also prevent the scattering of the beam at the edge of the rotating target wheel by using the beam chopper system. For this, the rotation angle of the wheel and thus the edge position was monitored by using a photo-sensor, whose signal was used to feed a high voltage to operate an electrostatic deflector to kick and stop the beam. The evaporation residues (ERs) were separated in flight from the primary beams and other reaction products by using the JAEA recoil mass separator and transported to a focal plane. At the focal plane, a silicon strip detector was mounted to detect the implanted recoils and subsequent alpha-decay chains. To measure a time-of-flight (TOF) of the implanted recoils, we mounted two timing detectors in front of the focal plane detectors. The TOF signal and implanted energy signal was used to make a rough estimate for the mass of ER, which can be well separated from the background particles.

---

[1] Japan Atomic Energy Agency (JAEA)
[2] Tohoku University
[3] China Institute of Atomic Energy (CIAE)
[4] GSI, Germany
[5] KEK

We accumulated a beam dose corresponding the production cross-section 10 pb. We are making a data analysis to search for the candidate of the production of ^{220}Pu.

References

[1] H. Koura, private communication.

[2] P. Moller, At. Data and Nucl. Data Table, 66 (1997) 131-343.

[3] K. Nishio *et al.*, Phys. Rev., C63 (2001) 044610.

[4] K.Satou *et al*., Phys.Rev., C73 (2006) 03460.

[5] W. Reisdorf and M. Schaedel, Z. Phys., A343(1992) 47.

3.7 Study of ^{218}U region near N=126 closed shell

Y. Wakabayashi[1], K. Nishio[1], S. Mitsuoka[1], I. Nishinaka[1], H. Makii[1], R. Takahashi[1],
S. Yan[1], H. Miyatake[2] and S. Ota[3]

Synthesis of new actinide nuclei near the N=126 closed shell is interesting to know the stability of the N=126 closed shell [1]. In order to study this stability, we have carried out the experiment to produce a new isotope ^{216}U in the fusion reaction of ^{82}Kr+^{138}Ba and to measure its alpha-decay energies and half-life.

The experiment to produce ^{216}U was performed using the ^{138}Ba (^{82}Kr, 4n) ^{216}U reaction. The calculated cross section of ^{216}U is estimated about 100 pb using the HIVAP code [2]. The ^{82}Kr^{12+} beam of 393 MeV was supplied from JAEA-tandem accelerator and used to bombard the rotating ^{138}Ba target foil. The ^{138}Ba target of 350 μg/cm^2 thickness was made by sputtering a 99%-enriched material of ^{138}Ba isotope on a 0.8 mm aluminum foil. A total dose of 3.6x10^{15} was irradiated on the target for two days. Evaporation residues (ER's) emitted to the beam direction were separated from the ^{82}Kr beam by a recoil mass separator (JAEA-RMS). The separated recoils were implanted into a double-sided position-sensitive strip detector (PSD; 73x55 mm^2). Two Multi Channel Plates (MCP's) were used for timing detectors to obtain the time-of-flight (TOF) signal of the ER's. One was placed in front of the PSD and the other 30 cm upstream the PSD, The presence of the signal in the timing detectors was also used to separate the α decay in the PSD from the recoil implantation.
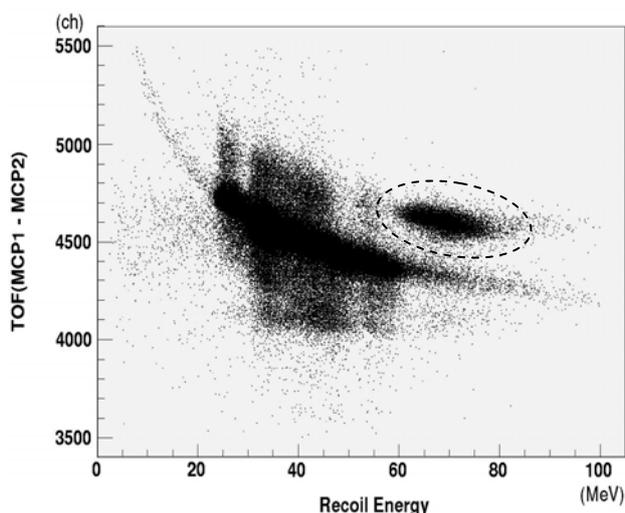
Fig. 1 Two dimensional spectrum of the energy versus TOF obtained from the ^{82}Kr+^{130}Te reaction. The unit of X and Y axis are MeV and ch, respectively. The region of dashed line is the part of ER's.

Figure 1 and 2 show two dimensional spectrum of the recoil energy versus TOF obtained from the calibration run of the ^{82}Kr+^{130}Te reaction and the run of the ^{82}Kr+^{138}Ba reaction, respectively. In Fig. 1, it was found that the ER's were discriminated from the background particles. Energy calibration of the PSD was performed using known α lines from ^{204}Rn(6.42 MeV), ^{209}Fr(6.65 MeV), and ^{207}Ra(7.13 MeV) produced in the ^{82}Kr+^{130}Te reaction. In Fig. 2, the region of dashed line shows the expected area of ER's produced by the ^{82}Kr+^{138}Ba reaction. We obtained an upper-limit cross-section of 50 pb for ^{216}U. Data analysis

[1] Japan Atomic Energy Agency (JAEA)
[2] High Energy Accelerator Research Organization (KEK)
[3] Center for Nuclear Study, University of Tokyo (CNS)

is now in progress.
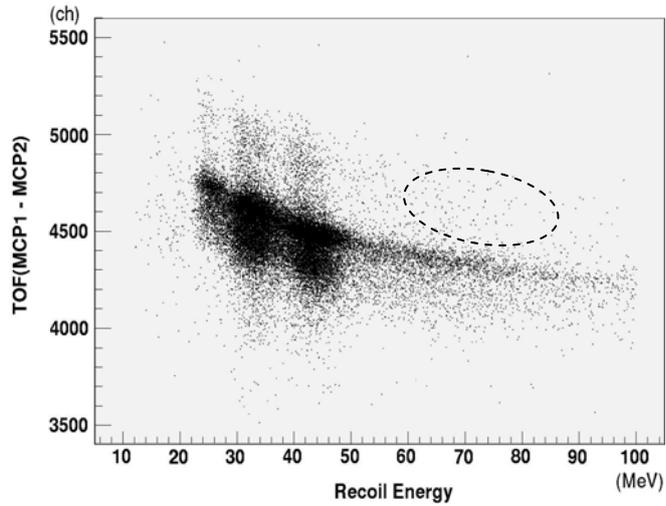
Fig. 2 Two dimensional spectrum of the energy versus TOF obtained from the ^{82}Kr+^{138}Ba reaction. The unit of X and Y axis are MeV and ch, respectively. The dashed line shows the expected area of ER's.

References

[1] H. Koura and T. Tachibana, BUTSURI, 60 (2005) 717-724 (in Japanese).

[2] W. Reisdorf and M. Schadel, Z. Phys., A343 (1992) 47-57.

3.8 Production of ^{256}Lr with the ^{249,250,251}Cf(^{11}B, xn) and ^{243}Am(^{18}O, $5n$) reactions

N. Sato[1], M. Asai[1], K. Tsukada[1], T.K. Sato[1], A. Toyoshima[1],

Z.J. Li[1], T. Kikuchi[1], S. Ichikawa[2] and Y. Nagame[1]

It is quite important to determine first ionization potentials (IPs) of superheavy elements (SHEs) to understand their electronic structure affected by increasingly strong relativistic effects. The IP of the last actinide, lawrencium, is predicted to be lower than those of other actinides. We are planning to measure the IP of Lr using a surface ionizer coupled with an isotope separator on-line at JAEA (JAEA-ISOL) with ^{256}Lr which has a relatively longer half-life of 27 ± 3 s and higher α-decay branching ratio of $85 \pm 10\%$ [1]. In the present study, to determine the optimum reaction and bombarding energy for the production of ^{256}Lr, we measured the excitation functions of the ^{249,250,251}Cf(^{11}B, xn) and ^{243}Am(^{18}O, $5n$) reactions.

A ^{249,250,251}Cf target (^{249}Cf: 62%, ^{250}Cf: 14%, and ^{251}Cf: 24%) with 0.185 mg/cm^2 thickness and an ^{243}Am target with 0.36 mg/cm^2 were irradiated with ^{11}B^{4+} and ^{18}O^{6+} beams, respectively. The beam energies were 57, 60, 63, 66, 69, and 72 MeV for ^{11}B and 93, 96, and 99 MeV for ^{18}O in the middle of the target. Nuclear reaction products recoiling out of the target were transported with a He/KCl gas-jet system through a 25-m long Teflon capillary to the rotating wheel α-particle detection system (MANON) at a He flow rate of 2.4 L/min. The gas-jet transport efficiency was estimated to be 30%. The transported products were deposited on a PET foil with 0.12 mg/cm^2 thickness and 20 mm diameter, eighty of which were arranged at the periphery of a wheel of MANON. After collection for 10 s, the wheel was stepped at 10-s intervals to successively place the deposited sample in front of 18 Si PIN photodiodes (Hamamatsu S3204). Each detector had 30% detection efficiency. Energy resolution of the detectors was 20 keV FWHM in average. Energy calibration was performed with a standard ^{241}Am α source and detecting α-particles from known nuclei produced in the target chamber and transported to the MANON system.

Figure 1 shows a typical α-particle spectrum measured in 10-180 s after collection in the bombardment of the ^{249,250,251}Cf target with the 63 MeV ^{11}B beam. Alpha-lines from ^{256}Lr are clearly observed at 8320, 8390, 8430, 8480, 8520, and 8620 keV. As discussed in Ref. [2], the 8430 keV peak would contain α-particles from ^{256}No fed by the EC decay of ^{256}Lr. The decay curve for 8480, 8520, and 8620 keV α-groups of ^{256}Lr is shown in Fig. 2. The half-life corresponding to these α-lines were determined to be 25 ± 2 s as shown in Fig.2, which is in agreement with the literature value [1]. Excitation functions of the ^{249,250,251}Cf(^{11}B, xn)^{256}Lr and ^{243}Am(^{18}O, $5n$)^{256}Lr reactions are shown in Figs. 3(a) and (b), respectively. For the ^{249,250,251}Cf(^{11}B, xn)^{256}Lr reactions, the maximum cross section of 200 ± 15 nb is found at the ^{11}B beam energy of 63 MeV. The present cross-section is smaller than the literature value of approximately 300 nb for the ^{249}Cf(^{11}B, 4n)^{256}Lr reaction at the same energy [2]. On the other hand, the maximum cross section of the ^{243}Am(^{18}O, $5n$)^{256}Lr reaction is 39 ± 4 nb at 96 MeV, which is slightly larger than the reported value of

---

~30 nb [3]. It seems that the previous cross section value was underestimated because α-particle energy of ^{256}Lr was not completely identified at that time. The ^{249,250,251}Cf + ^{11}B reaction is preferable to the ^{243}Am + ^{18}O reaction for the ^{256}Lr production. In the future, the first IP of Lr will be measured using a gas-jet transport system coupled with a surface ionizer in JAEA-ISOL.
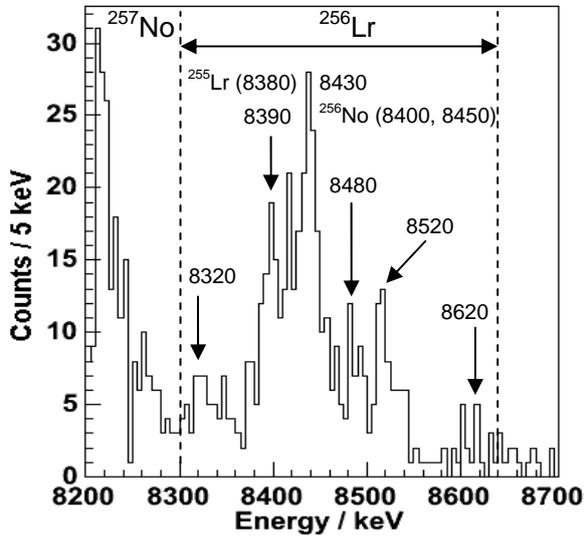
Fig. 1 Alpha-particle spectrum measured in the bombardment of the ^{249,250,251}Cf target with 63-MeV ^{11}B ions.
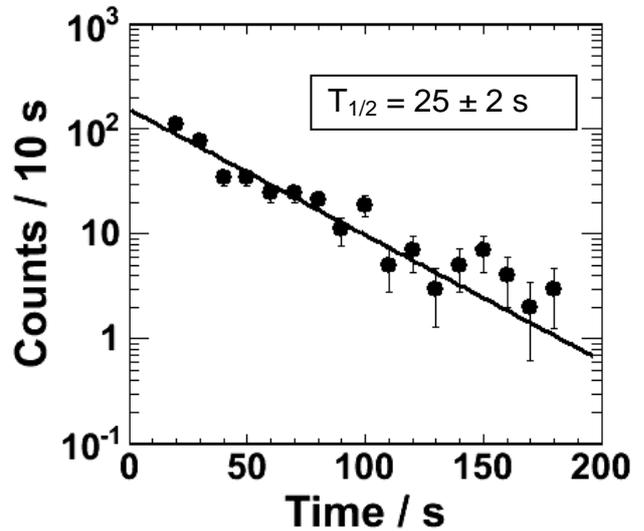
Fig. 2 Decay curve of ^{256}Lr from the sum of α-groups of 8480, 8520 and 8620 keV. The solid line shows the result of the exponential fit.
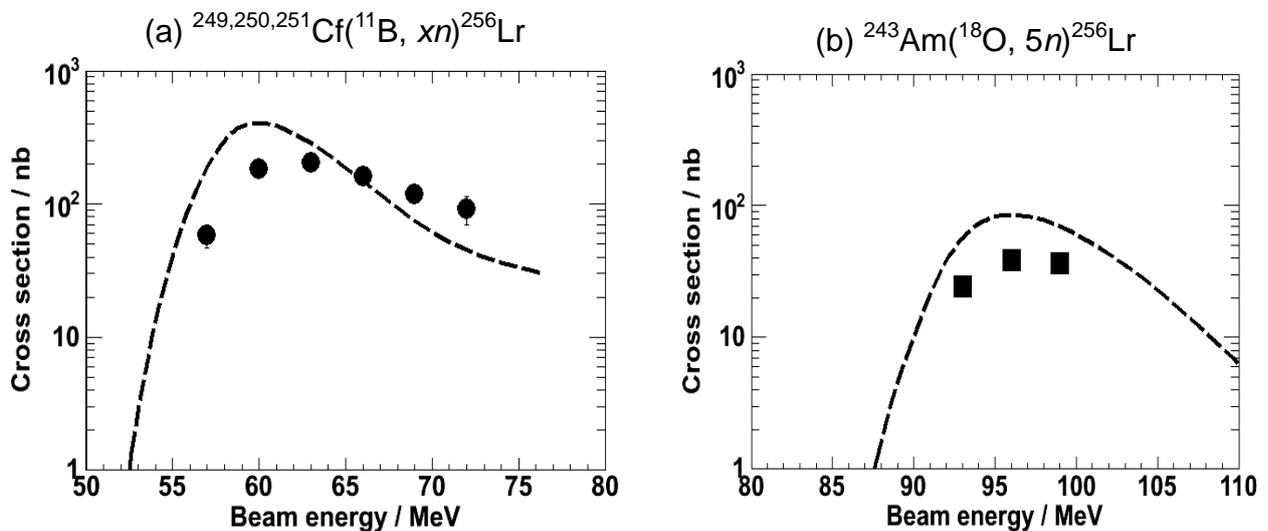
Fig. 3 Excitation functions of the reactions of (a) ^{249,250,251}Cf(^{11}B, xn)^{256}Lr and (b) ^{243}Am(^{18}O, $5n$)^{256}Lr. The broken lines represent results with a HIVAP code calculation, where the isotopic composition of the Cf target used was taken into consideration.

References

[1] Y.A. Akovali, Nucl. Data Sheets, 87 (1999) 249-316.

[2] K. Eskola et al., Phys. Rev., C 4 (1971) 632-642.

[3] G.N. Frelov et al., Nucl. Phys., A 106 (1968) 476-480.

3.9 Measurement of fission probability of ^{240}Pu produced by nucleon transfer reaction ^{238}U(^{18}O, ^{16}O)^{240}U

K. Nishio[1], I. Nishinaka[1], S. Mitsuoka[1], H. Makii[1], R. Takahashi[1], Y. Wakabayashi[1], K. Furutaka[1], K. Hirose[2], T. Ohtsuki[2], S. Yan[3] and S. Chiba[1]

Neutron-induced fission cross-section and neutron multiplicity per fission are important for the design of nuclear reactors. The next generation nuclear reactor is designed to have the relatively high energy neutrons to make an efficient production of the burnable isotopes and to transmute the long-lived minor actinides. To simulate such reactors, nuclear data for minor actinides with short half-life are also needed. However, few experiments were performed on such nuclei because of the difficulty to prepare such a target materials. Some of the data is practically impossible to obtain using a neutron source. To obtain these data, so called 'surrogate reactions' are proposed [1]. In this approach, a compound nucleus same as the one produced by neutron capture is populated by heavy-ion induced nucleon transfer reactions and the decay probability to fission is determined. The cross-section to form the compound nucleus is calculated in a model calculation, which is multiplied to the fission decay probability to determine the neutron-induced fission cross-section. We propose to investigate the reaction ^{238}U(^{18}O, ^{16}O)^{240}U for the surrogate of ^{239}U(n,f) (the half-life of ^{239}U is 23 min), and the test experiment was carried out to check the feasibility of the fission cross-section measurement. The fission probability is determined from the number of coincidence between ^{16}O and fission fragments divided by singles events for ^{16}O. In this experiment, a test experiment to see the coincidence rates between ^{16}O and fission fragments was carried out.

The experiment was carried out using the 144-MeV ^{18}O beams from the tandem accelerator. The ^{238}U target (82 μ g/cm^2) was made by electrically depositing the natural uranium on a nickel backing. The ^{16}O produced by nucleon transfer were separated by using a $\triangle$E – E silicon detector [2]. The detector covered the angle from 32$^{\rm o}$ to 49$^{\rm o}$ relative to the beam direction. The thickness of the $\triangle$E detector was chosen to be 75 μ m. An annular type Si-strip detector was used for the measurement of the residual energy. Energy resolution to determine the excitation energy for ^{240}U was 1.3 MeV (FWHM). Fission fragments following the nucleon transfer were detected in coincidence by using a position-sensitive multi-wire proportional counters (MWPCs) [3].

Figure 1 shows the number of fission events coincided with ^{16}O, plotted as a function of the excitation energy of ^{240}U. The equivalent neutron energy which gives the same energy scale in the reaction ^{239}U(n,f) is also shown. The coincidence events sharply increases at E* = 5.5 MeV, from which fission barrier height of ^{240}U is determined to be 5.5±0.6 MeV. This value is close to 5.7 MeV (inner barrier) determined from the (t,p) reaction [4] .

---

[1] Japan Atomic Energy Agency (JAEA)
[2] Tohoku University
[3] China Institute of Atomic Energy (CIAE)
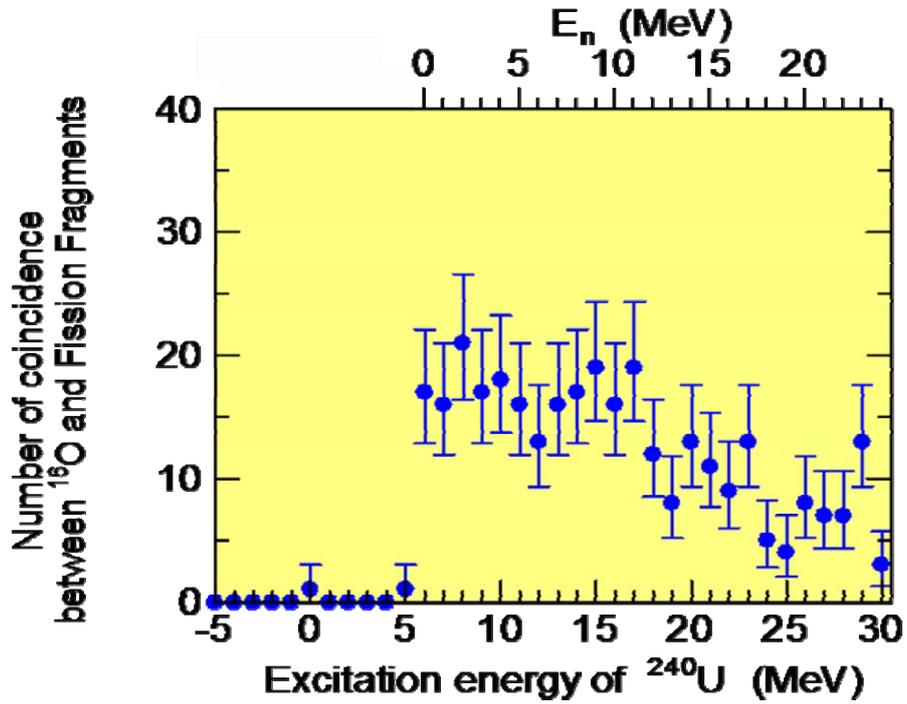
Fig. 1   Numer of fission events coincided with ^{16}O plotted as a function of the excitation energy of ^{240}U.

References

[1] S. Chiba et al., Phys. Rev., C81 (2010) 044604.

[2] T. Ishii et al., Phys. Rev., C78 (2008) 054309(1-11).

[3] K. Nishio et al., Phys. Rev., C77 (2008) 064607.

[4] S. Bjornholm and J.E.Lynn, Rev. Mod. Phys., 52 (1980) 725.

3.10   Development of a measurement system for (n,γ) cross sections using the surrogate reaction methods

H. Makii[1], T. Ishii[1], D. Nagae[2], R. Takahashi[3], S. Mitsuoka[1], S. Chiba[1],
H. Miyatake[4], S.C. Jeong[4], N. Imai[4] and Y. Hirayama[4]

Neutron-capture reaction with unstable nuclei plays an important role in the stellar nucleosynthesis. In the nucleosynthesis by slow neutron-capture process (s-process) half lives of some unstable nuclei are long lived that the (n,γ) reactions can compete with β decay. Such long-lived nuclei act as branching points in the reaction path of the s process. In order to understand the stellar conditions for the s-process nucleosynthesis, (n,γ) reaction rates of unstable nuclei over a wide stellar temperature range from $kT \sim 8$ keV to $kT \sim 90$ keV are required [1]. In addition, (n,γ) cross sections of long-lived fission products (LLFPs) are the most important physical quantities for the study on transmutation of nuclear wastes. Improvements in small errors of the cross section within the thermal and epithermal neutron energies below about 1 MeV are needed to develop the technology to efficiently transmute LLFPs using reactors (fast or thermal) or accelerator driven system. The measurement of the (n,γ) cross section of the unstable nuclei in the keV region are very difficult. The main reasons of the difficulty are due to a sample preparation and/or radioactivity of the sample. Recently, (^{3}He,p γ), (d,p γ), (^{3}He, ^{3}He' γ), and (^{3}He, ^{4}He γ) reactions have been proposed as surrogate reactions for (n,γ) reactions [2-4] on the basis of the assumption that the formation and decay of a composite nucleus are independent of each other (for each spin J and parity π). At the present time, however, the feasibility of the theses reactions have not been demonstrated; e.g., J^{π} distributions of composite nuclei and reaction mechanisms such as multi-nucleon transfer reactions are not assessed.

Hence, we designed a new experiment in order to measure the γ rays from the highly excited states produced by surrogate reactions in coincidence with outgoing particles. In this experiment, we will use a high-efficiency anti-Compton NaI(Tl) spectrometer with a large S/N ratio to detect the γ rays and Si ΔE-E detector with high resolution to detect the outgoing particles. The anti-Compton NaI(Tl) spectrometer consists of central NaI(Tl) detector with a diameter of 228.6 mm and a length of 203.2 mm, and an annular NaI(Tl) detector with a thickness of 50.8 mm and a length of 368.3 mm [5]. This spectrometer was used for the measurement of keV neutron capture cross section of a stable nucleus from an astrophysical interest [6,7]. The Si ΔE-E detector consists of two surface-barrier type Si detectors with a thickness of 80 μm (ΔE detector) and 4mm (E detector), and has an annular active-area covering an angle range of $123^{o} - 152^{o}$ with respect to the beam axis.

First on-line test of the measurement system was carried out using 24 MeV ^{3}He beam of 1.0 particle nA .

The target consisted of 266 μg/cm² ¹⁹⁶Pt (94.6% enrichment) deposited on 1.07 μm aluminum foil. Fig. 1 shows the time difference (Δt) between signals from the Si ΔE-E detector and the NaI(Tl) spectrometer. Observed events are given as a function of the time relative to the time (Δt = 0 ns) for the events at the ¹⁹⁶Pt target. In Fig. 1 we see clearly the peak at Δt = 0 ns which indicate that the γ-ray events were observed in coincidence with outgoing particles. From the result of the present on-line test, our new measurement system seems to have enough sensitivity to measure the γ rays from the ³He induced reactions in coincidence with outgoing particles.
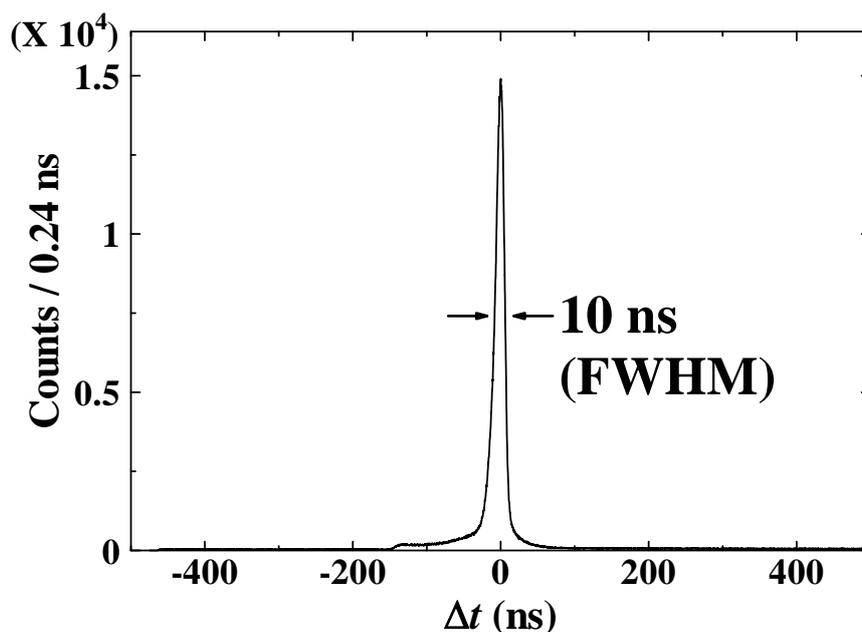
Fig. 1 Time difference (Δt) between signals from the Si ΔE-E detector and the NaI(Tl) spectrometer. Here, the detected events are shown as a function of the time relative to the time (Δt = 0 ns) for the events at the target position.

References

[1] F. Kappeler and A. Mengoni, Nucl. Phys., A777 (2006) 291-310.

[2] S. Boyer et al., Nucl. Phys., A775 (2006) 175-187.

[3] B.L. Goldblum et al., Phys. Rev., C78 (2008) 064606.

[4] J.M. Allmond et al., Phys. Rev., C79 (2009) 054610.

[5] T. Ohsaki et al., Nucl. Instrum. Methods Phys. Res., A425 (1999) 302-319.

[6] Y. Nagai et al., Astrophys. J., 372 (1991) 683-687.

[7] M. Igashira et al., Astrophys. J., 442 (1995) L89-L92.

3.11 High energy alpha particles emitted from nuclear reaction

N. Imai[1], H. Ishiyama[1], Y. Hirayama[1], S.C. Jeong[1], H. Miyatake[1], Y.X. Watanabe[1],
H. Makii[2], S. Mitsuoka[2] and K. Nishio[2]

When we performed the test experiment of proton resonance elastic scattering in inverse kinematics with ^{68}Zn beams and a polyethylene target, we observed much more heavier ions than atomic number Z = 1 as already reported elsewhere in this report.. The origin of the particles seems not to be explained by any reaction mechanisms. To discuss the reaction mechanism, we need experimental information of energies and angular distributions, as well as the particle identification. Since the gain of the detector used was optimized to the several MeV energy loss in order to measure the energy of protons precisely, however, we were not able to identify the heavy ions. Thus, we performed another experiment with lower gain and tried to identify the ions.

The experiment was performed at JAEA tandem accelerator facility. A ^{68}Zn beam of 5.5 MeV/nucleon was accelerated by tandem accelerator and superconducting booster linac. The beam of around several enA was focused on a 10 mg/cm^2 thick carbon. We put a 1.0 mm thick aluminum plate as an energy degrader just downstream of the target. The energy of recoil particles were measured by the three layers of silicon semiconductors (SSDs) of 50 x 50 mm^2 which were mounted 50 cm downstream of the target. The thickness of each SSD was 300 μm. As the first layer SSD, a position sensitive detector was used to obtain the hit position.

Figure 1 shows the energy correlation between the energy deposit in first layer SSD and the sum of energy losses in all SSDs. The alpha and protons were clearly separated. In addition to these particles, a large amount of ions which stopped in the first layer were detected, indicating that the charged particles whose atomic numbers were greater than Z=2 were also produced.

Even with the 1 mm thick aluminum energy degrader, some of alpha particles punched through the three SSDs. The smallest energy loss in the first layer of alpha was about 7.5 MeV. Assuming that the alpha particles were produced at the upstream surface of the target, the energy loss would be generated by alpha particles of 23 MeV/nucleon by taking into account the energy losses at the energy degrader and the target. When we selected the alpha particles punched through the SSDs, the hit positions at the SSDs were limited to be within 1 cm ϕ in 1 σ, giving rise to the scattering angles of as small as 1 degree.

The mechanisms to produce such a high-energy alpha particle may be a fusion-evaporation reaction, and/or a transfer reaction. When we calculate the energies and angular distributions of alpha particles using a fusion-evaporation code PACE4 [1], the alpha will be emitted at the angles larger than 10 degrees, showing

---

[1] High Energy Accelerator Research Organization (KEK)
[2] Japan Atomic Energy Agency (JAEA)

inconsistency with the experimental data. On the other hand, the energy of alpha particles produced by a transfer reaction of $^{12}C(^{68}Zn, \alpha)^{76}Se$ is calculated to be 33 MeV/nucleon when the ^{68}Zn beam of 5.5 MeV/nucleon reacted with ^{12}C nuclei, which seems consistent with the experimental data. However, according to the kinematics, the energy is as large as 32 MeV/nucleon even at 20 degrees in the laboratory frame. The theoretical angular distribution of high energy alpha particles appeared inconsistent with the experimental data.

In summary, we successfully identified alpha particles produced by nuclear reactions of the ^{68}Zn beam with the carbon target. The highest energy of alpha was estimated to be 23 MeV/nucleon. In addition to alpha, we observed heavier ions whose atomic numbers were larger than Z=2 nuclei. Two reaction models, fusion-evaporation and transfer reaction cannot explain the experimental data. Further detailed experiments are awaited to understand the phenomenon.
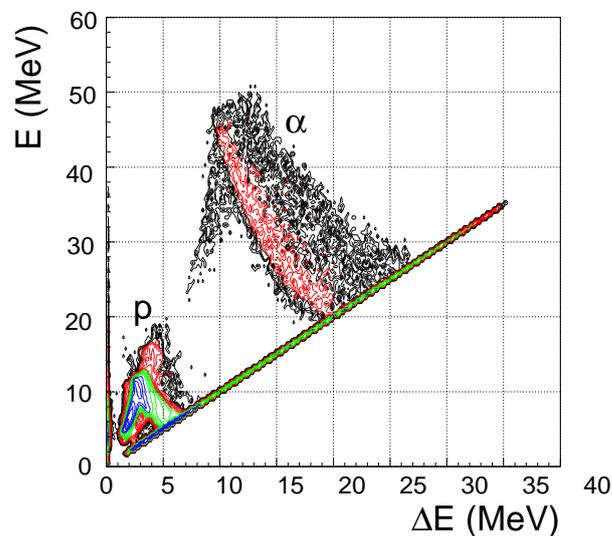
Fig. 1 Energy correlation between ΔE and E. Protons and α were clearly distinguished.

References

[1] A. Gavron, Phys. Rev., C21 (1980) 230.

3.12 Development of GEM-MSTPC for measurement of the ^{8}Li(α, n)^{11}B reaction

H. Ishiyama[1], K. Yamaguchi[2], Y. Mizoi[3], Y.X. Watanabe[1], S.K. Das[3], M-H. Tanaka[1], T. Hashimoto[5],

Y. Hirayama[1], N. Imai[1], H. Miyatake[1], T. Nomura[1], T. Fukuda[3], S. Mitsuoka[4], H. Makii[4], K. Nishio[4],

T.K. Sato[4], M. Matsuda[4], Y. Wakabayashi[4], H. Yamaguchi[5], S. Kubono[5] and S. Hayakawa[5]

We have developed an active-target type gas detector, a Gas Electron Multiplier [1] Multiple-Sampling and Tracking Proportional Chamber (GEM-MSTPC) operating with low-pressure He-base mixed gas, where He is used as a target for studies of astrophysical nuclear reactions, especially He capture reactions. The measurement of the ^{8}Li(α, n)^{11}B reaction cross sections is proposed using a high-intense (~10^5 pps) ^{8}Li beam from TRIAC (RNB07-K05). For high injection-rate capability, a 400 μm thick GEM (THGEM) [2] is adopted to overcome space-charge gain limitation of a wire counter. We examined performance of different kinds of THGEMs using low-energy heavy ion beam from TRIAC. The GEM-MSTPC consists of a drift space (active volume of 100 mm^3), one or more THGEM and an anode plate which is composed of backgammon-type electrodes to measure trajectories of charged particles in the horizontal plane. Typical operating gas and its pressure are He + CO_2 (10%) and 16 kPa, respectively, for the measurement of the ^{8}Li(α, n)^{11}B reaction cross sections.

First of all, the gas gain on the THGEM was measured under the required condition of the operating gas. The measured gas gain was high enough (~10^3) in the single THGEM configuration [3]. Then, we measured time dependence of pulse height of anode output by injecting ^{4}He from an ^{241}Am source and/or low-energy (E = 13.2 MeV) ^{12}C provided by TRIAC. In order to suppress ion feedback [3], the double GEM configuration was adopted. A pulse-height shift was observed with the previously developed THGEM [2]. This phenomenon comes from the gas-gain instability due to charge up of the insulator between the GEM electrodes. It strongly depends on the structure of micro holes punching through the electrodes [4]. In order to avoid the charge up, we modified the structure and the surface of the electrode. TABLE 1 shows a summary of the modifications together with observed pulse-height shifts under various injection rates. THGEM #1 indicates the previous THGEM having an insulator rim of 100 μm width around the hole. THGEM #2 has no rim and the gain shift was suppressed within 12% under the 10^4 pps ^{4}He injection rate. However, a discharge often occurred in several hours from the beginning of the 10^4 pps injection, and after that the gain became unstable. In order to avoid the discharge, the hole diameter of #3 was changed to be smaller than of #2. Although the gain shift for #3 was suppressed within 5% under the ^{4}He injection rate of 10^4 pps, it became larger (about 8%) in the case of the ^{12}C injection with the intensity of 10^5 pps as shown in the left panel of Fig. 1. Moreover, the gain shift for #3 gradually increased in several measurements for the 10^4 pps ^{4}He injection. Actually, the shift was about 1% at the 1st measurement, whereas it changed to be 5% at the 3rd measurement. This phenomenon could be explained as the 'ageing'

---

[1] High Energy Accelerator Research Organization (KEK)
[2] University of Tsukuba
[3] Osaka Electro-Communication University
[4] Japan Atomic Energy Agency (JAEA)
[5] Center for Nuclear Study (CNS), University of Tokyo

of the electrodes [5], such like, oxidation of the copper electrode surface. Hence, we coated the electrode of #4 with gold. THGEM #4 showed a good gain stability as shown in the right panel of Fig. 1. The pulse height became stable within 3% under the ^{12}C injection rate from 400 pps to 120 kpps.

THGEM#		#1	#2	#3	#4
Hole diameter [μm]		300	500	300	300
Rim		yes	no	no	no
Hole pitch [μm]		700	700	700	700
Electrode surface		Au	Cu	Cu	Au
Pulse height shift (%)	^{4}He (E = 5.4 MeV, 10^0 pps)	100	a few	n/a	n/a
	^{4}He (E = 5.4MeV, 10^4 pps)	n/a	12	1~5	n/a
	^{12}C (E = 13.2 MeV, 10^5 pps)	n/a	n/a	8	< 3

Table 1. Summary of modified THGEMs. The hole structure of THGEM was changed for #1, #2, #3. The surface of the copper electrode was coated by gold for #4. "n/a" indicates no measured value.
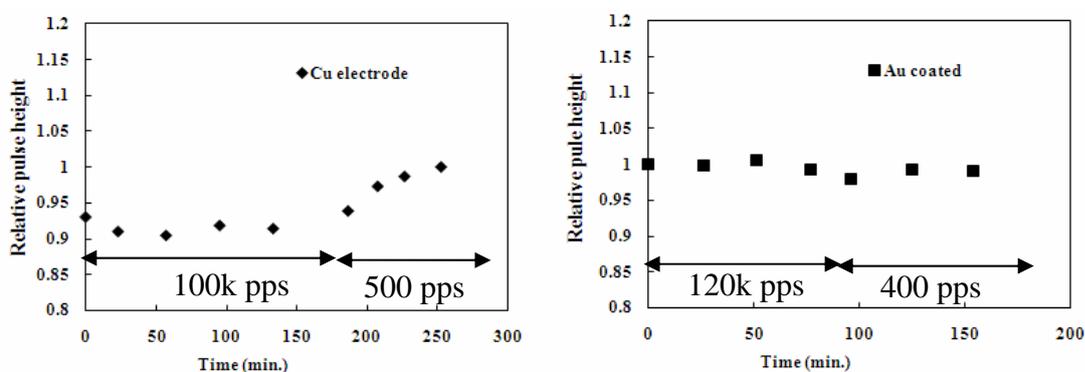
Fig. 1 Pulse-height shifts under the ^{12}C beam injection rate from 400 pps to 10^5 pps using THGEM #3 (left panel) and THGEM #4 (right panel). The horizontal axis indicates time from the beginning of the beam injection.

The energy resolution under the ^{12}C injection rate of 10^5 pps was also measured. It was obtained from the distribution of energy-loss signals for each segmented anode pad. The energy resolutions under the injection rate of 400 pps for #3 and for #4 were both 7% in σ. That under the injection rate of 10^5 pps for #3 was 13%, while for #4 it was improved to be 8%.

The characters of the gain stability and the energy resolution under the high injection rate for #4 satisfy experimental requirements. The GEM-MSTPC using THGEM #4 (400 μm thick, 300 μm hole diameter, Cu electrode coated by Au, no rim) was successfully applied to the measurement of the ^{8}Li(α, n)^{11}B reaction cross sections on April 2010.

References

[1] F. Sauli, Nucl. Instrum. Methods Phys. Res., A386 (1997) 531-534.

[2] C. Shalem, et al., Nucl. Instrum. Methods Phys. Res., A558 (2006) 475-489.

[3] K. Yamaguchi, et al., Nucl. Instrum. Methods Phys. Res., A (2010), doi:10.1016/j.nima.2010.02.173.

[4] J. Benlloch, et al., Nucl. Instrum. Methods Phys. Res., A419 (1998) 410-417.

[5] F. Sauli, Nucl. Instrum. Methods Phys. Res., A515 (2003) 358-363.

This is a blank page.

CHAPTER 4

Nuclear Chemistry

This is a blank page.

4. 1 Cation-exchange behavior of rutherfordium, $_{104}$Rf in H$_2$SO$_4$/HNO$_3$ mixed solution ([H$^+$] = 1.0 M)

Z.J. Li[1], A. Toyoshima[1], M. Asai[1], K. Tsukada[1], T.K. Sato[1], N. Sato[1], T. Kikuchi[1], X.H. Liang[2],

Y. Kasamatsu[3,4], Y. Nagame[1], S. Goto[5], H. Haba[3], Y. Takeda[6], S. Ikarashi[7], M. Murakami[5],

M. Nishikawa[6], Y. Komori[4], K. Ooe[4], K. Akiyama[8] and K. Sueki[7]

Transactinide elements with atomic numbers Z ≥ 104 are produced in heavy-ion-induced nuclear reactions at accelerators with extremely low production rates and are only available as short-lived isotopes. Any chemistry study must be carried out on an "atom-at-a-time" scale, completed within their life time, and repeated thousands of times to gain satisfied statistics. Such studies offer unique opportunities to obtain information on trends in the Periodic Table and to probe magnitude of the influence of relativistic effects [1]. So far, we have investigated complex formation of Rf using an automated ion-exchange separation apparatus coupled with the detection system for alpha-spectroscopy (AIDA): chloride, nitrate, and fluoride complexes [2]. In the present work, cation-exchange behavior of Rf in H$_2$SO$_4$/HNO$_3$ mixed solution ([H$^+$] = 1.0 M) has been studied using AIDA to clarify properties of Rf sulfate complexes by comparing them with those of the lighter homologues Zr and Hf complexes.

The isotope ^{261}Rf ($T_{1/2}$ = 78 s) was produced with a Cm/Gd mixed target using 94 MeV ^{18}O^{6+} beam from the JAEA tandem accelerator. 3.24 min-^{169}Hf was produced simultaneously in the Gd(^{18}O, xn) reaction to monitor behavior and chemical yields of Hf. Reaction products were transported to a chemistry lab by a He/KCl gas-jet and were deposited on a collection site of AIDA for 2 min. After deposition, the products were dissolved with 280 μL H$_2$SO$_4$/HNO$_3$ ([H$^+$] = 1.0 M) of various H$_2$SO$_4$ concentrations of 0.15, 0.25, 0.30, 0.35, 0.40, 0.50, and 0.69 M, and were fed onto a 1.6 mm i.d. × 7.0 mm cation-exchange column (CK08Y) at a flow rate of 670 μL/min. The effluent was collected on a Ta disk as fraction 1. The remaining ^{261}Rf and ^{169}Hf were stripped with 250 μL 0.1 M HF/0.1 M HNO$_3$ at a flow rate of 1000 μL/min and were collected on another Ta disk as fraction 2. Two fractions were evaporated to dryness and were automatically transferred to α-spectrometry stations of AIDA equipped with eight 600 mm^2 passivated ion-implanted planar silicon (PIPS) detectors. From the radioactivies A_1 and A_2 observed in fractions 1 and 2, respectively, adsorption probability (%ads) was evaluated using the equation of %ads = 100A_2/(A_1+A_2). After the α-particle measurement, the 493 keV γ-ray of ^{169}Hf was measured with Ge detectors. The chemical yields of Hf were approximately 60%. To investigate behavior of Zr and Hf simultaneously, 7.86 min-^{85}Zr and ^{169}Hf were produced with a Ge/Gd mixed target in the Ge(^{18}O, xn) and Gd(^{18}O, xn) reactions,

[1] Japan Atomic Energy Agency (JAEA)
[2] China Institute of Atomic Energy (CIAE)
[3] RIKEN
[4] Osaka University
[5] Niigata University
[6] Kanazawa University
[7] University of Tsukuba
[8] Tokyo Metropolitan University

respectively.

From the 2318 cycles of the [261]Rf experiments, a total of 185 α-events from [261]Rf (8.28 MeV) and its daughter 25 s-[257]No (8.22, 8.32 MeV) were registered in the energy range of 8.0−8.4 MeV, including 23 time-correlated α-α pairs of [261]Rf and [257]No. An accumulated α-spectrum obtained in the 0.15 M H_2SO_4/HNO_3 experiment is shown in Fig. 1. The contribution of [257]No formed during the collection and separation to [261]Rf was evaluated to be 1.1−28% based on separate cation-exchange studies of 3.1 min-[255]No, produced in the [248]Cm(^{12}C, 5*n*) reaction, under the identical conditions to the Rf experiments. The contribution of background and the growth and decay of [261]Rf and [257]No were also taken into account to evaluate the adsorption probability of [261]Rf.

Figure 2 shows variations of the adsorption probabilities of Rf, Zr, and Hf as a function of [HSO_4^-]. The adsorption probabilities of Hf measured in the separate two experiments agree well with each other. The adsorption probabilities of Rf, Zr, and Hf on the CK08Y resin decrease with an increase of [HSO_4^-], indicating successive formation of sulfate complexes of these elements. It is found that the %ads values of Rf decrease at much higher [HSO_4^-], indicating that the sulfate complex formation of Rf is much weaker than that of Zr and Hf. This trend is similar to that of the fluoride complex formation of the group-4 elements. In the previous study, the fluoride complex formation of Rf was found to be remarkably weaker than that of Zr and Hf. From the HSAB (hard-soft-acid-base concept) point of view, the sulfate ion SO_4^{2-} is a hard anion like F-, and interacts stronger with smaller (harder) cations. The ionic radius of Rf^{4+} is expected to be much larger than those of Zr^{4+} and Hf^{4+} [3], resulting in a weaker sulfate complex formation of Rf^{4+} as compared to Zr^{4+} and Hf^{4+}, which qualitatively explains the present complexation trend.
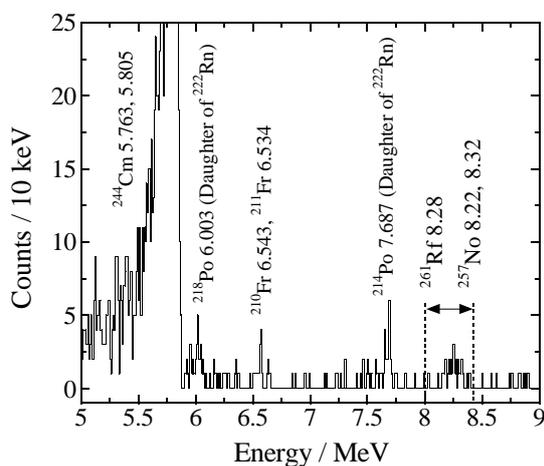
Fig. 1 α-spectrum accumulated from the 283 cycles of the Rf experiments with 0.15 M H_2SO_4/HNO_3.
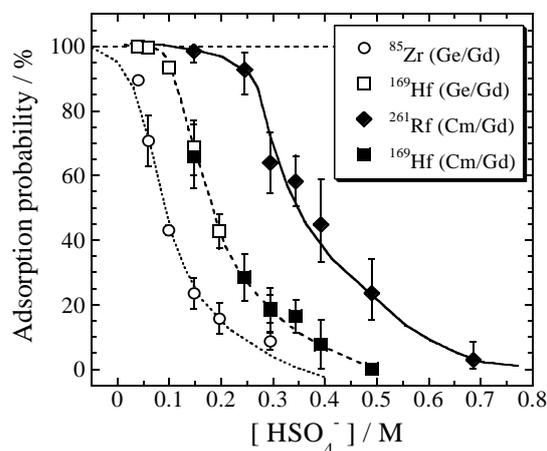
Fig. 2 variations of adsorption probabilities of Rf, Zr, and Hf on CK08Y as a function of [HSO_4^-].

References

[1] M. Schädel, Angew. Chem. Int. Ed., 45 (2006) 368-401.

[2] Y. Nagame, J. Nucl. Radiochem. Sci., 6 (2005) A21-28.

[3] V.G. Pershina, Chem. Rev., 96 (1996) 1977-2010.

4.2　Reduction of mendelevium using an electrochemistry apparatus

A. Toyoshima[1], K. Tsukada[1], M. Asai[1], T.K. Sato[1], Z.J. Li[1], N. Sato[1], T. Kikuchi[1], Y. Kitatsuji[1], Y. Nagame[1], K. Ooe[2], Y. Kasamatsu[2], A. Shinohara[2], H. Haba[3] and J. Even[4]

It is important to determine redox potentials of the heaviest actinides between divalent and trivalent states. Due to the drastic stabilization of the 5f orbital with increasing atomic number, divalent states are predicted to be stabilized at the end of the actinide series. Though pioneering chemical works demonstrated the stabilized divalent state at No, redox potentials of other heaviest actinides have not been precisely determined because of single atom chemistry. Purpose of our present study is the precise determination of a redox potential between Md^{2+} and Md^{3+} using our electrochemistry apparatus [1]. In this study, we first measured the excitation function of the $^{248}Cm(^{11}B, 4n)^{255}Md$ reaction to find an optimum production condition. Then the reduction of Md^{3+} to Md^{2+} was examined using the apparatus.

The 525 μg/cm^2-thick ^{248}Cm target was prepared by electrodeposition of a Cm compound in 2-propyl alcohol onto a 1.80 mg/cm^2 Be backing foil. The $^{11}B^{4+}$ ions of 58.2, 59.7, 61.2, 63.2, and 65.2 MeV passed through a 1.99 mg/cm^2 HAVAR window, 0.09 mg/cm^2 helium cooling gas, and the Be backing foil before entering the ^{248}Cm target material. An effective thickness of the Cm target for the production of ^{255}Md ions was evaluated to be ~250 μg/cm^2. The beam energy in the middle of the target was 52.5, 54.1, 55.8, 57.8, and 60.0 MeV, respectively. An average beam intensity was 945 particle nA. Reaction products recoiling out of the target were transported by a He/KCl gas-jet method to the chemistry laboratory through a Teflon capillary at a helium flow rate of 2.4 L/min. For 2 min, the transported products were deposited on a thin polyethylene telephtalate (PET) film, eighty of which were arrayed along a periphery of a wheel of the rotating wheel measurement system (MANON). After collection, the deposited sample was successively moved to stations by the stepwise rotation of the wheel at 2-min intervals. At the first 18 stations, α-particles of the samples were measured with 18 Si detectors placed at a distance of 5 mm.

In the reduction experiment of Md, the transported products by the He/KCl gas-jet method were deposited on a collection site of a chemistry apparatus for 10 min. After collection, the deposited products were dissolved with 0.1 M HCl and were subsequently fed into an HDEHP column to remove KCl from the collected sample because KCl in measured samples lowers α-energy resolution with a Si detector. The 0.1 M HCl effluent containing K^+ ions was discarded. After 9 cycles of the above procedures, the remaining products on the column were stripped with 6.0 M HCl. The effluent was collected on a Ta disk and was evaporated to dryness with a halogen lamp and a helium gas stream. After dissolution of the dried sample with 0.1 M HCl, the aliquot was injected into the electrochemistry apparatus with 0.1 M HCl which was beforehand electrolyzed using another electrolytic column apparatus to decrease dissolving oxygen in the

solution. The potentials applied to the electrode were 0 V and -0.9 V vs. an Ag/AgCl reference electrode in 1.0 M LiCl. The 0.1 M HCl effluent from the column working electrode was collected on 5 Ta disks. In another experiment, we verified that divalent ions such as Sr^{2+} and Eu^{2+} are eluted with 0.1 M HCl while trivalent ions of lanthanides are adsorbed on the working electrode under the given conditions. The adsorbed ions on the electrode were then stripped with 3.0 M HCl and the effluent was collected on separate 2 Ta disks. These 7 effluent samples were subjected to α-spectrometry with 7 Si detectors after evaporated to dryness with a halogen lamp and burned off with a burner.

Figure 1 shows a typical α-spectrum observed in the experiment with the 61.2-MeV $^{11}B^{4+}$ beam in the middle of the target. The α-peak of ^{255}Md is clearly found at the energy of ~7330 keV. Alpha-peaks of ^{211}Po, ^{254}Fm, and $^{252,255}Fm$ are also observed. We determined a half-life of ^{255}Md to be 29 ± 2 min by measuring the dried samples after the HDEHP separation in the chemical experiment totally for 5.8 hours. The present half-life value agrees well with the previous ones (27 ± 2 min) [2, 3] within statistic errors, representing no contamination from by-products in the energy region of interest. Figure 2 shows the excitation function of the $^{248}Cm(^{11}B, 4n)$ reaction. Curves show results of a calculation with the HIVAP code [4] for the production of Md isotopes in the $^{248}Cm + ^{11}B$ reactions. The measured peak of the excitation function for ^{255}Md is at around 58 MeV which is slightly higher than the energy expected with the calculation.

In the electrochemical experiment, it was found that ^{255}Md is completely adsorbed on the working electrode in eluting 0.1 M HCl at the applied potential of 0 V. This behavior was the same as that of $^{250}Bk^{3+}$ which was a by-product of the nuclear reactions, showing no reduction of Md^{3+} at the given potential. On the other hand, at -0.9 V, Md was eluted with 0.1 M HCl, which was quite similar to the behavior of Sr^{2+} and Eu^{2+} in our previous experiment. Therefore, it was found that Md^{3+} is successfully reduced to Md^{2+} with the electrochemistry apparatus. In the near future, we will determine the redox potential of Md.
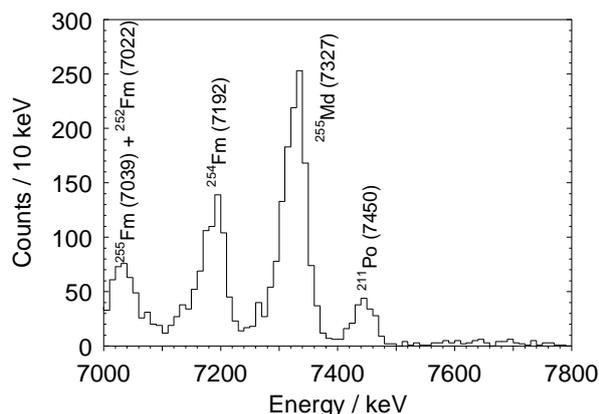
Fig. 1 Alpha spectrum observed in the experiment with the 61.2-MeV ^{11}B beam.
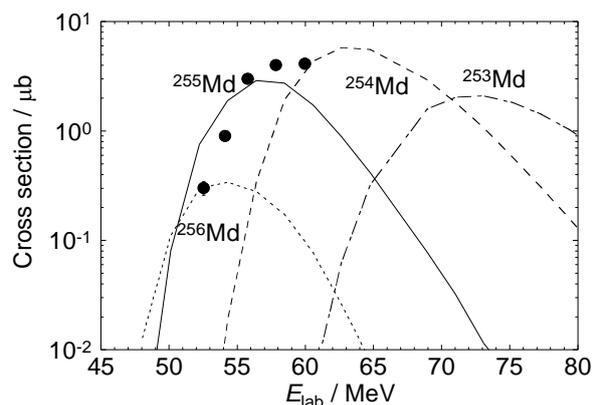
Fig. 2 Excitation function of the $^{248}Cm(^{11}B, 4n)^{255}Md$ reaction. Curves show results with the HIVAP code.

References

[1] A. Toyoshima et al., Radiochim. Acta, 96 (2008) 323-326.

[2] P. R. Fields et al., Nucl. Phys., A154 (1970) 407-416.

[3] R. W. Hoff et al., Nucl. Phys., A169 (1971) 641-650.

[4] W. Reisdorf and M. Schädel, Z. Phys. A343 (1992) 47-57.

4.3 On-line isothermal gas chromatographic behavior of group-5 elements as homologues of Db

T. K. Sato[1], K. Tsukada[1], M. Asai[1], A. Toyoshima[1], N. Sato[1],
Z.J. Li[1], T. Kikuchi[1,2], S. Liang[1] and Y. Nagame[1]

Dubnium (Db, $Z = 105$), one of transactinide elements dubnium, is expected to be a member of group-5 and a homologue of V, Nb, and Ta according to its place in the Periodic Table. In the gas phase the group-5 elements are most stable in their maximum oxidation state of +5 and therefore form pentachlorides in chlorinating atmosphere. Besides the pentachlorides, oxychlorides are stable. Oxychlorides are less volatile than the pentachlorides.

The chemical properties of Db compounds in gas phase have been still ambiguous since it was only reported that the retention behavior of chlorides of Db in an isothermal gas chromatography had two components at least owing to contamination of oxygen would lead production of both pentachloride and oxychloride simultaneously [1]. In this work, we performed the on-line experiments with short-lived Nb and Ta isotopes as the homologues of Db in gas phase with an apparatus we have developed under conditions to form only oxychloride species in order to compare volatilities of the same species among Db, Nb and Ta, each other.

Short lived Nb and Ta isotopes were produced in the reactions of ^{nat}Ge (^{19}F, xn) ^{88}Nb ($T_{1/2}$=14.5 min) and ^{nat}Gd (^{19}F, xn) ^{170}Ta ($T_{1/2}$=6.7 min), respectively at the JAEA Tandem accelerator facility. The on-line isothermal gas chromatographic apparatus was directly connected to a target chamber for efficient transportation of nuclear reaction
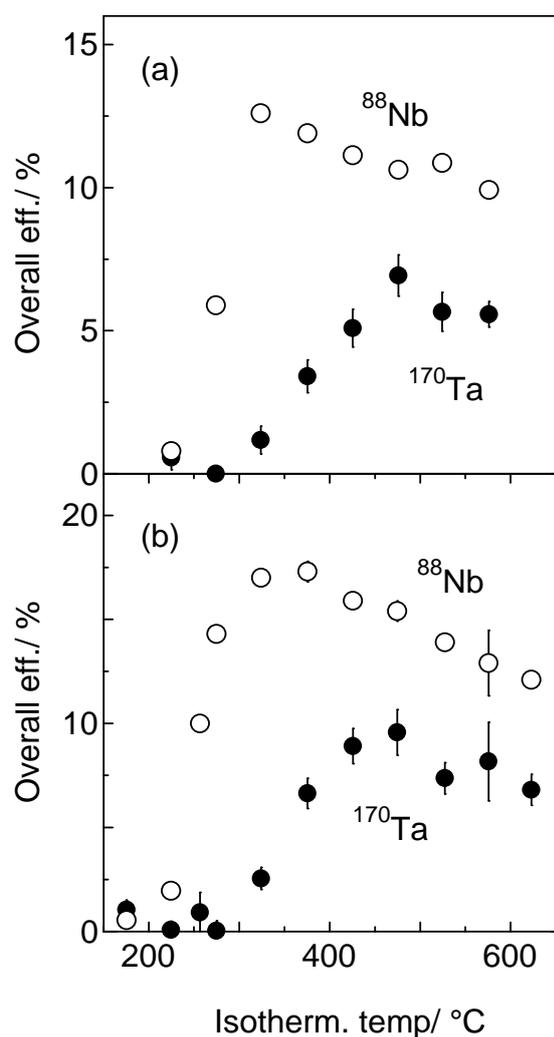
Fig. 1 Overall efficiencies observed for ^{88}Nb (○) and ^{170}Ta (●) with 200 ml min N_2 saturated $SOCl_2$ vapor with (a) 5% and (b) 2% of oxygen concentration as reactive gas are shown as a function of the isothermal column temprature.

---

[1] Japan Atomic Energy Agency (JAEA)
[2] Ibaraki University

products recoiling out of the target from the chamber to the apparatus by the He carrier gas flow. To optimize ranges of the nuclear reaction products, nitrogen gas was added to the He carrier gas. In the reaction room of the apparatus, the transported products were stopped on quartz wool where a reactive gas was introduced. Nitrogen saturated with $SOCl_2$ vapor with 5 % or 2 % oxygen concentration was used as the reactive gas to produce the volatile oxychlorides of the Nb and Ta. Volatile species produced in the reaction room were then transported along the isothermal column by the carrier gas flow. At the end of the isothermal column, volatile compounds leaving the column were attached to KCl aerosol particles in a gas-jet chamber and transported to a detection system. An HP-Ge detector was used to measure the γ-rays of each nuclide. We measured yields of the volatile compounds of ^{88}Nb and ^{170}Ta pass through the column as a function of isothermal temperature. These results were compared with direct measurements of the recoil products from the target using an Al catcher foil before chemical separation.

Figure 1 shows the variations of the overall efficiencies of Nb and Ta as a function of isothermal temperature for 5% and 2% of oxygen concentration in the reactive gas. The efficiencies for 5% oxygen were lower than those in the case of 2%. The maximum efficiency of Nb for 2% oxygen in the reactive gas reached about 18 % and that of Ta about 10 % while the maximum of Nb for 5 % oxygen was about 13 % and that of Ta was about 7 %.   The each behavior of Nb and Ta had only one component and was not changed between the both conditions of oxygen concentration. The Nb behavior was similar to that reported in the previous work in which HCl was used as a chlorinating agent with He carrier gas containing about 100 ppm of oxygen [2]. Therefore, in these conditions, only one volatile species of Nb might be formed. The chemical species would be identified as $NbOCl_3$ based on its volatility. According to the similarity with Nb, the Ta behavior would be due to $TaOCl_3$ in this experiment. These results showed the volatility of the Ta compounds is lower than that of Nb.

References
[1] A.Türler et al., Radiochim. Acta, 73 (1996) 55.
[2] H. W. Gaggler et al., J. Radioanal. Nucl. Chem., 183 (1994) 261.

4.4 Gas-phase chemistry of Zr and Hf using carbon cluster transport system

S. Goto[1], H. Murayama[1], M. Murakami[1], T. Kojima[1], H. Kudo[1],

K. Tsukada[2], M. Asai[2], T. K. Sato[2], N. Sato[2] and Y. Nagame[2]

A gas phase chemical separation has been applied to the investigation of chemical properties of superheavy elements because it allows separating them continuously and rapidly. Adsorption enthalpies of volatile compounds of these elements can be determined by their adsorption-desorption processes on a surface of gas chromatograph column. In this study, we investigated gas chromatographic behavior of volatile chloride compounds of Zr and Hf using a newly fabricated apparatus for the study of Rf.

The Zr and Hf isotopes were produced in the ^{nat}Ge and ^{nat}Gd(^{16}O, xn) and ^{nat}Ge and ^{nat}Gd(^{18}O, xn) reactions at the JAEA tandem accelerator facility. Nuclear reaction products were transported to the gas chromatographic apparatus with attaching on a carbon cluster in a He carrier gas flow. The transported products were collected on a quartz wool plugged in a quartz tube where a reactive HCl gas was added to form volatile chloride compounds. The formed volatile compounds were then fed into an isothermal chromatographic quartz column directly connected to the tube. The compounds of Zr and Hf through the column were re-transported attaching on a KCl cluster in a He carrier gas flow, and collected in a glass filter for γ-rays measurement to determine the yields of these elements which passed through the column. The passed-through yields for Zr and Hf were obtained as a function of the temperature of the isothermal column.

It was found that isothermalchromatographic behavior of Zr and Hf was similar with each other. The yields of both the elements increased with the temperature of the column between 300 and 450 ^{o}C. The behavior of Zr was almost the same as that of our previous report [1]. The overall efficiency to re-transportation was about 10% for Zr sat 450 ^{o}C of column temperature. It will be enough efficiency for Rf experiment.

References

[1] T. K. Sato et al., J. Nucl. and Radiochem. Sci., 6 (2005) N1–N3.

[1] Niigata University
[2] Japan Atomic Energy Agency (JAEA)

This is a blank page.

CHAPTER 5

Nuclear Theory

This is a blank page.

5.1 Analysis of surrogate reaction with unified model

Y. Aritomo[1], S. Chiba[1] and K. Nishio[1]

A proper description of nuclear fuel cycles for energy applications requires nuclear data on various types of compound reaction. Often the cross section needed for a particular application cannot be measured directly, as the relevant energy region is inaccessible or the target is too short-lived. To overcome the experimental limitations, indirect methods have to be developed, such as the surrogate nuclear reaction approach. To create the desired compound nucleus, we employ a different reaction with a more experimentally accessible combination of projectile and target. At energies below 1 MeV, it is considered that mismatches in the compound nucleus spin-parity distributions between the neutron-induced and surrogate reactions can affect the interpretation of a surrogate measurement.

To understand the reaction mechanism and clarify such mismatches, it is indispensable to establish a theoretical model to describe the whole process in surrogate reaction. Here, we try to apply the unified model to the surrogate reaction. The unified model has been developed by FLNR theoretical group in Dubna. This calculation model can treat all reaction processes in heavy- and superheavy-mass regions, which has been applied to several types of reactions [1, 2]. The unified model implies an unified dynamical approach and unified multidimensional potential energy [1]. We then perform a trajectory calculation on the time-dependent unified potential energy surface using the Langevin equation. Thus, the whole evolution of the heavy nuclear system can be traced starting from the infinite distance between the projectile and target to the end of each process.

We take into account the time evolution from the diabatic potential $V_{\text{diab}}(q)$ to the adiabatic potential $V_{\text{adiab}}(q)$, here q denotes the collective coordinates of nuclear deformation. The diabatic potential is calculated by the folding procedure with effective nucleon-nucleon interaction [1, 2]. We use the adiabatic potential energy of the nuclear system calculated using the two-center shell model. We connect the diabatic potential and adiabatic potential with a weight function as follows; $V = V_{\text{daiab}}(q) f(t) + V_{\text{adiab}}(q) [1 - f(t)]$, $f(t) = \exp(-t/\tau)$. Here, t is the time of interaction and $f(t)$ is a weight function on the relaxation time τ. We use the relaxation time $\tau = 10^{-21}$ s, which was suggested in references [3]. As the coordinates of nuclear deformation, we use the two-center parametrization [4, 5] and employ three parameters: z_0 (distance between two potential centers), δ (deformation of fragments), and α (mass asymmetry of the colliding nuclei) defined by $\alpha = (A_1 - A_2)/A_{\text{CN}}$, where A_1 and A_2 denote the mass numbers of the target and the projectile, respectively. A_{CN} denotes the mass number of the compound nucleus. We perform the trajectory calculation on the time-dependent unified potential energy using the Langevin-type equation. The multidimensional Langevin equation is described precisely in reference [1, 6].

---

[1] Japan Atomic Energy Agency (JAEA)
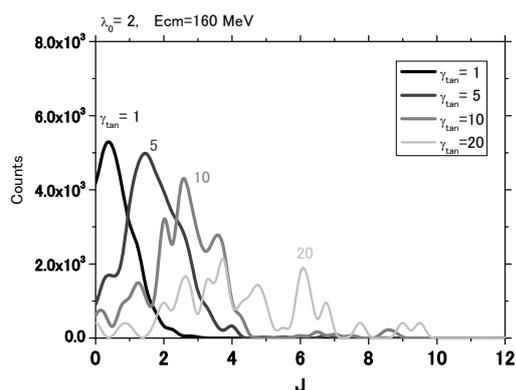
Fig. 1 Spin distribution of compound nucleus ^{240}U in the reaction ^{18}O+^{238}U $\rightarrow$ ^{16}O+^{240}U at the incident energy of $E_{c.m.}$ =160 MeV for several sliding friction.

Fig. 2 Spin distribution of compound nucleus ^{240}U and ^{238}U in the transfer reactions ^{18}O+^{238}U $\rightarrow$ ^{16}O+^{240}U at the incident energy of $E_{c.m.}$ =160 MeV ^{18}O+^{236}U $\rightarrow$ ^{16}O+^{238}U, respectively.

Recently, the surrogate ratio method is discussed and it was found that we need not know the spin-parity distributions populated by surrogate reaction, if (1) there exist two surrogate reactions whose spin-parity distributions of decaying nuclei are almost equivalent, and (2) difference of representative spin values between the neutron-induced and surrogate reactions is not much larger than $10\hbar$ [7]. Using our theoretical model, we calculate the spin of compound nucleus in surrogate reactions. Here, as an example of the surrogate reaction, we consider the two neutron transfer reaction; ^{18}O+^{238}U $\rightarrow$ ^{16}O+^{240}U. Figure 1 shows the spin distribution of compound nucleus ^{240}U at the incident energy of $E_{c.m.}$ =160 MeV. In the Langevin calculation, the sliding friction is mainly responsible for the dissipation of the angular momentum [1], though the value has uncertainty. We treat the sliding friction γ_{tan} as a parameter of the model. The unit of friction is 10^{-22} MeV s fm^{-2}. We can see the spin of compound nucleus is less than 10 $\hbar$ for each value of sliding friction. Figure 2 shows the spin distribution of compound nucleus ^{240}U and ^{238}U in the transfer reactions ^{18}O+^{238}U $\rightarrow$ ^{16}O+^{240}U and ^{18}O+^{236}U $\rightarrow$ ^{16}O+^{238}U, respectively. We use the sliding friction γ_{tan} =10$\times$10^{-22} MeV s fm^{-2}. The spin distributions of decaying nuclei by two reactions are almost equivalent. Such calculation results suggest the validity of the surrogate ratio method.

References

[1] V. Zagrebaev and W. Greiner, J. Phys., G31 (2005) 825.

[2] V. Zagrebaev and W. Greiner, J. Phys., G34 (2007) 1; J. Phys. G34., (2007) 2265; Phys. Rev. Lett., 101 (2008) 122701; Phys. Rev., C78 (2008) 034610.

[3] G.F. Bertsch, Z. Phys., A289 (1978) 103 (1978); W. Cassing and W. Norenberg, Z. Phys., A401 (1983) 467; A. Diaz-Torres, Phys. Rev., C69 (2004) 021603 (2004).

[4] J. Maruhn and W. Greiner, Z. Phys., 251 (1972) 431.

[5] K. Satoet al., Z. Phys., A288 (1978) 383.

[6] Y. Aritomo, Phys. Rev., C80 (2009) 064604.

[7] S. Chiba and O. Iwamoto, Phys. Rev., C81 (2010) 044604.

5.2 Shell-model description of multi-particle multi-hole states around ^{16}O and the role of correlation energy

Y. Utsuno[1] and S. Chiba[1]

Around oxygen isotopes, many low-lying states are known which cannot be described by the simple shell model assuming ^{16}O as an inert core. They are considered to be states dominated by a multi-particle multi-hole excitation across the N or Z=8 shell gap. For instance, the 0^+_2 state of ^{16}O, located at only 6.05 MeV, is widely accepted to consist predominantly of four-particle four-hole (4p-4h) configurations in spite of the existence of a large N or Z=8 shell gap ~10 MeV.

The large-scale shell model, in which particle-hole excitations from the p- to sd-shell are taken into account, is a promising method to describe the multi-particle multi-hole states microscopically. Previous shell-model studies [1, 2] included configurations up to 4ℏω excitation from the lowest, and succeeded in reproducing some multi-particle multi-hole states of ^{16}O by adjusting the N(Z)=8 shell gap. The resulting shell gap was however considerably smaller than the standard value, and the reason for that has not been clarified. The aim of the present study is giving a more comprehensive picture about the interplay between the shell gap and the multi-particle multi-hole states on the basis of the shell model. This should be of great help to the description of transfer reactions using oxygen beam.

We first revisit the shell gap. The single-particle energy is often associated with the experimental separation energy directly. The standard single-particle energy for the shell model is so determined, too. This works well if the ground state of ^{16}O is a complete closure without correlation energy. In order to evaluate the effect of correlation energy, we carry out shell-model calculations assuming the full p-sd shell as the valence shell. We use the PSDWBT interaction [3] as the effective interaction. Figure 1 shows the cross-shell correlation energy for nuclei around ^{16}O. Here, the cross-shell correlation energy is defined by the energy difference between that calculated in the full p-sd model space and that calculated without cross-shell excitation.

Fig. 1 Cross-shell correlation energies for ^{12}C, ^{15,16,17}O and ^{20}Ne.

The cross-shell correlation energy maximizes at ^{16}O. Namely, the one-neutron separation energy of ^{17}O, E(^{16}O)-E(^{17}O), enlarges, while that of ^{16}O reduces. This indicates that the single-particle energy of the sd shell must be lowered and that of the p shell must be raised when the

---

correlation energy is taken into consideration.

Based on the above discussion, we next construct a Hamiltonian with the "correct" single-particle energy: the single-particle energies and the overall strength of the p-shell and sd-shell interaction are adjusted so that the calculation can reproduces the energies sensitive to the shell gap, i.e., those of the $5/2^+_1$, $1/2^+_1$ and $3/2^+_1$ of ^{17}O, those of $1/2^-_1$ and $3/2^-_1$ of ^{15}O, and the ground-state energies of ^{20}Ne and ^{12}C. Figure 2 shows a partial level scheme of ^{16}O compared between experiment and calculation. Not only negative-parity states dominated by 1p-1h states (located ~6-10 MeV) but also members of 4p-4h states (0^+ to 6^+) are in good agreement between experiment and calculation. We stress that the shell gap used in this study is determined to reproduce the energy around the ground state but not to fit the multi-particle multi-hole state directly. When the original PSDWBT interaction is used, the 0^+_2 of ^{16}O appears around 12 MeV. Thus, the renormalization of single-particle energy is essential to describe the multi-particle-multi-hole states.
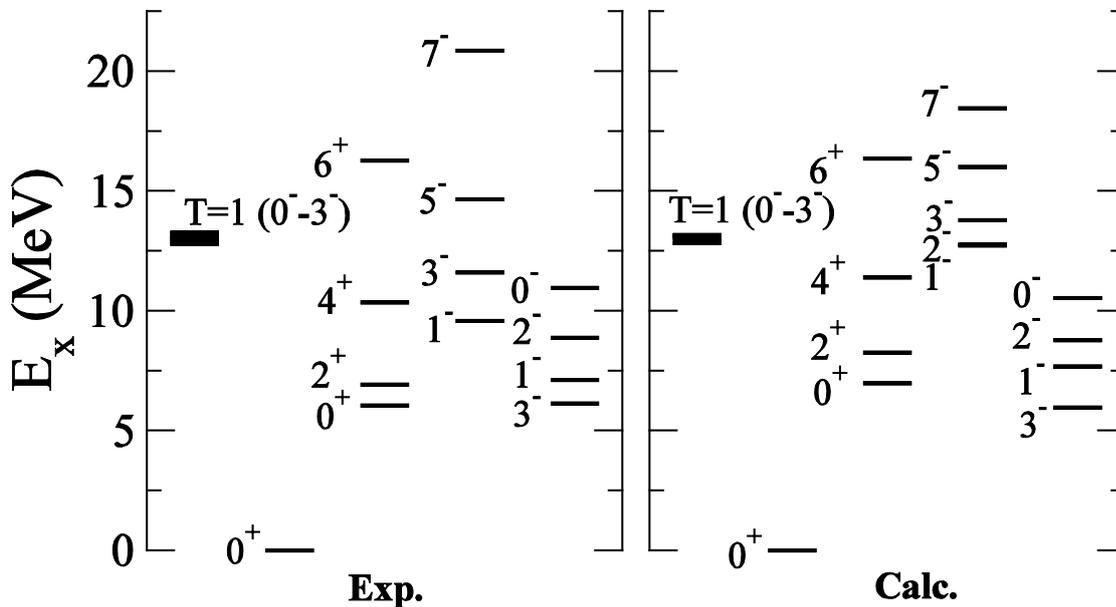
Fig. 2 Energy levels of ^{16}O compared between experiment (left) and calculation (right).

References
[1] W.C. Haxton and C. Johnson, Phys. Rev. Lett. 65 (1990) 1325-1328.
[2] E.K. Warburton, B.A. Brown, and D.J. Millener, Phys. Lett. B293 (1992) 7-12.
[3] E.K. Warburton and B.A. Brown, Phys. Rev. C46 (1992) 923-944.

5.3   Verification of the surrogate ratio method

S. Chiba[1] and O. Iwamoto[1]

With the advance of nuclear science and technology, neutron cross sections of unstable nuclei, such as minor actinides (MAs) and long-lived fission products (LLFPs), are becoming more and more necessitated. Neutron cross sections of radioactive nuclei also play important roles in astrophysical nucleosynthesis. In spite of the importance, however, measurement of neutron cross sections is extremely difficult for these nuclei since preparation of sample is difficult or practically impossible. At the same time, theoretical determination of the fission and capture cross sections still suffers from a large uncertainty if there exists no experimental data; an error of factor of 2, namely the uncertainty of 100 %, will be a reasonable estimate. These fundamental problems prevent us from accurate determination of neutron cross sections of unstable nuclei including MAs and LLFPs.

Recently, a new method, called the surrogate method, has come to be used actively to determine neutron cross sections of unstable nuclei. This is a method which uses (multi) nucleon transfer reactions (both stripping and pick-up) or inelastic scattering on available target nuclei and produce the same compound nuclei as those of the desired neutron-induced reactions, and measure the decay branching ratios leading to capture and/or fission channel. Identification of the produced compound nuclei and their excitation energies can be done by detection of the ejectile species and their energies.

At a first glance, it seems to be a simple and effective method to simulate the neutron-induced reactions. However, the thing is not easy. Even if we produce the same compound nuclei at the same excitation energy as produced in the desired neutron-induced reactions, the spin-parity distributions are plausibly different between them. Since we are interested in low-energy neutron cross sections relevant to reactor applications and astrophysics, the produced compound nuclei decay statistically, and the branching ratio is strongly influenced by the spin and parity. Therefore, difference of the spin-parity distributions between the surrogate and neutron-induced reactions must be properly taken into account in converting the branching ratio determined by the surrogate method to the one for neutron-induced reactions. Up to now, however, it has not been able to deduce the spin-parity distribution in the surrogate reactions, since they are normally multi-nucleon transfer reactions, the reaction mechanisms of which are not understood well.   On the other hand, it is also true that the surrogate method has yielded rather accurate cross sections, verified when the corresponding neutron data are available. Therefore, it is natural to expect that there is a certain condition to equate the results from the surrogate method and the neutron-induced reactions. However, the condition under which the surrogate method works is not clearly understood yet.

In this work, we investigate the spin-parity dependence of the branching ratios of Uranium and isotopes around mass 200 to the fission and capture channels and clarify the condition for the surrogate ratio method

---

[1] Japan Atomic Energy Agency (JAEA)

to work, and estimate the accuracy achievable by it.
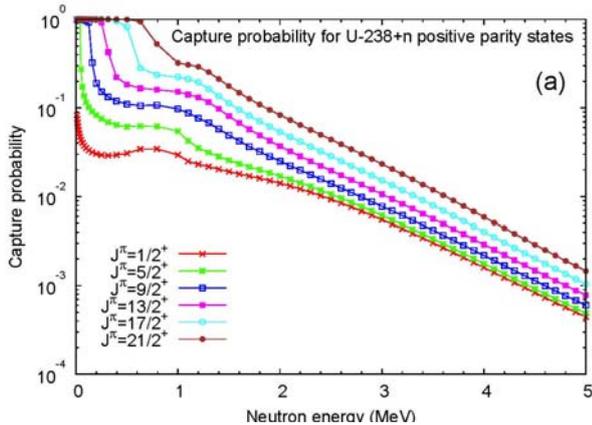
Fig. 1 J-dependence of the branching ratio to the capture channel from the positive-parity states produced in neutron capture by ^{238}U.
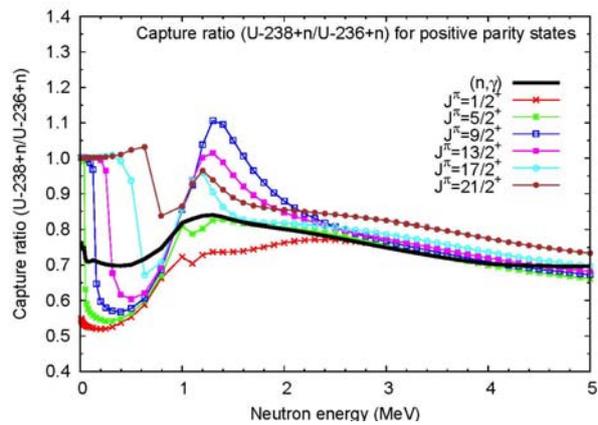
Fig. 2 J^π-by-J^π ratio of the branching ratios to the capture channel for ^{238}U+n and ^{236}U+n reactions

Figure 1 shows the decay branching ratio to the capture channel from various spin (J) states in the compound nucleus produced by capture of neutrons by ^{238}U calculated by a statitical model[1,2]. It is apparent that the branching ratio depends strongly on the J value of the decaying states. The deviation is around a factor of 5 even at neutron energy of 5 MeV where it is minimal. This fact shows that difference of the J^π distribution produced in the neutorn-induced reactions and the surrogate reactions might affect the net decay branching ratios. This difference would cause the results of both reactions quite different from each other, thus deteriorating the usefulness of the surrogate method. On the other hand, the change of the branching ratio (capture probability) is monotonic as a function of the spin values. We also notice the same tendency in the neutron-induced reactions of a neighboring nucleus ^{236}U. Since such a tendency was found also other combinations of nuclei around A = 200, we may expect that there is a possibility to cancel out the apparent J^π dependence in the branching ratio by taking ratios of them for each J^π. Results of such a calculation are shonwn in Fig. 2, where the ratios of decay branching ratio to capture channel for ^{238}U+n and ^{236}U+n reactions are shown for various J^+ values. We notice that this quantity shows a drastically good convergence. The factor of 5 difference in Fig. 1 is now reduced to around 10% above 2 MeV except for J^π value of $21/2^+$. Furthermore, these ratios nicely coincide with that of the neutron-induced reaction which is shown by the thick solid line in Fig. 2. The coincidence is even better for the fission channels. From these conciderations, we can conclude that the surrogate ratio method can yield the correct neutron cross section ratios if 1) such a coincidence as shown in Fig. 2 is realised, 2) the spin-parity distributions used in the two surrogate reactions are equivalent to each other, and 3) J values larger than 10 is not the major component[3]. Validity of these conditions can be verified by measuring the angular and energy distributions of emitted particles (such as protons in (t,p) reaction) or photons.

References

[1] W. Hauser and H. Feshbach, Phys. Rev., C87 (1952) 366.

[2] O. Iwamoto, J. Nucl. Sci. Technol., 44 (2007) 687.

[3] S. Chiba and O. Iwamoto, Phys. Rev., C81 (2010) 044604.

5.4 New formulation with CDCC for evaluating incomplete and complete fusion cross sections

S. Hashimoto[1], K. Ogata[2], S. Chiba[1,3] and M. Yahiro[2]

The interest of breakup effects on the fusion reaction has grown recently. Incomplete fusion processes, in which a part of the projectile is absorbed by the target with emitting the other fragment(s), play an important role in studying the reaction with weakly-bound nuclei. For deuteron induced reactions, the knowledge about the reaction mechanism and nuclear data of (d,n) reactions on various targets are required for studies on nuclear applications such as the International Fusion Materials Irradiation Facility (IFMIF). The inclusive (d,n) reaction on Li targets at incident energy 40 MeV is analyzed by Ye *et al.* [1], and they showed that contributions of the incomplete fusion reaction to the observables are very large. In Ref. [1], the incomplete fusion process is described by the Glauber model, and the result reproduces very well the experimental data added by elastic breakup contributions obtained with the Continuum-Discretized Coupled-Channels method (CDCC) [2]. Nevertheless, it is important to test the validity of the Glauber model in the low energy region by comparing it with that obtained fully quantum mechanically.

We propose a new approach [3] for evaluating cross sections of the incomplete and complete fusions using CDCC, which takes into account the effect of the breakup on the reaction and has been successfully applied to analyze various reactions with weakly-bound nuclei. Since imaginary parts of p-Li and n-Li optical potentials W_c (c=p and n) describe absorption (fusion) of the particle c, the total fusion cross section is given as

$$\sigma_{tot.fu.} \propto \int dr_p dr_n \Psi^*(r_p, r_n)(W_p(r_p) + W_n(r_n))\Psi(r_p, r_n), \tag{1}$$

where Ψ is the wave function in the framework of the three-body system, and r_p (r_n) is the coordinate of p (n) to the target. Using an absorption radius r_c^{ab}, which is an effective range of W_c, the integration intervals in Eq. (1) can be divided into four regions shown in Fig. 1. The contribution of the left-lower region, in which both p and n are located within the range of W_c and absorbed by the target, corresponds to the complete fusion process. In the right-lower region, n is assumed to be within the range of W_n, while p is free of the absorption. Then, the contribution of the region corresponds to the (d,n) incomplete fusion process. Similarly, that of the left-upper region corresponds to the (d,p) incomplete fusion. Therefore, we can obtain each fusion cross section by the integration over the region corresponding to the process.

This method is applied to analysis of the deuteron induced reaction on a ^{7}Li target up to 50 MeV of the deuteron incident energy E_d^L using CDCC codes [4]. In Fig. 2, results of the method are compared with those of the Glauber model. The panel a) shows the two incomplete fusion cross sections ((d,n) and (d,p)) calculated with the Glauber model and those with the new method, in which we used r_c^{ab}=4.0 fm

[1] Japan Atomic Energy Agency (JAEA)
[2] Kyushu University
[3] National Astronomical Observatory of Japan

determined by a condition that the result of (d,n) at 40 MeV obtained by the the present calculation agrees with that obtained by the Glauber model. It is found that for the incomplete fusion processes the Glauber model reproduces the results of the new method below 40 MeV, and works well. On the other hand, for the complete fusion a comparison between results obtained with our method and those with the Glauber model is shown in the panel b) of Fig. 2. One sees that the two models give significantly different results of even at 50 MeV.

In conclusion, we proposed a new method to evaluate the incomplete and complete fusion cross sections by means of CDCC, and applied to the analysis of the deuteron induced reaction on the Li target. Comparing the results obtained by the new method with those by the Glauber model, we found that the Glauber model describes the incomplete fusion process very well below 50 MeV, while for the complete fusion the two models give markedly different energy dependence. In order to investigate the reaction mechanism in detail, the development of the formulation is necessary to calculate the angular differential cross section or the energy spectrum of the reaction.
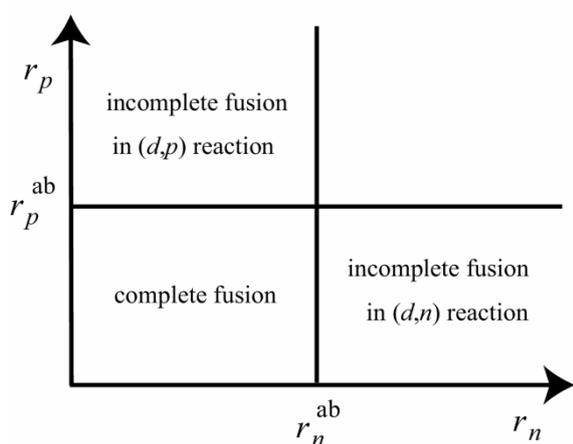
Fig. 1 Schematic illustration of divided integration intervals corresponding to each fusion reaction.
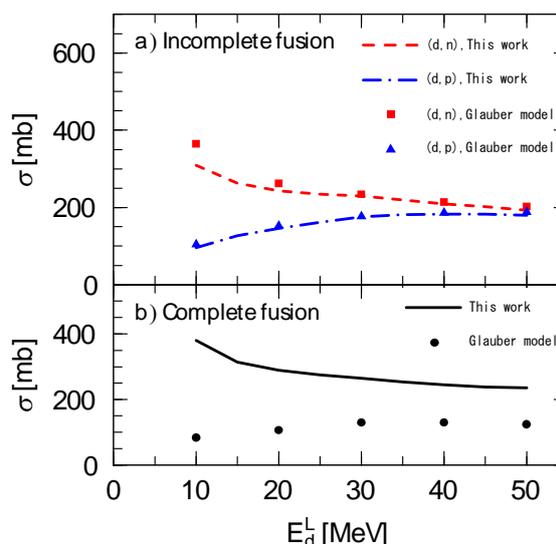
Fig. 2 Incomplete and complete fusion cross sections of d on ^{7}Li as a function of incident energy E_d^L calculated with the new method and the Glauber model.

References

[1] T. Ye, Y. Watanabe and K. Ogata, Phys. Rev., C80 (2009) 014604.
[2] M. Kamimura et al., Prog. Theor. Phys. Suppl., 89 (1986) 1.
[3] S. Hashimoto et al., Prog. Theor. Phys., 122 (2009) 1291-1300.
[4] Y. Iseri et al., Bull. Res. Comput. Syst. Comput. Commun. Cent. Kyushu Univ. Vol. 5, No. 3, (2006) 117-134 (CDCDEU); Vol. 1, No. 1, (2007) 16-28 (HICADEU).

5.5 Competition between allowed and first-forbidden transitions of beta decay in the neutron-rich mass region relevant to the r-process nucleosynthesis

H. Koura[1]

Beta decay in the neutron-rich mass region plays an important role on the r-process nucleosynthesis. Most of these nuclei are unknown or little nuclear data exists still now, so theoretical estimation is essentially necessary to study it. In some theoretical approaches, however, only the allowed transitions as the Fermi and the Gamow-Teller transition are considered, and no forbidden transitions are treated. In this report, we estimate the beta decay rate in the framework of the first version of the gross theory[1], and evaluate an influence of the first-forbidden transition in the neutron-rich mass region.

Generally, beta-decay rate up to the first-forbidden transition is expressed as

$$\lambda = \lambda_F + \lambda_{GT} + \lambda_1^{(0)} + \lambda_1^{(1)} + \lambda_1^{(2)}. \tag{1}$$

Here subscripts stand for Fermi, Gamow-Teller and first-forbidden transition, and superscripts in the first-forbidden represent the rank $L=0$, 1 and 2, respectively. According to the V-A beta-decay theory, decay constant (or decay rate) is obtained from the nuclear matrix element $|M(E)|^2$. In the case of the Gamow-Teller and the rank-2 first-forbidden transitions, the decay rates can be written as

$$\lambda_{GT} = \frac{m_e^5 c^4}{2\pi^3 \hbar^7} |g_A|^2 \int_{-Q}^0 |M(E)|^2 f(-E) dE \tag{2}$$

and

$$\lambda_1^{(2)} = \frac{m_e^5 c^4}{2\pi^3 \hbar^7} \left(\frac{m_e c}{\hbar}\right)^2 |g_A|^2 \int_{-Q}^0 \sum_{ij} |M_{ij}(E)|^2 f_1(-E) dE. \tag{3}$$

Here. m_e is a rest mass of electron, g_A is the axial-vector type coupling constant, f and f_1 are the integrated Fermi function of the allowed and the unique-first forbidden transition and Q is the beta-decay Q-value. In the Gross theory, we assume the nuclear matrix element $|M(E)|^2$ as an integral of a single-particle strength function so as to fulfill the sum rules of $|M(E)|^2$ and concentration (allowed) and non-concentration (forbidden) of the single-particle strength functions to isobaric analogue states. The beta-decay Q-values are obtained from the KTUY mass formula, which gives a good reproduction of ground-state nuclear masses, derivatives of masses as neutron, proton separation energies for known nuclei[2].

Due to the smallness of λ_F compared to λ_{GT} in the neutron-rich mass region excepting the quite light region like neutron and ^{3}H, we only compare the decay constants of the Gamow-Teller transition and the sum of the first-forbidden transition. Fig. 1 shows the dominant decay modes in the neutron-rich mass region. In many cases the Gamow-Teller transition rate is larger (or the partial half-life is longer) than the first-forbidden transition in the neutron-rich side. In the stable and rather neutron-rich region heavier than

---

[1] Japan Atomic Energy Agency (JAEA)

nuclei around $^{132}Sn_{82}$, however, the area of nuclei with larger rate of the first-forbidden transition than that of the Gamow-Teller spreads widely. If we consider the evolution of the simple single-particle levels to the neutron-rich side from $^{208}Pb_{126}$ as shown in Fig. 2, such a properties can be roughly discussed. In the case of the single-particle levels of the stable isotone of N=126, ^{208}Pb, there seems to be no allowed transition channel due to the hindrance from the selection rule of angular momentum and parity, and consequently the first forbidden transition is dominant. In the case of ^{192}Dy, however, some allowed transition channels are open, and the strength of the allowed transition may be comparative or larger than the forbidden transition. This property also supports the result of beta-decay rates in this report.
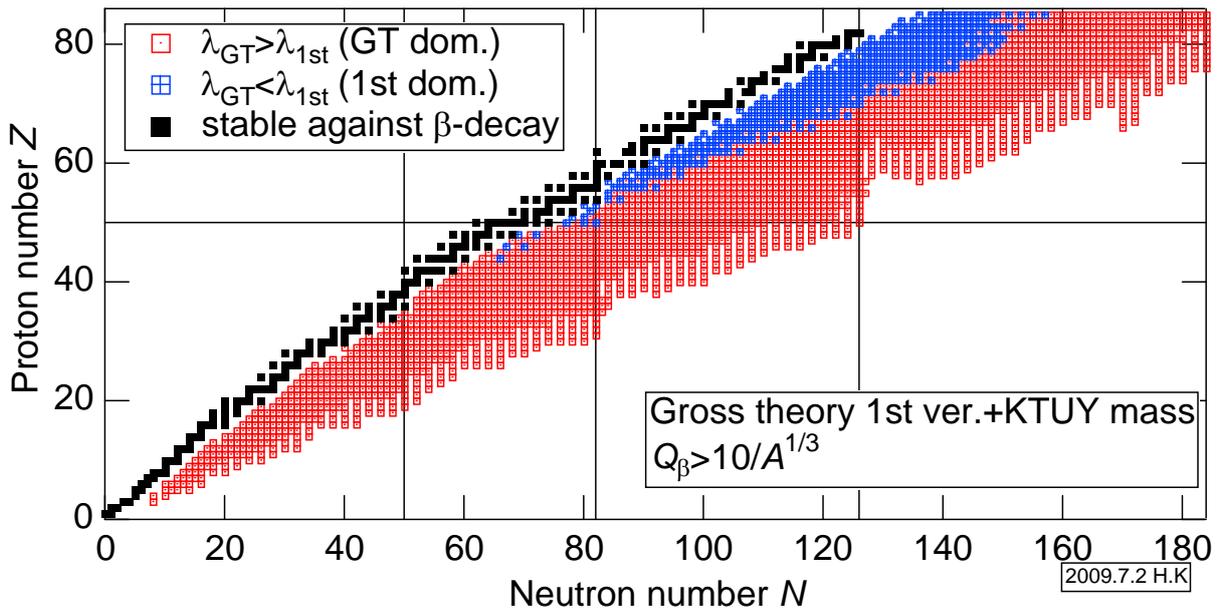
Fig. 1　Dominant transition mode between the Gamow-Teller and the first-forbidden transition of the beta decay in the neutron-rich mass region.
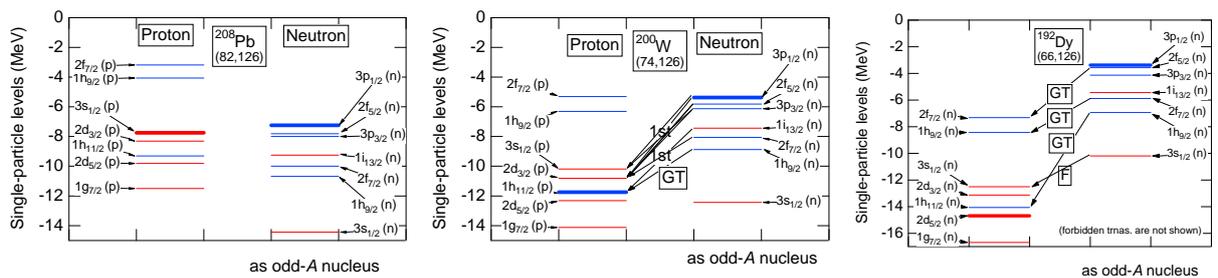
Fig. 2 Single-particle levels of N=126 isotones: ^{208}Pb (left), ^{200}W(middle), ^{192}Dy (right). We assume these nuclei are spherical and calculate the levels from a modified Woods-Saxon type potential[3].

References

[1] K. Takahashi, M. Yamada and T. Kondoh, At. Data and Nucl. Data Tables, 12 (1973) 101-142.

[2] H. Koura et al., Prog. of Theor. Phys., 113 (2005) 305-325.

[3] H. Koura and M. Yamada, Nucl. Phys., A671 (2000) 96-118.

CHAPTER 6

Atomic Physics and Solid State Physics

This is a blank page.

6.1 Coster-Kronig electron spectra of C- and N-like O^{q+} (q = 1,2)

K. Kawatsura[1,2], K. Takahiro[3], M. Sataka[4] M. Imai[5], H. Sugai[4], K. Kawaguchi[3],
T. Yoshimori[3], H. Shibata[5] and K. Komaki[6]

Recently we have reported on Coster-Kronig (C-K) electron spectra in high-energy collisions of 32 MeV O^{q+} (q = 3,4) ions with a He gas target [1,2]. For Be-like O^{4+} ions, a series of $1s^22p(^2P)nl - 1s^22s(^2S)\varepsilon l'$ (n = 6-11) C-K transitions was assigned. The high-resolution spectrum for the $1s^22p6l$ state has shown that the peak due to the low angular momentum $l = 1$ is the most intense, which obeys dipole selection rules. This result for the l distribution has been found to be different from those of the double electron capture (DEC) processes. For B-like O^{3+} ions, a series of $1s^22s2p(^3P)nl - 1s^22s^2(^1S)\varepsilon l'$ (n = 5-11) C-K transitions was assigned. The sharp lines on both sides of the cusp peak have been confirmed to be due to the very low energy transition from the $1s^22s2p(^3P)5s$ state. It is also found that states with the angular momenta of $l = 0$-3 are populated and the maximum intensity is attributed to the states with higher angular momenta $l \geq 2$. The C-K spectra were compared with those for the dielectronic recombination (DR) processes.

In the present study, we have systematically measured C-K electrons from high-Rydberg states produced in high-energy collisions of 30 MeV O^{2+} + He and 15 MeV O^+ + He for extending the investigation of C-K electron spectra past highly charged O^{q+} (q = 3,4) ions. The experiments were performed at the tandem accelerator facility at the Japan Atomic Energy Agency (JAEA) of Tokai, using the 20 MV tandem accelerator. Fig. 1 shows high-resolution spectrum of electrons ejected in the collision of 30 MeV O^{2+} ions with a He target. For this collision system, projectile O^{2+} ions have 6 electrons which are more than in the previous experiments for O^{3+} and O^{4+} ions. To our knowledge there is no report on C-K electron spectra for such a complicated collision system. Fig. 1 shows the C-K electron spectrum from O^{2+} $1s^22s2p^2nl$ states and other excited states which were produced by electron excitation/ionization processes during 30 MeV O^{2+} + He collision. Here, we calculate ejected electron energies arising from the possible C-K transitions using equation,

$$E_n = \Delta E - Q^2 R_y/n^2 \qquad (1),$$

where E_n is the C-K electron energy, n is the principal quantum number, ΔE is the energy difference between the initial and final states of the ion core configuration, taken from the compiled transition energy tables [3], Q is the effective charge of the ion core (assumed to be $q+1$ for this case), and R_y is the Rydberg energy (13.606 eV). In the figure, the representative peaks are assigned to a series of $1s^22s2p^2(^4P)nl - 1s^22s^22p(^2P)\varepsilon l'$ (n ≥ 4) C-K transitions and vertical bars in Fig. 1 indicate the line positions obtained by equation (1). In this spectrum, the transitions to the $^2P_{1/2}$ and $^2P_{3/2}$ final states are not resolved but some
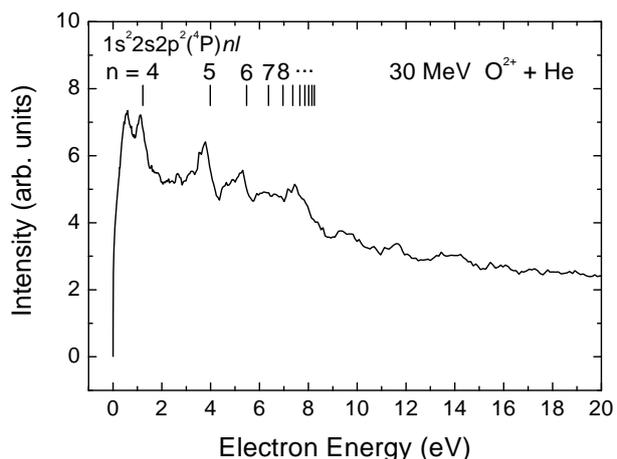
Fig. 1 Coster-Kronig electron spectrum ejected at $0°$ in collisions of 30 MeV O^{2+} on He. The vertical bars indicate the positions of the $1s^2 2s 2p^2 (^4P) nl$ Rydberg series.
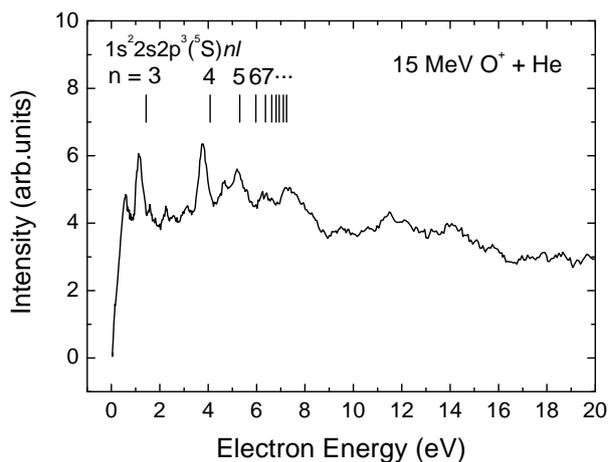
Fig. 2 Coster-Kronig electron spectrum ejected at $0°$ in collisions of 15 MeV O^+ on He. The vertical bars indicate the positions of the $1s^2 2s 2p^3 (^5S) nl$ Rydberg series.

structures are recognized at each value of n, to which the angular momentum (l) distribution should be responsible. Fig. 2 shows the measured electron spectrum resulting from the collisions of 15 MeV O^+ ions on He. For this collision system, projectile O^+ ions have 7 electrons which are even more than the above-mentioned collision system of 30 MeV O^{2+} +He. This figure shows the complicated C-K electron spectrum ejected from O^+ $1s^2 2s 2p^3 nl$ states and other excited states which were produced by electron excitation processes. Here, we calculate ejection energies for the possible C-K transitions by using equation (1), where Q is the effective charge of the highly exited O^+ ion core (assumed to be +2 for this case), adopting the values of ΔE given by Ref. [3]. In the figure, the representative peaks are assigned to a series of $1s^2 2s 2p^3 (^5S) nl – 1s^2 2s^2 2p^2 (^3P) \varepsilon l'$ ($n \geq 3$) C-K transitions and vertical bars indicate line positions obtained by equation (1). In this spectrum, difference among the transitions to final $^3P_0$, $^3P_1$ and $^3P_2$ states is not observed but structures in the peaks for each principal quantum number ($n \geq 3$), up to the series limit of 7.48 eV ($n \to \infty$), seem to reflect the angular momentum distribution. Moreover, some structures present in the higher energy region between 8.0 and 16 eV could be assigned to a series of $1s^2 2s 2p^3 (^3D) nl – 1s^2 2s^2 2p^2 (^3P) \varepsilon l'$ and/or $1s^2 2s 2p^3 (^3P) nl – 1s^2 2s^2 2p^2 (^3P) \varepsilon l'$ C-K transitions, whose series limits are 14.88 eV and 17.65 eV, respectively. However, a comprehensive analysis for high-resolution measurements of C-K electron spectra as well as precise theoretical calculations are needed to obtain more detailed information about the production of high-Rydberg states and their decay processes in the high-energy collision regime.

References

[1] K. Kawatsura et al., Nucl. Instrum. Methods Phys. Res., B205 (2003) 528-531.

[2] K. Kawatsura et al., Nucl. Instrum. Methods Phys. Res., B245 (2006) 44-46.

[3] NIST Atomic Spectra Database: http://www.physics.nist.gov/PhysRefData/ASD/(accessed 2010-05-05).

6.2   Charge state distribution of sulfur ions after penetration of C-foil targets

M. Imai[1], M. Sataka[2], H. Sugai[2], K. Kawatsura[3,4], K. Takahiro[5],
K. Komaki[6], K. Nishio[2] and H. Shibata[1]

Following injection into matter, swift heavy ions change their charge states until they establish charge equilibrium, in which increases and decreases in population of each charge state balance with each other, and the populations seem to remain unchanged. Charge state is one of the most important aspects of ion-matter interactions and affects various processes in matter, such as electron capture, ionization, and excitation of projectile and target electrons, as well as consequent phenomena such as energy deposition into the target, *i.e.* stopping of projectiles. Projectile charge state and its evolution are therefore essential to the study of the penetration of swift ions in matter and the data of charge-state distributions for various collision systems after exiting solid targets have been supplied [1], although the charge-state distribution changes somewhat upon exiting the target foil. As has been presented in the previous annual reports [2], we measured the exit charge state distributions for penetrations of $S^{6+} - S^{16+}$ ions through C-foil targets of 0.9 − 200 $\mu g/cm^2$ in thickness and performed calculations by ETACHA code [3] to succeed in reproducing the experimental results, although ETACHA has been designed for higher energy region (>10 MeV/u) [4]. We performed another simulation, in which the electron transfer cross sections $\sigma_{qq'}$ are calculated with codes applicable to the present collision energy [5]. In this report, mean charge states and distribution widths derived from our measurements at 2.0 MeV/u are presented as well as those from simulations.

The present experiments were performed at the LIR1−3 beam line of the 20UR Tandem Accelerator Facility. A beam of 2.0 MeV/u (64 MeV) S^{6+} or S^{7+} ions was provided from the Tandem Accelerator within an energy accuracy of 0.1%. A post-stripper C-foil of ~20 $\mu g/cm^2$, placed downstream from the energy-analyzing magnet, was used to produce higher charge states up to 16+. It should be noted here that high-voltage terminal equipment of the Tandem Accelerator has been replaced to improve beam transportation optics [6], enabling us to extract sufficient numbers of bare S^{16+} ions. Energy loss values at the post-stripper foil were assumed to be at most 0.7% based on separate measurements of cusp electron energies with zero-degree electron spectroscopy [7]. The S^{q+} ($q = 6-16$) ion beam was directed to self-supported carbon foil targets of 0.9−200 $\mu g/cm^2$ in thickness. The charge-state distributions after foil penetration were measured using the heavy ion magnetic spectrometer ENMA and a position-sensitive gas chamber detector. The vacuum conditions inside the collision chamber and the spectrometer were maintained below 10^{-4} and 10^{-6} Pa, respectively, to practically eliminate background charge-exchange collisions with residual gas, which was confirmed by measurements without a target foil.

---

[1] Kyoto University
[2] Japan Atomic Energy Agency (JAEA)
[3] Kansai Gaidai University
[4] Theoretical Radiation Research Laboratory
[5] Kyoto Institute of Technology
[6] RIKEN

The values of mean charge states $\overline{q} = \sum_q q F(q)$, where $F(q)$ denotes the fraction for charge state q, are plotted in Fig. 1(a), with those derived by solving rate equations for charge state fractions in Fig. 1(b).
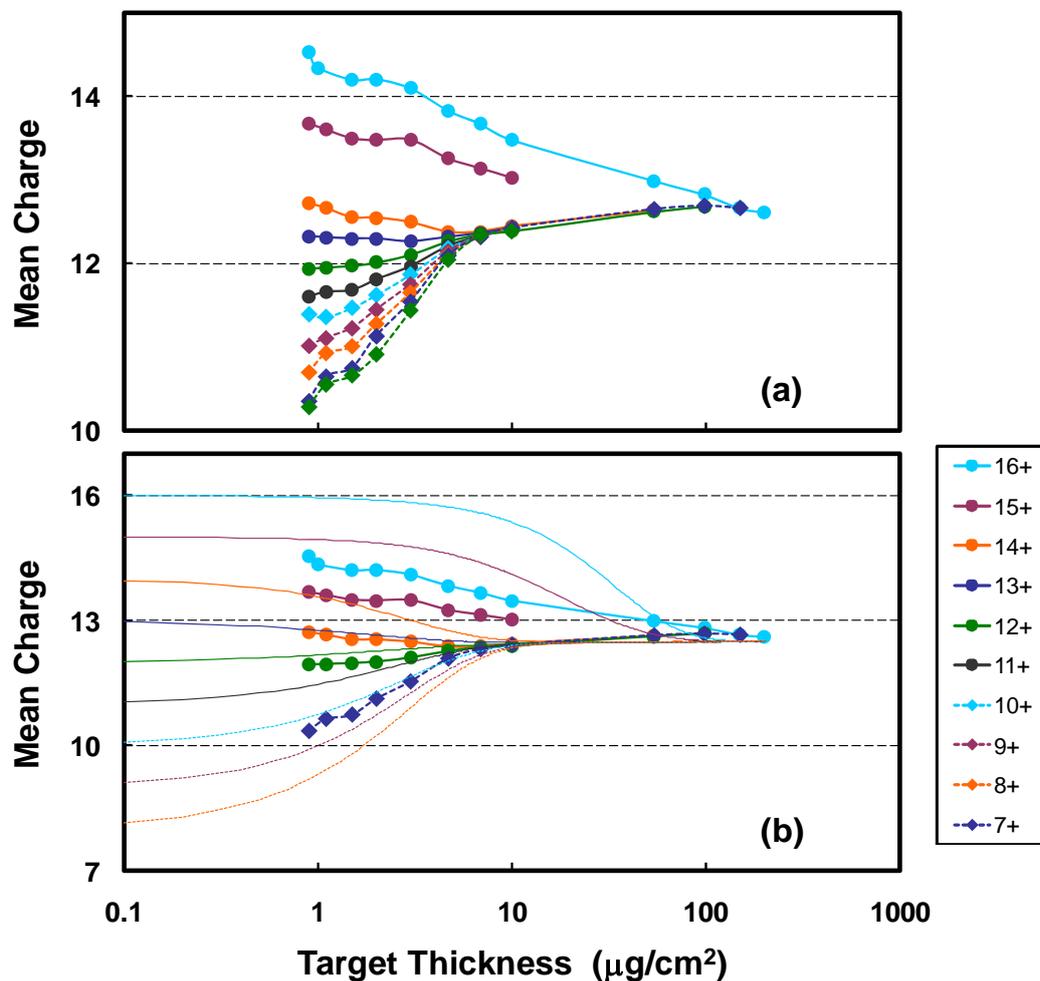
Fig. 1   Mean charge state (a) measured for 2.0 MeV/u $S^{6+} - S^{16+}$ ion incidences after passing through C-foil targets and (b) calculated by solving the rate equations accounting for single-electron transfers for 2.0 MeV/u $S^{8+} - S^{16+}$ ion incidences (full lines) with experimental results for S^{7+}, S^{12+}, and $S^{14+} - S^{16+}$ ion incidences (filled symbols).

References

[1] A. B. Wittkower and H. D. Betz, At. Data Nucl. Data Tables、5 (1973) 113-166; K. Shima et al., *ibid*. 51 (1992) 173-241; K. Shima et al., Nucl. Instrum. Methods Phys. Res., B33 (1988) 212-215.

[2] M. Imai et al., JAEA-Review 2007-046 (2008) 87-88; 2008-054 (2008) 89-90; 2009-036 (2009) 91-92.

[3] J. P. Rozet et al., J. Phys., B22 (1989) 33−48; Nucl. Instrum. Methods Phys. Res., B107 (1996) 67-70.

[4] M. Imai et al., Nucl. Instrum. Methods Phys. Res., B230 (2005) 63-67.

[5] M. Imai et al., Nucl. Instrum. Methods Phys. Res., B256 (2007) 11−15; *ibid*. B267 (2009) 2675-2679.

[6] M. Matsuda et al., J. Phys., Conf. Ser., 163 (2009) 012112 (4 pp.).

[7] M. Sataka *et al*., Phys. Rev., A65 (2002) 052704 (11 pp.); M. Imai *et al*., Nucl. Instrum. Methods Phys. Res., B67 (1992) 142-145.

6.3   Li diffusion in Li ionic conductors of NaTl-type intermetallic compounds

H. Sugai[1], M. Sataka[1], S. Okayasu[1], S. Ichikawa[1], K. Nishio[1], S. Mitsuoka[1],

S.C. Jeong[2], I. Katayama[2], H. Kawakami[2], Y.X. Watanabe[2],

H. Ishiyama[2], N. Imai[2], Y. Hirayama[2], H. Miyatake[2], T. Hashimoto[3] and M. Yahagi[3]

Non-destructive and on-line Li diffusion experiments in Li-ionic conductors are conducted using the short-lived α-emitting radiotracer of ^{8}Li. Li-8 decays through β-emission to ^{8}Be with a half lifetime of 0.84s, which immediately breaks up into two α-particles with energies broadly distributed around 1.6MeV with a full width at half maximum of 0.6MeV. The radiotracers produced as an energetic and pulsed ion beam (typically 4MeV with an intensity of 10^4 particles/s) from TRIAC [1] (Tokai Radioactive Ion Accelerator Complex) are implanted into a structural defect mediated Li ionic conductor of NaTl-type intermetallic compounds. The experimental time spectra of the yields of α-particles are compared with simulated results and Li diffusion coefficients in the samples [1] are extracted directly. After a series of experiments of LiGa, the experiments of LiIn was conducted in fiscal 2009. In this report, the temperature-dependence of diffusion coefficients obtained for LiIn with the Li content of 48 at.% are presented and the thermodynamic properties of Li vacancies in LiIn are discussed [1].

The crystal structure of Ia-IIIb intermetallic compounds (e.g., LiAl, LiGa and LiIn) is NaTl-type [2,3], which is composed of two interpenetrating diamond sublattices such that each atom has eight nearest neighbors: four like and four unlike atoms. The characteristic defect structure of LiA (A=Al, Ga, In) consists of two types of defects at room temperature, i.e. vacancies in the Li sublattice (V_{Li}) and Li antistructure atoms in the A sublattice (Li_A). For example, the concentrations of the point defects, $[V_{Li}]$ and $[Li_{Ga}]$, strongly depends on Li content; with increasing the Li content from 43 to 54%, $[V_{Li}]$ decreases from 11.4 to 2.8%, while $[Li_{Ga}]$ increases from 0 to 5.1% [4]. V_{Li} is the dominant defect for the Li-deficient region, while Li_{Ga} is the dominant defect for the Li-rich one. As mentioned above, we can control the Li-vacancy concentration which is a dominant path for the Li diffusion in the NaTl-type compounds with changing the Li content. Thus, the NaTl-type compounds provide a useful and suitable field to study the Li diffusion mechanism in Li-ionic conductors, which are key materials for Li-ion batteries.

The diffusion coefficients of Li and the electrical resistivity in LiIn of 48 at.% Li and in LiGa of 44 at.% Li are shown in Fig. 1 as a function of inverse temperature. The diffusion coefficients of Li in the LiGa of 44 at.% Li follow Arrhenius behavior in the region of higher temperature with an activation energy of 0.16 eV well consistent with the value in the reference [5]. In the lower temperature followed by a sudden change around 234K, the diffusion coefficients are observed as a constant, which is the lower limit of diffusion coefficients accessible by the present method; for the diffusion coefficients less than about 10^{-10} cm^2/s, any significant effect in the yields of alpha-particles due to the diffusing ^{8}Li could not be observed because of

---

[1] Japan Atomic Energy Agency (JAEA)
[2] High Energy Accelerator Research Organization (KEK)
[3] Aomori University

the short lifetime of the radiotracer. The sudden change in the value of the diffusion coefficient around 234K occurs at the temperature where the anomalous electrical resistivity is observed, as indicated by an arrow in the figure. The resistivity measurements were carried out using a van der Pauw method as used for LiAl [3]. This observation is closely related to the thermodynamic properties of the structural defects, already observed as the anomalies in heat capacity [6] and nuclear-spin lattice relaxation [5] at 233K near the critical composition of the Li-deficient LiGa. It has been suggested that these phenomena are related to the order–disorder transformation of Li vacancies in the compounds. The ordering of the

Fig. 1 Temperature-dependence of diffusion coefficients (closed square) and electrical resistivity (open square) for LiIn with 48 at.% Li, and that of diffusion coefficients (closed circle) and electrical resistivity (open circle) for LiGa with 44 at.% Li.

vacancies produces a sharp drop in the Li diffusion coefficients below the ordering temperature, since the vacancies are supposed to be the carriers of Li atom. The observed amount of change, more than two orders of magnitude in the value of diffusion coefficients in the case of LiGa, is quite clear as compared to those observed in the measurement of electrical resistivities where just a small change (at most 1/10) can be seen at the transformation temperature.

As shown in Fig. 1, the diffusion coefficients of Li in LiIn of 48 at.% Li follow Arrhenius behavior in both the temperature regions above and below 207K at which temperature the sudden changes of Li diffusion and electrical resistivities would be induced by the order-disorder transformation of Li vacancies as same as in the case of LiGa. The first-time observation of Li diffusion related to the order-disorder transformation of Li vacancies in LiIn showed that the activation energy of Li diffusion below 207K is larger than that above 207K. The detail analyses for the order-disorder features of Li vacancies in LiIn are now in progress compared with the case of LiGa.

References

[1] S.C. Jeong, H. Sugai and M. Yahagi, BUTSURI, 64 (2009) 687-691 (in Japanese).

[2] J.C. Tarczon, et al., Mater. Sci. and Eng., A101 (1988) 99-108.

[3] H. Sugai, et al., Phys. Rev., B52 (1995) 4050-4059.

[4] K. Kuriyama, et al., Phys. Rev., B54 (1996) 6015-6018.

[5] K. Nakamura, et al., Faradsy Discuss., 134 (2007) 343-352.

[6] H. Hamanaka, et al., Solid State Ionics, 113-115 (1998) 69-72.

6.4 Diffusion coefficient measurements on perovskite-type lithium ion conductor

S. Takai[1], S.C. Jeong[2], I. Katayama[2], H. Kawakami[2], H. Ishiyama[2], N. Imai[2], Y. Hirayama[2],
Y. Watanabe[2], H. Miyatake[2], M. Sataka[3], H. Sugai[3], S. Okayasu[3] and T. Nakanoya[3]

More and more attention has been attracted on the materials for the energy devices, e.g. fuel cells, lithium rechargeable batteries, or solar cells. Lithium ion conductors have been studied for the application of solid electrolite of the lithium rechargeable batteries as well as the gas sensors. Perovskite-type structured $La_{2/3-x}Li_{3x}TiO_3$ solid solutions ($0 < x < 0.166$) exhibit excellent lithium ion conduction and the compoisition around $x = 0.116$ has been reported the highest lithium ion conductive oxide so far [1]. In this system, La and Li ions occupy the A site of the perovskite-type structure accompanied by vacancy, while Ti ion occupy the B site. Lithium ion is supposed to migrate only when the adjacent A-site is vacant. The compositional dependence of lithium ion conductivity has been explained by the model that lithium ion conductivity was depressed in the lower and higher x region due to the smaller numbers of charge carriers and of vacancies, respectively. On the other hand, in terms of the diffusion coefficients, the samples of smaller lithium content are simply preferred for the benefit of the jump probability of lithium ions. We have measured the tracer diffusion coefficient measurements on $La_{2/3-x}Li_{3x}TiO_3$ system by means of neutron radiography technique [2]. Stable ^6Li tracer as the form of $LiNO_3$ was introduced from the surfaces of $La_{2/3-x}Li_{3x}TiO_3$ sample blocks composed of ^7Li and transmitted intensity of neutron were measured after diffusion annealing. Based on the large difference of neutron absorption coefficients between ^6Li and ^7Li, isotope concentration profiles can be obtained. However, due to the resolution limit of imaging plate for neutron, diffusion annealing above 200^oC were necessary to accomplish the diffusion experiment within the machine time. This implies that the diffusion coefficient cannot be directly measured around room temperature by this method.

A new technique employing the short lived ^8Li radiotracer ($t_{1/2} = 0.84$ s) has been recently developed [3]. The diffusion samples are irradiated by ^8Li particles which break up into α-particles in the sample through ^8Be with β-emission, and ^8Li tracer concentration profiles are calculated from the time dependence of the detected α-particles during the ^8Li beam-on/off cycles. The diffusion coefficients can be deduced from the calculated isotope concentration profiles. Since α particle detection is sensitive to the depth in the sample, diffusion coefficients were supposed to be measured even for lower temperatures despite of short lived-radiotracer. In the present study, we applied this procedure to the diffusion coefficient measurements on the Perovskite-type lithium ion conductors below 200^oC.

$La_{2/3-x}Li_{3x}TiO_3$ ($x = 0.067$, 0.117 and 0.167) samples were prepared by the conventional solid state reaction method. The sintering temperatures were selected in the range $1310 – 1350^oC$ depending on the

---

[1] Tottori University
[2] High Energy Accelerator Research Organization (KEK)
[3] Japan Atomic Energy Agency (JAEA)

composition. The sintered sample pellets with the diameter $\phi 10$ was polished to achieve the mirror finish on the surface. To remove the diamond abrasive powder and residual strain, samples were then annealed at $800^{\circ}C$. As the "quenched sample", those of x = 0.117 were partly heat treated up to $1200^{\circ}C$ followed by fast cooling using liquid N_2.

[8]Li radiotracer, provided by TRIAC (Tokai Radioactive Ion Accelerator Complex at Tandem Accelerator Facility in JAEA) of 0.46 MeV u^{-1} was periodically implanted to the sample with the fixed time sequence, 1.67 s and 5.00 s for beam-on and off, respectively. The α-particles came from the samples were detected by SSD (Solid State Detector) set in front of the sample surface. The time variations of α-intensity in the sequence were collected repeatedly to accumulate. The measurements were carried out in the temperature range between room temperature and $250^{\circ}C$.

Figure 1 shows the time spectra of the α-particle yields measured at $100^{\circ}C$, which were normalized by the intensity at the beam-off time. Although these profiles roughly resembled each other, they differed in detail as shown in the inset. The time spectrum of x = 0.117 was fitted based on the model assuming the decay and diffusion of [8]Li, which are also represented

Fig. 1 Time spectra of the α-particle yields for $La_{2/3-x}Li_{3x}TiO_3$ measured at $100^{\circ}C$. ○: x = 0.067, □: x = 0.117, ■: x = 0.117 (quenched), and △: x = 0.167.
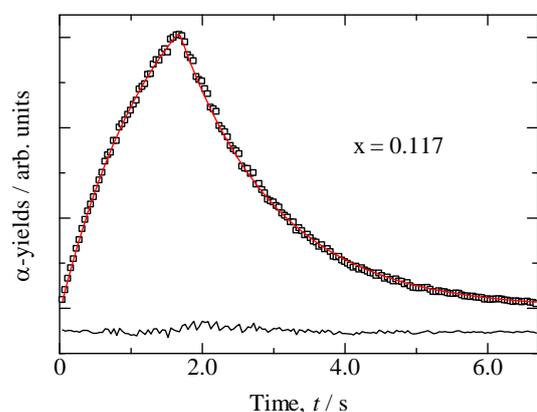
Fig. 2 Time spectrum of the α-yields for $La_{2/3-x}Li_{3x}TiO_3$ (x = 0.117) measured at $100^{\circ}C$. Rectangles: measured data as Fig. 1, red solid line: calculated and bottom solid line: difference.

in Fig. 2. By fitting profile, diffusion coefficients were tentatively deduced as 2.3×10^{-9} cm^2s^{-1}, which is close to the extrapolation of the high temperature diffusion data obtained by the previous neutron radiography.

More precise analyses are now in progress, but it should be noted that the quenched sample seemed to have higher diffusion coefficient. Further analyses would help not only the understanding of diffusion mechanism but also the designing of electrolyte devices.

References
[1] Y. Inaguma et al., Solid State Commun., 86 (1993) 689-693.

[2] S. Takai et al., Solid State Ionics, 176 (2005) 2227-2233.

[3] S.C. Jeong et al., Nucl. Instrum. Methods Phys. Res., B230 (2005) 596-600.

6.5 High-energy ion impact effects on atomic structure and optical property of In-doped ZnO films

N. Matsunami[1], M. Sataka[2], S. Okayasu[2] and H. Kakiuchida[3]

Zinc oxide (ZnO) doped with trivalent elements is known as n-type transparent semiconductor [1, 2]. We have studied atomic-structure and optical-property modifications of Al-doped ZnO (AZO) films under high-energy ion impact [3]. In this study, we have investigated modifications of In-doped ZnO (IZO) by high- and low-energy ion impact [4] to compare with those of AZO and of IZO by low-energy ion impact.

IZO films were prepared on SiO_2-glass substrates (~0.5x1x0.05 cm^3) at 500 ºC by using a RF-magnetron sputtering deposition (off-axis) method [4]. The X-ray diffraction (XRD) shows that the films are poly-crystalline with c-axis orientation of hexagonal wurtzite structure (Fig. 1). The substrate temperature was optimized to maximize the XRD intensity. The lattice parameter averaged over unirradiated 30 samples was obtained to be 0.5249 nm (sample variation of 0.4 %) and is larger by 0.8 % than 0.52069 nm in the literature [2]. Full-width at half-maximum (FWHM) of the XRD rocking curve of unirradiated films is 8±2.5 ° (Fig. 1 inset). Rutherford backscattering spectrometry (RBS) using 1.8 MeV He^+ ions was employed to evaluate the composition and thickness. In RBS analysis, Zn density is taken as $4.2x10^{22}$ cm^{-3} and the contribution of In to the stopping power [5] is discarded. The composition of the unirradiated films is very close to stoichiometric within RBS accuracy of 10%, i.e., $In_{1-x}Zn_xO$ with x≈0.94 (In/Zn≈6%). The film thickness is 100 to 150 nm. The films were irradiated with 100 MeV $^{136}Xe^{+11}$ and 100 keV Ne^+ ions at room temperature. It is found that the composition remains unchanged under the ion impact.

Figs. 1 shows XRD patterns of unirradiated IZO film and the film irradiated with 100 MeV Xe ions at $2.5x10^{12}$ cm^{-2}. The main diffraction peak is ZnO (002) at ~34 ° and peaks other than ZnO such as In and In_2O_3 were not observed. XRD intensity monotonically decreases with the ion fluence, reduction of the XRD intensity by ~30 % was observed at $3x10^{13}$ cm^{-2}. Interestingly, FWHM of the rocking curve decreases by 7 % (slightly larger than the estimated error of 5 %) after Xe ion impact at $2.5x10^{12}$ cm^{-2} (Fig. 1 inset). This could be due to grain-orientation alignment as observed for ZnO (a-axis orientation) on MgO [6], SiO_2 on Si(100) [7] and AlN on R-cut-Al_2O_3 [8]. FWHM increases for further ion irradiation. It also appears that the lattice parameter monotonically decreases by ion impact, and the lattice compaction of 1.7 % is observed at $1x10^{14}$ cm^{-2} of 100 MeV Xe. For, 100 keV Ne ion impact at $1x10^{17}$ cm^{-2}, a slight increase of the XRD intensity, reduction of rocking-curve FWHM by 12 % and lattice compaction of 0.8 % were observed. In view of XRD, atomic structure modification by high- and low-energy ion impact is insignificant, except for the lattice compaction.

Optical absorption spectrum of IZO film is shown in Fig. 2. The optical absorbance (OA, absorbance is defined as $\log_{10}(I_o/I)$, I_o and I being incident and transmitted photon intensity) of unirradiated films (more than ten samples with thickness of 60 to 400 nm) at the photon energy of 4 eV (310 nm) increases linearly with the film thickness and OA divided by the film thickness (L), called absorbance coefficient herein is determined to be $7.5x10^{-3}$ nm^{-1} with an estimated error of 10 % (or the absorption coefficient, α of $1.73x10^5$ cm^{-1}, I= I_o exp(-αL)) and is comparable with $6.67x10^{-3}$ nm^{-1} (α=$1.54x10^5$ cm^{-1}) for AZO [3]. The refractive index (n) of unirradiated film is approximately given by: n=1.93+0.00526/λ^2+0.00755/λ^4 with the sample variation of a few %, λ being the wavelength (μm), and n(IZO) is larger by 9-4 % than n(AZO) for λ=0.4-1.7 μm. Ion irradiation effects on the refractive index are under way.

---

[1] Division of Energy Science, EcoTopia Science Institute, Nagoya University
[2] Japan Atomic Energy Agency (JAEA)
[3] National Institute of Advanced Industrial Science and Technology (AIST)

Modifications of absorption spectra, bandgap and absorption-edge slope by 100 MeV Xe ions are seen in Fig. 2. The absorbance increases by several % up to 10^{13} cm^{-2} and decreases by ~4 % at 10^{14} cm^{-2}. The absorption-edge slope is obtained to be the slope in the linear part of absorbance vs photon energy (Fig. 2) and divided by the absorbance of the unirradiated film at 4 eV for normalization of the film thickness (an estimated error of 5%). The absorption-edge slope monotonically decreases from 1.7 eV^{-1} (smaller than 3.3 eV^{-1} of unirradiated AZO) to 1.2 eV^{-1} for 100 MeV Xe at 1×10^{14} cm^{-2}, similarly to AZO under 100 MeV Xe ion irradiation. The bandgap E_g is determined by using a relation for direct bandgap: (absorbance*E)^2 is proportional to $(E - E_g)$, E being the photon energy. The bandgap of unirradiated IZO films is obtained to be 3.2 eV ($\pm 2\%$) and this is somewhat smaller than that of AZO, 3.37 eV [3]. The bandgap increases by 0.25 eV for 100 MeV Xe ion at 10^{14} cm^{-2} (Fig. 2, inset).

For 100 keV Ne, the absorbance coefficient increases from 8.1×10^{-3} nm^{-1} with the Ne ion fluence and reaches saturation of 9.7×10^{-3} nm^{-1} (~20 % increase) at $\sim 1 \times 10^{17}$ cm^{-2}, the absorption-edge slope decreases to 0.73 eV^{-1} at 1×10^{17} cm^{-2} and E_g increases by ~0.045 eV comparable with the accuracy of 0.06 eV at 1×10^{16} cm^{-2} and for further irradiation E_g decreases by 0.11 eV at 1×10^{17} cm^{-2}. The decrease of the bandgap by the 100 keV Ne contrasts with the increase in the bandgap of IZO and AZO under 100 MeV Xe ion impact [3]. As mentioned earlier, the XRD intensity shows insignificant change. A speculation is that the optical property is more sensitive to ion impact than XRD and disorder induced by ion irradiation reflects in the optical absorption.
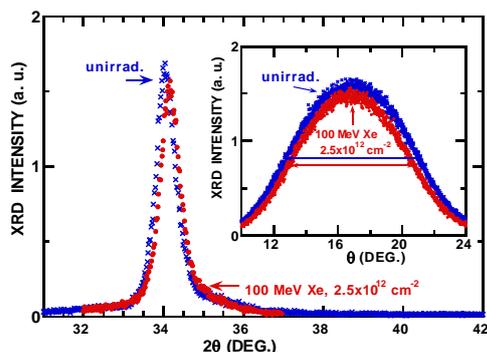
Fig. 1 XRD patterns and rocking curves (inset) before and after 100 MeV Xe^{+11} ion impact at 2.5×10^{12} cm^{-2}. The peak at ~34 ° corresponds to ZnO (002) diffraction peak (i.e., c-axis orientation), ~31 ° and 32.6 ° (In_2O_3), and 33 ° (In) were not observed. In the inset, horizontal lines indicate the full-width at half-maximum (8.45 and 7.83 ° before and after the ion impact).
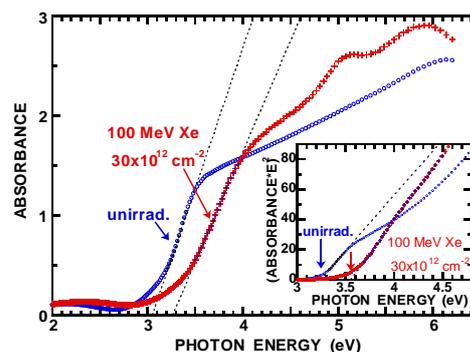
Fig. 2 Optical absorption spectra of unirradiated IZO film and the film irradiated with 100 MeV Xe^{+11} at 3×10^{13} cm^{-2}. Dotted lines indicate the absorption-edge slope. The inset shows the square of absorbance times photon energy (E) vs E, illustrating the band gap (E_g) indicated by vertical lines (E_g =3.239 and 3.546 eV before and after the ion impact).

References

[1] T. Minami et al., Jpn. J. Apl. Phys., 24 (1985) L781.
[2] S. J. Pearton et al., Prog. Mater. Sci., 50 (2005) 293.
[3] O. Fukuoka etal., Nucl. Instrum. Methods Phys. Res., B250 (2006) 295.
[4] N. Matsunami et al., Nucl. Instrum. Methods Phys. Res., B, 2010, in print.
[5] J.F. Ziegler, J.P. Biersack and U. Littmark, "The Stopping and Range of Ions in Solids", Pergamon Press, New York (1985).
[6] N. Matsunami et al., Nucl. Instrum. Methods Phys. Res., B245 (2006) 231.
[8] N. Matsunami et al., Nucl. Instrum. Methods Phys. Res., B257 (2007) 433.

6.6 Electrical property modifications of In-doped ZnO films by high-energy ion impact

N. Matsunami[1], M. Sataka[2], S. Okayasu[2] and H. Sugai[2]

We have studied electrical property modifications of Al-doped ZnO (AZO) films, known as n-type transparent semiconductors [1], under high-energy ion impact and found drastic increase in the electrical conductivity [2]. The conductivity increase is ascribed to the carrier density increase due to replacement of Zn on the lattice site by Al on site other than lattice site (called ion-induced dopant-replacement). It is of interest whether ion-induced dopant-replacement takes place for trivalent element other than Al or not. In this study, we have investigated electrical property modifications of In-doped ZnO (IZO) by high- and low-energy ion impact [3] to compare with those of AZO and of IZO by low-energy ion impact.

Preparation of IZO films on SiO_2-glass substrates, characterization of the films and modifications of atomic-structure and optical-property by high-energy ions are described [3] (Tandem Report 2009, 7.2). The composition of the unirradiated film is very close to stoichiometric within RBS accuracy of 10%, and In/Zn≈6%. The films were irradiated with 100 MeV $^{136}Xe^{+11}$ and 100 keV Ne^+ ions at room temperature. It is found that the composition remains unchanged under the ion impact. DC resistivity was measured with four-terminal method in situ in the irradiation chamber and Hall-effect was measured after take the sample outside from the chamber.

The electrical conductivity of unirradiated IZO films appears to scatter by two orders of magnitude (0.1 to 10 Scm^{-1}) depending on samples (Fig. 1). The possibilities for the scatter are: Firstly, a small but certain fraction of In has already occupied Zn site and secondary, impurities especially hydrogen exist in the films and their content varies with sample. In spite of large scatter of the initial conductivity, the very similar maximum conductivity of 400 and 200 Scm^{-1}, comparable with the conductivity in [1], has been reached after impact of 100 MeV Xe^{+11} and 100 keV Ne^+ ions, respectively (Fig. 1 and Table 1). Here, the thickness of two films used for 100 keV Ne^+ impact is ~0.18 μm (larger than the projected range of 0.12 μm [4]) and the effective depth is taken to be the projected range for evaluating the conductivity and carrier density. The main source of the conductivity increase (three to four orders of magnitudes) is the increase of the carrier density by ~$4x10^4$ from ~10^{17} to 10^{21} cm^{-3} (Fig. 2 and Table 1), which is ascribed to In-dopant replacement induced by ion impact. No simple relation is found between the conductivity and optical property modifications. The beam current density is ~3 nA cm^{-2} and 1-3 μAcm^{-2} for 100 MeV Xe and 100 keV Ne ions. The temperature rise during the ion impact is estimated to be ~40 °C [5], which is insignificant. It appears that temperature (T) dependence of the conductivity from 180 to 300 K is proportional to $exp(-E_a/kT)$, i.e., semiconductor behavior for IZO both unirradiated and irradiated with 100 keV Ne at $1x10^{17}$ cm^{-2}. The activation energy (E_a) is obtained to be 0.09 and 0.024 eV, respectively. Here k is the Boltzmann constant. T-dependence of the conductivity is under way for the films irradiated with 100 MeV Xe ions.

Displacement per atom (dpa) due to the elastic collisions is estimated to be 13 for 100 keV Ne at $5x10^{16}$ cm^{-2} (Table 1) [6]. From similarity of the conductivity enhancement in IZO and AZO by 100 MeV Xe ion, it appears that the electronic excitation plays dominant role in high-energy ion impact. The electronic sputtering yield of ZnO by 100 MeV Xe is estimated to be 8.0 [7]. The equivalent dpa, proportional to the ratio of the electronic over elastic sputtering yields, is obtained to be 0.8 for 100 MeV Xe at $3.8x10^{14}$ cm^{-2}. Thus, the efficiency of dopant-replacement by electronic excitation is higher than the elastic collisions. In view of ionic radius, dopant-replacement looks easy, though the ion-induced mechanism has not been established yet. Here, ionic radius in 4 coordinates of Zn^{2+}, In^{3+} and Al^{3+} is 0.074, 0.076 and 0.053 nm [8].

_____

[1] Division of Energy Science, EcoTopia Science Institute, Nagoya University
[2] Japan Atomic Energy Agency (JAEA)
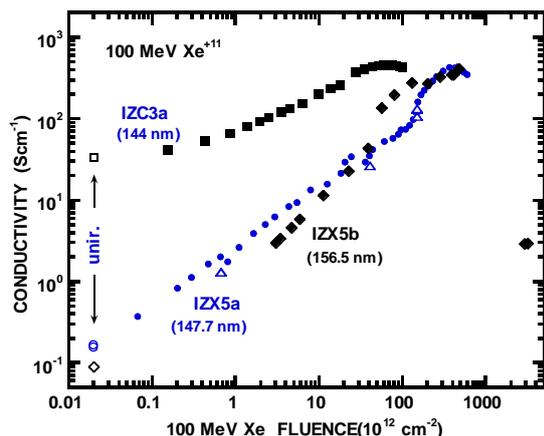
Fig. 1 Conductivity of IZO films vs 100 MeV Xe^{+11} ion fluence for three samples with thickness given in the parenthesis. Open symbols ($\bigcirc$, $\diamondsuit$, $\square$) indicate the conductivity of unirradiated films. Open triangles ($\triangle$) mean conductivity decrease during the ion beam break for Hall measurements in air (sample-IZX5a).
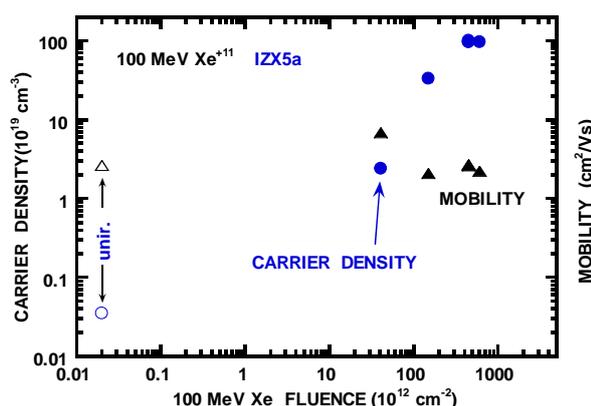
Fig. 2 Carrier density ($\bullet$) and mobility ($\blacktriangle$) of IZO films vs 100 MeV Xe^{+11} ion fluence. Open symbols ($\bigcirc$, $\triangle$) indicate carrier density and mobility of unirradiated film.

Table 1 Projected range (R_p), electronic (S_e) and nuclear (S_n) stopping powers (keV/nm) near surface of ZnO for 100 MeV $^{136}Xe^{+11}$ and 100 keV Ne^+ ion irradiation, $S_{nd}= S_n$-ionization by recoils, maximum conductivity (σ), fluence (F) at which σ takes its maximum, carrier density (N) and mobility (μ). Values in parentheses in the 2nd row are S_e, S_n and S_{nd} averaged over R_p for 100 keV Ne^+. dpa for 100 keV Ne and equivalent dpa for 100 MeV Xe are also given (see text). The values in bracket below N are the enhancement factor of N by ion irradiation. R_p, S_e, S_n and S_{nd} were calculated using TRIM97 [4].

Ion	R_p (μm)	S_e	S_n (keV/nm)	S_{nd}	dpa	σ (Scm^{-1})	F (cm^{-2})	N (cm^{-3})	μ (cm^2/Vs)
100 MeV Xe	9.4	21.1	0.195			0.8	423	3.8×10^{14}	9.6×10^{20} [3.3 $\times 10^4$]	2.7
100 keV Ne	0.12	0.265 (0.253)	0.242 (0.368)	0.212 (0.247)	13	200	5×10^{16}	3.5×10^{21} [5 $\times 10^4$]	0.32

References
[1] T. Minami et al., Jpn. J. Appl. Phys.. 24 (1985) L781.
[2] H. Sugai et al., Nucl. Instrum. Methods Phys. Res., B250 (2006) 291.
[3] N. Matsunami et al., Nucl. Instrum. Methods Phys. Res., B, 2010, in print.
[4] J.F. Ziegler, J.P. Biersack and U. Littmark, "The Stopping and Range of Ions in Solids", Pergamon Press, New York (1985).
[5] N. Matsunami, T. Yajima, H. Iwahara, Nucl. Instrum. Methods. Phys. Res.,B65(1992)278.
[6] N. Matsunami et al., Surf. Coatings Technol., 196(2005)50.
[7] N. Matsunami et al., Nucl. Instrum. Methods Phys. Res., B209(2003)288.
[8] M. W. Barsoum, "Fundamentals of Ceramics", McGraw-Hill, 1997.

CHAPTER 7

Radiation Effects in Materials

This is a blank page.

7.1   Ion charge dependence on diameter of ion tracks in UO_2

T. Sonoda[1], T. Sawabe[1], N. Ishikawa[2] and M. Sataka[2]

In order to understand the formation and growth mechanism of a crystallographic exchange in high burnup fuels such as "rim structure [1]", clarification of radiation effects under nuclear fissions such as the electronic excitation effects, accumulation of radiation damage and fission products (FPs) should be needed. In this study, high density electronic excitation effects on the accumulation process of radiation damages in LWR fuels [2-4] have been clarified. The diameter of ion tracks of high energy ion irradiation to the thin foil samples was investigated. In previous study, though, the charge of irradiated ion may not be equilibrium charge in materials. Therefore, in order to understand the "real" diameter of ion tracks in UO_2 under nuclear fission, the effect of ion charge on the diameter of ion tracks should be clarified. In this study, several charge and energy ions such as 100 MeV Xe^{25+}, 100 MeV Zr^{10+}, 210 MeV Xe^{16+}, 210 MeV Xe^{29+}, 150 MeV Xe^{27+}, 150 MeV Au^{27+}, 310 MeV Au^{27+} are irradiated to the non-irradiated thin UO_2 samples that are fabricated by FIB (Focused Ion Beam) method. Microstructure evolutions in the irradiated samples are observed in a FE-SEM (JSM-6340F) and a FE-TEM (HF-3000) at CRIEPI. This work was partly supported by MEXT KAKENHI (21360474).

Figure 1 (a) to (g) indicate the typical bright field images of ion tracks in UO_2 irradiated with (a) 100 MeV Xe^{25+}, (b) 100 MeV Zr^{10+}, (c) 210 MeV Xe^{16+}, (d) 210 MeV Xe^{29+}, (e) 150 MeV Xe^{27+}, (f) 150 MeV Au^{27+}, and (g) 310 MeV Au^{27+}ions at room temperature. The elliptical circle images in these pictures correspond to the cross-section images of ion tracks, and the diameter is defined as the length of minor axis of the circles. The mean diameter of ion tracks is (a) 2.0 $\pm$0.1 nm, (b) 1.8 $\pm$0.1 nm, (c) 4.9 $\pm$0.1 nm, (d) 4.4 $\pm$0.1 nm, (e) 3.7 $\pm$0.1 nm, (f) 3.6 $\pm$0.1 nm, and (g) 5.0 $\pm$0.1 nm, respectively.

Figure 2 indicates the mean diameter of ion tracks in UO_2 and CeO_2 [4] as a function of irradiation energy. The diameter of ion tracks in UO_2 become bigger as increasing irradiation energy, and the size tends to saturate over 210 MeV. The tendency of the curve is similar of that of CeO_2, though, the diameter of ion tracks in UO_2 is much smaller than that of CeO_2. These results indicate that the sensitivity of high density electronic excitation of UO_2 is much less than that of CeO_2. Moreover, the comparison between (c) and (d) indicates that the diameter of ion tracks is almost same in case of different ion charge. This result suggests that the differences of ion charges are not so effective on the diameter of ion tracks. Figure 3 shows the square of mean diameter of ion tracks in UO_2 and CeO_2 [4] as a function of electronic stopping power (S_e). This figure indicates that the gradient of the square of diameter from 100 MeV Xe to 210 MeV Xe is tend to be same and it suggests that the square of diameter of ion tracks tend to be proportional to electronic stopping power (S_e). In order to understand the relationship among S_e, diameter of tracks and irradiation conditions, additional ion irradiation examination should be needed.

---

[1] Central Research Institute of Electric Power Industry (CRIEPI)
[2] Japan Atomic Energy Agency (JAEA)
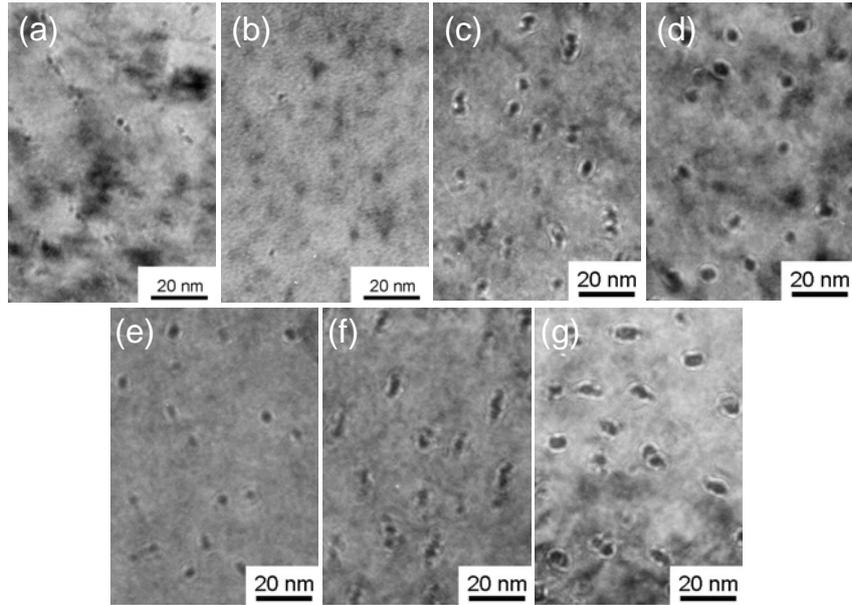
Fig. 1 TEM image of UO$_2$ irradiated with (a) 100 MeV Xe^{+25}, (b) 100 MeV Zr^{+10}, (c) 210 MeV Xe^{+16}, (d) 210 MeV Xe^{+29}, (e) 150 MeV Xe^{+27}, (f) 150 MeV Au^{+27}, and (g) 310 MeV Au^{27+}ions to a fluence of 5 x 10^{11} ions/cm^2 at room temperature.
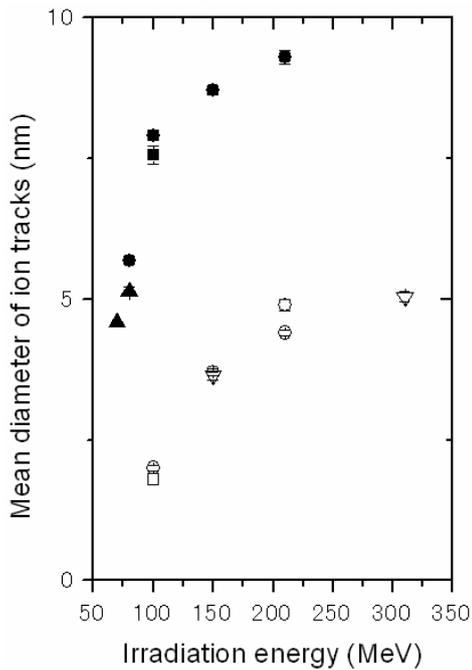
Fig. 2 Mean diameter of ion tracks in UO$_2$ and CeO$_2$ at room temperature as a function of irradiation energy (MeV).
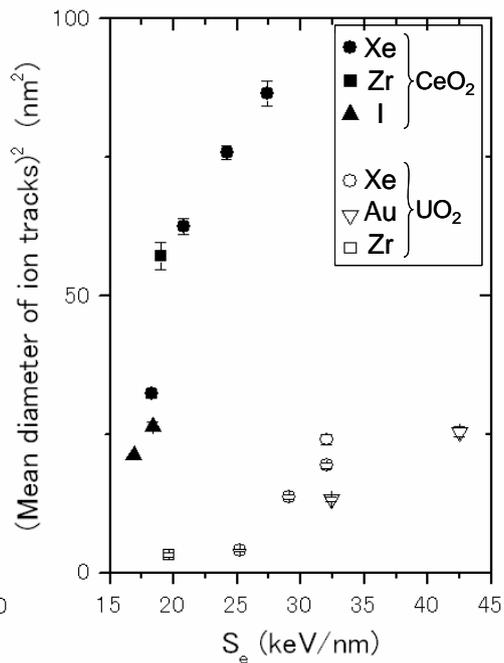
Fig. 3 The square of the mean diameter of ion tracks in UO$_2$ and CeO$_2$ at room temperature as a function of electronic stopping power (S$_e$).

References

[1] J.O. Barner et al., HBEP-61, 1990, Battelle Pacific Northwest Laboratories.

[2] T. Sonoda et al., Nucl. Instrum. Methods Phys. Res., B191 (2002) 622-628.

[3] T. Sonoda et al., Nucl. Instrum. Methods Phys. Res., B250 (2006) 254-258.

[4] T. Sonoda et al., Nucl. Instrum. Methods Phys. Res., B266 (2008) 2882-2886.

7.2   Microstructure observations and distribution of chemical compositions of metal precipitates in Zircaloy-2 irradiated with 210 MeV Xe ions

T. Sonoda[1], T. Sawabe[1], N. Ishikawa[2] and M. Sataka[2]

In order to progress high burnup extension of light water reactor (LWR) fuels, the improvement of anti-corrosion and hydrogen resistance of nuclear fuel claddings (Zirconium alloy; Zircaloy-2 for boiling water reactor) is indispensable. In previous researches, it becomes clear that the degradation of anti-corrosion and hydrogen resistance is concerned with the composition and size of metal precipitates in zirconium alloy, and the precipitates are deformed under irradiation with high energy neutron in a reactor [1]. In order to clarify the mechanism of corrosion and hydrogen pickup in Zircaloy and the correlation between the degradation of fuel cladding and the deformation of metal precipitates in claddings, microstructure observations and ion irradiation examinations have been done. Especially, there are no information about the deformation of metal precipitates in cladding materials under high energy ion irradiation condition such as the bonding layer of cladding inner surface and fuel pellet. In this report, microstructure and atom distribution of alloy elements and impurity (Fe, Ni, Cr, and Si) in Zircaloy-2 under irradiation with 210 MeV Xe ions at room temperature have been clarified by means of a transmission electron microscope (JEM-2100 with EDS system) at CRIEPI. Ion irradiation examinations have been done at JAEA-Tandem accelerator facility.

Figure 1 (a) to (c) indicates the typical microstructure of Zircaloy-2 irradiated with 210 MeV Xe ions to a fluence of 5 x 10^{15} ions/cm^2 at room temperature, and (a)' to (c)' indicates the EDS spectrum at the position of "002", "020" and "013" in (a) to (c), respectively. The black circle contrasts correspond with the metal precipitates in Zircaloy-2, and (a)' to (c)' shows that the precipitate in (a) and (b) is a metal precipitate of (Fe, Cr) base and (c) is of (Fe, Ni) base. The depth position of (a) from the irradiation surface is over 5 μm, and (b) and (c) is less than 2 μm, respectively. The size of precipitates are almost same as that of non-irradiation sample whose size is around 50 – 300 nm. Table 1 indicates the Fe, Ni and Cr atom concentration (at%) and the ratio of Fe/Cr and Fe/Ni of metal precipitate in (a) to (c). In case of (a) that the metal precipitate of (Fe, Cr) base at the deeper position from irradiation surface, the ratio of Fe/Cr is 0.85 and the ratio is not so changed. Though, in case of the metal precipitate of (Fe, Cr) base at shallow position from the surface as shown in (b) , the ratio of Fe/Cr is 0.49 and it becomes clear that Fe atom tend to dissolve from precipitate to the matrix priory. In case of precipitate of (Fe, Ni) base at shallow position from the surface as shown (c), the ratio of Fe/Ni is around 1.25 and the concentration of Fe and Ni is around 14.4 and 11.5 at%, respectively. The ratio and the concentration of Fe and Ni are almost same as non-irradiated materials. These results suggest that the irradiation accelerate the dissolution of Fe ions in matrix priory in case of (Fe, Cr) base precipitates, and not accelerate the dissolution of Fe ions in case of (Fe, Ni) base precipitates. These tendencies of Fe ion are almost same as that of high burnup fuel cladding [1]. In order to clarify the irradiation effects, such as electronic excitation, on the degradation of metal

---

[1] Central Research Institute of Electric Power Industry (CRIEPI)
[2] Japan Atomic Energy Agency (JAEA)

precipitates, further irradiation examination will be treated in near future.
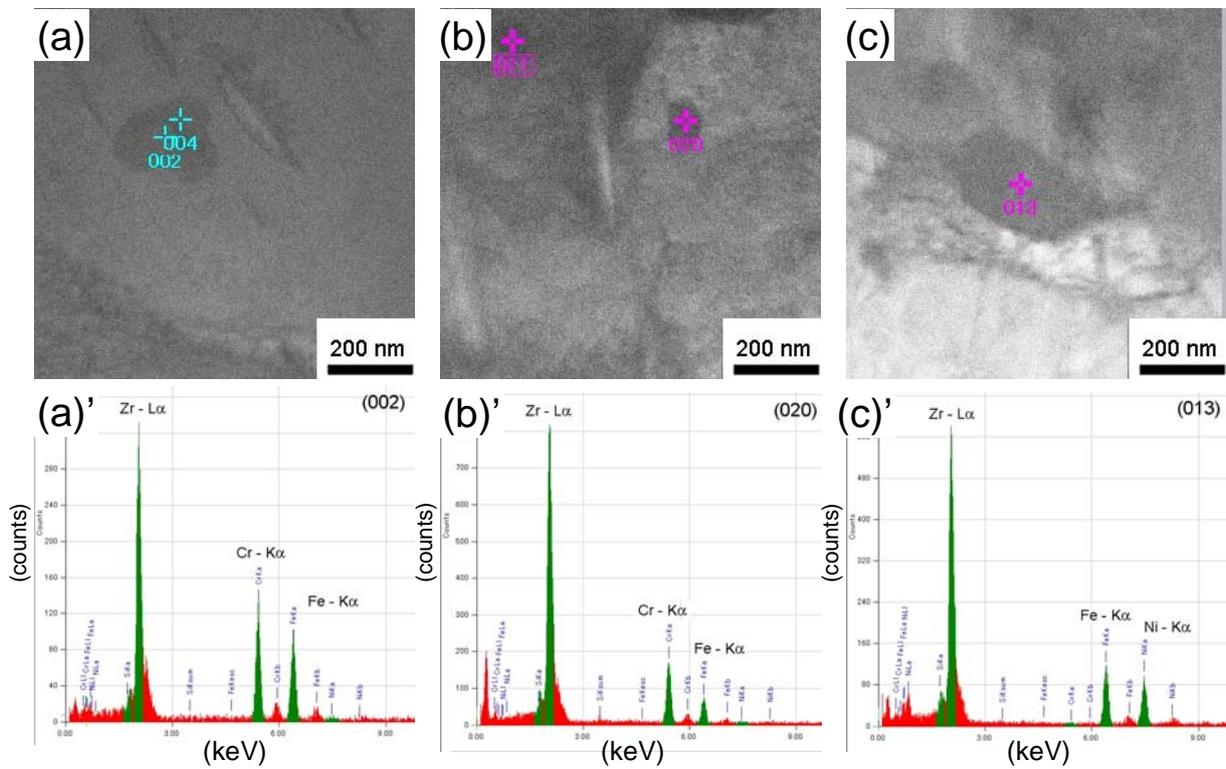
Fig.1 Typical microstructure of Zircaloy-2 irradiated with 210 MeV Xe ions to a fluence of 5 x 10^{15} ions/cm^2 at room temperature, and (a)' to (c)' indicates the EDS spectrum at the position of "002", "020" and "013" in (a) to (c), respectively. The precipitate of (a) and (b) is the metal precipitates of (Fe, Cr) base and (c) is the precipitate of (Fe, Ni) base.

Table 1. Fe, Ni and Cr atom concentration (at%) and the ratio of Fe/Cr and Fe/Ni of metal precipitate in (a) (b) and (c).

position	Fe (at%)	Cr (at%)	Ni (at%)	Zr	Fe/Cr	Fe/Ni	Type
002	17.09	20.06	0	balance	0.85	--	Zr(Fe, Cr)$_2$
020	6.9	14.08	0	balance	0.49	--	Zr(Fe, Cr)$_2$
013	14.38	0.21	11.49	balance	--	1.25	Zr$_2$(Fe, Ni)

References

[1] Y. Etoh, et al., J. Nucl. Mater., 200 (1993) 59.

7.3 Electrical conductivity change in CeO_2 irradiated with high-energy heavy ions

N. Ishikawa[1] and K. Takegahara[1,2]

Radiation damage in nuclear fuel can be classified into various types in term of its defect structure, such as 1) point-like defects created by relatively low energy particle irradiation, 2) continuous damage region (ion-track) created by high energy particle irradiation, and 3) strain fields created by accumulation of fission gas.   In this study, in order to simulate the second process, i.e. radiation damage process by high energy fission fragments in nuclear fuel, oxide ceramic material (CeO_2) with same fluorite crystallographic structure as UO_2 is irradiated with high energy particles using tandem accelerator at JAEA-Tokai. The characterization of radiation damage is done by in-situ electrical resistivity measurement.

Thin films of CeO_2 were prepared on single crystal sapphire substrates by sputtering methods. The film thickness was about 300 nm. The films were irradiated at room temperature with 120MeV Xe from the tandem accelerator at JAEA-Tokai. The objective of the irradiation with 120MeV Xe ions is to simulate radiation damage behavior due to high energy fission fragments. Current is measured in-situ when voltage is applied in the range from -100V to 100V. The current-voltage relation is measured by two-probe method using Keithley 6517 (Electrometer/High Resistance System). The electrodes are prepared by depositing gold on the sample using sputtering technique. Before irradiation the electrical conductivity was around 10^{-6} ohm$^{-1} \cdot$ m^{-1}.

Figure 1 shows the current-voltage relation of CeO_2 before and after the irradiations. It is found that the current-voltage relation is linear both for unirradiated and irradiated samples, indicating that electrical conductivity can be defined as constant value irrespective of the applied voltage value.   Another important result from this figure is that the slope of the I-V curve increases monotonically as a function of fluence, indicating that the electrical conductivity increases as fluence increases.   In Fig.2 we find that the electrical conductivity increases three orders of magnitude at high fluence of 10^{13} ions/cm^2. In the fluence range from 10^{12} ions/cm^2 to 10^{12} ions/cm^2, where the occupancy of ion-tracks in the sample is expected to vary from 30% to 98% if track diameter of 7nm is assumed [1], prominent electrical conductivity increase is observed.   On the other hand, in the high fluence range of around 10^{14} ions/cm^2 where multiple overlapping of ion-tracks is dominant, increase in electrical conductivity tends to saturates, suggesting that the multiple overlapping of ion-tracks does not efficiently lead to increase in electrical conductivity.

References

[1] T. Sonoda et al., Nucl. Instrum. Methods Phys. Res., B250 (2006) 254.

---

[1] Japan Atomic Energy Agency (JAEA)
[2] Ibaraki University
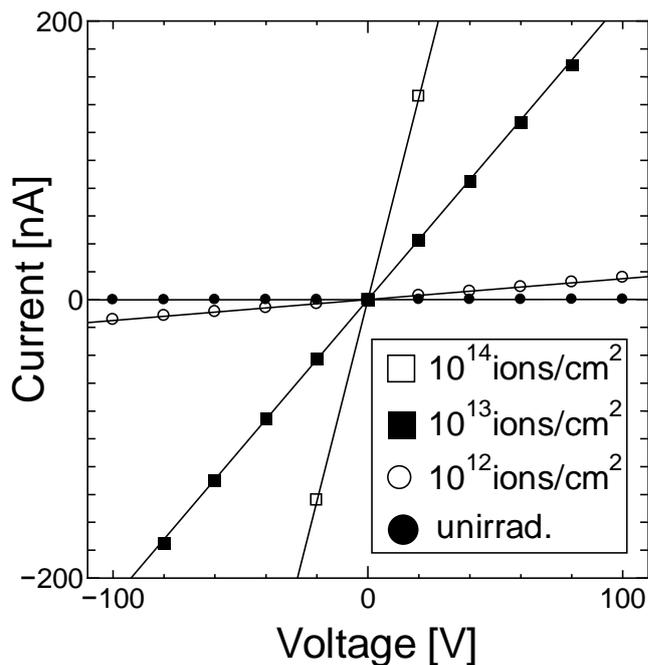
Fig. 1 Current-Voltage characteristics observed for a CeO$_2$ thin film before and after the irradiation with 120MeV Xe ions. The solid lines are the results of linear fitting of the data in the voltage range from -100V to 100V.
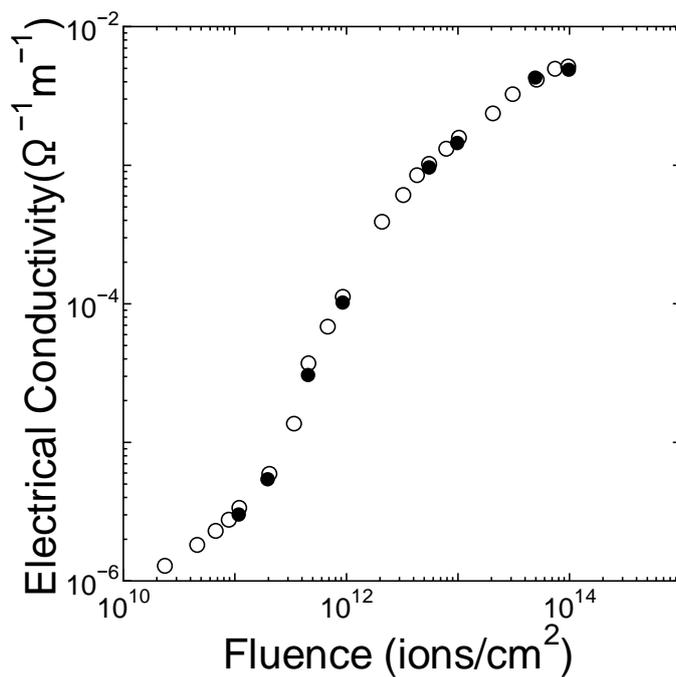
Fig. 2 Fluence dependence of electrical conductivity for a CeO$_2$ thin film irradiated with 120MeV Xe ions. The solid circles are the values measured based on linear fitting of current-voltage relations. The open circles are the values measured based on the current value at applied voltage of 100V.

7.4 Effects of energetic heavy ion irradiation on the crystal structure in Gd_2O_3-doped CeO_2

Y.Tahara[1], B.Zhu[1], S.Kosugi[1], N.Ishikawa[2], Y.Okamoto[2],

Y. Baba[2], N. Hirao[2], F. Hori[1], T.Matsui[1] and A.Iwase[1]

In present light-water nuclear power plants, it is useful to dope some elements called burnable poisons, which have a high neutron absorption cross section, into enriched fission fuels (UO_2) in order to control the initial reactivity of UO_2 fuels. Actually, gadolinium trioxide (Gd_2O_3) has already been doped into UO_2 as a burnable poison. During the operation of light-water power reactors, UO_2 fuels are exposed to irradiation with high energy fission products which have energies around 100MeV. Therefore, it is important to study the effects of high energy fission products on UO_2 fuels doped with Gd_2O_3.

For previous studies in irradiation effects on nuclear fuels[1,2], cerium dioxide (CeO_2) has been used so far as a simulation material for UO_2 because it has the same fluorite structure as that of UO_2 and has the similar properties such as lattice constant and thermal conductivity to those of UO_2. In this study, therefore, CeO_2 pellets doped with Gd_2O_3 were irradiated with 200MeV Xe^{14+} ions using a tandem accelerator at JAEA-Tokai to simulate the irradiation effects of high energy fission products on UO_2 doped with Gd_2O_3. The X-ray diffraction (XRD) method and the extended X-ray absorption fine structure (EXAFS) measurement were used to estimate the effects of the Gd-doping and the irradiation.

Figure.1 shows the change in XRD spectra around (331) peaks of pure and 10mol% Gd_2O_3 doped CeO_2 for various ion-fluences. The peak is sifted to higher angle for unirradiated samples by Gd_2O_3 doping, which means that the lattice constant decreases by doping. On the other hand, the peaks are sifted to lower angle by the irradiation, which means that the lattice constant increases by the irradiation and it increases with increasing the ion ion-fluences. The figure shows that the effect of the irradiation on lattice constant becomes more remarkable by Gd_2O_3 doping.

Figure.2 shows the change in the Fourier transformations of Gd L3-edge EXAFS spectra by doping and irradiation. When paying attention to the effects of Gd-doping, the intensity of the first and second neighboring peaks decrease with increasing the amount of Gd-doping. It means that the structure around Gd atoms is disordered locally by Gd_2O_3 doping. In addition, as can be seen in Fig.3, the intensity of the peaks decreases also by the irradiation. It is found that the irradiation induces a local disordering around Gd atoms. Detailed analysis for EXAFS FT spectra is now in progress.

[1] Osaka Prefecture University

[2] Japan Atomic Energy Agency (JAEA)
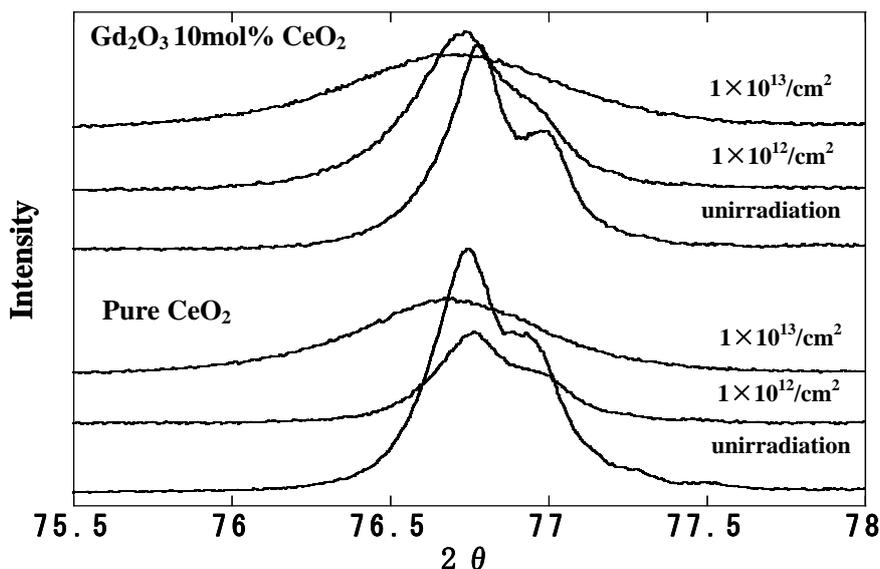
Fig. 1   XRD spectra around (331) of undoped CeO_2 and those doped with 10mol% Gd_2O_3 for various ion-fluences.
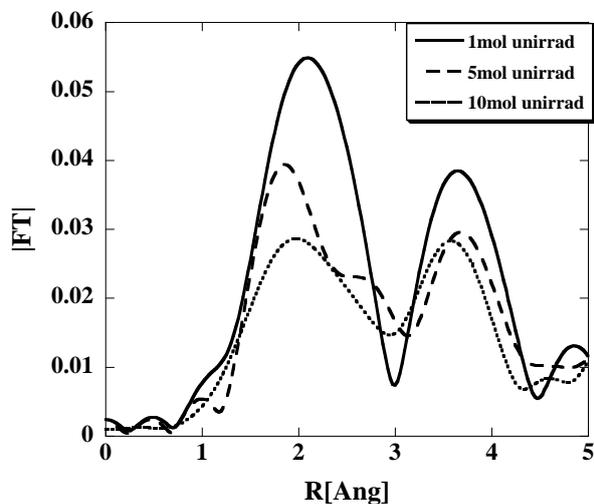
Fig. 2 Dependence of FT spectrum on the amount of Gd_2O_3 for unirradiated specimens.
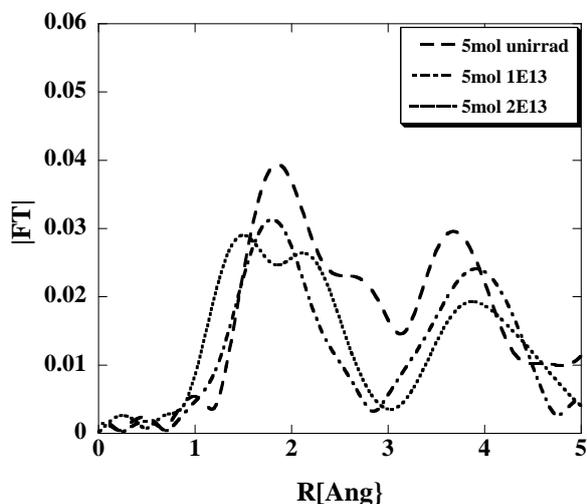
Fig. 3 Dependence of FT spectrum on ion-fluence for CeO_2 doped with 5 mol% Gd_2O_3.

References

[1] M. Kinoshita et al., Nucl. Instrum. Methods , Phys. Res. B267 (2009) 960.

[2] H.Ohno et al., Nucl. Instrum. Methods Phys. Res., B266 (2008) 30.

7.5   Effect of high temperature annealing on ferromagnetism induced by swift heavy ion irradiation in FeRh alloy

S. Kosugi[1], N. Fujita[1], N. Ishikawa[2], F. Hori[1], T. Matsui[1] and A. Iwase[1]

In the previous studies, we have found that energetic ion irradiation induces a ferromagnetic state in Fe-Rh alloys at low temperatures and this phenomenon is dominated by the energy deposition through elastic collisions [1, 2]. As the effect remains unchanged at room temperature for a long time, the disordering of atomic arrangements or lattice defects induced by the irradiation causes the ferromagnetism at low temperatures. In this report, we discuss the relationship between the irradiation-induced ferromagnetism in Fe-50at.%Rh alloy and the thermal stability of atomic disordering or lattice defects.

Specimens of Fe-50at.%Rh with the dimension of 5x5x0.2 mm^3 were irradiated at room temperature with 200MeV Au ions by using a tandem accelerator at JAEA-Tokai. After the irradiations, the samples were isochronally annealed up to 773K. Isochronal anneals were for 60 minute periods at temperature interval of 100K. Effects of thermal annealing on magnetization were measured by using the superconducting quantum interference device (SQUID). The scanning range of the applied magnetic field was from -6000 to 6000Oe and the measurement temperature was 20K.

Figures.1 and 2 shows the magnetic moment-magnetic filed curves for FeRh specimens annealed with 200 MeV Au ions irradiation. For the ion-fluence of 1x10^{13}/cm^2, the value of the saturated magnetization, <Ms>, continues to decrease until 773K. For the ion-fluence of 5x10^{13}/cm^2, the value of <Ms>, shows the maximum after the annealing at 573K and the value of <Ms> decreases rapidly with increasing annealing temperature. In Fig.3, the values of <Ms> are plotted against the annealing temperature. The values of <Ms> can be well correlated with the annealing temperature. The present result indicates that the irradiation-induced ferromagnetism of FeRh alloy is strongly related to the thermal stability of irradiation-introduced lattice defects.
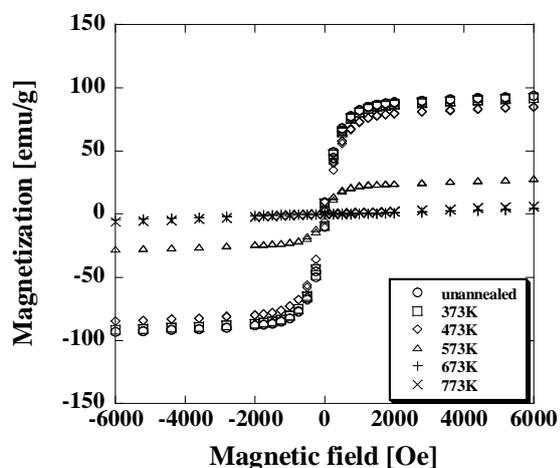
Fig. 1 Irradiation induced magnetic moment at 20K as a function of applied magnetic field for Fe-50at.%Rh irradiated with 200MeV Au to the ion-fluence of 1x10^{13}/cm^2.

[1] Osaka Prefecture University
[2] Japan Atomic Energy Agency (JAEA)
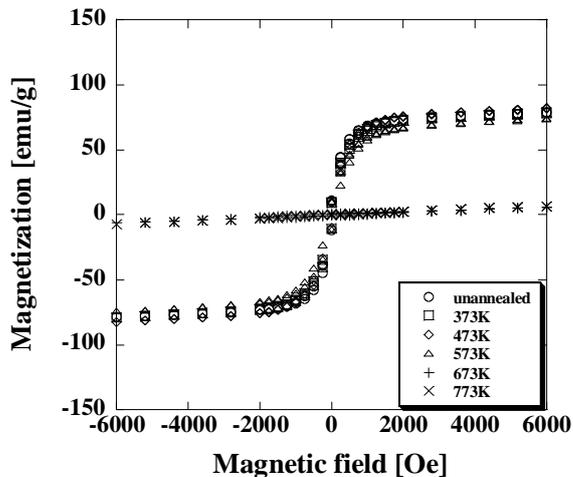
Fig. 2 Irradiation induced magnetic moment at 20K as a function of applied magnetic field for Fe-50at.%Rh irradiated with 200MeV Au to the ion-fluence of 5×10^{13}/cm^2.
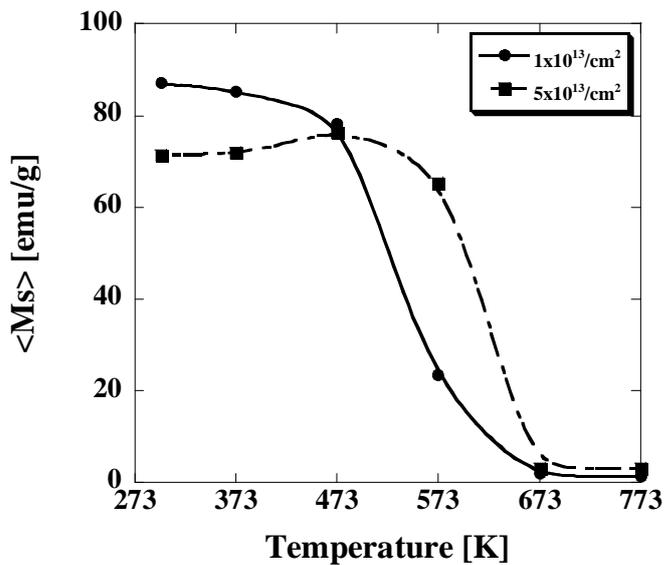
Fig. 3 Average values of saturation magnetization, <Ms>, for the region expect around the ion range, as a annealing temperaturte.

References

[1] S. Kosugi et al., Nucl. Instrum. Methods Phys. Res., B267 (2009) 1612-1615.

[2] A. Iwase et al., Nucl. Instrum. Methods Phys. Res., B256 (2007) 429-433.

7.6　Shape and property control of Zn and ZnO nanoparticles by swift heavy ions

H. Amekura[1], N. Ishikawa[2], K. Mitsuishi[1], Y. Nakayama[1] and N. Kishimoto[1]

When metal nanoparticles (NPs) embedded in silica glass (SiO_2) are irradiated by swift heavy ions (SHI), elongation of the NPs, i.e., the transformation from spheres to rods along the ion beam direction, is induced [1-4]. Contrary non-metal NPs of Ge show deformation perpendicular to the ion beam direction, i.e., the deformation to disk-shape [5]. Although the mechanism of the elongation of metal NPs is still under hot debate, a practically-assumed criterion is whether the NPs melt by thermal spike effect or not [3,4]. If the criterion is true, large elongation is expected for NPs with low melting point, e.g., Zn, even though the NP size is relatively large. On the other hand, ZnO NPs are highly efficient luminescent material. Control of the luminescent properties with SHI irradiation via the shape deformation is also attractive, if it is possible. These demonstrations have been going on in this study.

Zn NPs were formed by implantation of Zn ions of 60 keV to silica glass up to a fluence of 1.0×10^{17} ions/cm^2. No post-implantation annealing was carried out. ZnO NPs were formed by thermal oxidation of the Zn NPs embedded in silica glass [7]. The samples were irradiated by the SHI of 200 MeV Xe^{14+} from the tandem accelerator at JAEA-Tokai, with an incident angle of 45 deg from the sample surface. The SHI fluence per unit area of the inclined sample surface (45 deg) was varied from 7.1×10^{10} to 3.5×10^{13} ions/cm^2.

Optical transmission spectroscopy with linearly-polarized light was conducted with an incident angle of surface normal in the wavelength region of 215 – 1700 nm at room temperature. The results are shown in Fig. 1, in the form of the optical density - $\log_{10} T$, where T denotes the transmittance. The polarization angle of 0 deg corresponds to the direction of the major axes of elongated NPs. In unirradiated state and at the fluence of 7.1×10^{10} ions/cm^2, both the polarizations (0 and 90 deg) give the identical spectrum, indicating that the NPs are in spherical forms. At the fluence of 7.1×10^{11} ions/cm^2, small but clear deviation is visible between the 0 and 90 deg polarizations. This is one of the evidence of the elongation of NPs. With increasing the SHI fluence, the spectrum of the 0 deg polarization shifts to the high energy side, while that of the 90 deg polarization shifts to the low energy side. These behaviors are ascribed to further elongation of the NPs. More clear evidence of the elongation of NPs was obtained by cross-sectional transmission electron microscopy (XTEM). Fig. 2 shows the XTEM images in (a) unirradiated state and (b) after the irradiation to 3.5×10^{13} ions/cm^2. While NPs are in the spherical shapes before the irradiation, NPs are elongated along the beam direction as shown in Fig. 2(b). It should be noted again that the samples were irradiated with an incident angle of 45 deg from the surface normal.

---

[1] National Institute for Materials Science (NIMS)
[2] Japan Atomic Energy Agency (JAEA)

Consequently, it was shown that the elongation of Zn NPs in SiO$_2$ is induced by SHI irradiation. Also the linearly-polarized optical spectroscopy was confirmed as a sensitive detection method for the elongation of metal NPs in SiO$_2$.
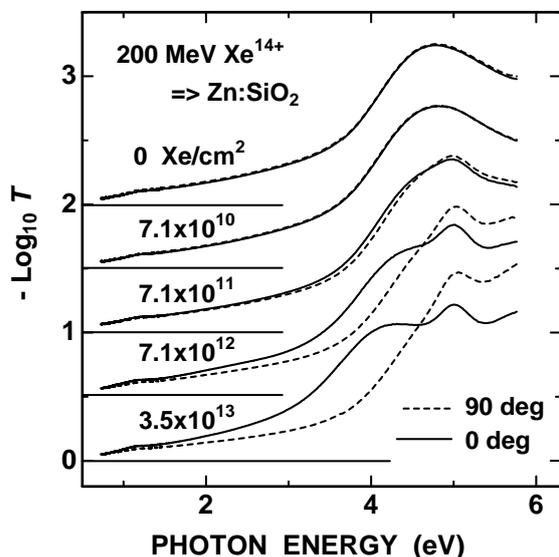
Fig. 1 Optical density spectra of Zn NPs in silica glass in unirradiated state and after irradiation of 200 MeV Xe^{14+} ions to four different fluences. Linearly polarized light with the polarization of 0 and 90 deg was used. The spectra are vertically shifted with each other for clarity and the horizontal lines indicate the base lines.
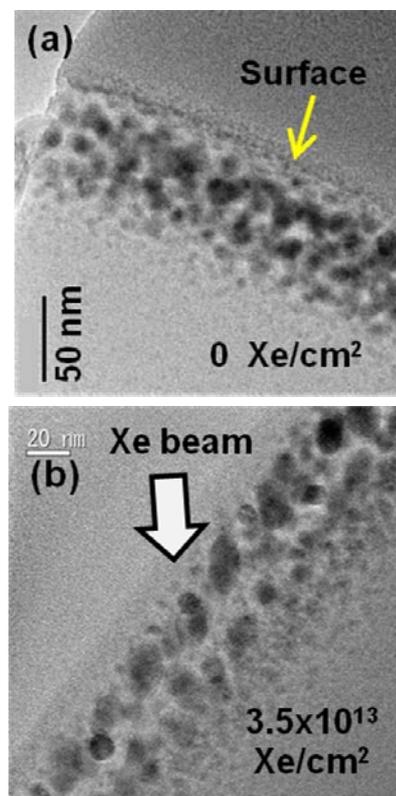
Fig. 2 Cross-sectional TEM images of Zn NPs in silica glass in (a) unirradiated state and after (b) irradiation of 200 MeV Xe$^+$ ions to a fluence of 3.5×10^{13} Xe/cm^2. As indicated by an arrow in (b), the sample was irradiated with an incident angle of 45 deg from the surface normal.

References

[1] C. D'Orleans et al., Phys. Rev., B67 (2003) 220101.

[2] A Oliver et al., Phys. Rev., B74 (2006) 245425.

[3] K. Awazu et al., Phys. Rev., B78 (2008) 054102.

[4] F. Singh et al., Nucl. Instrum. Methods Phys. Res., B267 (2009) 936-940.

[5] B. Schmidt et al., Nucl. Instrum. Methods Phys. Res., B257 (2007) 30-32.

[6] H. Amekura et al., Nanotechnology 18 (2007) 395707.

[7] H. Amekura and N. Kishimoto, Springer Lecture Notes in Nanoscale Science and Technology Vol. 5, Springer, Dordrecht, Heidelberg, London, New York (2009) 1-75.

7.7   Elongation of Au nanoparticle in SiO$_2$ matrix irradiated with swift heavy ions

M. Shirai[1], K. Yasuda[1], S. Matsumura[1] and N. Ishikawa[2]

Nanogranular thin films, in which nanometer-size particles are embedded in nonmagnetic or optical transparent matrix, attract a great attention as various functional new materials, such as for ultrahigh density magnetic recording media. We have investigated morphological change in nanoparticles induced by ion irradiation in order to control the size, shape and dispersion [1,2]. Ion irradiations of 2.4 MeV Cu and 210 MeV Xe ions were found to induce elongation of FePt nanoparticles in amorphous Al$_2$O$_3$ matrix along ion-beam directions. The present report deals with the morphological change in Au nanoparticles embedded in SiO$_2$ matrix induced by with 210 MeV Xe ions.

Nano-granular thin film with Au-nanoparticle in SiO$_2$ matrix was fabricated on Si wafer substrate by a series of chemical reactions with use of APTS (3-Amino-Propyl-Triethoxy-Silicate) solution, TEOS (Tetrasthoxy sililane) and Chloroauric acid (HAuCl$_4$). Prepared thin film specimens were finally annealed in air at 1173 K for 2 hours to homogenize and densify SiO$_2$ matrix. The detailed procedure of the specimen preparation has been reported elsewhere [3]. Figure 1(a) shows a cross sectional bright-field image of the fabricated thin film specimen, in which Au nanoparticles were embeded in amorphous SiO$_2$ matrix. The thickness of SiO$_2$ matrix was ranged from 100 to 300 nm depending on the position of the film. Gold nanoparticles were distributed rather homogeneously with diameter ranging from 5 to 60 nm as shown in Fig.1 (b). The shape of the Au nanoparticles was confirmed to be spherical before ion irradiation. These specimens were irradiated with 210 MeV Xe ions at ambient temperature at the Tandem Accelerator Facility of JAEA-Tokai to fluence ranging from 1.0×10^{17} to 1×10^{19} ions/m^2. The electronic stopping power of 210 MeV Xe ions in the film were evaluated to be 48 and 15 keV/nm for Au and SiO$_2$ phase, respectively, at the specimen surface. Morphological changes in the nanoparticles were examined by transmission electron microscopy with cross-section samples at High Voltage Electron Microscopy Laboratory, Kyushu University.

Figure 2(a) is an example of bright-field image of the thin film specimen irradiated with 210 MeV Xe ions to 1×10^{18} ions/m^2. It is seen that a part of Au nanoparticles is elongated along the ion beam direction. Size distribution of Au particles is shown in Fig.2 (b) as functions of the sizes perpendicular ($D_\perp$) and parallel ($D_{\parallel}$) to the ion beam direction. The Au particles are seen to elongate parallel to the ion beam direction especially for the larger particles. The elongation of Au particles was observed at fluence higher than 5×10^{17} ions/m^2, which suggests the existence critical fluence, or critical overlapping times for the observable elongation of Au particles. Another interesting point is that no significant morphological changes were observed for smaller particles less than 20 nm. This is consistent with previously reported results in Pt nanoparticles in SiO$_2$ matrix irradiated swift Au ions [4].

---

[1] Department of Applied Quantum Physics and Nuclear engineering, Kyushu University
[2] Tokai Research Center, Japan Atomic Energy Agency
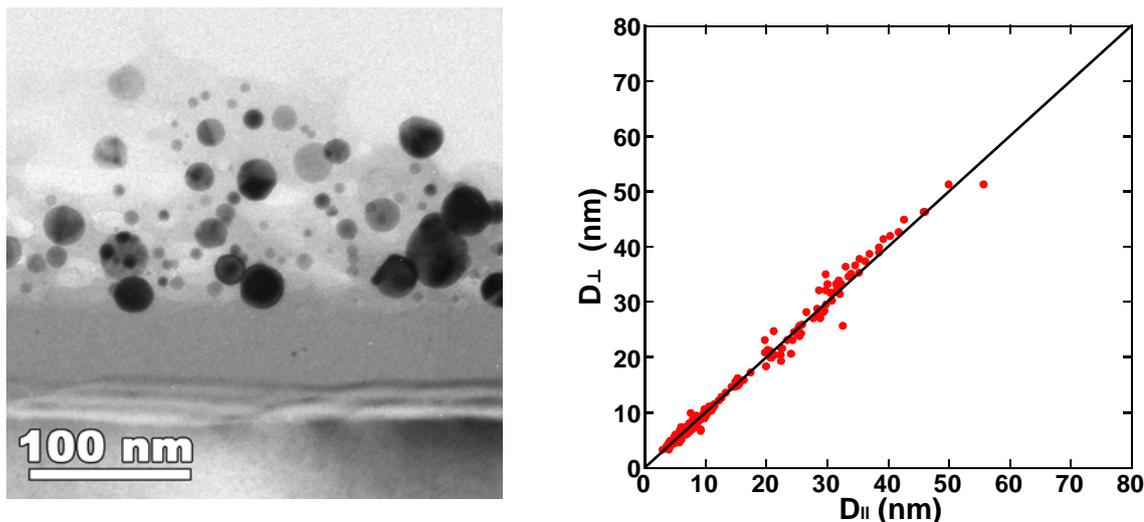
Fig. 1 Bright-field cross section view of thin film specimen before ion irradiation (a), illustrating Au nanoparticles in SiO_2 matrix. Size distribution of Au nanoparticles as functions of diameters measured parallel and perpendicular to the direction to film thickness (b).
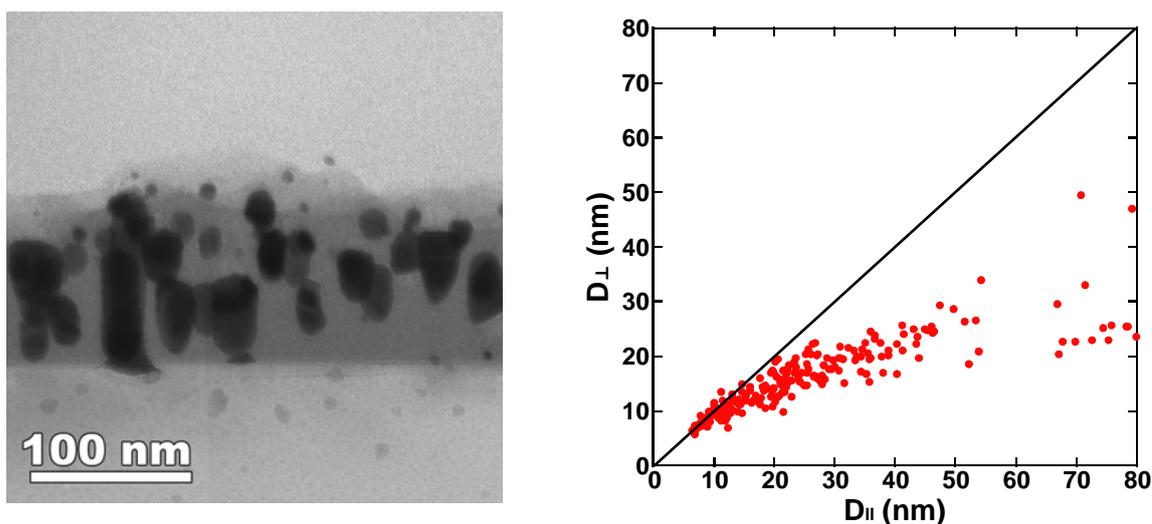
Fig. 2 Bright-field cross section view of the thin film specimen irradiated at ambient temperature with 210 MeV Xe ions to a fluence of 1×10^{18} ions/m^2 (a). The direction of ion irradiation was perpendicular to the film thickness direction. Size distribution of Au nanoparticles as functions of diameters measured parallel and perpendicular to the direction to film thickness or ion beam direction (b).

References

[1] M. Shirai et al., Mater. Trans., 47 (2006) 52

[2] M. Shirai et al., Nucl. Instrum. Methods Phys. Res., B267 (2009) 1787.

[3] M. Shirai, doctoral thesis, Kyushu University (2010) (in Japanese).

[4] M.C. Ridgway et al., Nucl. Instrum. Methods Phys. Res., B267 (2009) 931.

7.8 Radiation damage test for Virtex-5 FPGA

Y. Yamada[1], T. Tanaka[2], T. Inamori[2], H. Idobata[2], Y. Nagame[3], K. Tsukada[3], T. K. Sato[3], S. Mitsuoka[3] and K. Nishio[3]

We performed the radiation damage test for Virtex-5 FPGA (Field Programmable Gate Array), which we are planning to use our astrometric satellite named Nano-JASMINE (JASMINE is the abbreviation of Japan Astrometric Satellite Mission for Infrared Exploration) using the tandem accelerator at JAEA-Tokai. Nano-JASMINE will be launched at Aug. 2011 from Alcantara launch site by Cyclone 4 launch vehicle. The purpose of the test is to evaluate the error frequency in orbit radiation environment.   At satellite orbit, error occurs in electric devices operation due to the radiation [1].   There are two types of errors, single event effect and total dose effect.   This experiment is planned to evaluate the probability of single event effect.   We should take measures to deal with the error, for example, use expensive radiation hard devices, implements error correction software and etc.   We first measure the error frequency for considering the way we can do against the error.

For such tests, we expose high LET beam (30 MeV/micro g / cm^2) at radiation sensitive region of the device, and monitor error behavior.   Furthermore, the FPGA has circuit connection point at the surface. For expose the beam under operating the device, the beam should be exposed from the leer side of the device.   We shave the device until 100 micro m.   The beam is required to have 30 MeV/micro g / cm^2 after passing 100 micron Si layer.   For this, the beam energy behind the Si is larger than 80 MeV.   For this reason, we use 650, 622.8, 600, and 588.5 MeV Ni beam.   The beam is available by using the tandem accelerator and booster.

The fluence rate is 6.5 / sec in average.   If the fluence rate is large, the error occurs with higher frequency than we can count.   We cannot realize such low fluence in accelerator beam condition.   We use beam chopper.   The beam fluence at upstream is about 1.6 x 10^6 / sec and the beam can go to downstream in only 1 micro second in every 250 ms.

Evaluation of the on-orbit frequency of the error is ordinary performed in two steps.   First we get the relation between LET and the error frequency.   Second, multiplying LET distribution of on-orbit radiation environment and the frequency we get, and integrated it by LET.   For the first steps, the relation between LET and the probability of single event effect is well approximated by Weibull function [2],

$$F(x) = A\left(1 - \exp\left\{-\left[\frac{x - x_0}{W}\right]^s\right\}\right),$$

---

[1] Kyoto University
[2] University of Tokyo
[3] Japan Atomic Energy Agency (JAEA)

where x is LET, A, x_0, W, and S are unknown parameters.   For determining these parameters, we measure the error probabilities with several LETs.   The formula is applicable to the LET at the radiation sensitive region of the device.   The beam energy decreases after going through the Si layers.   We computed the beam energy by SRIM.

We can have the relation between injected ion LET and an error frequency.   By using this, we evaluated the error frequency in on-orbit environment to be 1 time / 10 days.   This value is acceptable for Nano-JASMINE satellite.

Now, the ultra-small satellite becomes exciting.   Traditionally, satellites were made by national space agencies using huge amount of money.   In such cases, very expensive – about a thousand times more expensive than the devices used on the ground – radiation-resistent devices are available.   But for small satellite, such expensive hardware could not available.   On the other hand, high performance of the present day electric devices can be reached by high density implementation of circuits.   Generally speaking, the frequency of error due to radiation becomes larger when the circuit density becomes high. The evaluation of Virtex-5's availability may be helpful for other satellite mission which needs high performance CPUs.

Table 1. Experimental results and estimated cross sections.

Energy	Errors	Exposure time	Incident particles	Error rate	Cross section
650 MeV	60	1788 s	12675	1/29.8	2.63×10^{-03} cm^2
622.8	80	2248	17010.5	1/29.9	2.56×10^{-03}
600	18	5257	29393	1/292	2.50×10^{-04}
588.5	3	3648	20936.5	1/1216	4.21×10^{-05}

References

[1] Holmes-Siedle, A. G., and Adams, Len, "Handbook of Radiation Effects", Oxford Science Publications (1993).

[2] E. Normand and T. J. Baker, IEEE Trans. Nucl. Sci., 40 (1993), 40.

7.9 Transport properties of (β-FeSi$_2$) thin films

S. Okayasu[1] and M. Sasase[2]

Iron disilicide (β-FeSi$_2$) is one of the candidates of compound semiconductor, which contains harmless elements to the human bodies, natural resources and the environment [1]. Another attractive feature of β-FeSi$_2$ is transformation to the metal phase α-FeSi$_2$ when heated above 1246 K. Since the bulk α-FeSi$_2$ has electric resistivity as low as 2.5 x 10^{-4} Ω cm, one may consider if a small part of β-FeSi$_2$ can be transformed into α-FeSi$_2$ selectively, it can be used as the electrode of a β-FeSi$_2$ based device.

When high-energy heavy ions are irradiated into materials, most of their energies are dissipated through an electronic excitation [2]. This leads to strong localization of the dissipated energy along the projectile path. The density of energy deposition is high enough, compared with bond or displacement energy of the target materials, so that nanostructural changes take place such as amorphization and phase transition etc. We attempted to perform phase transition from β-FeSi$_2$ into other phase by the high-energy heavy ion irradiation.

The specimens used in this study were β-FeSi$_2$ films fabricated with the ion beam sputter deposition method by depositing Fe on Si(100) substrates with the thickness 500 nm at certain temperatures [3]. In our previous report, we obtained preliminary transport data which the sign of Hall coefficient alternates with temperature. The simplest interpretation of this result is the altertating of transport carriers from holes to electrons with temperature. However, we have to confirm where the most part of current flows in a FeSi$_2$ layer or Si substrate. We are conducting careful transport measurements.

Our results showed only the structural change by high energy heavy ion irradiations with different electric stopping power *Se*. No phase transition of β-FeSi$_2$ to α phase is confirmed yet with the irradiations at room temperature. Therefore, we make a plan to irradiate the samples at high temperature near the transition.

References
[1] K. Yamaguchi and K. Mizushima, Phys. Rev. Lett., 25 (2001) 6006.
[2] M. Toulemonde, S. Bouffard and F. Studer, Nucl. Instrum. Methods Phys. Res., B91 (1994) 108.
[3] M. Sasase et al., Thin Solid Films, 401 (2001) 73.

[1] Japan Atomic Energy Agency (JAEA)
[2] The Wakasa-wan Energy Research Center (WERC)

7.10 Formation of metal microstructure induced by ion irradiation in Ag-zeolite

S. Okayasu[1] and Y. Sasaki[2]

Zeolite, a sort of alminosillicate constructed with degenerated SiO_4 and AlO_4 tetrahedrons sharing oxygen atoms with their neighbors, has a cage structure including large porous inside. Alkali or alkaline earth cations (usually Na^+) of the same amount of Al^{3+} ions are absorbed in the cage structure to compensate the charge imbalance. The molecular formula of zeolite can be expressed as

$$(M^I, M^{II}_{1/2})_m(Al_m Si_n O_{2(m+n)}) \cdot xH_2O \quad : n \geqq m \tag{1},$$
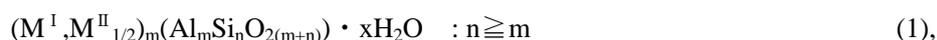
where M^I and M^{II} are univalent and divalent cations included inside the cage. A crystal structure of a LTA-zeolite is classified into type-A (a ratio of Si/Al =1) . The alkali or alkaline earth cations inside the cage structure are easily replaced other cations Ag^+, Mn^{2+}, etc. We synthesized Ag-zeolite samples for irradiation study.

In our previous study, we found the separation and clustering of Ag atom after 200keV electron irradiation on Ag-LTA zeolite samples. In the next stage of our study, we try to align the clusters along heavy ion tracks. Synthesized Ag-zeolite samples were irradiated with 200MeV Au ions in the Tandem accelerator in JAEA at room temperature with a fluence of 1×10^{11} ions/cm^2. We prepared the sample for the cross sectional observation of Transmission Electron Microscope (TEM). A result is shown in Fig.1. The Ag clusters are aligned along the ion tracks. We apply for a patent on the phenomenon (2009-213741).
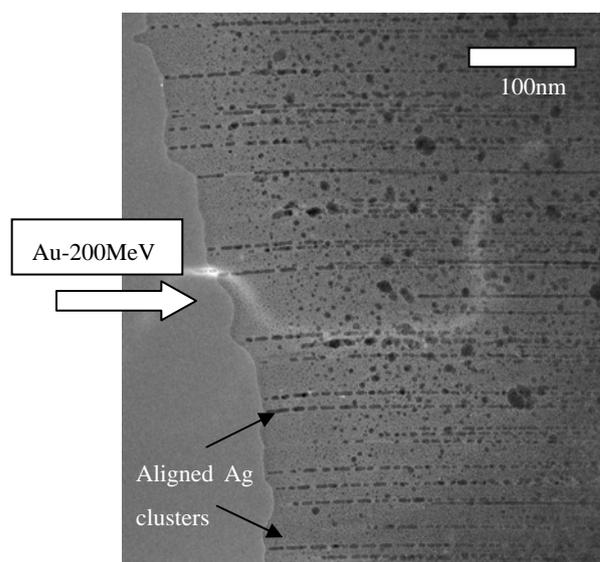
Fig. 1 A photo of cross-section TEM of Au-irradiated Ag-LTA zeoilte. Ag clusters are aligned along ion tracks.

[1] Japan Atomic Energy Agency (JAEA)
[2] Japan Fine Ceramics Center (JFCC)

7.11   Angular dependences of flux pinning properties
in YBCO thin films with crossed columnar defects

T. Sueyoshi[1], T. Sogo[1], K. Yonekura[1], T. Fujiyoshi[1], F. Mitsugi[1], T. Ikegami[1] and N. Ishikawa[2]

The columnar defects (CDs) formed by the heavy-ion irradiation into high-T_c superconductors have been known to be the most typical one-dimensional 1-D pinning centers (PCs) and are effective for the large enhancement of the in-field critical current density J_c at $B \parallel c$ and the reduction of the anisotropy of J_c which is one of the serious problems for the practical applications of superconductors [1]. The heavy-ion irradiation also enables us to produce the crossed 1-D PCs consisting of a finite number of the CD directions around c-axis. Several groups have reported the experimental enhancements of J_c due to the crossed CDs compared to the parallel CDs [2]. Most of these experiments, however, has been carried out only for the enhancement of J_c at $B \parallel c$, and therefore the effect of the crossed CDs on the angular dependence of critical current density $J_c(\theta)$ has not been well-studied yet. In this work, the influence of the dispersion in the directions of the 1-D PCs on the $J_c(\theta)$ is systematically investigated in YBa$_2$Cu$_3$O$_y$ (YBCO) thin films.

Samples used in this work were c-axis oriented YBCO thin films prepared by the pulsed laser deposition (PLD) method on SrTiO$_3$ substrates. The CDs were produced by irradiating the samples at room temperature with 200MeV Xe ions from a tandem accelerator at JAEA-Tokai. To install the crossed CDs, the incident ion beam was tilted off the c-axis by $\pm\theta_i$ and was always directed perpendicular to the longer direction bridge of the sample so that the crossed CDs consist of two parallel CD families at $\pm\theta_i$ relative to the c-axis. As a reference, a sample with the parallel CDs inclined at θ_i relative to the c-axis was prepared. The total density of CDs corresponds to the dose equivalent matching field $B_\phi = 2$ T. The transport properties were measured using the four probe method. The transport current was applied in the direction perpendicular to the magnetic field, the c-axis, and the CDs at any time. The critical current density J_c was defined by a criterion of the electrical field $E = 1$ μV/cm. The $J_c(\theta)$ was evaluated under the magnetic field, where θ is the angle between the magnetic field and the c-axis of the film. In case of the samples with the crossed CDs, the magnetic field was rotated in a splay plane where two parallel CD families are crossing each other.

Fig. 1 shows the $J_c(\theta)$ properties for (a) sp10 ($\theta_i=\pm10°$) and (b) sp45 ($\theta_i=\pm45°$), respectively. Generally, the peak at $\theta = 90°$ is attributed to the stacking faults or to the intrinsic pinning due to the CuO$_2$ planes. In contrast, the additional peak around $\theta = 0°$ originates from the introduced CDs. For sp10, the shapes of the additional peaks are sharp and single around $B \parallel c$. This would be ascribed to the splay effect, in which the suppression of motion of flux lines from one CD to another is caused by the slight dispersion in the direction of CDs [3]. For sp45, on the other hand, the crossover from a broad peak around $B \parallel c$ to double

---

[1] Kumamoto University
[2] Japan Atomic Energy Agency (JAEA)

peaks at two directions of the irradiation is observed. In lower magnetic fields, the pre-existed *c*-axis correlated PCs such as screw or edge dislocations would be effective around $\theta = 0°$. This would be reflected in the plateau observed in $J_c(\theta)$ of sp45 at 1.5 T within the angle range from $-45°$ to $45°$. As the magnetic field increases, the pre-existed *c*-axis correlated PCs would be weak and the two parallel CD families dominantly affect the $J_c(\theta)$ so that the double peaks appear at $\theta=\pm45°$. To discuss the differences of the additional peaks among the configurations of the CDs quantitatively, we adopt a simple approach, in which the additional peak is characterized by defining two parameters as its height and width; the height of the additional peak is evaluated from the ratio of the value of the peak, J_{cp} to the minimum value of $J_c(\theta)$, J_{cm} [4] and the width θ_a is defined as the difference between angles of J_{cp} and J_{cm} [5]. In Fig. 2(a), the J_{cp}/J_{cm} initially increases with magnetic field and reaches a maximum around a half of B_ϕ for all irradiated samples. For $B > B_\phi$, the decreases of J_{cp}/J_{cm} in the crossed configurations are more pronounced compared to those in the parallel configuration (pa06). The dispersion in the direction of CDs would prevent the correlation of flux pinning along the *c*-axis in high magnetic fields, which occurs in the parallel CD configurations due to the collective pinning of flux lines including the interstitial flux lines between the directly pinned flux lines by CDs. In Fig. 2 (b), the values of θ_a, which approximately represent the accommodation angle where the flux pinning by CDs effectively disappears, abruptly decrease with increasing magnetic field in the crossed CD configurations for $B > B_\phi$. One of reasons for this is that the sliding of the flux lines along one of the two parallel CD families occurs in the magnetic field tilted off the *c*-axis [6]. In high magnetic fields, the interstitial flux lines appear between the CDs. There is a possibility that the interstitial flux lines slide along one of the two parallel CD families, which also promotes the motion of flux lines pinned along the other one through the elastic interaction.
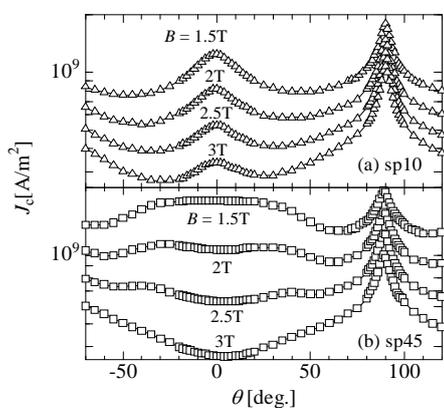
Fig. 1 Angular dependence of J_c at 77.3K and 1T for (a) sp10 and (b) sp45.
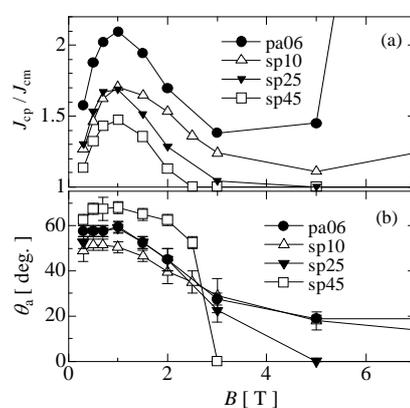
Fig. 2 Magnetic field dependence of (a) J_{cp}/J_{cm} and (b) θ_a at 77.3 K.

References

[1] L. Civale et al., Phys. Rev. Lett., 67 (1991) 648.

[2] L. Krusin-Elbaum et al., Phys. Rev. Lett., 76 (1996) 2563.

[3] T. Hwa et al., Phys. Rev. Lett., 71 (1993) 3545.

[4] S. Awaji et al., Appl. Phys. Lett., 90 (2007) 122501.

[5] L. Civale et al., Appl. Phys. Lett., 84 (2004) 2121.

[6] Th. Schuster et al., Phys. Rev., B50 (1994) 9499.

7.12   Swift ion implantation for fabrication of optical waveguides

F. Qiu[1], T. Narusawa[1], A. Osa[2] and M. Sataka[2]

The optical waveguide is not only one of key elements in integrated optical circuits but also it has several possibilities as active and/or passive optical devices. In order to fabricate various waveguides (different substrates including glasses and crystals) effectively as well as easily, the present study utilizes swift Ar ion implantation with energy of 60MeV and dose of 2×10^{12} ions/cm^2. Due to relatively large electronic stopping cross sections of swift and heavy Ar ions, the planar waveguide structure can be fabricated with several orders smaller dosages than conventional ion implantation.

The substrates used in the present study are listed in Table 1 together with the ideas behind the choice of each material. After the implantation, the prism-coupling method was used to observe the guided optical modes in these samples. We have found that planar waveguides are certainly formed in these substrates, except for Er:Yb:Phosphate glass. Figure 1 shows the results from GLSO glass and Nd:MgO:LiNbO$_3$ (TE mode at the wavelength of 632.8nm). Sharp downward cusps in Fig.1 indicate guided optical modes. The reason why the Er:Yb:Phosphate glass was no good is yet to be resolved.

After carefully polishing the end-faces of these waveguides, the near-field intensity distributions have been measured by the end-fire coupling method. We have so far obtained the distributions for Nd:MgO:LiNbO$_3$ and Nd:YAG. Figure 2 shows the result for Nd:YAG (TM$_0$ mode at the wavelength of 632.8nm). As we can see from the intensity distribution curve, only one mode (the fundamental mode) propagates in the waveguide. This is requisite for waveguide laser operation and the finding is encouraging for our future works.

Table 1 Substrates for swift ion implantation and possible applications

Substrate materials	Idea of applications
Nd:MgO:LiNbO$_3$	Solid-State Laser with Emission at 1085nm
Nd:YAG	Solid-State Laser with Emission at 1030nm
Nd:YVO$_4$	Solid-State Laser with Emission at 914, 1064 and 1342nm
KTP (KTiOPO$_4$)	Second Harmonic Generation
Nd:GLS Glass	Solid-State Laser with Emission at 1080nm
Ho:GLS Glass	Solid-State Laser with Emission at 3040nm
Er:Yb:Phosphate Glass	Er Doped Waveguides Amplifier
Gallium Lanthanum Sulphide (GLS) and Gallium Lanthanum Oxysulfide (GLSO) Glasses	Infrared Transmission from Telecommunication Windows to Long-Wavelength Infrared

---

[1] Kochi University of Technology (KUT)

[2] Japan Atomic Energy Agency (JAEA)
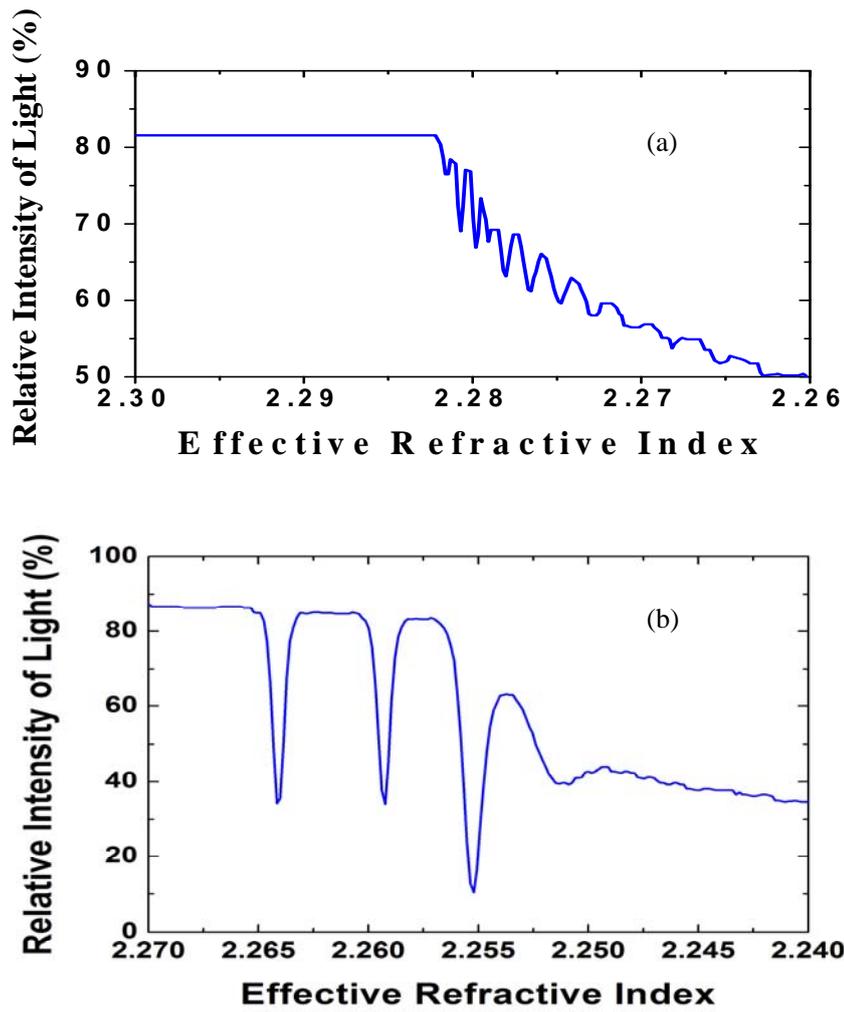
Fig. 1 Prism-coupling results for (a) GLSO glass (b) Nd:MgO:LiNbO$_3$
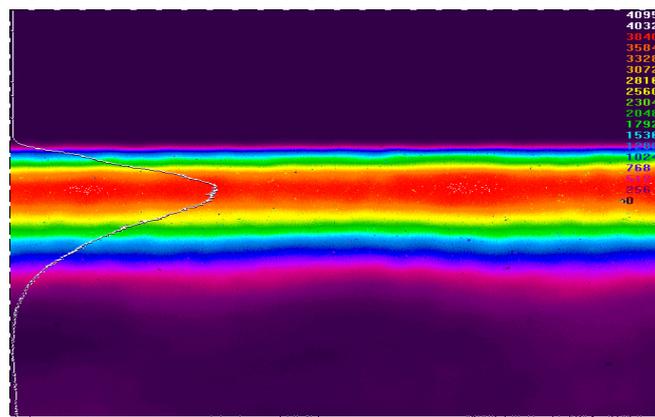
Fig. 2 Near-field intensity distribution for Nd:YAG
(The inset numbers are digitizer units and dimensionless)

In future works, we will measure the optical loss of these waveguides and the lasing properties. The relationship of the refractive index change and the implantation-induced damages will also be studied.

7.13 Dynamic nuclear polarization study of meso-scale spatial distribution of free radicals generated by carbon and electron beams

T. Kumada[1], Y. Noda[1] and N. Ishikawa[1]

Dynamic nuclear polarization (DNP) results from transferring spin polarization from electrons to nuclei by microwave, thereby aligning the nuclear spins to the extent that electron spins are aligned. Polarization P_{DNP} achieved by DNP is determined by a balance between the build-up rate A of the nuclear polarization and spin-lattice relaxation rate T_{1n}^{-1} of nuclear spins,

$$P_{DNP} = \frac{A}{A + T_{1n}^{-1}} P_e,$$ (1)

where P_e is the electron polarization at the thermal equilibrium. Both larger A and smaller T_{1n}^{-1} are essential for higher P. In most of DNP studies, the nuclear polarizations are built up by the cross effect (CE) and thermal mixing (TM), Both of the CE and TM rely on a three electron-electron-nucleus spin flip processes, whose efficiency depends on two electron-electron spin interactions. High concentration C_e of free radicals is essential not only to increase microwave absorbance for DNP but also to increase the electron-electron spin interaction for the CE and TM. On the other hand, T_{1n}^{-1} increases with increasing C_e. C_e should be optimized based on a compromise over two conflicting requests for larger A and smaller T_{1n}^{-1}.

Because of multi-spin processes, DNP should be sensitive not only to C_e but also to the heterogeneity of the spatial distribution of the polarizing agents. We came up with the idea that the DNP technique can be used for the study of meso-scale spatial distribution of free radicals produced by radiolysis of solid materials. In this study, we compare DNP results of C^{6+}- and electron-beam irradiated low-crystallinity polyethylene (e-LPE, C-LPE) with TEMPO-doped one (T-LPE), (2,2,6,6-tetramethylpiperidine 1-oxyl) to discuss the spatial distribution of free radicals produced by these beams by the analysis of DNP results.

C-LPE was prepared by irradiation of C^{6+} (100 MeV) ion beams to the total dose of $10^9 - 10^{13}$ ions / cm^2 to LPE sheets with the thickness of 0.5 mm on a bottom tip of a cryostat cooled by liquid nitrogen. Electron beams (2 MeV, 0.2-2 mA, 2 s − 30 min.) for e-LPE was irradiated at JAEA Takasaki in a similar manner. T-LPE was prepared by a permeation of TEMPO vapor in glassware under vacuum at 330 K for 1 day. C_e of alkyl radicals for C-LPE and e-LPE, and that of TEMPO for T-LPE were determined by ESR at 77 K. We took care to avoid absorption of oxygen molecules in air, which enhance nuclear spin relaxation and suppress P_{DNP}. The DNP measurements were carried out at 1.2 T and 1.5 K with microwave of ~34.5 GHz.

Figure 1 shows enhancements of polarization compared with thermally equilibrated proton polarization at

---

[1] Japan Atomic Energy Agency (JAEA)

4.2 K $P_{TE}(4.2K)$. The T-LPE showed a sharp maximum for $C_e = 4 \times 10^{19}$ spins / cm^3. The e-LPE also showed a maximum but less significant. The enhancement of P_{DNP} for C-LPE was much less than that for T-LPE and e-LPE, and poorly depended on C_e. We found that the build-up and decay rates of the proton polarizations rather than P_{DNP} more remarkably depend on C_e. Figs. 2 and 3 show the build-up rate and T_{1n}^{-1} determined by grow and decay behaviors of P_{DNP} after switching on and off of the microwave, respectively. $T_{1n}^{-1} \propto C_e^2$ was obtained for T-LPE, but $T_{1n}^{-1} \propto C_e$ was for C-LPE. E-LPE showed $T_{1n} \propto C_e^{-1}$ below $C_e = 7 \times 10^{19}$ spins cm^{-3} but $T_{1n} \propto C_e^{-2}$ above. Although the relation for C_e was less clear, A for C-LPE and e-LPE depend less on C_e than that for T-LPE.

The efficiency of DNP by CE and TM depends both on absorbance of microwave and dipolar electron spin-spin interaction. The absorbance linearly increases with C_e. On the other hand, the dipolar spin-spin interaction increases in proportional to local concentration of free radicals, where they are localized. It is known that free radicals produced by C_6^+-beam are localized along the path of the track of the beams, and electron-beams generate spur, blobs, and short tracks, where 3-4 or more free radicals are localized, whereas the TEMPO free radicals are homogeneously distributed in T-LPE. Therefore, although it can be referred to as C_e for T-LPE, the local concentration for C-LPE and e-LPE is independent of C_e as long as the spurs, blobs and tracks do not overlap for each other, whereas it increases in proportional to C_e for T-LPE. Since T_{1n}^{-1} behaved in a similar manner as A, the main proton-spin relaxation path is also assigned as the three electron-electron-nucleus spin flip process. The steeper dependence of T_{1n}^{-1} on C_e above $C_e = 7 \times 10^{19}$ spins cm^{-3} for e-LPE than that below is probably due to overlap of spurs, blobs, and short tracks at higher radiation dose.

In this way, heterogeneity of free-radical distribution can be studied by the analysis of power function of the build-up and decay of P_{DNP} as a function of C_e. We hope that this technique would be a general technique to measure sizes of the spurs, blobs, and tracks produced by radiolysis of non-metallic solids.
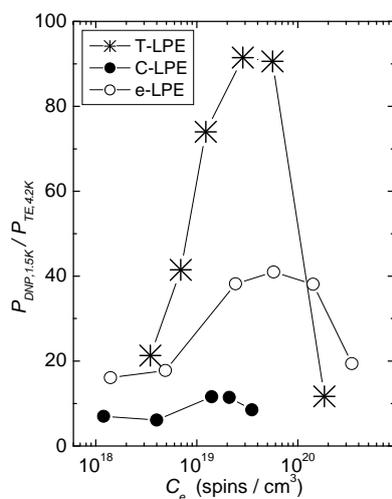
Fig. 1 $P_{DNP}(1.5K) / P_{TE}(4.2K)$.   Fig. 2   Build-up rate.   Fig. 3 T_{1n}^{-1}.
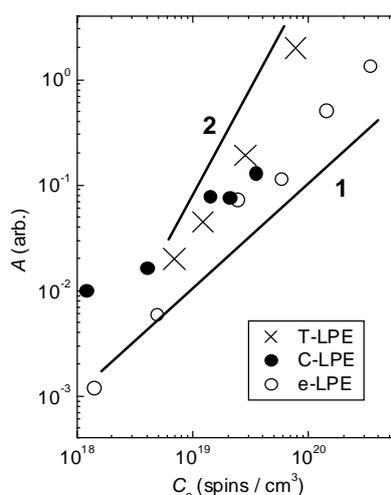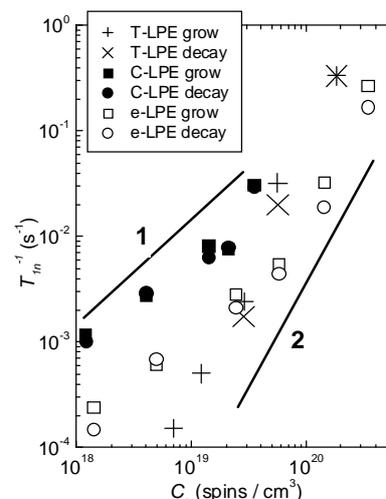
7.14   Track characterization of oxygen ions in solid state track detector

M. Tampo[1], K. Nishio[2], Y. Fukuda[1], H. Sakaki[1], S. Mitsuoka[2] and K. Kondo[1]

The ion track detector consisting of organic polymer is one of the highly sensitive detectors that can catch a single ion and is insensitive to x-rays, gamma-rays and electrons. It is then appropriate to detect ion signals from an ultra-intense-laser created plasma, which simultaneously generates intense electrons, x-rays and gamma-rays with p-sec bunch. The detector reveals the ions as a few micron pit by chemically etching an ion damaged trail, which is created along ion incidental path. The diameter of pits depends on ion energy and species. This ion track response has been investigated under the ambient air conditions. Track diameter also has dependency on vacuum condition since a creation mechanism of ion track also depends on oxygen dissolving into the detector [1]. However, track response under vacuum is not understood well in heavy ions. Then, it is required to know what species ions are accelerated from the cluster gas target from the interaction between an ultra-intense-laser light and a He-CO2 gas cluster target under the condition of vacuum [2], In this report, we describe an experimental investigation to assign the vacuum effect of ion track response for MeV Oxygen ions on the ion track detector in different energy range.

Irradiation by Oxygen ions of the ion track detectors was conducted in JAEA Tandem Accelerator. As ion track detector, we used sheets of a plastic track detector called as CR-39 (BARYO TRACK delivered from FUKUBI Co. Ltd.) with 0.1mm thickness. The detector was stacked with several sheets to resolve different energy ranges by energy filtering due to the stopping power of each CR-39 sheet. The stacked CR-39 detector was irradiated with a 286 MeV Oxygen beam after being accelerated in booster line. The beam fluence was reduced by as much as $10^6/cm^2$ with beam flipper. To investigate the vacuum effect, the stacked CR-39 was placed under vacuum at 10^{-7} torr, varying time durations during which the stacked CR-39 is in vacuum before the irradiation by the Oxygen beam. The time durations were 1, 3, and 7 hour before the irradiation. The stacked CR-39 was separated into the single sheets on removal from the chamber, and then etched by a 6N-KOH solution at 70 degree Celsius. The step of etching and pit observation by an optical microscope was repeated with 3times so that we could obtained a time development of pit diameters with 0.5, 1.5 and 3hour in different energy ranges as shown in Fig. 1.

Figure 1 shows that shorter time placement of the CR-39 in vacuum results in more effective enlargement of pit diameter. This result can be interpreted that sensitivity of track creation strongly depends on a density of Oxygen gas dissolved into the CR-39 since such oxygen gas is degassed by vacuum. This oxygen effect for track creation has been discussed in the case of protons and alpha particles, when decreasing of the oxygen

[1] Photo-Medical Research Center, Kansai Photon Science Institute of Japan Atomic Energy Agency (JAEA)
[2] Advanced Science Research Center, Japan Atomic Energy Agency (JAEA)
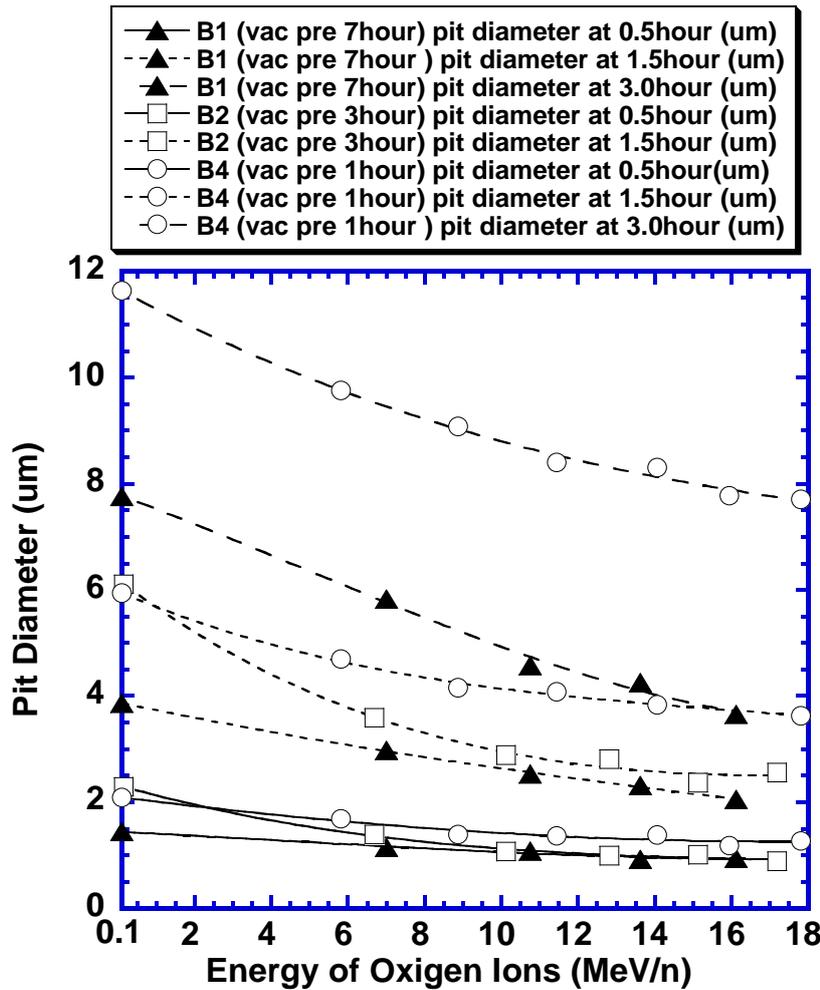
Fig. 1
Pit diameters of Oxygen ions related to ion energy, time duration of vacuum placement and etching time. Ion energies were evaluated with stopping energy range of CR-39 using SRIM code. Error of pit diameter was 20% at 0.5hour etch and 5% at 1.5 and 3.0 hour etch.

density from degassing by vacuum brings reduction of track creation sensitivity [3]. Our result also shows the reduction of track creation sensitivity even for heavy ions such as oxygen, which means oxygen gas effect plays an important role of track creations. On the other hand, we are discussing a track response at short time etching in Fig. 1. While we varied time duration placing the CR-39 in vacuum as 1, 3, and 7 hour, difference of pit diameter at 0.5 hour etching was not big change. This can be discussed a possibility of track creation mechanism independent on the density of Oxygen gas.

References

[1] T. Yamauchi et al., Nucl. Instrum. Methods Phys. Res., B208 (2003) 489-494.

[2] Y. Fukuda et al., Phys. Rev. Lett., 103 (2009) 165002.

[3] B. Dorschel et al.,Radiation Measurerements., 40 (2004) 234-239.

CHAPTER 8

Publication in Journal and Proceedings and Contribution to Scientific Meetings

This is a blank page.

8.1 Accelerator Operation and Development

Journal/Proceedings

T. Ishii, M. Matsuda, H. Kabumoto and A. Osa
Recent Activities in Tandem, Booster and TRIAC at Tokai
Perspectives in Nuclear Physics, Proc. 6th Japan-Italy Symposium on Heavy-Ion Physics,
(2008) ; AIP Conf. Proceedings, 1120 (2009) 235-240.

M. Okada, K. Niki, S. Arai and I. Katayama
Development of multi layer chopper
Proc. 6th Particle Accelerator Society Meeting of Japan, (2009) 1114-1116.

K. Niki, H. Ishiyama, M. Okada, H. Miyatake, Y.X. Watanabe, S. Arai and H. Makii
Design of the 2-4 MHz pre-bunch system at TRIAC
Proc. 6th Particle Accelerator Society Meeting of Japan, (2009) 1117-1119.

Y. Otokawa, A. Osa, T.K. Sato, M. Matsuda, S. Ichikawa and S.C. Jeong
Development of radioactive ion beam production systems for Tokai Radioactive Ion Acceleration Complex
-High temperature ion source for short-lived isotopes
Rev. Sci. Instrum., 81 (2010) 02A902.

H. Kabumoto, S. Takeuchi, N. Ishizaki, T. Yoshida, T. Ishiguro and K. Yamaguchi
Recovery of acceleration field gradients of superconducting booster resonators by high pressure water jet rinsing
Proc. 6th Particle Accelerator Society Meeting of Japan, (2009) 1120-1122.

H. Kabumoto, S. Takeuchi, M. Matsuda, N. Ishizaki and Y. Otokawa
Superconducting twin quarter wave resonator for acceleration of low velocity heavy ions
Proc. 14th Int. Conf. on RF superconductivity, (2009) 849-853.

H. Kabumoto, S. Takeuchi, M. Matsuda, N. Ishizaki and Y. Otokawa
Superconducting twin quarter wave resonator for acceleration of low velocity heavy ions
Nucl. Instrum. Methods Phys. Res., A612 (2010) 221-224.

H. Kabumoto, S. Takeuchi, N. Ishizaki, T. Yoshida, T. Ishiguro and K. Yamaguchi
Recovery of superconducting booster's performance by high pressure water jet rinsing
Proc. 22nd Meeting for Tandem Accelerators and their Associated Technologies, UTTAC-J-18, (2009) 129-132.

M. Matsuda, T. Ishii, Y. Tsukihashi, S. Hanashima, S. Abe, A. Osa, N. Ishizaki, H. Tayama, T. Nakanoya, H.

Kabumoto, M. Nakamura, K. Kutsukake, Y. Otokawa and T. Asozu

Present Status of JAEA-Tokai Tandem Accelerator

Proc. 22nd Meeting for Tandem Accelerators and their Associated Technologies, UTTAC-J-18, (2009) 10-14.

M. Matsuda, T. Asozu, K. Kutsukake, T. Nakanoya, S. Hanashima and S. Takeuchi

Use of an ECR ion source in the large electrostatic accelerator

Proc. 6th Particle Accelerator Society Meeting of Japan, (2009) 827-829.

M. Matsuda, T. Asozu, T. Nakanoya, K. Kutsukake, S. Hanashima and S. Takeuchi

Highly charged ion injector in the terminal of tandem accelerator

J. Phys. Conf. Ser., 163 (2009) 012112.

M. Matsuda

Use of an ECR ion source in the large electrostatic accelerator

J. Particle Accelerator Society of Japan, 6 (2009) 213-221.

S. Hanashima

Present status of the control system of JAEA-Tokai tandem accelerator

Proc. 22nd Meeting for Tandem Accelerators and their Associated Technologies, UTTAC-J-18 (2009) 65.

T. Asozu, M. Makoto, K. Kutsukake and M. Nakamura

Influence of the median potential in an electrostatic steerer

Proc. 22nd Meeting for Tandem Accelerators and their Associated Technologies, UTTAC-J-18 (2009) 123-126.

T. Nakanoya, H. Tayama, H. Kabumoto, M. Matsuda and Y. Tsukihashi

Emission Management of SF$_6$ gas at the JAEA-Tokai tandem accelerator

Proc. 22nd Meeting for Tandem Accelerators and their Associated Technologies, UTTAC-J-18 (2009) 66-68.

Meetings

T. Ishii

Recent Activities at Tokai Tandem Accelerator

Nuclear Physics Trends: 7th China-Japan Joint Nuclear Physics Symposium, Tsukuba, Japan (Nov. 9-13, 2009).

M. Okada, K. Niki, S. Arai and I. Katayama

Development of multi layer chopper

Particle Accelerator Society Meeting 2009, Tokai, Japan (Aug. 5-7, 2009).

K. Niki, H. Ishiyama, M. Okada, H. Miyatake, Y. Watanabe, S. Arai and H. Makii
Design of the 2-4 MHz pre-bunch system at TRIAC
Particle Accelerator Society Meeting 2009, Tokai, Japan (Aug. 5-7, 2009).

K. Niki, H. Ishiyama, M. Okada, H. Miyatake, Y. Watanabe, S. Arai and H. Makii
Development of the 2-4 MHz pulsed ion beams for measurement of 12C(α, γ)16O reaction
Annual meeting of the Physical Society of Japan, Okayama, Japan (Mar. 20-23, 2010).

Y. Otokawa, A. Osa, T. K. Sato, M. Matsuda, S. Ichikawa and S. C. Jeong
Development of radioactive ion beam production systems for Tokai Radioactive Ion Acceleration Complex
-High temperature ion source for short-lived isotopes
13th Int. Conf. on Lon Sources, Gatlinburg, U.S.A. (Sep. 20-25, 2009).

H. Kabumoto, S. Takeuchi, N. Ishizaki, T. Yoshida, T. Ishiguro and K. Yamaguchi
Recovery of acceleration field gradients of superconducting booster resonators by high pressure water jet rinsing
Particle Accelerator Society Meeting 2009, Tokai, Japan (Aug. 5-7, 2009).

H. Kabumoto, S. Takeuchi, M. Matsuda, N. Ishizaki and Y. Otokawa
Superconducting twin quarter wave resonator for acceleration of low velocity heavy ions
14th Int. Conf. on RF superconductivity, Berlin, Germany (Sep. 20-25, 2009).

H. Kabumoto, S. Takeuchi, N. Ishizaki, T. Yoshida, T. Ishiguro and K. Yamaguchi
Recovery of superconducting booster's performance by high pressure water jet rinsing
22nd Meeting for Tandem Accelerators and their Associated Technologies, Tsukuba, Univ. of Tsukuba, Japan (Jul. 16- 17, 2009).

M. Matsuda, T. Ishii, Y. Tsukihashi, S. Hanashima, S. Abe, A. Osa, N. Ishizaki, H. Tayama, T. Nakanoya, H. Kabumoto, M. Nakamura, K. Kutsukake, Y. Otokawa and T. Asozu
Present Status of JAEA-Tokai Tandem Accelerator
22nd Meeting for Tandem Accelerators and their Associated Technologies, Tsukuba, Japan (Jul. 16-17, 2009).

M. Matsuda, T. Asozu, K. Kutsukake, T. Nakanoya, S. Hanashima and S. Takeuchi
Use of an ECR ion source in the large electrostatic accelerator
Particle Accelerator Society Meeting 2009, Tokai, Japan (Aug. 5-7, 2009).

S. Hanashima
Present status of the control system of JAEA-Tokai tandem accelerator
22nd Meeting for Tandem Accelerators and their Associated Technologies, Tsukuba, Japan (Jul. 16-17,

2009).

T. Asozu, M. Makoto, K. Kutsukake and M. Nakamura
Influence and measures of the median potential in electrostatic steerers on beam optics
Particle Accelerator Society Meeting 2009, Tokai, Japan (Aug. 5-7, 2009).

T. Asozu, M. Makoto, K. Kutsukake and M. Nakamura
Influence of the median potential in an electrostatic steerer
22nd Meeting for Tandem Accelerators and their Associated Technologies, Tsukuba, Japan (Jul. 16-17, 2009).

M. Nakamura, M. Matsuda, M. Sataka, K. Takahiro and N. Matsunami
Heavy ion Rutherford backscattering spectrometry (HIRBS) at JAEA Tokai Tandem accelerator
Annual Meeting of the Physical Society of Japan, Okayama, Japan (Mar. 20-23, 2010).

T. Nakanoya, H. Tayama, H. Kabumoto, M. Matsuda and Y. Tsukihashi
Emission Management of SF_6 gas at the JAEA-Tokai tandem accelerator
22nd Meeting for Tandem Accelerators and their Associated Technologies, Tsukuba, Japan (Jul. 16-17, 2009).

8.2 Nuclear Structure

Journal/Proceedings

Y. H. Zhang, M. Hasegawa, W. T. Guo, M. L. Liu, X. H. Zhou, G. de Angelis, T. M. Axiotis,
A. Gadea, N. Marginean, Martinez, D. R. Napoli, C. Rusu, Zs. Podolyak, C. Ur, D. Bazzacco,
F. Brandolini, S. Lunardi, S. M. Lenzi, R. Menegazzo, R. Schwengner, A. Gargano, W. von Oertzen
and S. Tazaki
High-spin level structure in $^{94,95}Mo$
Phys. Rev., C79 (2009) 044316.

Y. H. Qiang, Y.H. Zhang, X.H. Zhou, Y. Liu, J. Hu, M.Oshima, H. Harada, M. Koizumi, K. Furutaka,
F. Kitatani, S. Nakamura, Y. Toh, A. Kimura, Y. Hatsukawa, M. Ohta, K. Hara, T. Kin and J. Meng
High-spin level structure of odd-odd ^{168}Ta
Sciences in China, G39 (2009) 2-10.

W. Hua, X.H. Zhou, Y.H. Zhang, Y.X. Guo, M. Oshima, Y. Toh, M. Koizumi, A. Osa, B. Qi, S.Q. Zhang,
J. Meng and M. Sugawara
Study of the $vi^{-1}_{13/2}$ band in ^{189}Pt
Chinese Phys., C33 (2009) 743-747.

Y.H. Zhang
High-spin states of odd-odd nuclei in the A ~ 170 mass region
Nucl. Phys., A 834 (2010) 32c–35c.

W. Hua, X. H. Zhou, Y. H. Zhang, Y. Zheng, M.L. Liu, F. Ma, S. Guo, L. Ma, S.T. Wang, N.T. Zhang,
Y.D. Fang, X.G. Lei, Y.X. Guo, M. Oshima, Y. Toh, M. Koizumi, Y. Hatsukawa, B. Qi, S.Q. Zhang,
J. Meng and M. Sugawara
Properties of the rotational bands in the transitional nucleus ^{189}Pt
Phys. Rev., C80 (2009) 034303.

H. Iimura and F. Buchinger
*Charge radii in modern macroscopic-microscopic mass models: The role of dynamic quadrupole
deformation*
Eur. Phys. J., A42 (2009) 559-563.

Meetings

D. Nagae, T. Ishii, R. Takahashi, M. Asai, H. Makii, A. Osa, T.K. Sato, S. Ichikawa, Y.R. Shimizu and
T. Shoji
Lifetime Measurements for the First 2^+ States in $^{162,\ 164}Gd$ Populated by the β Decay of $^{162,\ 164}Eu$
Int. Symp. on Exotic Nuclei, Sochi, Russia (Sep. 29, 2009).

H. Hayashi, M. Shibata, M. Asai, A. Osa, T.K. Sato, M. Koizumi, A. Kimura and M. Oshima
Beta decay energy measurements of $^{160-165}$Eu with a total absorption clover Ge detector
Symp. on Slow and Stop Radioisotope, Tokyo, Japan (Mar. 2, 2010).

H. Hayashi, M. Shibata, M. Asai, A. Osa, T.K. Sato, M. Koizumi, A. Kimura and M. Oshima
Beta decay energy measurements of A~160 nuclei using total absorption detector
Annual meeting of the Physical Society of Japan, Okayama, Japan (Mar. 20-23, 2010).

H. Hayashi, M. Shibata, M. Asai, A. Osa, T.K. Sato, M. Koizumi, A. Kimura and M. Oshima
Study on nuclear data by using a high intensity pulsed neutron source for advanced nuclear system: (10) Measurements of beta-decay energies
Spring meeting of the Atomic Energy Society of Japan, Mito, Japan (Mar. 26-28, 2010).

M. Asai, K. Tsukada, Y. Kasamatsu, T. K. Sato, A. Toyoshima, Y. Ishii, R. Takahashi, Y. Nagame, T. Ishii, I. Nishinaka, D. Kaji, K. Morimoto and Y. Kojima
Alpha-gamma coincidence spectroscopy of ^{259}Rf using a mixed Cf target
3rd Joint Meeting of the Nuclear Physics Division of the APS and JPS, Waikoloa, U.S.A. (Oct. 13-17, 2009).

M. Asai, K. Tsukada, Y. Kasamatsu, T. K. Sato, A. Toyoshima and Y. Nagame
Production of long-lived Fm and Es tracers using a Cf target and its application to nuclear spectroscopy
53th Symp. on Radiochemistry, Tokyo, Japan (Sep. 28-30, 2009).

N. Imai, Y. Hirayama, H. Ishiyama, S.C. Jeong, H. Miyatake, Y.X. Watanabe, H. Makii, S. Mitsuoka, D. Nagae, I. Nishinaka, K. Nishio and K. Yamaguchi
Isobaric analog resonance of ^{69}Zn by thick target inverse kinematics proton resonance scattering
Direct Reaction with Exotic Beams 2009, Tallahassee, U.S.A. (Dec. 16-19, 2009).

N. Imai, Y. Hirayama, H. Ishiyama, S.C. Jeong, H. Miyatake, Y.X. Watanabe, H. Makii, S. Mitsuoka, D. Nagae, I. Nishinaka, K. Nishio and K. Yamaguchi
Neutron single particle states in neutron-rich nuclei studied by proton resonance scattering
Int. workshop on "Physics with Stopped and Slow Radioisotope Beams", Tokyo, Japan (Mar. 1-2, 2010).

8.3 Nuclear Reaction

Journal/Proceedings

K. Nishio, H. Ikezoe, S. Mitsuoka, I. Nishinaka, Y. Watanabe, Y. Nagame, T. Ohtsuki, K. Hirose and S. Hofmann
Effects of nuclear orientation on fusion and fission process in heavy ion reactions
Proc. 6th Japan-Italy symposium on Heavy-Ion Physics, ASR2008, AIP Conf. Proc., 1120 (2009) 275- 279.

K. Nishio, H. Ikezoe, S. Mitsuoka, I. Nishinaka, Y. Watanabe, Y. Nagame, T. Ohtsuki, K. Hirose and S. Hofmann
Effects of nuclear orientation on fission fragment mass distributions in the reactions of $^{34,36}S + ^{238}U$.
Proc. New Aspects of heavy Ion Collisions Near the Coulomb Barrier, AIP Conf. Proc., 1098 (2009) 289 –294.

K. Nishio, H. Ikezoe, S. Mitsuoka, I. Nishinaka, Y. Watabnabe, Y. Nagame, T. Ohtsuki, K. Hirose and S. Hofmann
Effects of nuclear orientation on fission fragment mass distributions for the reactions using actinide target nuclei
Proc. 4th Int. Workshop on Nuclear Fission and Fission Products Spectroscopy, AIP Proc. Conf., 1175 (2009) 111-118.

I. Nishinaka
Nuclear-charge polarization at scission in fission from moderately excited light-actinide nuclei
Proc. 2009 Int. Congress on Advances in Nuclear Power Plants, The Atomic Energy Society of Japan, CD-ROM (2009) 93112-1-6.

I. Nishinaka, M. Tanikawa, Y. Nagame and H. Nakahara
Nuclear-charge polarization at scission in proton-induced fission of light actinides
AIP Conf. Proc., 1098 (2009) 320-325.

H. Ikezoe, S. Mitsuoka, K. Nishio, Y. Watanabe, S. C. Jeong, I. Nishinaka, T. Ohtsuk and K. Hirose
Dependence of barrier distribution and fusion-fission process on entrance channel
Nucl. Phys., A834 (2010) 172c-175c.

A.N. Andreyev, S. Antalic, D. Ackermann, L. Bianco, S. Franchoo, S. Heinz, F.P. Hessberger, S. Hofmann, M. Huyse, I. Kojouharov, B. Kindler, B. Lommel, R. Mann, K. Nishio, R.D. Page, J.J. Ressler, P. Sapple, B. Streicher, S. Saro, B. Sulignano, J. Thomson, P. Van Duppen and M. Venhart
Alpha decay of ^{194}At
Phys. Rev., C79 (2009) 064320(1-12).

F. P. Heßberger, S. Antalic, B. Sulignano, D. Ackermann, S. Heinz, S. Hofmann, B. Kindler,
J. Khuyagbaatar, I. Kojouharov, P. Kuusiniemi, M. Leino, B. Lommel, R. Mann, K. Nishio, A. G. Popeko,
Š. Šáro, B. Streicher, J. Uusitalo, M. Venhart and A. V. Yeremin
Decay studies of K isomers in ^{254}No
Eur. Phys. J., A43 (2010) 55-66.

H. Ishiyama, T. Hashimoto, K. Yamaguchi, Y.X. Watanabe, N. Imai, Y. Hirayama, H. Miyatake,
M.H. Tanaka, N. Yoshikawa, S.C. Jeong, Y. Fuchi, I. Katayama, T. Nomura, T. Ishikawa, S.K. Das,
Y. Mizoi, T. Fukuda, K. Nishio, S. Mitsuoka, H. Ikezoe, M. Matsuda, S. Ichikawa, T. Shimoda, K. Otsuki
and T. Kajino
A Systematic Study of Astrophysical Reaction Rates through Li
AIP Conf. Proc., 1120 (2009) 177-182.

T. Hashimoto, H. Ishiyama, Y.X. Watanabe, Y. Hirayama, N. Imai, H. Miyatake, S.C. Jeong, M.H. Tanaka,
N. Yoshikawa, T. Nomura, S. Mitsuoka, K. Nishio, T.K. Sato, A. Osa, S. Ichikawa, M. Matsuda, H. Ikezoe,
S.K. Das, Y. Mizoi, T. Fukuda, A. Sato, T. Shimoda, K. Otsuki and T. Kajino
A new measurement of the astrophysical ^{8}Li(d, t)^{7}Li reaction
Phys. Lett., B674 (2009) 276-280.

H. Ishiyama, T. Hashimoto, T. Ishikawa, K. Yamaguchi, Y.X. Watanabe, Y. Hirayama, N. Imai, H. Miyatake,
M-H. Tanaka, N. Yoshikawa, S.C. Jeong, Y. Fuchi, T. Nomura, I. Katayama, H. Kawakami, S. Arai,
M. Okada, M. Oyaizu, S. Mitcuoka, A. Osa, T.K. Sato, K. Nishio, M. Matsuda, S. Ichikawa, H. Ikezoe,
Y. Mizoi, S.K. Das, T. Fukuda, T. Shimoda, K. Otsuki and T. Kajino
Determination of astrophysical nuclear reaction rates using light neutron-rich RNBs
Proc. Science (NIC X), (2009) 134 (5pp).

Meetings

K. Nishio, H. Ikezoe, S. Mitsuoka, I. Nishinaka, H. Makii, Y. Watanabe, Y. Nagame, T. Ohtsuki, K. Hirose
and S. Hofmann
Measuremet of the quasifission properties in the reactions of ^{30}Si, ^{31}P, ^{40}Ar + ^{238}U
Fall meeting of the Atomic Energy Society of Japan, Sendai, Japan (Sep.16-18, 2009).

K. Nishio, S. Hofmann, F.P. Hessberger, D. Ackermann, S. Antalic, V.F. Comas, Ch.E. Duellmann,
A. Gorshkov, R. Graeger, S. Heinz, J.A. Heredia, K. Hirose, H. Ikezoe, J. Khuyagbaatar, B. Kindler,
I. Kojouharov, B. Lommel, R. Mann, S. Mitsuoka, Y. Nagame, I. Nishinaka, T. Ohtsuki, A.G. Popeko,
S. Saro, M. Schaedel, A. Tuerler, Y. Watanabe and A.V. Yeremin
Effects of nuclear deformation of ^{238}U on the fission fragment mass distribution in the reaction of ^{30}Si + ^{238}U
Annual meeting of the Physical Society of Japan, Okayama, Japan (Mar.20-23, 2010).

K. Nishio, S. Hofmann, F.P. Hessberger, D. Ackermann, S. Antalic, V.F. Comas, Ch.E. Duellmann, A. Gorshkov, R. Graeger, S. Heinz, J.A. Heredia, K. Hirose, H. Ikezoe, J. Khuyagbaatar, B. Kindler, I. Kojouharov, B. Lommel, R. Mann, S. Mitsuoka, Y. Nagame, I. Nishinaka, T. Ohtsuki, A.G. Popeko, S. Saro, M Schaedel, A. Tuerler, Y. Watanabe and A.V. Yeremin

Effects of nuclear deformation of ^{238}U on the fission fragment mass distribution in the reaction of ^{30}Si + ^{238}U

Spring meeting of the Atomic Energy Society of Japan, Mito, Japan (Mar.26-28, 2010).

K.Nishio, H.Ikezoe, S. Mitsuoka, I. Nishinaka, Y. Nagame, K. Hirose, T. Ohtsuki, S.Hofmann,

Effects of nuclear orientation on fusion and fission in the reaction using ^{238}U target nucleus

Compound Nuclear Reactions and Related Topics, Bordeaux, France (Oct.05-08, 2009).

K. Nishio

Effects of nuclear orientation on fusion and fission process for reactions using actinide target nucleus

Workshop on Super-heavy Element Chemistry, RIKEN, Wako, Japan (Feb.2, 2010).

K. Nishio, H. Ikezoe, S. Hofmann, F.P. Heßberger, D. Ackermann, S. Antalic, V.F. Comas, Ch.E. Düllmann, A. Gorshkov, R. Graeger, S. Heinz, J.A. Heredia, K. Hirose, J. Khuyagbaatar, B. Kindler, I. Kojouharov, B. Lommel, H. Makii, R. Mann, S. Mitsuoka, Y. Nagame, I. Nishinaka, T. Ohtsuki, A.G. Popeko, S. Saro, M. Schädel, A. Türler, Y. Watanabe, A. Yakushev and A.V. Yeremin

Effects of nuclear orientation on fusion and fission process for reactions using uranium target nuclei

Int. Symp. on Exotic Nuclei, Sochi, Russia (Sep.28-Oct.2, 2009).

K. Nishio, H. Ikezoe, S. Hofmann, F.P. Heßberger, D. Ackermann, S. Antalic, V.F. Comas, Ch.E. Düllmann, A.Gorshkov, R. Graeger, S. Heinz, J.A. Heredia, K.Hirose, J. Khuyagbaatar, B. Kindler, I. Kojouharov, B. Lommel, H. Makii, R. Mann, S. Mitsuoka, Y. Nagame, I. Nishinaka, T. Ohtsuki, A.G. Popeko, S. Saro, M. Schädel, A. Türler, Y. Watanabe, A. Yakushev and A.V. Yeremin

Effects of nuclear orientation on fusion and fission process for reactions using ^{238}U target nucleus

Tours Symposium on Nuclear Physics and Astrophysics VII, Kobe, Japan (Nov.16-20, 2009).

I. Nishinaka

Nuclear-charge polarization at scission in fission from moderately excited light-actinide nuclei

Int. Congress on Advances in Nuclear Power Plants, Tokyo, Japan (May 10-14, 2009).

I. Nishinaka, Y. Kasamatsu, M. Tanikawa, S. Goto and M. Asai

Sub-barrier fusion hindrance in ^{19}F + ^{209}Bi reaction

Annual Meeting of the Japan Society of Nuclear and Radiochemical Sciences, Tokyo, Japan (Sep. 28-30, 2009).

I. Nishinaka, Y. Kasamatsu, M. Tanikawa, S. Goto, and M. Asai

Radiochemical study of sub-barrier fusion hindrance in ^{19}F + ^{209}Bi reaction

Asia-Pacific Symposium on Radiochemistry '09, Napa, California, USA (Nov. 29-Dec.1, 2009).

S. Mitsuoka, H. Ikezoe, K. Nishio, Y. Watanabe, S.C. Jeong, H. Ishiyama, Y. Hirayama, N. Imai and H. Miyatake
Barrier distribution of quasi-elastic backward scattering in very heavy reaction systems
Int. Conf. on Nuclear Reactions on Nucleons and Nuclei, Messina, Italy (Oct. 4-9, 2009).

H. Ikezoe, S. Mitsuoka, K. Nishio, Y. Watanabe, S. C. Jeong, I. Nishinaka, T. Ohtsuki and K. Hirose
Dependence of barrier distribution and fusion-fission process on entrance channel
Int. Conf. on Nucleus-Nucleus Collisions, Beijing, China (Aug. 16-21, 2009).

K. Yamaguchi, H. Ishiyama, Y. Mizoi, Y.X. Watanabe, T. Hashimoto, M.-H. Tanaka, H. Miyatake,
Y. Hirayama, N. Imai, Y. Fuchi, S.C. Jeong, T. Nomura, S.K. Das, T. Fukuda, H. Makii, S. Mitsuoka, I. Arai,
H. Yamaguchi, S. Kubono, Y. Wakabayashi and S. Hayakawa
Development of the GEM-MSTPC for studies of astrophysical nuclear reaction rates
10th Int. Symp. on Origin of Matter and Evolution of the Galaxies, Osaka, Japan(Mar. 8-Mar. 10, 2010).

8.4 Nuclear Chemistry

Journal/Proceedings

A. Toyoshima, Y. Kasamatsu, K. Tsukada, M. Asai, Y. Kitatsuji, Y. Ishii, H. Toume, I. Nishinaka, H. Haba, K. Ooe, W. Sato, A. Shinohara, K. Akiyama and Y. Nagame
Oxidation of element 102, nobelium, with flow electrolytic column chromatography on an atom-at-a-time scale
J. Am. Chem. Soc., 131 (2009) 9180.

Z.J. Li, A. Toyoshima, K. Tsukada and Y. Nagame
Ion-exchange behavior of Zr and Hf as homologues of element 104, Rf, in H_2SO_4 and $H_2SO_4/HClO_4$ mixed solutions
Radiochim. Acta, 97 (2009) 1-6.

Y. Kasamatsu, A. Toyoshima, M. Asai, K. Tsukada, Z.J. Li, Y. Ishii, H. Toume, T.K. Sato, T. Kikuchi, I. Nishinaka, Y. Nagame, H. Haba, H. Kikunaga, Y. Kudou, Y. Oura, K. Akiyama, W. Sato, K. Ooe, H. Fujisawa, A. Shinohara, S. Goto, T. Hasegawa, H. Kudo, T. Nanri, M. Araki, N. Kinoshita, A. Yokoyama, F. Fan, Z. Qin, C.E. Düllmann, M. Schädel, and J.V. Kratz
Anionic fluoro complex of element 105, Db
Chem. Lett., 38 (2009) 1084.

Meetings

Y. Nagame, M. Asai, H. Haba, Y. Kasamatsu, Z.J. Li, T.K. Sato, A. Toyoshima and K. Tsukada
Chemical equilibrium in atom-at-a-time chemistry
2009 Asia-Pacific Symposium on Radiochemistry, Napa, U.S.A. (Nov. 29-Dec. 4, 2009).

Y. Nagame, M. Asai, Y. Ishii, T. Kikuchi, Z.J. Li, T.K. Sato, A. Toyoshima, K. Tsukada, Y. Kasamatsu, H. Haba and K. Akiyama
Chemical investigation of Rf and Db at JAEA
2009 Asia-Pacific Symposium on Radiochemistry, Napa, U.S.A. (Nov. 29 – Dec. 4, 2009).

K. Sueki, Y. Nagasaki, T. Kamitsukasa, K. Akiyama, K. Tsukada, M. Asai, A. Toyoshima and Y. Nagame
Synthesis of water-soluble encapsulated-radioisotope fullerenes
2009 Asia-Pacific Symposium on Radiochemistry, Napa, U.S.A. (Nov. 29-Dec. 4, 2009).

Y. Nagame, K. Akiyama, M. Asai, H. Haba, Y. Ishii, Y. Kasamatsu, Z.J. Li, T.K. Sato, A. Toyoshima and K. Tsukada,
Aqueous chemistry of Rf and Db
7th Workshop on the Chemistry of the Heaviest Elements, Mainz, Germany (Oct. 11-13, 2009).

Y. Kasamatsu, A. Toyoshima, M. Asai, K. Tsukada, Z.J. Li, Y. Ishii, T.K. Sato, I. Nishinaka, T. Kikuchi,
Y. Nagame, H. Haba, H. Kikunaga, Y. Kudou, N. Sato, Y. Oura, K. Akiyama, W. Sato, K. Ooe,
H. Fujisawa, A. Shinohara, S. Goto, H. Kudo, M. Araki, N. Kinoshita, M. Nishikawa, A. Yokoyama,
F. Fan, Z. Qin and Ch. E. Düllmann
Anion-exchange experiment of Db with AIDA-II
7th Workshop on the Chemistry of the Heaviest Elements, Mainz, Germany (Oct. 11-13, 2009).

K. Tsukada, Y. Kasamatsu. M. Asai, A. Toyoshima, Y. Ishii, Z.J. Li, T. Kikuchi, T.K. Sato, I. Nishinaka,
Y. Nagame, S. Goto, T. Hasegawa, H. Kudo, H. Haba, Y. Kudou, K. Ooe, H. Fujisawa, W. Yahagi,
W. Sato, A. Shinohara, Y. Oura, T. Nanri, M. Araki, A. Yokoyama and F. L. Fan
Anion-exchange behavior of Db in HF/HNO$_3$ mixed solution using a new on-line chemical apparatus
8th Actinides Conference (Actinides2009), San Francisco, U.S.A. (July 12-17, 2009).

A. Toyoshima, K. Tsukada, M. Asai, T.K. Sato, Z.J. Li, N. Sato, T. Kikuchi, Y. Kitatsuji, Y. Nagame,
K. Ooe, A. Shinohara, Y. Kasamatsu, H. Haba and E. Julia
Reduction of mendelevium (Md) with electrochemistry
Spring Meeting of the Chemical Society of Japan, Higashi-Osaka, Japan (Mar. 26 -29, 2010).

A. Toyoshima, K. Tsukada, M. Asai, Y. Kitatsuji, Y. Ishii, T.K. Sato, Z.J. Li, N. Sato, T. Kikuchi,
I. Nishinaka, Y. Nagame, Y. Kasamatsu, H. Haba, K. Ooe, A. Shinohara, W. Sato and K. Akiyama
Electrochemistry of the heaviest elements at JAEA
2009 Asia-Pacific Symposium on Radiochemistry, Napa, U.S.A. (Nov. 29-Dec. 4, 2009).

R. Takayama, K. Ooe, W. Yahagi, H. Fujisawa, K. Komori, H. Kikunaga, T. Yoshimura, N. Takahashi,
K. Takahisa, H. Haba, Y. Kudou, Y. Ezaki, A. Toyoshima, M. Asai, Y. Nagame, T. Saito, T. Mitsugashira
and A. Shinohara
Solvent extraction of trivalent actinides with di(2-ethylhexyl) phosphoric acid and thenoyltrifluoroacetone
2009 Asia-Pacific Symposium on Radiochemistry, Napa, U.S.A. (Nov. 29-Dec. 4, 2009).

A. Toyoshima, K. Tsukada, M. Asai, Y. Kitatsuji, T.K. Sato, Z.J. Li, N. Sato, T. Kikuchi, Y. Ishii,
I. Nishinaka, Y. Nagame, Y. Kasamatsu, H. Haba, K. Ooe, A. Shinohara, H. Haba, K. Akiyama and
W. Sato
Electrochemical studies of the heaviest actinides
7th Workshop on the Chemistry of the Heaviest Elements, Mainz, Germany (Oct. 11-13, 2009).

A. Toyoshima, K. Tsukada, M. Asai, T.K. Sato, Z.J. Li, N. Sato, T. Kikuchi, Y. Kitatsuji, Y. Nagame,
K. Ooe, A. Shinohara, Y. Kasamatsu and H. Haba
Reduction of element 101, mendelevium, with flow electrolytic column chromatography
53rd Symp. on Radiochemistry, Tokyo, Japan (Sep. 28-30, 2009).

Z.J. Li, A. Toyoshima, K. Tsukada, M. Asai, T.K. Sato, T. Kikuchi, N. Sato and Y. Nagame
Cation-exchange behavior of Zr, Hf, and Th in H$_2$SO$_4$/HNO$_3$ mixed solutions–towards to study on sulfate complexation of ^{104}Rf
53rd Symp. on Radiochemistry, Tokyo, Japan (Sep. 28-30, 2009).

T. K. Sato, K. Tsukada, M. Asai, A. Toyoshima, Y. Kasamatsu, Y. Ishii, Z.J. Li, N. Sato, T. Kikuchi, H. Haba, S. Goto, H. Kudo and Y. Nagame
Development of an On-line Isothermal Gas Chromatographic Appratus for Db and Sg
2009 Asia-Pacific Symposium on Radiochemistry, Napa, U.S.A (Nov. 29-Dec. 4, 2009).

T.K. Sato, K. Tsukada, M. Asai, A. Toyoshima, Y. Kasamatsu, Z.J. Li, N. Sato, T. Kikuchi, and Y. Nagame
On-line Isothermal Gas Chromatographic Behaviour of Group-5 Elements Nb and Ta as Homologues of Db
53rd Symp. on Radiochemistry, Tokyo, Japan (Sep. 28, 2009).

N. Sato, M. Asai, K. Tsukada, T.K. Sato, A. Toyoshima, Z.J. Li, X. H. Liang, T. Kikuchi, Y. Nagame and S. Ichikawa
Measurement of the ionization potential of Lr (Z = 103)
6th Int. Workshop on "Physics with Stopped and Slow Radioisotope Beams, Tokyo, Japan (Mar. 1-2, 2010).

8.5 Nuclear Theory

Journal/Proceedings

Y. Aritomo

Analysis of dynamical processes using the mass distribution of fission fragments in heavy-ion reactions

Phys. Rev., C80 (2009) 064604.

Y. Aritomo

Analysis of dynamical process with mass distribution of fission fragment in heavy ion reactions

Eur. Phys. J., Web of Conferences 2(2010) 07004.

R. Kanungo, C. Nociforo, A. Prochazka, T. Aumann, D. Boutin, D. Cortina-Gil, B. Davids, M. Diakaki, F. Farinon, H. Geissel, R. Gernhauser, J. Gerl, R. Janik, B. Jonson, B. Kindler, R. Knobel, R. Krucken, M. Lantz, H. Lenske, Y. Litvinov, B. Lommel, K. Mahata, P. Maierbeck, A. Musumarra, T. Nilsson, T. Otsuka, C. Perro, C. Scheidenberger, B. Sitar, P. Strmen, B. Sun, I. Szarka, I. Tanihata, Y. Utsuno, H. Weick and M.Winkler

One-Neutron Removal Measurement Reveals ^{24}O as a New Doubly Magic Nucleus

Phys. Rev. Lett., 102 (2009) 152501-1-4.

Y. Utsuno, T. Otsuka, B.A. Brown, M. Honma and T. Mizusaki

Shell evolution in the sd-pf shell studied by the shell model

6th Japan-Italy Symposium on Heavy-Ion Physics, Tokai, Japan (Nov. 11-15, 2008)

AIP Conf. Proc., 1120 (2009) 81-86.

M. De Rydt, G. Neyens, K. Asahi, D.L. Balabanski, J.M. Daugas, M. Depuydt, L. Gaudefroy, S. Grevy, Y. Hasama, Y. Ichikawa, P. Morel, T. Nagatomo, T. Otsuka, L. Perrot, K. Shimada, C. Stodel, J.C. Thomas, H. Ueno, Y. Utsuno, W. Vanderheijden, N. Vermeulen, P. Vingerhoets and A. Yoshimi

Precision measurement of the electric quadrupole moment of ^{31}Al and determination of the effective proton charge in the sd-shell

Phys. Lett., B678 (2009) 344-349.

M. Ionescu-Bujor, A. Iordachescu, S.M. Lenzi, D.R. Napoli, N. Marginean, N.H. Medina, D. Bazzacco, D. Bucurescu, G.de Angelis, F. Della Vedova, E. Farnea, A. Gadea, R. Menegazzo, S. Lunardi, C.A. Ur, S. Zilio, T. Otsuka and Y. Utsuno

High-spin structure of ^{37}Cl, intruder excitations, and the sd-fp shell gap

Phys. Rev., C80 (2009) 034314-1-12.

T. Nakamura, N. Kobayashi, Y. Kondo, Y. Satou, N. Aoi, H. Baba, S. Deguchi, N. Fukuda, J. Gibelin, N. Inabe, M. Ishihara, D. Kameda, Y. Kawada, T. Kubo, K. Kusaka, A. Mengoni, T. Motobayashi, T. Ohnishi, M. Ohtake, N.A. Orr, H. Otsu, T. Otsuka, A. Saito, H. Sakurai, S. Shimoura, T. Sumikama, H. Takeda, E. Takeshita, M. Takechi, S. Takeuchi, K. Tanaka, K.N. Tanaka, N. Tanaka, Y. Togano, Y. Utsuno, K. Yoneda, A. Yoshida and K. Yoshida
Halo Structure of the Island of Inversion Nucleus ^{31}Ne
Phys. Rev. Lett., 103 (2009) 262501-1-4.

T. Otsuka, T. Suzuki, M. Honma, Y. Utsuno, N. Tsunoda, K. Tsukiyama and M. Hjorth-Jensen
Novel Features of Nuclear Forces and Shell Evolution in Exotic Nuclei
Phys. Rev. Lett., 104 (2010) 012501-1-4.

J.Y. Lee, I. Hahn, Y. Kim, S.W. Hong, S. Chiba and E.S. Soukhovitskii
Optical potentials for nuclear level structures and nucleon interactions data of tin isotopes based on the soft-rotator model
Phys. Rev., C79 (2009) 064612.

O. Iwamoto, T. Nakagawa, N. Otuka, S. Chiba, K. Okumura, G. Chiba, T. Ohsawa and K. Furutaka
JENDL Actinoid File 2008
J. Nucl. Sci. Tech., 46 (2009) 510.

S. Kunieda, S. Chiba, K. Shibata, A. Ichihara, O. Iwamoto, N. Iwamoto, T. Fukahori and E.Sh. Soukhovitski
An Extensive Study of the Soft-rotator Model Hamiltonian Parameters for Medium and Heavy Even-even Nuclei
J. Nucl. Sci. Technol., 46 (2009) 914.

F. Minato, S. Chiba and K. Hagino
Fission of heavy Λ hypernuclei with the Skyrme-Hartree-Fock approach
Nucl. Phys., A 831 (2009) 150.

T. Maruyama, T. Tatsumi and S. Chiba
Liquid-gas phase transition in asymmetric nuclear matter at finite temperature
Nucl. Phys., A834 (2010) 561.

M. Kohno and S. Hashimoto
Ξ-nucleus potential and (K-,K+) inclusive spectrum at Ξ production threshold region
Prog. Theor. Phys., 123 (2010) 157-167.

S. Hashimoto, K. Ogata, S. Chiba and M. Yahiro

New Approach for Evaluating Incomplete and Complete Fusion Cross Sections with Continuum-Discretized Coupled-Channels Method

Prog. Theor. Phys., 122 (2009) 1291-1300.

O.V. Bespalova, I.N. Boboshin, V.V. Varlamov, T.A. Ermakova, B.S. Ishkhanov, S.Yu. Komarov, H. Koura, E.A. Romanovskii and T.I. Spasskaya

Energies of the Single-Particle Proton 1f and 2p States in the ^{58,60,62,64}Ni Isotopes

Bull. Russian Academy of Science: Physics, 73 (2009) 820-823.

K. Morita, K. Morimoto, D. Kaji, H. Haba, K. Ozeki, Y. Kudou, N. Sato, T. Sumita, A. Yoneda, T. Ichikawa, Y. Fujimori, S. Goto, E. Ideguchi, K. Katori, Y. Komori, H. Koura, H. Kudo, K. Ooe, A. Ozawa, F. Tokanai, K. Tsukada, T. Yamaguchi and A. Yoshida

Decay properties of ^{266}Bh and ^{262}Db produced in the ^{248}Cm + ^{23}Na reaction

J. Phys. Soc. Jpn, 78 (2009) 064201.

T. Tachibana, H. Koura and S. Chiba

Calculation of beta-delayed fission and neutron emission probabilities with the use of gross theory and KTUY mass formula

JAEA-Conf 2009-004 (2009)129-134.

H. Koura, T. Tachibana and S. Chiba,

Global Properties of Nuclear Decay Modes

JAEA-Conf 2009-004 (2009) 135-140.

Meetings

Y. Aritomo

Analysis of Dynamical process with mass distribution of fission fragments using actinide target nuclei

Int. symp. on Exotic Nuclei, Sochi, Russia (Sep. 28, 2009).

Y. Aritomo

Analysis of dynamical process with mass distribution of fission fragment in heavy ion reactions

2nd Int. Workshop on Compound Nuclear Reactions and Related Topics, Bordeaux, France (Oct. 5, 2009).

Y. Aritomo

Fusion-fission and quasi-fission processes in reactions using actinide target nuclei

Int. Conf. on Nuclear Reactions on Nucleons and Nuclei, Messina, Italy (Oct. 8, 2009).

Y. Aritomo

Potential energy surface and fission dynamics for heavy and superheavy mass nuclei

Workshop of nuclear data 2009, Tokai, Japan (Nov. 26, 2009).

Y. Aritomo, S. Chiba and S. Hashimoto

Analysis of surrogate reaction with unified model

Annual meeting of the Physical Society of Japan, Okayama, Japan (Mar. 20-23, 2010).

Y. Aritomo, S. Chiba, S. Hashimoto, Y. Utsun and H. Koura

Description of surrogate reaction with unified model

Annual Meeting of the Atomic Energy Society of Japan, Mito, Japan (Mar. 26-28, 2010).

Y. Utsuno, T. Otsuka, B.A. Brown, M. Honma and T. Mizusaki

Shell evolution in N~28 unstable nuclei studied by the shell model

Arctic FIDIPRO-EFES Workshop "Future Prospects of Nuclear Structure Physics", Saariselkä, Finland (Apr. 20, 2009).

Y. Utsuno and S. Chiba

Towards a microscopic nuclear-structure calculation of medium-heavy and heavy nuclei for the practical purpose

2nd Japan Forum of Nuclear Astrophysics Workshop "Nuclear Data in Japan−Nuclear Energy in the Heaven and the Earth," Wako, Japan (Jul. 27, 2009).

Y. Utsuno

Evolution of shell and nuclear structure in the neutron rich region

Third Joint Meeting of the Nuclear Physics Divisions of the APS and JPS, Waikoloa, U.S.A. (Oct. 13-17, 2009).

Y. Utsuno, T. Otsuka, B.A. Brown, M. Honma and T. Mizusaki

Shell evolution of exotic nuclei beyond N=28 described by the universal monopole picture

EFES-NSCL Workshop on Perspectives on the Modern Shell Model and Related Experimental Topics, East Lansing, U.S.A. (Feb. 4, 2010).

Y. Utsuno, T. Otsuka, B.A. Brown, M. Honma and T. Mizusaki

Structure of exotic nuclei around and beyond N=28

Workshop on Exotic Nuclei and Modern Shell Model, Tokyo, Japan (Feb. 9, 2010).

Y. Utsuno and S. Chiba

Description of multi-particle multi-hole states around oxygen isotopes with the p-sd shell model

Annual Meeting of the Physical Society of Japan, Okayama, Japan (Mar. 20-23, 2010).

Y. Utsuno and S. Chiba

Theoretical research on surrogate reaction‐4. Unified description of multi-particle multi-hole states in oxygen isotopes by the shell model

Annual Meeting of the Atomic Energy Society of Japan, Mito, Japan (Mar. 26-28, 2010).

S. Chiba, E. Sh. Soukhovitskij, R. Capote and J.M. Quesada

A Dispersive, Lane-consistent Coupled-channel Optical Model Based on Soft-rotator Theory for Accurate Calculation of Nuclear Reaction Data

Int. Cong. on Advances in Nuclear Power Plants, Tokyo, Japan (May 12, 2009).

S. Chiba

Surrogate Project at JAEA

Fall Meeting of the Atomic Energy Society of Japan, Sendai, Japan (Sep. 16-18, 2009).

S. Chiba

Fission Fragment Mass Distribution and r-process Nucleosynthesis

Tours Symp. on Nuclear Physics and Astrophysics VII, Kobe, Japan (Nov. 18, 2009).

S. Chiba

Application of the Surrogate Method to Researches in Nuclear Energy

Annual Meeting of the Physics Society of Japan, Okayama, Japan (Mar. 20-23, 2010).

S. Chiba and O. Iwamoto

Verification of the Surrogate Ratio Method

Annual Meeting of the Atomic Energy Society of Japan, Mito, Japan (Mar. 26-28, 2010).

D. Ichinkhorloo, T. Matsumoto, Y. Hirabayashi, K. Kato and S. Chiba

^{6}Li+n Inelastic Reactions in the continuum Discretized Coupled channels (CDCC) method

Annual Meeting of the Atomic Energy Society of Japan, Mito, Japan (Mar. 26-28, 2010).

S. Hashimoto, S. Chiba, Y. Aritomo and Y. Utsuno

Theoretical Research on Surrogate Reaction -3. Study of excited states produced by direct reaction process-

Spring Meeting of the Atomic Energy Society of Japan, Mito, Japan (Mar. 26-28, 2010).

S. Hashimoto, K. Ogata, S. Chiba and M. Yahiro

Analysis of deuteron induced incomplete fusion reactions on heavy targets with Continuum-Discretized Coupled-Channels method

Annual Meeting of the Physical Society of Japan, Okayama, Japan (Mar. 20-23, 2010).

S. Hashimoto, K. Ogata, S. Chiba and M. Yahiro

New Approach with CDCC for Evaluating Incomplete and Complete Fusion Cross Sections

Int. Workshop on Direct Reactions with Exotic Breams, Florida, U.S.A.(Dec. Dec. 13-17, 2009).

H. Koura

Global properties of nuclei and nuclear data -- nuclear masses and related ones --

Workshop on Nuclear Data and its Application to Nuclear Astrophysics, Wako, Japan (Apr. 20, 2009).

M.S. Smith, E. Lingerfelt, K. Bucker, C.D. Nesaraja, H. Koura and F. Kondev

Masses of Unstable Nuclei: Visualization and Analysis at nuclearmasses.org

8th Int. Conf. of Radioactive Nuclear Beams, Grand Rapids, U.S.A. (May. 26-30,2009).

K. Morimoto, K. Morita, D. Kaji, H. Haba, K. Ozeki, Y. Kudou, N. Sato, T. Sumita, A. Yoneda, T. Ichikawa, Y. Fujimori, S. Goto, E. Ideguchi, Y. Kasamatsu, K. Katori, Y. Komori, H. Koura, H. Kudo, K. Ooe, A. Ozawa, F. Kokanai, K. Tsukada, T. Yamaguchi and A. Yoshida

Production and decay properties of ^{266}Hs and its daughter nuclei

53rd Symp. on Radiochemistry, Tokyo, Japan (Sep.28-30, 2009).

D. Kaji, K. Morimoto, N. Sato, H. Haba, T. Ichikawa, E. Ideguchi, H. Koura, Y. Kudou, A. Ozawa, K. Ozeki, T. Sumita, T. Yamaguchi, A. Yoneda, A. Yoshida and K. Morita

Production and decay properties of a new isotope of ^{263}Hs

53rd Symp. on Radiochemistry, Tokyo, Japan (Sep. 28-30, 2009).

H. Koura

Decay modes and a limit of existence of nuclei in the superheavy mass region

4th Asia-Pacific Symposium on Radiochemistry '09, Napa, U.S.A. (Nov. 29-Dec. 5, 2009).

H. Koura

Decay modes and a limit of existence of nuclei in the heavy and superheavy mass region

Annual Meeting of the Physical Society of Japan, Okayama, Japan (Mar. 20-23, 2010).

M.S. Smith , E.J. Lingerfelt, C.D. Nesaraja, H. Koura and F.G. Kondev

Nuclear Masses: Sharing, Visualization, and Analysis at nuclearmasses.org

APS Spring Meeting in Feb. 2010, Washington DC, U.S.A. (Feb.13-16, 2010).

M.S. Smith, E. Lingerfelt, C.D. Nasaraja, H. Koura and P.G. Kondev

Nuclear Mass Visualization and Analysis at nuclearmsses.org

10th Int. Symp. on Origin of Matter and Evolution of Galaxies, Osaka, Japan (Mar.8-10, 2010).

8.6   Atomic Physics and Solid-state Physics

Journal/Proceedings

K. Kawatsura, K. Takahiro, M. Sataka, M. Imai, H. Sugai, K. Ozaki, K. Kawaguchi, H. Shibata and K. Komaki
Coster-Kronig electrons from N^{q+} and O^{q+} Rydberg states produced in high-energy collisions with He
J. Phys.: Conference Series, 163 (2009) 012048(1-6).

M. Imai, M. Sataka, K. Kawatsura, K. Takahiro, K. Komaki, H. Shibata, H. Sugai and K. Nishio
Equilibrium and non-equilibrium charge-state distributions of 2 MeV/u sulfur ions passing through carbon foils
Nucl. Instrum. Methods Phys. Res., B267 (2009) 2675.

S.C. Jeong, H. Sugai and M. Yahagi
Diffusion experiment with the accelerated, short-lived radioactive beam of ^{8}Li
BUTSURI, 64 (2009) 687-691 (in Japanese).

N. Matsunami, H. Kakiuchida, M. Tazawa, M. Sataka, H. Sugai and S. Okayasu
Electronic and atomic structure modifications of copper-nitride films by ion impact and phase separation
Nucl. Instrum. Methods Phys. Res., B267 (2009) 2653.

Meetings

N. Matsunami, J. Fukushima, M. Sataka, S. Okayasu H. Sugai and H. Kakiuchida
Electrical property modifications of In-doped ZnO films by ion irradiation
15th Int. Symp. Radiation Effects in Insulators, Padova, Italy (Aug. 30-Sept. 4, 2009).

N. Matsunami, M. Sataka, S. Okayasu and H. Kakiuchida
Ion irradiation effects on tungsten-oxide films and charge state effect on electronic erosion
15th Int. Symp. Radiation Effects in Insulators, Padova, Italy (Aug. 30-Sept. 4, 2009).

N. Matsunami, H. Kakiuchida, M. Tazawa, M. Sataka, H. Sugai and S. Okayasu,
Ion irradiation effects on tungsten-oxide films and charge state effect on electronic erosion
Annual Meeting of the Physical Society of Japan, Okayama, Japan (Mar. 20-23, 2010).

8.7 Radiation Effects in Materials

Journal/Proceedings

Y.Sasaki and T.Suzuki,
Formation of Ag Clusters by Electron Beam Irradiation on Ag-Zeolite
Materials Transactions, 50 (2009) 1050.

S. Kosugi, Nao Fujita, Y. Zushi, T. Matsui, A. Iwase, N. Ishikawa and Y. Saito
Modification of magnetic properties of FeRh intermetallic compounds by energetic ion beam bombardment
Nucl. Instrum. Methods Phys. Res., B267 (2009) 1612-1615.

A. Iwase, H. Ohno, N. Ishikawa, Y. Baba, N. Hirao, T. Sonoda and M. Kinoshita
Study on the behavior of oxygen atoms in swift heavy ion irradiated CeO_2 by means of synchrotron radiation X-ray photoelectron spectroscopy
Nucl. Instrum. Methods Phys. Res., B267 (2009) 969-972.

M. Shirai , K. Tsumori, M. Kutsuwada, K. Yasuda and S. Matsumura
Morphological change in FePt nanogranular thin films induced by swift heavy ion irradiation
Nucl. Instrum. Methods Phys. Res., B267 (2009) 1787-1791.

Meetings

H. Amekura, N. Ishikawa, K. Mitsuishi, Y. Nakayama, D. Tsuya, Ch. Buchal, S. Mantl and N.Kishimoto
Irradiation effects of swift heavy ions on Zn and ZnO nanoparticles
15th Int. Symp. on Radiation Effects in Insulators, Padova, Italy (Aug. 30-Sept. 4, 2009).

H. Amekura, N. Ishikawa, K. Mitsuishi, Y. Nakayama, D. Tsuya, Ch. Buchal, S. Mantl and N.Kishimoto
Irradiation effects of swift heavy ions on Zn and ZnO nanoparticles
16th Int. Conf. on Surface Modification of Materials by Ion Beams, Tokyo, Japan (Sep. 13-18, 2009).

H. Amekura, N. Ishikawa, K. Mitsuishi, Y. Nakayama, D. Tsuya, Ch. Buchal, S. Mantl and N.Kishimoto
Irradiation effects of swift heavy ions on Zn and ZnO nanoparticles
19th MRS-J Academic Symposium, Yokohama, Japan (Dec. 7-9, 2009).

M. Sasase, K. Shimura, K. Yamaguchi, H. Yamamoto, S. Shamoto and K. Hojou
Sputter etching effect of the substrate on the microstructure of β-FeSi$_2$ thin film prepared by ion beam sputter deposition method
17th Int. Vacuum Congress, Stockholm, Sweden (July 2-6, 2007).

S. Kosugi, Nao Fujita, Y. Tahara, N. Ishikawa, T. Matsui, F. Horiand and A. Iwase
Effect of high temperature annealing on the irradiation-induced magnetic properties of FeRh alloy

Fall Meeting of the Physical Society of Japan, Kumamoto, Japan (Sep. 25-28, 2009).

M. Shirai, K. Tsumori, K. Yasuda and S. Matsumura,

Modification of Structure and Composition of FePt Nanoparticles Embeded in Amorphous Al$_2$O$_3$ Matrix by Swift Heavy Ions Irradiation

12th Frontiers of Electron Microscopy in Materials Sciemnce, Sasebo, Japan (Sep.27-Oct.2, 2009).

S. Matsumura, T. Yamamoto and K. Yasuda

Atomic-scale Analysis of Irradiation-induced Structural Change in Magnesium Aluminate Spinel Compound

2009 MRS Fall Meeting, Boston, U.S.A. (Nov. 30-Dec. 4, 2009).

K. Yasuda, M. Etoh, S, Kawasoe, T. Yamamoto and S. Matsumura,

Accumulation of disordered zone in MgAl$_2$O$_4$ irradiated with swift heavy ions

15th Int. Symp. on Radiation Effects in Insulators, Padova, Italy (Aug. 30-Sept. 4, 2009).

N. Ishikawa and K. Takegahara

Radiation damage due to high-density electronic excitation in CeO$_2$ irradiated with high-energy ions

Fall Meeting of the Physical Society of Japan, Kumamoto, Japan (Sep. 25-28, 2009).

N. Ishikawa, H. Sugai and T. Sonoda

Irradiation damage in CeO$_2$ irradiated with high-energy heavy ions

15th Int. Symp. on Radiation Effects in Insulators, Padova, Italy (Aug. 30-Sept. 4, 2009).

T. Sueyoshi, S. Yutani, T. Sogo, A. Adachi, K. Yonekura, T. Fujiyoshi, F. Mitsugi, T. Ikegami, N. Ishikawa, S. Awaji and K. Watanabe

Angular dependence of critical current densities in YBCO thin films with crossed columnar defects

22nd Int. Symp. on Superconductivity, Tsukuba, Japan (Nov. 3, 2009).

T. Sonoda, M. Kinoshita, N. Ishikawa, M. Sataka, A. Iwase and K. Yasunaga

Clarification of high density electronic excitation effects on the microstructural evolution in UO$_2$

15th Int. Conf. of Radiation Effects in Insulators, Padova, Italy (Aug. 30-Sept. 4, 2009).

T. Kumada, Y. Noda, S. Koizumi and T. Hashimoto

Spatial distribution of electron spins studied by polarized protons and polarized neutrons

Annual Meeting of the Japanese Society of Neutron Science, Tokai, Japan (Dec. 9, 2009).

CHAPTER 9

Personnel and Committee

This is a blank page.

9.1 Personnel

Department of Research Reactor and Tandem Accelerator

Kiyonobu	Yamashita	Director
Tsuyoshi	Kusunoki	Deputy Director
Yuichi	Terakado	Manager of Administration Section
Masao	Sataka	
Suehiro	Takeuchi	

Department of Research Reactor and Tandem Accelerator

*Tandem Accelerator Section (* General Manager)*

Scientific Staff

Tetsuro	Ishii*
Akihiko	Osa
Makoto	Matsuda

Technical Staff

Yoshihiro	Tsukihashi
Susumu	Hanashima
Shin-ichi	Abe
Nobuhiro	Ishizaki
Hidekazu	Tayama
Takamitsu	Nakanoya
Hiroshi	Kabumoto
Masahiko	Nakamura
Ken-ichi	Kutsukake
Yoshinori	Otokawa
Takuhiro	Asozu

Entrusted Operators

Takahiro	Yoshida
Takayuki	Ishiguro
Kazushi	Yamaguchi
Nobuo	Seki
Teruo	Onodera
Hikaru	Nisugi

Department of Radiation Protection

Facility Radiation Control Section I

Kunio	Kawarai
Katsuji	Yasu

Hayato   Hiraga

Daisuke   Higashi

Susumu   Kinase

Advanced Science Research Center

Yoshihiko   Hatano   Director

Hiroshi   Ikezoe   Deputy Director

Advanced Science Research Center

*Research Group for Shell Structure and Reaction Properties of Heavy Nuclei far from Stability (* Group Leader)*

Hiroari   Miyatake*

Satoshi   Chiba

Toshiki   Maruyama

Shin-ichi   Mitsuoka

Katsuhisa   Nishio

Hiroyuki   Koura

Yutaka   Utsuno

Ichiro   Nishinaka

Hiroyuki   Makii

Daisuke   Nagae   (Post Doc. to July 31)

Shintaro   Hashimoto   (Post Doc.)

Yasuo   Wakabayashi   (Post Doc)

Shin-ichi   Ichikawa   (to Aug. 31)

Ryuta   Takahashi   (Student)

Advanced Science Research Center

*Research Group for Nuclear Chemistry of the Heaviest Elements (* Group Leader)*

Yuichiro   Nagame*

Kazuaki   Tsukada

Masato   Asai

Tetsuya K. Sato

Atsushi   Toyoshima   (Senior Post Doc.)

Zi Jie   Li   (Post Doc.)

Nozomi   Sato   (Post Doc.)

Takahiro   Kikuchi   (Student)

Advanced Science Research Center

Research Group for Material Design under Extreme Conditions

Satoru   Okayasu

Norito   Ishikawa

Hiroyuki Sugai

Teruo   Kato   (to Sep. 30)

Advanced Science Research Center

Research Group for Strongly Correlated Supermolecules

Takayuki Kumada

Yohei   Noda   (Post Doc.)

Nuclear Science and Engineering Directorate

*Innovative Nuclear Science Research Group (* Group Leader)*

Masumi   Oshima[*]

Hideo   Harada

Hideki   Iimura

Mitsuo   Koizumi

Kazuyoshi Furutaka

Fumito   Kitatani

Shoji   Nakamura

Yosuke   Toh

Atsushi   Kimura

Yasuki   Nagai   (Invited Researcher)

Kaoru   Hara   (Senior Post Doc.)

Tadahiro Kin   (Senior Post Doc.)

Futoshi   Minato   (Post Doc.)

Nuclear Science and Engineering Directorate

*Research Group for Irradiation Field Materials (* Group Leader)*

Shiro   Jitsukawa[*]

Nariaki   Okubo

Quantum Beam Science Directorate

Laser Accelerator Group

Toshiyuki Shizuma

Takehito   Hayakawa

Quantum Beam Science Directorate

Neutron Imaging and Activation Analysis Group

Yuichi   Hatsukawa

Nuclear Safety Research Center

Reactor Component Reliability Research Group

      Yasuhiro   Chimi

      Tohru   Tobita

High Energy Accelerator Research Organization (KEK)
- Institute of Particle and Nuclear Studies –

*Radioactive Nuclear Beams Project Group (* Group Leader)*

      Sun-Chan Jeong*

      Hiroari   Miyatake

      Hironobu   Ishiyama

      Yutaka   Watanabe

      Nobuaki   Imai

      Yoshikazu Hirayama

      Michihiro Oyaizu

      Ichiro   Katayama

      Hirokane   Kawakami

      Shoji   Suzuki

High Energy Accelerator Research Organization (KEK)
- Accelerator Laboratory -

      Kazuaki   Niki

      Masashi   Okada

9.2 Research Planning and Assessment Committee

Chairman	Shigeru	Kubono	(Professor, The University of Tokyo)
Vice Chairman	Ken-ichiro	Komaki	(Professor, National Center for University Entrance Examination)
Member	Tadashi	Kambara	(Senior Scientist, RIKEN)
	Kenji	Kimura	(Professor, Kyoto University)
	Noriaki	Matsunami	(Associate Professor, Nagoya University)
	Tetsuo	Noro	(Professor, Kyushu University)
	Tsutomu	Ohtsuki	(Associate Professor, Tohoku University)
	Tadashi	Shimoda	(Professor, Osaka University)
	Koichi	Hagino	(Associate Professor, Tohoku University)
	Motoharu	Mizumoto	(Adjunct Professor, Tokyo Institute of Technology)
	Naotaka	Yoshinaga	(Professor, Saitama University)
	Yuichi	Hatsukawa	(Quantum Beam Science Directorate, JAEA)
	Shiro	Jitsukawa	(Nuclear Science and Engineering Directorate, JAEA)
	Kazumasa	Narumi	(Advanced Science Research Center, JAEA)
	Tetsuro	Ishii	(Deputy Director, Dep. Research Reactor and Tandem Accelerator, JAEA)
	Suehiro	Takeuchi	(Dep. Research Reactor and Tandem Accelerator, JAEA)
	Masao	Sataka	(Dep. Research Reactor and Tandem Accelerator, JAEA)
	Kiichi	Hojo	(Advanced Science Research Center, JAEA)
Organizer Secretary			
	Shin-ichi	Mitsuoka	(Advanced Science Research Center, JAEA)
	Norito	Ishikawa	(Advanced Science Research Center, JAEA)
	Masato	Asai	(Advanced Science Research Center, JAEA)
	Hiroshi	Ikezoe	(Deputy Director, Advanced Science Research Center, JAEA)

This is a blank page.

CHAPTER 10

Cooperative Researches and Common Use in JAEA

10.1 Cooperative Research Programs

10.2 Common Use Programs in JAEA

This is a blank page.

10.1 Cooperative Research Programs

Title	Contact Person & Organization
1. Production of neutron-deficient actinide nuclei with closed neutron shell 126	Hiroari MIYATAKE High Energy Accelerator Research Organization (KEK)
2. Study of new fission channels populated by quai-fission	Tsutomu OHTSUKI Tohoku University
3. Reduction of mendelevium using an electrochemistry apparatus	Atsushi SHINOHARA Osaka University
4. Sulfate complexation of rutherfordium in H_2SO_4/HNO_3 mixed solution	Hisaaki KUDO Niigata University
5. Mechanism of grain subdivision process due to irradiation of FP in UO_2	Takeshi SONODA Central Research Institute of Electric Power Industry
6. Metal-semiconductor transition control on a $FeSi_2$ thin film with high energy heavy ion irradiations	Masato SASASE The Wakasa-wan Energy Research Center
7. Nano-fabrication of zeolite with high energy ion irradiations	Yukichi SASAKI Japan Fine Ceramics Center
8. Effects on clad material by swift heavy ion irradiation	Takeshi SONODA Central Research Institute of Electric Power Industry
9. Electrical property modifications of In-doped ZnO films by high-energy ion impact	Noriaki MATUNAMI Nagoya University
10. Heavy ion irradiation effects on CeO_2 including other elements	Akihiro IWASE Osaka Prefecture University
11. Charge state evolution of heavy ions passing through solid targets	Makoto IMAI Kyoto University

10.1 Cooperative Research Programs (cont.) from FY2007 and FY2008

12. Barrier distribution derived from quasi-electric backscattering in heavy nucleus-nucleus collision leading to superheavy element production	Sun-Chan JEONG High Energy Accelerator Research Organization(KEK)
13. Laser Spectroscopy of the Neutron Deficient Isotopes in Tungsten Region	Takayashi HORIGUCHI Hiroshima International University
14. Study of nuclear fission from excited states of heavy actinide nuclei	Akihiko YOKOYAMA Kanazawa University
15. Development of spectrometer for in-beam γ-ray spectroscopy of super-heavy nuclei	Toshiyuki KOUNO Tokyo Institute of Technology
16. Development of a method for indirect determination of the (n,γ) cross sections by in-beam gamma-ray spectroscopy	Hiroari MIYATAKE KEK

10.1 Cooperative Research Programs (cont.) using TRIAC

Title	Contact Person & Organization
17. Development of accelerator technology for short-lived radioactive nuclear beam	Sun-Chan JEONG KEK
18. Development of the GEM-MSTPC for the measurement of the $^8Li(\alpha, n)^{11}B$ reaction	Tomokazu FUKUDA Osaka Electro-Communication University
19. Search for highly excited ^{11}Be states in ^9Li+d reactions	Takashi TERANISHI Kyushu University
20. Diffusion coefficient measurements on perovskite-type lithium ion conductor	Shigeomi TAKAI Tottori University
21. Diffusion coefficient measurements of perovskite-type lithium ion conductive oxides	Sun-Chan JEONG KEK
22. Coulomb excitation of ^{130}Ba at 1.1 MeV/nucleon	Nobuaki IMAI KEK

10.2 Common Use Programs in JAEA

Title	Contact Person & Organization
1. Heavy ion irradiation induced ferromagnetism in FeRh alloys	Akihiro IWASE Osaka Prefecture University
2. Elongation of Au nanoparticle in SiO_2 matrix irradiated with swift heavy ions	Syo MATSUMURA Faculty of Engineering, Kyushu University
3. High-energy ion impact effects on atomic structure and optical property of In-doped ZnO films	Noriaki MATUNAMI Nagoya University
4. Decay study on fission products with on-line isotope separator	Michihiro SHIBATA Nagoya University
5. Gas-phase chemistry of Zr and Hf using carbon cluster transport system	Shin-ichi GOTO Niigata University
6. Zero-degree electron spectroscopy of collision induced highly charged ions and electronic processes	Makoto IMAI Kyoto University
7. Fission properties of the neutron-deficient nucleus ^{180}Hg produced in heavy ion reactions	Andrei N. ANDREYEV The University of the West of Scotland
8. Shape and property control of Zn and ZnO nanoparticles by swift heavy ions	Hiroshi AMEKURA National Institute for Materials Science
9. Angular dependences of flux pinning properties in YBCO thin films with crossed columnar defects	Tetsuro SUEYOSHI Graduated School of Kumamoto University
10. Radiation damage test for Virtex5 FPGA	Yoshiyuki YAMADA Graduate School of Kyoto University
11. High energy alpha particles emitted from nuclear reaction	Nobuaki IMAI KEK
12. Swift ion implantation for fabrication of optical waveguides	Tadashi NARUSAWA Kochi University of Technology
13. Indirect determination of neutron radioactive capture cross section on medium nuclei	Nobuaki IMAI KEK
14. Systematic study of signature inversion and shape coexistence in high-spin states of medium-heavy nuclei	Xiao Hong ZHOU Institute of Modern Physics Chinese Academy of Science

This is a blank page.

国際単位系（SI）

表1．SI 基本単位

基本量	SI 基本単位 名称	記号
長　　さ	メートル	m
質　　量	キログラム	kg
時　　間	秒	s
電　　流	アンペア	A
熱力学温度	ケルビン	K
物　質　量	モル	mol
光　　度	カンデラ	cd

表2．基本単位を用いて表されるSI組立単位の例

組立量	SI 基本単位 名称	記号
面　　　　積	平方メートル	m²
体　　　　積	立法メートル	m³
速さ，速度	メートル毎秒	m/s
加　速　度	メートル毎秒毎秒	m/s²
波　　　数	毎メートル	m⁻¹
密度，質量密度	キログラム毎立方メートル	kg/m³
面　積　密　度	キログラム毎平方メートル	kg/m²
比　　体　　積	立方メートル毎キログラム	m³/kg
電　流　密　度	アンペア毎平方メートル	A/m²
磁界の強さ	アンペア毎メートル	A/m
量濃度 (a)，濃度	モル毎立方メートル	mol/m³
質　量　濃　度	キログラム毎立法メートル	kg/m³
輝　　　　度	カンデラ毎平方メートル	cd/m²
屈　折　率 (b)	（数字の）1	1
比　透　磁　率 (b)	（数字の）1	1

(a) 量濃度（amount concentration）は臨床化学の分野では物質濃度（substance concentration）ともよばれる。
(b) これらは無次元量あるいは次元1をもつ量であるが、そのことを表す単位記号である数字の1は通常は表記しない。

表5．SI 接頭語

乗数	接頭語	記号	乗数	接頭語	記号
10²⁴	ヨ　タ	Y	10⁻¹	デ　シ	d
10²¹	ゼ　タ	Z	10⁻²	センチ	c
10¹⁸	エクサ	E	10⁻³	ミ　リ	m
10¹⁵	ペ　タ	P	10⁻⁶	マイクロ	µ
10¹²	テ　ラ	T	10⁻⁹	ナ　ノ	n
10⁹	ギ　ガ	G	10⁻¹²	ピ　コ	p
10⁶	メ　ガ	M	10⁻¹⁵	フェムト	f
10³	キ　ロ	k	10⁻¹⁸	ア　ト	a
10²	ヘクト	h	10⁻²¹	ゼプト	z
10¹	デ　カ	da	10⁻²⁴	ヨクト	y

表6．SIに属さないが、SIと併用される単位

名称	記号	SI 単位による値
分	min	1 min=60s
時	h	1h =60 min=3600 s
日	d	1 d=24 h=86 400 s
度	°	1°=(π/180) rad
分	’	1’=(1/60)°=(π/10800) rad
秒	”	1”=(1/60)’=(π/648000) rad
ヘクタール	ha	1ha=1hm²=10⁴m²
リットル	L, l	1L=1l=1dm³=10³cm³=10⁻³m³
トン	t	1t=10³ kg

表3．固有の名称と記号で表されるSI組立単位

組立量	SI 組立単位 名称	記号	他のSI単位による表し方	SI基本単位による表し方
平　　面　　角	ラジアン (b)	rad	1 (b)	m/m
立　　体　　角	ステラジアン (b)	sr (c)	1 (b)	m²/m²
周　波　数	ヘルツ (d)	Hz		s⁻¹
力	ニュートン	N		m kg s⁻²
圧　力，応　力	パスカル	Pa	N/m²	m⁻¹ kg s⁻²
エネルギー, 仕事, 熱量	ジュール	J	N m	m² kg s⁻²
仕事率, 工率, 放射束	ワット	W	J/s	m² kg s⁻³
電　荷，電　気　量	クーロン	C		s A
電位差（電圧），起電力	ボルト	V	W/A	m² kg s⁻³ A⁻¹
静　電　容　量	ファラド	F	C/V	m⁻² kg⁻¹ s⁴ A²
電　気　抵　抗	オーム	Ω	V/A	m² kg s⁻³ A⁻²
コンダクタンス	ジーメンス	S	A/V	m⁻² kg⁻¹ s³ A²
磁　　　　束	ウェーバ	Wb	Vs	m² kg s⁻² A⁻¹
磁　束　密　度	テスラ	T	Wb/m²	kg s⁻² A⁻¹
インダクタンス	ヘンリー	H	Wb/A	m² kg s⁻² A⁻²
セルシウス温度	セルシウス度 (e)	℃		K
光　　　　束	ルーメン	lm	cd sr (c)	cd
照　　　　度	ルクス	lx	lm/m²	m⁻² cd
放射性核種の放射能 (f)	ベクレル (d)	Bq		s⁻¹
吸収線量, 比エネルギー分与, カーマ	グレイ	Gy	J/kg	m² s⁻²
線量当量, 周辺線量当量, 方向性線量当量, 個人線量当量	シーベルト (g)	Sv	J/kg	m² s⁻²
酸　素　活　性	カタール	kat		s⁻¹ mol

(a)SI接頭語は固有の名称と記号を持つ組立単位と組み合わせても使用できる。しかし接頭語を付した単位はもはやコヒーレントではない。
(b)ラジアンとステラジアンは数字の1に対する単位の特別な名称で、量についての情報をつたえるために使われる。実際には、使用する時には記号rad及びsrが用いられるが、習慣として組立単位としての記号である数字の1は明示されない。
(c)測光学ではステラジアンという名称と記号srを単位の表し方の中に、そのまま維持している。
(d)ヘルツは周期現象についてのみ、ベクレルは放射性核種の統計的過程についてのみ使用する。
(e)セルシウス度はケルビンの特別な名称で、セルシウス温度を表すために使用される。セルシウス度とケルビンの単位の大きさは同一である。したがって、温度差や温度間隔を表す数値はどちらの単位で表しても同じである。
(f)放射性核種の放射能（activity referred to a radionuclide）は、しばしば誤った用語で"radioactivity"と記される。
(g)単位シーベルト（PV,2002,70,205）についてはCIPM勧告2（CI-2002）を参照。

表7．SIに属さないが、SIと併用される単位で、SI単位で表される数値が実験的に得られるもの

名称	記号	SI 単位で表される数値
電　子　ボ　ル　ト	eV	1eV=1.602 176 53(14)×10⁻¹⁹J
ダ　ル　ト　ン	Da	1Da=1.660 538 86(28)×10⁻²⁷kg
統一原子質量単位	u	1u=1 Da
天　文　単　位	ua	1ua=1.495 978 706 91(6)×10¹¹m

表8．SIに属さないが、SIと併用されるその他の単位

名称	記号	SI 単位で表される数値
バ　　ー　　ル	bar	1 bar=0.1MPa=100kPa=10⁵Pa
水銀柱ミリメートル	mmHg	1mmHg=133.322Pa
オングストローム	Å	1 Å=0.1nm=100pm=10⁻¹⁰m
海　　　　　里	M	1 M=1852m
バ　　ー　　ン	b	1 b=100fm²=(10⁻¹²cm)2=10⁻²⁸m²
ノ　　ッ　　ト	kn	1 kn=(1852/3600)m/s
ネ　ー　パ	Np	SI単位との数値的な関係は、対数量の定義に依存。
ベ　　ル	B	
デ　ジ　ベ　ル	dB	

表4．単位の中に固有の名称と記号を含むSI組立単位の例

組立量	SI 組立単位 名称	記号	SI 基本単位による表し方
粘　　　　　度	パスカル秒	Pa s	m⁻¹ kg s⁻¹
力のモーメント	ニュートンメートル	N m	m² kg s⁻²
表　面　張　力	ニュートン毎メートル	N/m	kg s⁻²
角　　速　　度	ラジアン毎秒	rad/s	m m⁻¹ s⁻¹=s⁻¹
角　加　速　度	ラジアン毎秒毎秒	rad/s²	m m⁻¹ s⁻²=s⁻²
熱流密度, 放射照度	ワット毎平方メートル	W/m²	kg s⁻³
熱容量, エントロピー	ジュール毎ケルビン	J/K	m² kg s⁻² K⁻¹
比熱容量, 比エントロピー	ジュール毎キログラム毎ケルビン	J/(kg K)	m² s⁻² K⁻¹
比エネルギー	ジュール毎キログラム	J/kg	m² s⁻²
熱　伝　導　率	ワット毎メートル毎ケルビン	W/(m K)	m kg s⁻³ K⁻¹
体積エネルギー	ジュール毎立方メートル	J/m³	m⁻¹ kg s⁻²
電　界　の　強　さ	ボルト毎メートル	V/m	m kg s⁻³ A⁻¹
電　荷　密　度	クーロン毎立方メートル	C/m³	m⁻³ sA
表　面　電　荷	クーロン毎平方メートル	C/m²	m⁻² sA
電束密度, 電気変位	クーロン毎平方メートル	C/m²	m⁻² sA
誘　　電　　率	ファラド毎メートル	F/m	m⁻³ kg⁻¹ s⁴ A²
透　　磁　　率	ヘンリー毎メートル	H/m	m kg s⁻² A⁻²
モルエネルギー	ジュール毎モル	J/mol	m² kg s⁻² mol⁻¹
モルエントロピー, モル熱容量	ジュール毎モル毎ケルビン	J/(mol K)	m² kg s⁻² K⁻¹ mol⁻¹
照射線量（X線及びγ線）	クーロン毎キログラム	C/kg	kg⁻¹ sA
吸　収　線　量　率	グレイ毎秒	Gy/s	m² s⁻³
放　射　強　度	ワット毎ステラジアン	W/sr	m⁴ m⁻² kg s⁻³=m² kg s⁻³
放　射　輝　度	ワット毎平方メートル毎ステラジアン	W/(m² sr)	m² m⁻² kg s⁻³=kg s⁻³
酵素活性濃度	カタール毎立方メートル	kat/m³	m⁻³ s⁻¹ mol

表9．固有の名称をもつCGS組立単位

名称	記号	SI 単位で表される数値
エ　ル　グ	erg	1 erg=10⁻⁷ J
ダ　イ　ン	dyn	1 dyn=10⁻⁵N
ポ　ア　ズ	P	1 P=1 dyn s cm⁻²=0.1Pa s
ス　ト　ー　ク　ス	St	1 St =1cm² s⁻¹=10⁻⁴m² s⁻¹
ス　チ　ル　ブ	sb	1 sb =1cd cm⁻²=10⁴cd m⁻²
フ　ォ　ト	ph	1 ph=1cd sr cm⁻² 10⁴lx
ガ　ル	Gal	1 Gal =1cm s⁻²=10⁻²ms⁻²
マ　ク　ス　ウ　ェ　ル	Mx	1 Mx =1G cm²=10⁻⁸Wb
ガ　ウ　ス	G	1 G =1Mx cm⁻²=10⁻⁴T
エルステッド (c)	Oe	1 Oe ≙ (10³/4π)A m⁻¹

(c) 3元系のCGS単位系とSIでは直接比較できないため、等号「 ≙ 」は対応関係を示すものである。

表10．SIに属さないその他の単位の例

名称	記号	SI 単位で表される数値
キ　ュ　リ　ー	Ci	1 Ci=3.7×10¹⁰Bq
レ　ン　ト　ゲ　ン	R	1 R = 2.58×10⁻⁴C/kg
ラ　ド	rad	1 rad=1cGy=10⁻²Gy
レ　ム	rem	1 rem=1 cSv=10⁻²Sv
ガ　ン　マ	γ	1 γ =1 nT=10-9T
フ　ェ　ル　ミ		1フェルミ = 1 fm=10-15m
メートル系カラット		1メートル系カラット = 200 mg = 2×10-4kg
ト　ル	Torr	1 Torr = (101 325/760) Pa
標　準　大　気　圧	atm	1 atm = 101 325 Pa
カ　ロ　リ　ー	cal	1cal=4.1858J（「15℃」カロリー），4.1868J（「IT」カロリー）4.184J（「熱化学」カロリー）
ミ　ク　ロ　ン	µ	1 µ =1µm=10-6m